3-12-2009

Least-Squares Finite Element Formulation for Fluid-Structure Interaction

Cody C. Rasmussen

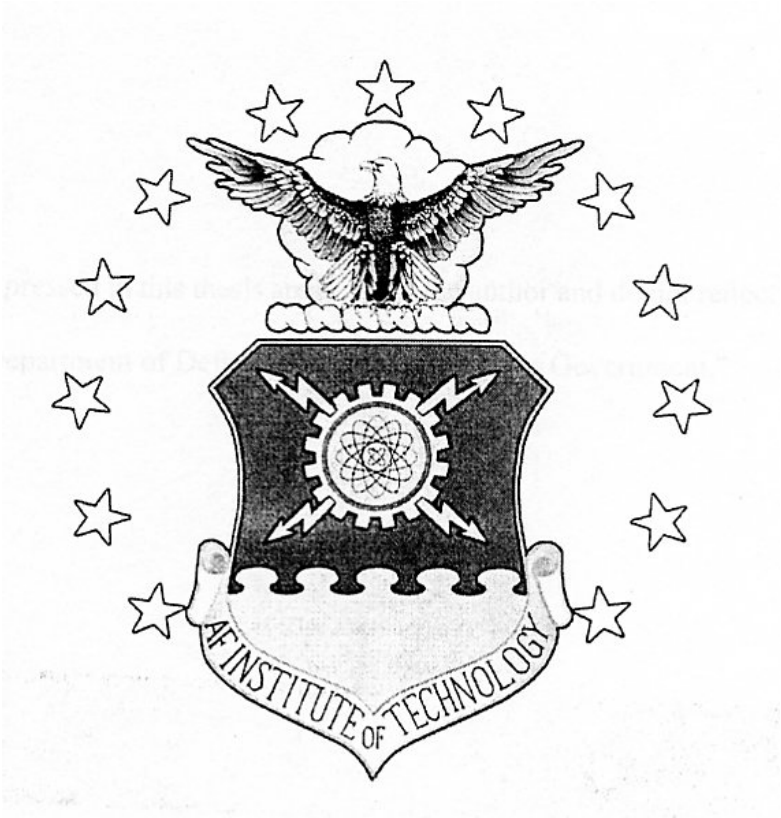

LEAST-SQUARES FINITE ELEMENT FORMULATION FOR FLUID-STRUCTURE INTERACTION

DISSERTATION

Cody C Rasmussen, Major, USAF

AFIT/DS/ENY/09-M16

DEPARTMENT OF THE AIR FORCE
AIR UNIVERSITY

AIR FORCE INSTITUTE OF TECHNOLOGY

Wright-Patterson Air Force Base, Ohio

The views expressed in this thesis are those of the author and do not reflect the official policy or position of the United States Air Force, Department of Defense, or the United States Government.

AFIT/DS/ENY/09-M16

LEAST-SQUARES FINITE ELEMENT FORMULATION FOR FLUID-STRUCTURE INTERACTION

DISSERTATION

Presented to the Faculty

Department of Aeronautics and Astronautics

Graduate School of Engineering and Management

Air Force Institute of Technology

Air University

Air Education and Training Command

In Partial Fulfillment of the Requirements for the

Degree of Philosophy

Cody C Rasmussen

Major, USAF

March 2009

APPROVED FOR PUBLIC RELEASE; DISTRIBUTION UNLIMITED

AFIT/DS/ENY/09-M16

LEAST-SQUARES FINITE ELEMENT FORMULATION FOR FLUID-STRUCTURE INTERACTION

Cody C Rasmussen

Major, USAF

Approved:

Robert A. Canfield — 27 Feb 09

Dr. Robert A. Canfield — Date
Committe Chair/Advisor

Andrew J. Lofthouse — 27 Feb 09

Maj Andrew J. Lofthouse — Date
Committee Member

Edward W. Swim — 27 Feb 09

Dr. Edward W. Swim — Date
Committee Member

JNReddy — 27 Feb 09

Dr. J.N. Reddy — Date
Committee Member

Accepted:

M U Thomas — 12 Mar 09

Dr. Marlin U. Thomas — Date
Dean, Graduate School of
Engineering and Management

AFIT/DS/ENY/09-M16

Abstract

Fluid-structure interaction problems prove difficult due to the coupling between fluid and solid behavior. Typically, different theoretical formulations and numerical methods are used to solve fluid and structural problems separately. The least-squares finite element method is capable of accurately solving both fluid and structural problems. This capability allows for a simultaneously coupled fluid structure interaction formulation using a single variational approach to solve complex and nonlinear aeroelasticity problems. The least-squares finite element method was compared to commonly used methods for both structures and fluids individually. The fluid analysis was compared to finite volume methods and the structural analysis type compared to traditional Weak Galerkin finite element methods. The simultaneous solution method was then applied to aeroelasticity problems with a known solution. Achieving these results required unique iterative methods to balance each domain's or differential equation's weighting factor within the simultaneous solution scheme. The scheme required more computational time but it did provide the first hands-off method capable of solving complex fluid-structure interaction problems using a simultaneous least-squares formulation. A sequential scheme was also examined for coupled problems.

Table of Contents

List of Figures

List of Tables

List of Symbols

Symbol	Definition
p	Highest order of finite element shape functions
h	Parameter of element size
ω_m	Numbered gust frequency
A	Linear differential matrix operator acting within domain
u	Generalized Field Variable
f	Differential equation right hand side vector
Ω	Domain
B	Linear differential matrix operator on boundary
g	Differential equation right hand side vector
Γ	Boundary
u^h	Approximate field variable
x	Spatial coordinate
c	Vector of unknown parameters
R_A	Least-squares residual error in domain
R_B	Least-squares residual error on boundary
I	Least-squares functional
W_i	Residual weighting factor for particular domain, element, or equation
ψ	Element shape functions
N_m	Number of modes

Symbol ..... Definition

u_j ..... Modal values at j^{th} mode

V^h ..... Finite element subspace

N ..... Vector of shape functions

K ..... "Stiffness" matrix

U ..... Vector of degrees of freedom

F ..... "Force" vector

K_e ..... Element "stiffness" matrix

F_e ..... Element "force" vector

K_Ω ..... Domain "stiffness" matrix

K_Γ ..... Boundary "stiffness" matrix

F_Ω ..... Domain "force" matrix

F_Γ ..... Boundary "force" matrix

f_p ..... Right hand side function for Poisson's equation

v_1 ..... Secondary variable for Poisson's equation

v_2 ..... Secondary variable for Poisson's equation

ξ_t ..... Nonzero triplet

η_t ..... Nonzero triplet

ζ_t ..... Nonzero triplet

u_{exact} ..... Exact field variable

C^k ..... Enforced continuity order at element boundary

$P_p^{\alpha,\beta}$ ..... Jacobi polynomials of order p

Symbol	Definition
ξ	Generalized spatial coordinate
η	Generalized spatial coordinate
τ	Generalized temporal coordinate
C_{xi}	Coordinate coefficient in x-direction
C_{yi}	Coordinate coefficient in y-direction
J	Jacobian
j	Resultant jacobian
g	Minimum gauss quadrature integration order
β	Angle to normal vector pointing out of surface
C	Transformation matrix
C_σ	Stress transformation matrix
TOL	Prescribed tolerance level
ρ^r	Balancing ratio for under-relaxation scheme
θ	Explicit-implicit scaling parameter
θ_c	Explicit-implicit scaling parameter for pure steady-state portion
Δt	Time step
v^f	Fluid velocity
v^s	Structure velocity
σ^f	Fluid stress
σ^s	Structure stress
d^s	Structural deformation

Symbol	Definition
u^s	Structural deformation
x^f	Fluid coordinate
w^s	Vertical bending displacement
$q_{bending}$	Applied bending distributed load
E	Modulus of Elasticity
I	Second moment of inertia
θ^s	Slope of vertical bending displacement
V^s	Internal bending shear force
M^s	Internal bending moment
N^s	Internal axial force
f_{axial}	Applied axial distributed load
ρ^s	Structural density
H	Displacement gradient
G	Modulus of Rigidity
v	Poisson's ratio
Π_p	Potential energy
U_e	Strain energy
Ω_p	Potential of applied loads
f_b	Body forces
Φ	Vector of surface tractions
M	Mass matrix

Symbol	Definition
c	Wave speed
μ	Viscosity
L	Length
CFL	Courant-Friedrich-Lewy Condition
v_g^f	Grid fluid velocity
w	Characteristic wave
Λ	Matrix of eigenvalues across diagonal
Λ_c	Maximum characteristic wave speed
S^I	Element face area

Acknowledgements

I would first like to thank my advisor, Dr. Robert Canfield, for his questioning insight and review efforts. I am also thankful to my committee for their great advice and efforts throughout this entire process. I gratefully acknowledge the support of the AFRL Senior Aerospace Engineers Dr. Raymond Kolonay, Dr. Phillip Beran, and Dr. Maxwell Blair. The Air Force Research Laboratory (AFRL), Air Vehicles Directorate funded this research. Finally I would like to thank my wife and son for all of their emotional support.

Cody C Rasmussen

LEAST-SQUARES FINITE ELEMENT FORMULATION FOR FLUID-STRUCTURE INTERACTION

I. Introduction

1.1 Motivation

The joined-wing sensor-craft is a conceptual aircraft based on an Air Force need for advanced, long-endurance tactical surveillance using current and future sensor packages [1–3]. A potential vehicle design is a joined-wing configuration that could lead to improved radar capabilities, increased aerodynamic performance, and structural weight savings. Analyses have shown that an example joined-wing configuration exhibited large geometric nonlinearity. The nonlinear deformations were larger than the wing's panel width when compared to the linear deformations. Nonlinear analysis was critical to correctly model sensor-craft configurations in the past [1]. Figure 1.1 shows a nominal configuration.

The Air Force Chief of Staff and the Air Force Secretary identify Information Superiority and Agile Combat Support as two of the Air Force's six core competen-

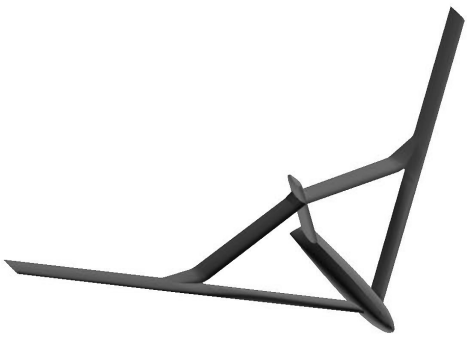

Figure 1.1 Sample Joined-Wing Configuration

cies [4]. The Air Force Research Laboratory, Air Vehicles Directorate, has identified Persistent Intelligence, Surveillance, and Reconnaissance (ISR) as one of the cornerstones of its Future Capabilities Technology Investment that will support these two core competencies. As an indication of its importance, Persistent ISR was one of two key areas examined at a recent meeting of Air Force leaders who conducted a future capabilities assessment [5]. An Air Force report to Congress also stated the importance of Persistent Integrated ISR,

> Currently, ISR assets are limited and can provide persistent coverage only of selected areas. To meet demands of the war on global terrorism, United States Air Force is accelerating development, fielding, and integration of ISR assets [6].

In pursuit of developing technology to enhance Persistent ISR, as a complement to its own in-house research, Air Vehicles Directorate initiated contracts in 2001 with Boeing, Lockheed-Martin, and Northrop-Grumman to study sensor-craft concepts. Those studies identified gust loads as one of the critical structural design factors [7]. Collaborative research with the Air Force Institute of Technology not only confirmed that gust loads were critical, but also demonstrated that nonlinear deformations were important for accurately capturing the gust response of a joined wing sensor-craft similar to the Boeing vehicle concept [1, 3, 8]. Whereas the contractor studies neglected nonlinear response, the Air Force Institute of Technology studies included nonlinearity, but used rather simplistic, equivalent static gust models. The need for a detailed nonlinear transient gust response was shown in these studies. A detailed simulation would be useful as a "truth model" in assessing how adequate the simplistic models are for preliminary design of this type of vehicle.

The joined-wing sensor-craft is considered a "grand-challenge" problem for Fluid-Structure Interaction (FSI) due to its nonlinear structural and aerodynamic behavior. Solving such a challenging problem requires a formulation with a number of unique capabilities:

1. Time-dependent nonlinear fluid dynamics
2. Time-dependent structures with geometric and follower force nonlinearities
3. Fully-coupled FSI
4. Complex model geometry
5. Time-accurate and complex mesh deformation
6. Accurately account for transient input
7. Arbitrary Lagrangian-Eulerian fluid schemes

It is proposed here that using least-squares finite elements is a method capable of accurately handling the above mentioned requirements. The unique approach of the least-squares approach has not been successfully applied to FSI problems before. The goal within this research was to show the feasibility of each of these capabilities and to compare their accuracy to other commonly used methods. These capabilities, proven to be feasible and accurate, lead to the detailed gust analysis of the joined-wing sensor-craft.

1.2 The Least-Squares Finite Element Method

The Least-Squares Finite Element Method (LSFEM) has received extensive consideration in recent years. The method is based on minimizing the L_2 norm of the residuals produced from the finite element shape function approximation of systems of differential equations [9]. The weak-form Galerkin approach is commonly used in standard finite element formulations. Unfortunately, the Galerkin approach presents difficulties when applied to non-self-adjoint equations in problems such as fluid dynamics and other transport problems. These difficulties include oscillations and instabilities of the solution and poor approximation of its derivatives [9, 10]. LSFEM has received a great deal of attention recently because of its potential to avoid these difficulties.

A significant advantage of LSFEM is that its formulation always leads to a symmetric positive-definite system of algebraic equations, even for non-self-adjoint systems [9]. This offers great advantages from a computational point of view. The use of robust iterative methods to solve the system of equations developed through LSFEM becomes possible. In addition, iterative solution techniques such as preconditioned conjugate gradient methods can be implemented without the need of global assembly. For this method, large-scale problems can be solved using a fully parallel environment and without the need of global assembly [10–12].

LSFEM has also been shown to provide greater accuracy for the derivatives of primal variables than traditional finite elements based on Weak Galerkin methods [13]. These derivatives, often referred to as secondary variables, are the response that is most commonly shared between domains for FSI problems. This provides a distinct reason to use LSFEM in coupled problems.

The accuracy of the secondary variables in the least-squares formulation originates from the implementation of mixed methods for LSFEM. Mixed methods use both primal and secondary responses as direct degree of freedom responses. This increases the total number of system degrees of freedom, but the enhanced accuracy and ability to directly share and assemble the secondary degrees of freedom for coupled problems improves the accuracy at the interface which should improve the accuracy of the solution overall.

The finite element method has traditionally been the numerical solution technique of choice for structural problems. Use of the finite element method in other problems, such as fluids, is a subject of great concentration in recent years. Traditional Weak Galerkin FEM has shown difficulty solving some non-structural problems. Since LSFEM may handle fluid and transport problems with fewer issues, the finite element method, based on least-squares, may be used as a numerical approximation technique for a wide range of problems.

The Weak Galerkin FEM has long been considered the traditional finite element method of choice because of its high solution accuracy and its low differentiability requirements on its shape functions. A Strong Galerkin approach is not as commonly used because it requires full differentiability of the shape functions. For example, a fourth-order differential equation would require shape functions that are fourth-order differentiable for a Strong Galerkin approach whereas a Weak Galerkin approach would only require that the shape functions are second-order differentiable. This reduction in differentiability requirements is because the Weak Galerkin approach applies integration by parts to the original Galerkin functional. In addition, the integration by parts, which results in the Weak Galerkin method, conveniently results in the Raleigh Ritz method using the Principle of Minimum Potential Energy [13].

Least-squares finite-elements were examined intensely in the 1970s [14]. For a period after that, least-squares finite elements were not a commonly used formulation. The method did not receive more consideration until recent years. This was mainly because of the realization that the higher polynomial order of the finite element shape functions is an essential part of using LSFEM [9, 15–18]. The use of higher-order p-elements resolved the main concerns raised in the 1970s.

1.3 Simultaneously Coupled Fluid-Structure Interaction

Bendiksen has shown, with conclusive results, that a loosely-coupled FSI scheme produces time lag errors that add with each iteration [19]. These errors are typically avoided by a finer mesh or through a very small time step. He showed that this produces slow convergence and that large errors still exist for some problems with complex geometries or complex fluid flow dynamics. Bendiksen was able to solve such problems using a simultaneously coupled scheme with relatively coarse meshes and larger time steps [19]. This improvement in convergence and accuracy is a significant advantage of the simultaneously coupled scheme.

The nature of LSFEM makes it a methodology that can be easily implemented into a simultaneously coupled scheme (also called directly-coupled [20], tightly-coupled [21], or monolithic [22]). Since LSFEM can be used for the fluid domain, the structural domain, the mesh deformation domain, and even the interface conditions, it provides a method to solve a coupled problem using the same variational principle.

1.4 Research Goals

The problem statement that summarizes the core objective of this research is:

> *Compare the least-squares finite element method to other commonly used methods and implement the least-squares finite element formulation for complex, simultaneously coupled FSI problems.*

To accomplish this core objective, this research was split into two main goals:

1. Compare the least-squares finite element method to other common numerical methods such as finite differencing and Weak Galerkin finite elements and compare the simultaneously coupled fluid structure interaction method to a sequentially coupled method.
2. Demonstrate each unique capability required to accomplish a transient gust scenario for the joined-wing sensor-craft.

The first research goal provided a "proof of technology" for the least-squares finite element method in the context of FSI. The second research goal used a challenging problem to show that the simultaneously coupled fluid structure interaction method is applicable to a complex problem using LSFEM.

1.5 Research Contributions

The work completed here had new and unique aspects relevant to the aerospace research community. Very little work has been completed using least-squares finite elements for FSI problems. Also, very little work has been completed using

simultaneous solution methods for FSI problems. In fact, no success has been previously observed for nonlinear FSI problems with mesh deformation using LSFEM. Specifically, no one has previously implemented compressible Euler fluid analysis in the simultaneously coupled LSFEM FSI. For the single previous attempt to apply simultaneous LSFEM to FSI, there was great difficultly and inaccuracies shown when using LSFEM for both the fluid and structural domain for a simultaneously coupled solution [23, 24]. The simultaneously coupled LSFEM exhibited extensive problems with respect to the residual weighting scheme both by Kayser-Herold and Matthies [23, 24] and the current effort. In addition, very low accuracy has been observed for transient structural problems when using LSFEM [23, 24]. A unique residual weighting scheme was proposed and used within this research. The method was successful for some LSFEM FSI problems. The work contained in this dissertation examined and corrected many of the issues surrounding the LSFEM structural problems observed by Kayser-Herold and Matthies.

1.6 Overview of Remaining Chapters

The second chapter in this document provides short descriptions of other work that has been completed in LSFEM and FSI. Other relevant work such as mesh deformation, nonconformal meshes, and mixed finite elements is also discussed here. The third chapter presents the theory behind finite element methods. This includes both least-squares and Weak Galerkin finite element methods. Unique considerations for higher-order polynomial shape functions are discussed. The fourth chapter applies the theory of least-squares and Weak Galerkin finite element methods to structural problems in two-dimensions. Both transient and steady-state equations and problems are examined. The fifth chapter reviews the theory and application of using LSFEM for fluid dynamics problems. Arbitrary Lagrangian-Eulerian methods are also discussed. The sixth chapter covers the theory and methodology of fluid-structure interaction when considering simultaneous or sequential LSFEM

formulations. The seventh chapter covers problems related to steady-state FSI problems, including residual weighting methods. An iterative residual balancing scheme is introduced and shown to be practical here. The eighth chapter applies the LSFEM FSI methodology to transient FSI problems with nonlinear properties. The ninth chapter provides conclusions that were drawn from this work and suggests future work to be completed within the field of LSFEM and work to be completed to solve the transient joined-wing sensor-craft gust scenario.

II. Background

2.1 Least-Squares Finite Elements

Eason performed a survey of published work in the field of least-squares for solving partial differential equations in 1976. He concluded that least-squares provides a solid framework for solving a wide variety of problems to include structures, aerodynamics and transport problems. LSFEM provides theoretical and computational advantages in the implementation of finite element models over those based on the weak-form Galerkin method. The weak-form Galerkin approach is commonly used in standard finite element formulations. Unfortunately, the Galerkin approach presents difficulties when applied to non-self-adjoint equations in problems such as fluid dynamics and other transport problems. These difficulties include oscillations and instabilities of the solution and poor approximation of its derivatives [9, 10]. LSFEM has been shown to avoid these difficulties for non-self-adjoint equations. LSFEM provides great flexibility in developing the differential equation formulation for many types of analysis. Another significant advantage of LSFEM is that its formulation always leads to a symmetric positive-definite system of algebraic equations even for non-self adjoint systems [9]. This offers a computational advantage. The use of robust iterative methods to solve the system of equations developed through LSFEM becomes possible. In addition, iterative solution techniques such as preconditioned conjugate gradient methods can be implemented without the need of global assembly. For this method, large-scale problems can be solved using a fully parallel environment and without the need of global assembly [10–12]. LSFEM has also been shown to provide greater accuracy for the derivatives of primal variables than traditional finite elements based on Weak Galerkin methods [13]. These derivatives, often referred to as secondary variables, are the response that is most commonly shared between domains for FSI problems. This provides a distinct reason to use LSFEM in coupled problems. LSFEM automatically supplies an error indicator in

the form of the residuals that are minimized by the procedure [14]. The accuracy of the secondary variables in the least-squares formulation originates from the implementation of mixed methods for LSFEM. Mixed methods use both primal and secondary responses as direct degree of freedom responses. This increases the total number of system degrees of freedom, but the enhanced accuracy and ability to directly share and assemble the secondary degrees of freedom at the interface for coupled problems must also be factored.

A gap in least-squares work was observed between Eason's survey paper (1976) until the 2000s. Eason noted that least-squares exhibited poor accuracy for some problems. More importantly convergence rates did not consistently meet theoretical criteria nor would solutions converge to their exact answer despite refining mesh size. He mentioned that least-squares convergence is purely problem dependent [14]. This problem was not resolved until two decades later when Pontaza and Reddy discovered how critical the element polynomial order (p-value) was when considering least-squares formulations.

Pontaza and Reddy [17] found that p-refinement provides better results and results that properly converge to a correct result when using LSFEM. p-refinement involves increasing the polynomial order of the approximation functions (see Equation 3.17) in order to improve the solution. Low-order nodal expansions have been used commonly in the past. These types of expansions may easily exhibit locking mechanisms in LSFEM. Reduced order integration is often used to resolve these problems [9]. Higher-order expansions can prevent locking altogether [17]. p-refinement was examined in this study. The results showed very high sensitivity to the element p-value. It was also shown, in this dissertation, that residual weight balancing is essential in generating proper accuracy for some types of analysis, such as transient elasticity and multi-domain problem.

Pontaza and Reddy also published several papers discussing the LSFEM formulation for several different types of problems. They showed formulations for

shells [15, 16], plates [18], and the Navier-Stokes equations [17]. Their papers provided the foundation necessary to build the least-squares methodology described here.

2.2 Simultaneously Coupled Fluid-Structure Interaction

Bendiksen performed a survey of the main challenges in computational aeroelasticity. He proposed that the direct Eulerian-Lagrangian computational scheme is a consistent and efficient method to couple the fluid-structure problem. This treats the problem as a single dynamic system. It eliminates the virtual surface at the boundary and eliminates phase integration errors typically observed using classical methods [19].

He noted that a loosely-coupled FSI scheme produces time lag errors that add with each iteration. These errors are typically avoided by a finer mesh or through a very small time step. Bendiksen showed that this produces slow convergence and that large errors still exist for some problems with complex geometries or complex fluid flow dynamics. Bendiksen was able to solve problems using his fully-coupled scheme with relatively coarse meshes with a smaller time steps [19]. This is a significant advantage of the fully-coupled scheme. Even though the structural problem was solved as many times as the fluid problem, the overall computation time was much less than when loosely coupled.

Bendiksen also noted that some modern aeroelastic problems use millions of degrees of freedom for the fluid domain but only dozens of degrees of freedom for the structural domain. He noted that the structure problem is not less important. Previous problems were successful with a low number of degrees of freedom for the structural domain because simple geometries were used. He mentioned that for advanced problems that include complex geometries or higher-level fluid problems, such as transonic flow, a higher number of structural degrees of freedom are required [19].

Hübner *et al.* used a monolithic finite element approach to FSI problems [22]. They used finite elements for both domains. Viscous fluid differential equations were used to approximate the fluid behavior and nonlinear structural properties in their FSI problems. Their method exhibited strong convergence properties for coupled problems with strong interaction characteristics. The study used traditional finite element methods with simultaneous solution techniques instead of a loosely-coupled sequential technique. This produced ill-conditioned matrices with zero entries on the diagonal, requiring a stronger solver. LSFEM is a method that will avoid ill-conditioned system matrices completely.

Sequential solution methods have shown good accuracy for most steady state problems and only for transient problems when a small enough time step is used [19]. Some have implemented unique schemes to alleviate difficulties observed when accurate sequential methods are desired without the need for a very small time step [25, 26].

Jaiman *et al.* applied a loosely-coupled sequential scheme for transient FSI problems using Combined Interface Boundary Conditions (CIBC). It improves the influence of the boundary interface for both the velocity and momentum fluxes. CIBC provides a correction factor to the boundary interface terms such that each domain can be solved in a staggered manner, or rather a sequential manner [25]. A corrected velocity field for the fluid velocity (v^f) is corrected using both the structural interface velocity v^s and some correction factor δv_n^* based on the previous time step

$$v_{n+1}^f = v_{n+1}^s + \delta v_n^* \tag{2.1}$$

The corrected structural momentum flux P^s is corrected using both the fluid interface momentum flux P^f and some correction factor δP_n^*

$$P_{n+1}^s = P_{n+1}^f + \delta P_{n+1}^* \tag{2.2}$$

The correction factors are defined by

$$\delta v_n^* = \Delta t \left[\left(\frac{\partial P^f}{\partial n^f} \right)^n - \frac{w_c}{\rho_n^f} \left\{ \left(\frac{\partial P^f}{\partial t} \right)^n - \left(\frac{\partial P^s}{\partial t} \right)^n \right\} \right] \quad \text{on} \quad \Gamma^s \tag{2.3}$$

$$\delta P_n^* = \Delta t \left[- \left(\frac{\partial P^s}{\partial t} \right)^{n+1} + \frac{1}{w_c} \left\{ \left(\rho^f \frac{\partial v^s}{\partial t} \right)^{n+1} - \left(\frac{\partial P^f}{\partial n^f} \right)^{n+1} \right\} \right] \quad \text{on} \quad \Gamma^s \tag{2.4}$$

where w_c is a positive coupling parameter used to ensure dimensional consistency.

Crivelli and Farhat have applied Finite Element Tearing and Interconnecting (FETI) to improve boundary interaction characteristics. They did so those interaction effects were properly implemented into the sequential solution. FETI is based on a hybrid variational principle that allows the computing of the incomplete subdomain displacement fields and can extract the dual tractions at the subdomain interfaces [26]. Each global domain can be split into several subdomains

$$\{\Omega^s\}_{s=1}^{N_s} \tag{2.5}$$

where a neighboring domain to Ω^s is defined as Ω^q where the interface conditions are matched weakly at each neighboring domain interface $\Gamma^{s,q}$. This method can be used within any primary domain such as a structure domain split into several subdomains or within an FSI problem split between the fluid and structure domains. They observed great efficiency and convergence properties in a parallel computing environment using this method for both a single global domain type or within a multiple domain type such as FSI. Convergence was improved since each subdomain will have slow and fast convergence properties. Those subdomains that converge quickly require fewer nonlinear subiterations within each time step. In order to help improve overall convergence and interface accuracy, the interface conditions are smoothed through an advancing half time step using

$$v_{n+1}^s = v_{n+\frac{1}{2}}^s + \frac{\Delta t}{2} \frac{\partial v^s}{\partial t}_{n+\frac{1}{2}} \tag{2.6}$$

This time integration method is used subdomain by subdomain.

FETI and CIBC allow for larger time steps when using a sequential approach while still maintaining accuracy for either steady-state or transient problems.

2.3 Simultaneously Coupled Fluid-Structure Interaction Using Least Squares Finite Elements

Kayser-Herold and Matthies [23, 24] were the first to complete extensive research on a unified least-squares approach to FSI problems. They considered both steady-state and transient cases. While LSFEM was accurate for fluids, they did show difficulty in handling transient structural problems. Instabilities were observed for many different LSFEM structural formulations which showed poor conservation at the FSI boundary. They did successfully examine a simultaneously coupled formulation using a Weak-Galerkin formulation for the structural domain. The work contained in this dissertation examined and corrected many of the issues surrounding the LSFEM structural problems observed by Kayser-Herold and Matthies.

2.4 Fluid Analysis

Karniadakis and Sherwin examined several fluid problems using spectral-*hp* element methods. They argued against many modern critics who have said that finite element methods of any type will result in poor results for fluid problems. They pointed out that the *hp*-spectral method, which considers both the mesh size and shape function order, is essential for improving accuracy when solving a given fluid problems using finite elements. They showed accurate results for several types of fluid problems with great success using finite element methods [27]. This success was shown for both subsonic and supersonic fluid cases. However, there are still many critics who are convinced that finite elements can never perform as well as finite volume or finite volume methods for fluid problems [28, 29]. A comparison of LSFEM to finite differencing was accomplished in this dissertation.

2.5 Mesh Deformation

Many FSI methods may include complete remeshing of the fluid domain as the structural domain deforms [30, 31]. This technique leads to poor results because of the inherent numerical diffusion that occurs when interpolating data from the old grid to the new grid. Effects such as weak secondary shocks or contact discontinuities are lost [32].

To avoid a time consuming remeshing process, a moving boundary without remeshing was considered by Pettit and Beran. A transpiration boundary condition was applied at the interaction point in the model. This involved setting various differential equations to zero at the moving wall [33]. The transpiration boundary conditions were limited to small displacements of the boundary surface.

Kolonay *et al.* also used transpiration boundary conditions to approximate the response of an aeroelastic problem [34]. The goal was to minimize drag over the wing through the optimization of numerous control surfaces that control the lift profile of the wing. These numerous control surfaces would produce a significant computational cost if each control surface was fully modeled. Through the use of transpiration boundary conditions, each control surface's effect on the lift and drag profile was approximated accurately with low computational requirements.

Bartels [35] used an elasticity-based moving mesh scheme to approximate mesh deformation due to structural boundary movement. Bartels applied this method to three-dimensional aeroelastic problems successfully. This method was shown as a robust method for coupled problems. The method performs well to maintain cell/element shape and propagates boundary deformation properly throughout the domain interior. In addition, this method fits well within a finite-element framework.

Martineau and Georgala also used a time-dependent elastic-spring analogy for a mesh movement algorithm for various complex geometries [36]. The elastic-spring analogy is a common algorithm [24, 37], but Martineau and Georgala improved the

algorithm through a novel predictor-corrector scheme. This improved the robustness of the method. The spring-analogy algorithm was also used in this least-squares study.

Sackinger *et al.* leveraged the elastic-spring analogy to derive a pseudo-solid mesh deformation scheme using finite elements [37]. This allowed them to map any fluid domain shape and handle complex geometry with structured or unstructured meshes while considering a free and moving boundary.

Etienne *et al.* also implemented the pseudo-solid approach using a fully monolithic approach where the problem physics were modeled using unsteady conditions [38]. They used unsteady Navier-Stokes equations with a hyper-elastic solid. The nonlinear behavior was handled using Newton-Raphson methods to reach quick convergence. They showed good convergence properties with a scheme using the pseudo-solid approach in a purely monolithic scheme.

2.6 Nonconformal Meshes

Mortar element schemes have received interest as of late due to their proposed ability to match two or more meshes in a nonconforming manner where element location and element polynomial order do not need to be the same at the interface boundary. Anagnostou *et al.* developed the basic concept of mortar elements [39]. It was done in a very generalized way to help for a large class of problems. Seshaiyer and Suri [40] and Belgacem *et al* [41] examined the use of mortar elements for both fluid and structural problems. They conducted studies in which they examined the *hp*-spectral convergence of the mortar elements using Weak Galerkin finite element methods. Not only did they see good accuracy, but convergence rates were properly matched to theory.

Swim and Seshaiyer examined nonconformal meshes using a three-field formulation for a FSI problem [42]. They showed that the theoretical formulation is stable and consistent.

Least-squares can easily be used similar to the mortar element framework. It can be used to match two meshes within a domain or it can match interface conditions between two different domains, such as those in a FSI problem. LSFEM nonconformal meshes were examined here within the LSFEM scheme using methods similar to mortar methods.

2.7 Arbitrary Lagrangian-Eulerian (ALE) Schemes

Lagrangian meshes are typically used in structural mechanics problems [43]. Eulerian meshes are typically used in fluid problems [11]. The mixture of these two types of meshes/coordinate systems has proven problematic [44]. The ALE technique does not exhibit these problems. The technique does not follow the material deformation nor does it remain spatially fixed at each node. The mesh changes in an arbitrary manner independent of material deformation. The mesh may move with the fluid, remain fixed, or move in any other prescribed way [45, 46]. The ALE technique modifies the fluid elements such that the convective velocities used within the fluid equations represent the relative velocity between the actual and grid velocities [45, 46]. This allows for the fluid mesh to move with a prescribed boundary deformation generated from the structural domain and still remain accurate throughout the entire fluid domain's mesh deformation.

Unfortunately, ALE methods are computationally expensive. To address this, Tan and Belytschko used a blended mesh method where the ALE mesh overlaps the fluid Eulerian mesh. Data from the ALE mesh is then coupled with the Eulerian mesh through blended functions [44]. This exhibited benefits observed using ALE methods, while reducing computational costs. ALE methods were investigated in this study.

2.8 Mixed Finite Elements

The use of a mixed formulation within the finite element framework has attracted interest for quite some time now. Especially in the case where coupling between different types of physics, the mixed formulation becomes valuable. Relationships such as pressures, displacements, and velocities can be shared within the mixed framework. Brezzi and Bathe performed a detailed study of mixed finite element formulations on both fluids and structures [47]. They examined the stability and optimal error bounds in mixed methods. They discovered little difficulty with Navier-Stokes fluid analysis but they had extensive difficulty with the structural domain. They proposed many different types of mixed plate and shell elements but none were able to satisfy the mathematical conditions of stability and optimal error bounds. This has been a common issue with many mixed type elements. Mixed formulations have truly exhibited mixed results.

Arnold *et al.* [48] have taken a very mathematical approach to mixed finite elements for two-dimensional elasticity. They have managed to come up with a mathematically consistent formulation that exhibits proper convergence rates with a large enough minimum polynomial order [48]. Arnold *et al.* were the first to provide an accurate mixed formulation using standard Weak Galerkin methods.

2.9 High Altitude Long Endurance Aircraft

The joined-wing sensor-craft is a High-Altitude Long-Endurance (HALE) aircraft [49] by virtue of its extremely high-aspect ratio wings. HALE aircraft typically have aeroelastic effects that are nonlinear and require unique considerations due to their lightweight wing structure with long span length [50–53].

Drela [51] described a preliminary design methodology for HALE aircraft using nonlinear structures and control effects. Drela used a violent gust encounter as a critical load case. The nonlinear behavior mixed with the gust load case showed critical changes in the design of the sample HALE aircraft. The methodology is

good for preliminary design only, since it is a low-fidelity model. Linear lattice panel models were used for the fluid domain [51]. Drela's study did not involve a highly detailed analysis. In addition, the gust loads were approximated as static. A full transient analysis of a HALE aircraft is of special interest.

Similarly, Patil *et al.* [50] also implemented nonlinear aeroelastic effects in the analysis of a HALE aircraft. They noted that their results for a fully nonlinear aeroelastic HALE aircraft would differ completely if they had not considered nonlinear flexibility effects [50]. In addition, Patil and Taylor produced models with wings of uniform and non-uniform characteristics and models that could be solved nonlinearly in both frequency and time domains [54,55]. All models and results were accurate for geometrically exact wings. Patil *et al.* produced a reliable methodology to handle gust response for HALE aircraft [55].

Strganac *et al.* [53] also showed that nonlinear interdisciplinary interactions occur for HALE aircraft. More importantly, this was shown for the joined-wing sensor-craft concept. Their study was not fully-coupled and there was no gust analysis performed [53].

2.10 Aircraft Gust Loads and Response

Gust loads are often critical load cases, because of the sudden and dynamic addition of vertical velocity components that result in a change in the vehicle's effective angle of attack [56]. Past research has been completed on the joined-wing concept using only an instantaneous static gust load case [1, 8]. These studies showed that the gust load case was a critical load for the design of the joined-wing. Unfortunately, a transient nonlinear analysis of the joined-wing has not been performed due to its complexity. An accurate time-dependent FSI analysis code is required to handle such a problem.

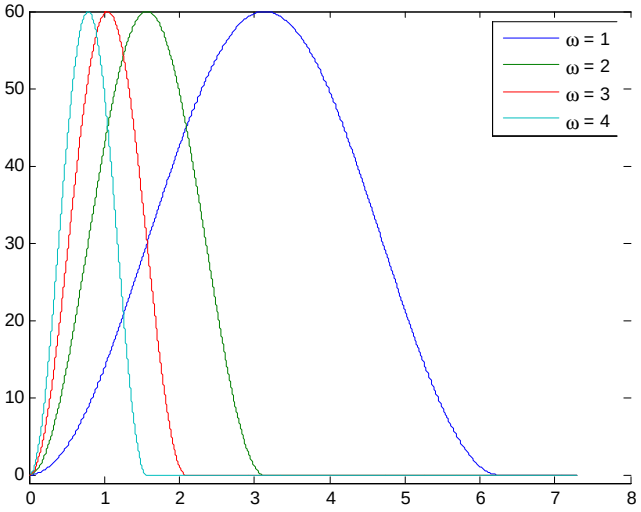

Figure 2.1 Sample Discrete and Nonlinear Transient Gust Response for Various Sample Frequencies

The work performed here is traceable to a complex joined-wing transient gust analysis problem. A sample discrete and nonlinear response such as

$$y(t) = \left\{ \begin{array}{ccc} M\left[1 - \cos\left(\omega_m t\right)\right] & : & 0 < t < \frac{2\pi}{\omega_m} \\ 0 & : & \frac{2\pi}{\omega_m} < t < \infty \end{array} \right\} \tag{2.7}$$

is adequate for an initial transient gust analysis. This provides the gust influence on a vehicle for a nonlinear input. Several gust frequencies (ω), which affect the gust length, can be used individually throughout the gust frequency range and a user defined magnitude (M) could help specify gust speed. Figure 2.1 shows a number of possibilities for discrete gust inputs. The methodology discussed in this dissertation is capable of handling the transient discrete gust response profile shown while still accurately solving for the nonlinearities of the fluid and structural domains.

III. Finite Element Methods

3.1 Basic Theory and Methodology of the Least Squares Finite Element Method

Eason [14] considers least-squares through a traditional boundary value problem

$$Au = f \quad \text{in domain } \Omega \tag{3.1}$$

$$Bu = g \text{ on boundary } \Gamma \tag{3.2}$$

where A and B are first-order differential operators, u is the vector of field variables of the system, and f and g on the right hand side of the equations are functions that do not depend on u. A trial solution is used and is represented as

$$u(x) \approx u^h(x, c) \tag{3.3}$$

where c is the vector of unknown parameters and h denotes that it is a discretized response. The residuals measure the error of the approximation, i.e.,

$$R_A = Au^h - f \tag{3.4}$$

$$R_B = Bu^h - g \tag{3.5}$$

where R_A and R_B represent the interior residual and boundary residual, respectively.

The least-squares functional weighs the residuals through the L_2 norm ($|\cdot|_0$). It is defined as

$$I(u) = \frac{1}{2}\int_{\Omega} \left|Au^h - f\right|_0^2 d\Omega + \frac{1}{2}\int_{\Gamma} \left|Bu^h - g\right|_0^2 d\Gamma \tag{3.6}$$

where the L_2 norm for a single one-dimensional response $u(x)$ is

$$|u(x)|_0 = \left(\int_\Gamma |u(x)|^2 \, dx \right)^{\frac{1}{2}} \tag{3.7}$$

The next norm, which tests continuity and smoothness of the response $u(x)$, is the H^1 norm of $u(x)$ which is defined as

$$|u(x)|_1 = \left(\int_\Gamma \left[|u(x)|^2 + |u'(x)|^2 \right] dx \right)^{\frac{1}{2}} \tag{3.8}$$

In general, the H^k norm is defined as

$$|u(x)|_k = \left(\sum_{i=1}^{k} \int_\Gamma \left[\left| \frac{\partial^i u(x)}{\partial x^i} \right|^2 \right] dx \right)^{\frac{1}{2}} \tag{3.9}$$

In addition, the L_2 norm can be defined for u with multiple responses using the inner product

$$|u|_0 = (u, u)^{\frac{1}{2}} \tag{3.10}$$

where the inner product is defined as

$$(u, v) = \int_\Omega u^T v \, d\Omega \tag{3.11}$$

The dual norm, or rather the negative norm, is defined using the inner product

$$|u|_{-k} = \sup_{0 \neq v \epsilon H^k} \left(\frac{(u, v)}{|v|_k} \right) \tag{3.12}$$

The half norm $H^{1/2}$ and negative half norm $H^{-1/2}$ are theoretical in basis only. Practical implementation or calculation of these norms is typically performed using

hieristic means in conjuction with an easy to implement L_2 norm [23]

$$|u|^2_{1/2} \approxeq \sqrt{h}\,|u|^2_0 \tag{3.13}$$

$$|u|^2_{-1/2} \approxeq \frac{1}{\sqrt{h}}\,|u|^2_0 \tag{3.14}$$

The solution improves as the functional goes to zero, or equivalently as the residuals go to zero. The user may prescribe differing weights between the norms to give priority or to change the error balancing of the problem. Then the least-squares functional may take the form

$$I(u) = \sum W_{\Omega_i} \int_{\Omega_i} \left| Au^h - f \right|^2_0 d\Omega_i + \sum W_{\Gamma_i} \int_{\Gamma_i} \left| Bu^h - g \right|^2_0 d\Gamma_i \tag{3.15}$$

where the W's signify the weight of each domain Ω_i or boundary Γ_i. The necessary condition for the minimum of the functional is to set the first variation of the functional to zero [11]

$$\delta I(u) = \int_{\Omega} R_A \frac{dR_A}{dc} d\Omega + \int_{\Gamma} R_B \frac{dR_B}{dc} d\Gamma = 0 \tag{3.16}$$

Jiang discretizes and divides the domain into finite elements for the above functional and its variation using

$$u^h_e(x) = \sum_{j=1}^{N_m} \psi_j \begin{Bmatrix} u_1 \\ u_2 \\ \vdots \\ u_j \\ \vdots \\ u_m \end{Bmatrix} \tag{3.17}$$

where u_j represents the modal values at the j^{th} mode, h denotes the mesh parameter [9]. N_m defines the number of modes which includes edge mode coefficients, bubble mode coefficients, and nodal values. Finally, ψ are the element shape functions. The shape functions must be admissible within the domain

$$u^h \in V^h = \left\{ u^h \in H^m(\Omega) : u^h(\Gamma) = 0 \right\} \tag{3.18}$$

In other words, the trial functions u^h must fall within the finite element subspace V^h such that the trial functions u^h are continuous piecewise polynomials within the Hilbert space ($H^m(\Omega)$). A discussion of the selected shape functions is detailed later in this research. The vector of shape functions, N, is defined as

$$N = \left[\psi_1, \psi_2, \ldots, \psi_{N_m} \right] \tag{3.19}$$

Inserting the finite element approximation into Equation (3.16) creates a set of simultaneous linear algebraic equations

$$KU = F \tag{3.20}$$

where K is called the "stiffness matrix," U represents the degrees of freedom of the system, and F is the "force vector." K and F are calculated for each element using

$$K_{\Omega_e} = \int_{\Omega} \left[A\psi_1, A\psi_2, \ldots, A\psi_{N_n} \right]^T \left[A\psi_1, A\psi_2, \ldots, A\psi_{N_n} \right] d\Omega \tag{3.21}$$

$$F_{\Omega_e} = \int_{\Omega} \left[A\psi_1, A\psi_2, \ldots, A\psi_{N_n} \right]^T f \; d\Omega \tag{3.22}$$

The differential operator A is applied to the discretized system, i.e.,

$$A\psi_j = \sum_{i=1}^{N_d} \frac{\partial \psi_j}{\partial x_i} A_i + \psi_j A_0 \tag{3.23}$$

where A_i denotes the coefficients applied to the spatial derivatives in all dimensions (N_d) and A_0 are the coefficients applied to the responses without derivatives. Once each K_e and F_e are determined for every element in the system, the global K and F are assembled. The known U values are applied as defined from the boundary conditions or included in the boundary residual. The unknown U values can now be found [9]. Jiang's LSFEM formulation was used on all problems in this study.

If the boundary integral portion of Equation (3.6) is considered, K and F are composed in a slightly different form. K and F are composed of boundary and domain parts.

$$(K_\Omega + K_\Gamma)\, U = (F_\Omega + F_\Gamma) \tag{3.24}$$

The domain parts are assembled globally and may include their respective weights,

$$\left(\sum W_{\Omega_i} K_{\Omega_i} + \sum W_{\Gamma_i} K_{\Gamma_i}\right) U = \left(\sum W_{\Omega_i} F_{\Omega_i} + \sum W_{\Gamma_i} F_{\Gamma_i}\right) \tag{3.25}$$

The domain contributions (Ω) are generated from Equations (3.21) and (3.22). The boundary contributions (Γ) are generated through

$$K_{\Gamma_e} = \int_\Gamma \left[B\psi_1, B\psi_2, \ldots, B\psi_{N_n}\right]^T \left[B\psi_1, B\psi_2, \ldots, B\psi_{N_n}\right] d\Gamma \tag{3.26}$$

$$F_{\Gamma_e} = \int_\Gamma \left[B\psi_1, B\psi_2, \ldots, B\psi_{N_n}\right]^T f d\Gamma \tag{3.27}$$

As an example case to demonstrate the development of the differential operators, a simple differential equation is considered. Poisson's equation is

$$-\nabla^2 u = f_p \tag{3.28}$$

where u is the primal response and f_p is the right hand side of Poisson's equation specified over the two-dimensional domain. The Laplacian operator ∇^2 in expanded

form and applied to the Poisson's equation is

$$\nabla^2 u = \frac{\partial^2 u}{\partial x^2} + \frac{\partial^2 u}{\partial y^2} \tag{3.29}$$

The first step is to convert the original differential equation to mixed first order form. Two secondary variables (v_1, v_2) are formed to represent the derivatives of the primal variable u, i.e.,

$$-\frac{\partial v_1}{\partial x} - \frac{\partial v_2}{\partial y} = f_p \tag{3.30}$$

$$v_1 - \frac{\partial u}{\partial x} = 0 \tag{3.31}$$

$$v_2 - \frac{\partial u}{\partial y} = 0 \tag{3.32}$$

In this form, the three equations and three unknowns are identified and thus, the system of equations is exactly determined. The differential operator A becomes

$$A = \begin{bmatrix} 0 & -1 & 0 \\ -1 & 0 & 0 \\ 0 & 0 & 0 \end{bmatrix} \frac{\partial}{\partial x} + \begin{bmatrix} 0 & 0 & -1 \\ 0 & 0 & 0 \\ -1 & 0 & 0 \end{bmatrix} \frac{\partial}{\partial y} + \begin{bmatrix} 0 & 0 & 0 \\ 0 & 1 & 0 \\ 0 & 0 & 1 \end{bmatrix} \tag{3.33}$$

The differential operator A can be simplified to the form

$$A = A_1 \frac{\partial}{\partial x} + A_2 \frac{\partial}{\partial y} + A_0 \tag{3.34}$$

The rows of the matrix correlate to the different differential equations and each column correlates to each degree of freedom. The degrees of freedom are also represented in matrix form,

$$U = \begin{Bmatrix} u \\ v_1 \\ v_2 \end{Bmatrix} \tag{3.35}$$

The right side of the equation is represented through

$$f = \left\{ \begin{array}{c} f_p \\ 0 \\ 0 \end{array} \right\} \tag{3.36}$$

The above equations can then simply be applied to the basic K and F LSFEM operators defined by (3.21) and (3.22).

Ellipticity of the selected formulation is mathematically desirable because the internal and external characteristic derivatives can be uniquely determined for the system of differential equations. An elliptic formulation consists of purely negative characteristic roots whereas a non-elliptic formulation could have positive or repeated positive roots. Jiang [9] provided a way to determine if a system of differential equations is elliptic or non-elliptic. For some nonzero triplets (ξ_t, η) applied to only the derivative portions of the differential operator, if

$$\det\left(A_1\xi_t + A_2\eta_t\right) \neq 0 \tag{3.37}$$

then the system of differential equations is elliptic [9]. For systems with an odd number of differential equations, ellipticity is impossible since all the characteristic roots within an elliptic system must be complex and must come in pairs. In many cases, it is appropriate to add equations, such as differential symmetry, to ensure an even number of equations. For systems with an odd number of responses, but an even number of equations, the above test can be applied by providing a dummy variable to ensure that the A operator is square [9].

It is important to consider that the mixed form results in a non-elliptic form. It has been proven that elliptic differential equations will show optimal convergence

rates for a problem formulated in LSFEM. The upper bound

$$\text{Elliptic:} \quad \left|u - u^h\right|_0 \leq C_1 h^{p+1} \left|u\right|_{p+2} \tag{3.38}$$

holds for the error convergence rates for elliptic problems [9, 57]. In other words, if the problem is elliptic and smooth with respect to the $p+2$ order of the exact solution, the slopes of the error norm (m) should be greater or equal to $p+1$ when plotted with respect to element size (h). In cases where discontinuities, the $\left|u\right|_{p+2}$ norm will become very large and will dominate the overall error bound since that norm is a test for solution smoothness since that norm consists of error with respect to u's derivatives up to its $p+2$ order. For a problem such as a fluid shock problem, the error rate of $p+1$ will not be the only determination for the bound of the solution error.

For non-elliptic problems, only a slope of p is guaranteed, i.e.,

$$\text{Non-Elliptic:} \quad \left|u - u^h\right|_0 \leq C_2 h^{p} \left|u\right|_{p+1} \tag{3.39}$$

However, just because a proof does not exist *a priori* for non-elliptic problems does not imply that non-elliptic problems do not achieve the same convergence rates as elliptic formulations. Note that the optimal convergence rates are a guaranteed minimum and is only applicable for fully continuous solutions or for discontinuous solutions with a perfectly graded mesh [27]. The $p+1$ convergence rate has been proven only for error norm of the finite element approximation (u^h) relative to exact solution (u). The least-squares residual error (R) convergence rate is guaranteed to be p for either elliptic or non-elliptic formulations.

$$\text{LSFEM Residual:} \quad \left|R\left(u^h\right)\right|_0 \leq C_3 h^{p} \left|u\right|_{p+1} \tag{3.40}$$

To make the mixed formulation of Poisson's equation elliptic, only one equation must be added to the system. A symmetry constraint equation is added to the system, e.g.,

$$\frac{\partial v_1}{\partial y} - \frac{\partial v_2}{\partial x} = 0 \tag{3.41}$$

The new differential operator A now takes the form

$$A = \begin{bmatrix} 0 & -1 & 0 \\ -1 & 0 & 0 \\ 0 & 0 & 0 \\ 0 & 0 & -1 \end{bmatrix} \frac{\partial}{\partial x} + \begin{bmatrix} 0 & 0 & -1 \\ 0 & 0 & 0 \\ -1 & 0 & 0 \\ 0 & 1 & 0 \end{bmatrix} \frac{\partial}{\partial y} + \begin{bmatrix} 0 & 0 & 0 \\ 0 & 1 & 0 \\ 0 & 0 & 1 \\ 0 & 0 & 0 \end{bmatrix} \tag{3.42}$$

The U vector does not change since the response types are the same. However, the vector F must change with the number of equations, e.g.,

$$f = \begin{Bmatrix} f_p \\ 0 \\ 0 \\ 0 \end{Bmatrix} \tag{3.43}$$

This results in a new formulation that is elliptic. As a side note, the elliptic and non-elliptic forms were applied to the sample solution below. The results and their comparative error to the problem's exact solution did not change.

A sample problem was considered using Poisson's equation. The problem considered here had a known exact result

$$u_{exact}(x, y) = \left(7x + x^7\right) \cos(\pi y) \tag{3.44}$$

The problem was solved by providing one boundary condition at each wall of the square domain $[-1,1] \times [-1,1]$. The following boundary conditions were applied

$$v_1 = 14\cos(\pi y) \text{ applied at } x = -1 \tag{3.45}$$

$$v_2 = 0 \text{ applied at } y = -1 \ \& \ y = 1 \tag{3.46}$$

$$u = 8\cos(\pi y) \text{ applied at } x = 1 \tag{3.47}$$

with a user-prescribed right hand function of

$$f_p = -\cos(\pi y)\left(42x^5 - 7\pi^2 x - \pi^2 x^7\right) \tag{3.48}$$

With the exact solution known for all primal and secondary variables, an error norm relating the finite element response to the exact solution was calculated. The error norms can be plotted on an hp-refinement plot where as the p-value is increases, the mesh size is increased to maintain the overall system degrees of freedom. If done properly, the error should reduce as the p-value increases even though the total number of system degrees of freedom remain the same. This shows that the p-method can provide "free" improvement in accuracy without the need to increase the problem size.

The error norm can provide a way to verify the implemented LSFEM code by relating hp-convergence rates for all responses and the least-squares functional/residual. For the error norm, a slope of 1 was predicted and was correctly observed on an hp-spectral refinement plot (Figure 3.1). The hp-spectral refinement plot refines the p-value while coarsening the mesh. This maintains the total number of modes used throughout the refinement while increasing the polynomial order. Both least-squares residual errors were shown and the L_2 error norms with respect to the FEM and exact solution were shown. This figure shows the proper slope ($m = 1$) and verifies

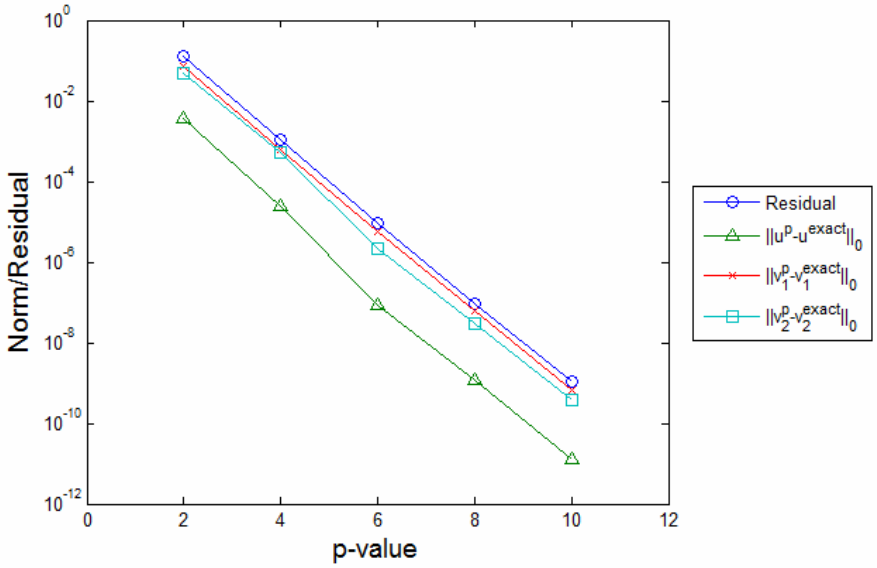

Figure 3.1 *hp*-Spectral Refinement for Poisson's Problem Analyzing Integrated Response Error Norm Across the Domain

the LSFEM code. This plot directly compares to results published by Pontaza and Reddy [17].

3.2 The p-Method and LSFEM

Pontaza and Reddy have stressed the importance of a higher p-value when using LSFEM [18]. The least-squares method has enjoyed renewed interest in recent years, mainly because of the realization that p-refinement is an essential part of using LSFEM. Low order least-squares finite elements often display poor results when using full-order numerical integration. Reduced-order integration may alleviate this problem for these lower-order elements, but the predictive capabilities of these elements is reduced, especially when considering distorted elements [18]. The use of higher-order elements resolves those problems. Pontaza and Reddy observed that as long as the element p-value is high enough, full-order integration can be used with accuracy for LSFEM mixed formulations [15]. This section discusses the implementation challenges of higher-order elements.

For a mixed LSFEM formulation applied to a system of first order differential equations, the p-method is applied using the same p-value across all levels of responses. It does not matter whether a response is a primal or secondary response because the same polynomial order of each response is the same. This is a convenient factor of the mixed first-order LSFEM form. There is no need for mixed order integration. Additionally, the mixed first-order LSFEM does not require continuous derivatives at the element boundaries. This means that nodal and modal expansions only require C^0 continuity at element boundaries. However, in cases where a secondary variable is directly identified to be a derivative of a primal variable and is solved as a direct finite element response, then an improved level of accuracy is observed for that primal variable. This improved level of accuracy is due to the fact that global continuity is weakly enforced when using a mixed formulation [17]. This is because of the secondary variables being continuous at element boundaries and this creates primal variables that are smooth or nearly smooth at its boundaries. It was strongly recommended by Pontaza and Reddy to select a system p-value with an order equal to or higher than the highest order derivative observed in the original differential equation form. In the case of a linear Euler-Bernoulli beam, the original differential equation is a 4^{th} order equation. In the mixed LSFEM form, the equation results in four first order differential equations. In this case, a p-value of 4 or greater is suggested. However, the problem can still be solved successfully using p-values lower than 4, but global continuity might not hold in a weak sense.

It has been observed that matrix "banding" does not occur within the global stiffness matrix when using the p-method. Using direct matrix solution procedures creates poor "banding" and can result in solutions that take longer to solve or apply reduction techniques. In the case of LSFEM, conjugate gradient methods are commonly used and avoid the need for global assembly, thus reducing the required system memory. In this case, poor banding is not an issue.

3.2.1 Shape Functions. In a modal expansion, the shape functions used in (3.17) are based on the C^0 p-type hierarchical basis

$$\psi_i(\xi) = \left\{ \begin{array}{cc} \frac{1-\xi}{2}, & i = 1, \\ \left(\frac{1-\xi}{2}\right)\left(\frac{1+\xi}{2}\right) P_{p-2}^{\alpha,\beta}, & 2 \leq i \leq p, p \geq 2, \\ \frac{1+\xi}{2}, & i = p+1 \end{array} \right\} \tag{3.49}$$

where $P_p^{\alpha,\beta}$ are the Jacobi polynomials of order p and ξ are the generalized coordinates ranging from $[-1, 1]$ [27]. The first and last mode are considered nodal responses which equal the response at the element node locations. The other modes are coefficients of shape functions of second order and higher. In this research, ultraspheric symmetric polynomials were used with $\alpha = \beta = 0$ which are also known as the Legendre polynomials [17,27]. The Legendre polynomials are formed through

$$P_{n+1}^{0,0}(\xi) = \frac{(2n+1)}{(n+1)}\left[\xi P_n^{0,0}(\xi) - n P_{n-1}^{0,0}(\xi)\right] \qquad n = 1, 2, ... \tag{3.50}$$

where the first two polynomials, which start the series, are defined as [27]

$$P_0^{0,0}(\xi) = 1 \qquad\qquad P_1^{0,0}(\xi) = x \tag{3.51}$$

The above modal expansion was specified for a one-dimensional element. For the two-dimensional case, the coordinates of an element are mapped to a bi-unit square ($\Omega_e(\xi, \eta) = [-1, 1] \times [-1, 1]$) using generalized coordinates (ξ, η). For the two-dimensional case, a full-tensor product of the one-dimensional expansion basis is used, i.e.,

$$\psi_{jk}(\xi, \eta) = \psi_j(\xi)\,\psi_k(\eta) \tag{3.52}$$

This full-tensor product expansion becomes apparent by examining Pascal's Triangle [27]. The expansion basis for an example p-value of 3 is shown in Figure 3.2. The full-tensor product expansion uses coupled modes of a higher polynomial order than

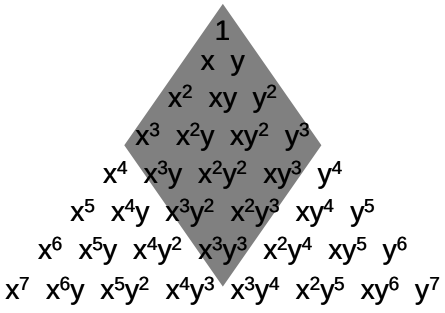

Figure 3.2 Mode Selection for Full-Tensor Product Expansion Shape Functions

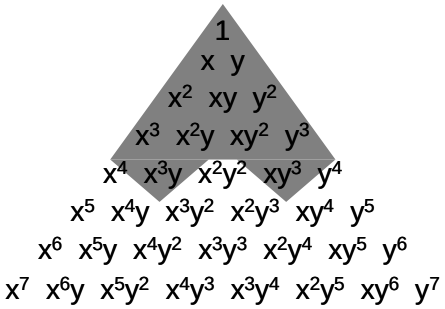

Figure 3.3 Mode Selection for Serendipity Shape Functions

is necessary to reach the specified p-value. However, a high number of coupled modes are used and can increase accuracy for problems where a high coupling between x and y coordinates are observed. For this expansion, all terms with exponents less than or equal to 3 are used.

A second set of shape functions which are worthwhile to consider are the serendipity elements where the minimum number of modes are considered for a given polynomial order. An example p-value of 3 is shown in Figure 3.3. As the figure shows, the serendipity mode selection includes very few coupled modes with an order beyond a given p-value. The serendipity expansion is a subset of the full-tensor product expansion.

The serendipity expansion basis will reach a higher polynomial order with fewer degrees of freedom than the full-tensor expansion [27]. However, accuracy might become a factor since many coupled modes are eliminated. A study comparing

the two shape function expansions was completed within this research. Both of the expansion bases shown are admissible for all response types within the mixed first-order LSFEM form.

3.2.2 Bubble Mode Condensation. The most noteworthy advantages of using the p-method is the improvement in accuracy and the ability to condense element bubble modes (those modes that do not correlate to element edge responses). The p-method may include some additional pre- and post-processing, but the reduction in the overall size of the global system matrix can reduce computation time when solving the system of linear algebraic equations (3.20). Only the bubble modes may be condensed for each element. The nodal responses must be assembled at the vertices of other elements and the edge modes must be shared at the element faces. The node and edge mode responses are considered to be the modes that are to be recovered (u_r) and the bubble mode responses are to be condensed (u_c). The system of algebraic equations are parsed with respect to recovered and condensed modes

$$\begin{bmatrix} K_{rr} & K_{rc} \\ K_{cr} & K_{cc} \end{bmatrix} \begin{Bmatrix} U_r \\ U_c \end{Bmatrix} = \begin{Bmatrix} F_r \\ F_c \end{Bmatrix} \tag{3.53}$$

The new system of equations results in the equation

$$\left(K_{rr} - K_{rc}K_{cc}^{-1}K_{cr}\right) U_r = \left(F_r - K_{rc}^{-1}F_c\right) \tag{3.54}$$

after some algebraic conditioning. It takes the standard form where a new K_{result} and F_{result} are used, i.e.,

$$K_{result}U_r = F_{result} \tag{3.55}$$

The condensed responses are then recovered in a post-processing manner through

$$U_c = K_{cc}^{-1}\left(F_c - K_{cr}U_r\right) \tag{3.56}$$

This means that the K_{cc}, F_c, and K_{cr} matrices must be saved for each element so they can be used to recover the condensed bubble modes after the solution is complete. These matrices should be saved on a hard drive disk instead of held within system memory to help decrease memory requirements.

To consider the impact of bubble mode condensation, the number of each type of mode must be considered. For a given p-value, a sample two-dimensional element will have four node responses and $(p-1)$ number of edge modes on each of the four edges, which results in $4\,(p-1)$ responses and $(p-1)^2$ bubble modes. This means, for a two-dimensional full-tensor product expansion basis, there will be $4p$ recovered modes and $(p-1)^2$ condensed modes. As an example, for a given p-value of 12, the number of responses solved with the global system matrix is reduced by 71.6%. If solution capability is limited by memory size, bubble mode condensation is a means to reduce the problem's memory requirements by a significant factor.

3.2.3 Isoparametric Curved Edge Elements. With the use of higher order p-elements comes the possibility of using a higher order mapping of element coordinates. In other words, quadrilateral elements can evolve from the simple straight edged elements to elements with curved edges specified with an order as high as the element's p-value (Figure 3.4). This is especially useful when using large elements with a high p-value around geometries with curved edges.

Isoparametric elements involve using the same shape functions to describe both the response and the coordinate mapping from the master element to the physical element. An element's Jacobian is used to approximate the generalized coordinate mapping of the derivatives and integrals used to develop the stiffness matrix and force vector [43]. The first step is to develop the generalized coordinate mapping using the element's shape functions. The x and y coordinates are mapped as

$$x = \sum \psi_i\,(\xi, \eta)\, x_i \tag{3.57}$$

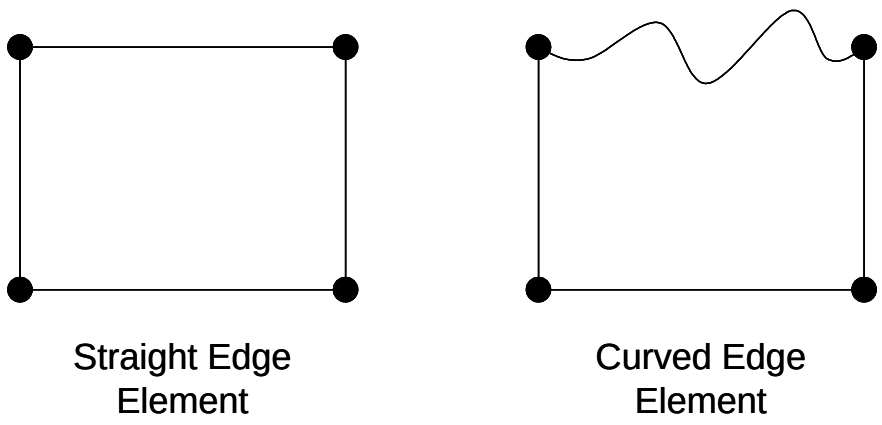

Figure 3.4 Elements Are Modeled as Either Straight Edge Elements With Nodal Mapping or Curved Edge Elements with Higher Order Element Coordinate Mapping

$$y = \sum_i \psi\left(\xi, \eta\right) y_i \tag{3.58}$$

where x_i and y_i are the modal coefficients which are prescribed through the mesh properties [43]. For a straight edged quadrilateral element, only the nodal values are needed to prescribe an element's coordinates and the higher order shape functions are ignored. For a curved edged element, the element edge that is curved utilizes the edge modes to help describe the curved edge coordinates.

The Jacobian matrix is formed by using the derivatives of the shape functions multiplied the coordinate nodes and modes.

$$J = \begin{bmatrix} \frac{\partial x}{\partial \xi} & \frac{\partial y}{\partial \xi} \\ \frac{\partial x}{\partial \eta} & \frac{\partial y}{\partial \eta} \end{bmatrix} = \begin{bmatrix} J_{11} & J_{12} \\ J_{21} & J_{22} \end{bmatrix} = \begin{bmatrix} \frac{\partial}{\partial \xi}\begin{bmatrix} \psi_1 & \psi_2 & \cdots & \psi_{(p+1)^2} \end{bmatrix} \\ \frac{\partial}{\partial \eta}\begin{bmatrix} \psi_1 & \psi_2 & \cdots & \psi_{(p+1)^2} \end{bmatrix} \end{bmatrix} \begin{bmatrix} x_1 & y_1 \\ x_2 & y_2 \\ x_3 & y_3 \\ x_4 & y_4 \\ C_{x_1} & C_{y_1} \\ C_{x_2} & C_{y_2} \\ \vdots & \vdots \end{bmatrix} \tag{3.59}$$

The Jacobian matrix provides the derivatives of the actual coordinates with respect to the generalized coordinates. The inverse Jacobian provides the useful derivatives. It approximates the generalized coordinates with respect to the actual coordinate system, i.e.,

$$J^{-1} = \begin{bmatrix} \frac{\partial \xi}{\partial x} & \frac{\partial \eta}{\partial x} \\ \frac{\partial \xi}{\partial y} & \frac{\partial \eta}{\partial y} \end{bmatrix} = \begin{bmatrix} (J_{11})^{-1} & (J_{12})^{-1} \\ (J_{21})^{-1} & (J_{22})^{-1} \end{bmatrix} \tag{3.60}$$

These derivatives are useful when applying spatial derivatives to the system of differential equations [43]. The chain rule applied to the standard spatial derivatives in terms of generalized coordinates are

$$\frac{\partial}{\partial x} = \frac{\partial}{\partial \xi}\frac{\partial \xi}{\partial x} + \frac{\partial}{\partial \eta}\frac{\partial \eta}{\partial x} = \frac{\partial}{\partial \xi}J_{11}^{-1} + \frac{\partial}{\partial \eta}J_{12}^{-1} \tag{3.61}$$

$$\frac{\partial}{\partial y} = \frac{\partial}{\partial \xi}\frac{\partial \xi}{\partial y} + \frac{\partial}{\partial \eta}\frac{\partial \eta}{\partial y} = \frac{\partial}{\partial \xi}J_{21}^{-1} + \frac{\partial}{\partial \eta}J_{22}^{-1} \tag{3.62}$$

The differential operator, A, now takes the form

$$A = A_1\left(\frac{\partial}{\partial \xi}J_{11}^{-1} + \frac{\partial}{\partial \eta}J_{12}^{-1}\right) + A_2\left(\frac{\partial}{\partial \xi}J_{21}^{-1} + \frac{\partial}{\partial \eta}J_{22}^{-1}\right) + A_0 \tag{3.63}$$

The Jacobian can also change the nature of an integral which is in terms of generalized coordinates, i.e.,

$$\int_{\Omega}[\cdot]\,d\Omega = \int_{-1}^{1}\int_{-1}^{1}[\cdot]\,j\,d\xi d\eta \tag{3.64}$$

where the resultant Jacobian j is defined as [43]

$$j = \det(J) \tag{3.65}$$

3.2.4 Numerical Integration. Even though the Jacobian uses the same order shape functions that are used for the finite element response, the numerical integration order normally is not adjusted for its presence [43]. Only the order of the

response shape functions are considered for the integration scheme. For a system of linear differential equations applied to the LSFEM functional, the maximum possible polynomial order is $2p$. Considering a one-dimensional integral, the minimum Gauss integration order g (number of gauss points) is dictated by

$$2g - 1 \geq \text{maximum polynomial order} = (2p) \tag{3.66}$$

or rather

$$g \geq p + \frac{1}{2} \tag{3.67}$$

In other words, the minimum Gauss order g must be $g \geq p + 1$. For a nonlinear system of differential equations, the assumed worst case operand is $u \cdot u$. If the shape function has an order of p, it can take the form $\psi\left(\xi^p\right)$. If the operator A matches the worst case scenario, then the operator will also have an order of p and can take the form $A\left(\xi^p\right)$. The LSFEM integral now takes the form

$$K = \int_\Omega \left[A\psi\right]^T \left[A\psi\right] d\Omega = \int_\Omega \left[A\left(\xi^p\right)\psi\left(\xi^p\right)\right]^T \left[A\left(\xi^p\right)\psi\left(\xi^p\right)\right] d\Omega \tag{3.68}$$

which results in the highest possible polynomial order of the integrand to be $4p$. The minimum Gauss order is now required to be

$$g \geq 2p + \frac{1}{2} \tag{3.69}$$

or rather the minimum Gauss order g must be $g \geq 2p + 1$.

The number of Gauss points N_g is dictated by the Gauss quadrature order g. For a Gauss-Legendre numerical integration scheme, the Gauss points are generated by solving for the zeros of the polynomial $P_{N_g}^{\alpha,\beta}$ of order N_g interior to the interval $-1 < \xi < 1$.

3.2.5 Boundary Condition Considerations When Using the p-Method.
When using higher order elements, boundary conditions become more complex. More than just the nodal values must be specified at the domain boundaries; the edge mode coefficients must also be specified. Two methods were used in this study. One method used the collocation method and the other uses LSFEM.

The collocation method uses samples on the boundary to determine the edge mode coefficients. The boundary condition values at the boundary are provided by the user and used to solve the unknown coefficients using a set of linear algebraic equations. Consider an example boundary condition where

$$u\left(x,0\right)=g(x) \tag{3.70}$$

For an example p-value of 4, the set of equations may take the form

$$\left\{\begin{array}{c} g_1 \\ g_2 \\ g_3 \\ g_4 \\ g_5 \end{array}\right\} = \left[\begin{array}{ccccc} \psi_1\left(\xi_1\right) & \psi_2\left(\xi_1\right) & \psi_3\left(\xi_1\right) & \psi_4\left(\xi_1\right) & \psi_5\left(\xi_1\right) \\ \psi_1\left(\xi_2\right) & \psi_2\left(\xi_2\right) & \psi_3\left(\xi_2\right) & \psi_4\left(\xi_2\right) & \psi_5\left(\xi_2\right) \\ \psi_1\left(\xi_3\right) & \psi_2\left(\xi_{31}\right) & \psi_3\left(\xi_3\right) & \psi_4\left(\xi_3\right) & \psi_5\left(\xi_3\right) \\ \psi_1\left(\xi_4\right) & \psi_2\left(\xi_4\right) & \psi_3\left(\xi_4\right) & \psi_4\left(\xi_4\right) & \psi_5\left(\xi_4\right) \\ \psi_1\left(\xi_5\right) & \psi_2\left(\xi_5\right) & \psi_3\left(\xi_5\right) & \psi_4\left(\xi_5\right) & \psi_5\left(\xi_5\right) \end{array}\right] \left\{\begin{array}{c} u_1 \\ C_1 \\ C_2 \\ C_3 \\ u_2 \end{array}\right\} \tag{3.71}$$

where the boundary condition values g_i are evaluated at five points along the element edge $(\xi_1, \xi_2, \xi_3, \xi_4, \xi_5)$. It is suggested here that the sample points along the edge be located at predetermined Gauss points of the same order as the number of samples along the boundary. The unknown nodal values (u_1, u_2) and coefficients (C_1, C_2, C_3) can be solved using the above set of equations.

When using LSFEM, the least-squares functional takes the form

$$I\left(u\right)=\int_{\Gamma}\left|u-g\right|_0^2 d\Gamma \tag{3.72}$$

The typical least-squares methods are then applied to create the standard K_Γ and F_Γ matrices using (3.26) and (3.27). In this case, the boundary edge mode coefficients and nodal values can be solved either beforehand or simultaneously within the full problem domain Ω. It has been observed in this study that solving the boundary unknowns beforehand ensures an adequate accuracy with respect to the boundary since a residual weighting factor with respect to the boundary condition is not required. The error will be consistent with LSFEM. However, if the boundary unknowns are solved simultaneously within the full problem domain, the error between the boundary and the inner domain are balanced. A simultaneous solution is preferred for a well-balanced least-squares functional, since the total error of the entire problem is reduced overall and will provide a better overall result. However, if the functional is not well-balanced or if it is unknown whether the function is properly balanced through the residual weights, then it is suggested to solve for the boundary result beforehand to ensure guaranteed accuracy at the boundary.

Both methods discussed above have shown solid accuracy. However, the collocation method can sometimes show oscillations. This problem is usually alleviated when the sample points at the boundary are located at the Gauss points [27]. Another issue with the collocation method is that it would not be a consistent solution scheme if LSFEM is the preferred method and is used for all fields within the problem. For a well-balanced least-squares residual, solving all fields and boundary integrals and boundary conditions simultaneously would provide the best balanced error across the problem. This was observed for several well-balanced problems within this dissertation.

3.2.6 Angled Boundary Condition Considerations for Higher Order Elements. Special considerations must be taken when solving problems with angled boundary conditions. For example, a slip wall boundary condition used for an inviscid flow problem is generated by enforcing a no penetration rule where the normal velocity relative to the wall must be zero. The normal and tangential velocities are deter-

mined using β which is the angle of the vector normal to the surface. The equations relating the Cartesian fluid velocities v_x^f,v_y^f to the normal and tangential velocities v_n^f,v_t^f are

$$\left\{ \begin{array}{c} v_n^f \\ v_t^f \end{array} \right\} = \left[\begin{array}{cc} \cos(\beta) & \sin(\beta) \\ \sin(\beta) & -\cos(\beta) \end{array} \right] \left\{ \begin{array}{c} v_x^f \\ v_y^f \end{array} \right\} = [C] \left\{ \begin{array}{c} v_x^f \\ v_y^f \end{array} \right\} \tag{3.73}$$

The matrix C is unitary, i.e.,

$$C = C^T = C^{-1} \tag{3.74}$$

Similarly, stresses can be rotated using

$$\{\sigma'\} = [C_\sigma] \{\sigma\}$$

where C_σ is the stress transformation matrix. It is defined as

$$C_\sigma = \left[\begin{array}{ccc} \cos^2(\beta) & \sin^2(\beta) & 2\cos(\beta)\sin(\beta) \\ \sin^2(\beta) & \cos^2(\beta) & -2\cos(\beta)\sin(\beta) \\ \cos(\beta)\sin(\beta) & -\cos(\beta)\sin(\beta) & \left(\sin^2(\beta) - \cos^2(\beta)\right) \end{array} \right] \tag{3.75}$$

One useful property of C_σ is C_σ=C_σ^{-1}. This is a useful property since the pre- and post- processing of these angled responses uses the same matrix.

There are two options to implement the above coordinate rotation. One option is to directly rotate each degree of freedom and the other option is to apply a boundary integral condition which is solved simultaneously with the field domain. To rotate each degree of freedom, consider the i^{th} component to be rotated. For a given equation $KU = F$, the i^{th} component of U is modified by using C in the

following form for n number of global degrees of freedom [9]:

$$\begin{bmatrix} K_{11} & K_{12} & \cdots & K_{1i}C & \cdots & K_{1n} \\ K_{21} & K_{22} & \cdots & K_{2i}C & \cdots & K_{2n} \\ \vdots & \vdots & \ddots & \vdots & & \vdots \\ K_{i1} & K_{i2} & \cdots & K_{ii}C & \cdots & K_{in} \\ \vdots & \vdots & & \vdots & \ddots & \vdots \\ K_{n1} & K_{n2} & \cdots & K_{ni}C & \cdots & K_{nn} \end{bmatrix} \begin{Bmatrix} U_1 \\ U_2 \\ \vdots \\ U_i^* \\ \vdots \\ U_n \end{Bmatrix} = \begin{Bmatrix} F_1 \\ F_2 \\ \vdots \\ F_i \\ \vdots \\ F_n \end{Bmatrix} \tag{3.76}$$

This produces a non-symmetric K matrix. This is easily modified by multiplying the entire i^{th} row by C.

$$\begin{bmatrix} K_{11} & K_{12} & \cdots & K_{1i}C & \cdots & K_{1n} \\ K_{21} & K_{22} & \cdots & K_{2i}C & \cdots & K_{2n} \\ \vdots & \vdots & \ddots & \vdots & & \vdots \\ CK_{i1} & CK_{i2} & \cdots & CK_{ii}C & \cdots & CK_{in} \\ \vdots & \vdots & & \vdots & \ddots & \vdots \\ K_{n1} & K_{n2} & \cdots & K_{ni}C & \cdots & K_{nn} \end{bmatrix} \begin{Bmatrix} U_1 \\ U_2 \\ \vdots \\ U_i^* \\ \vdots \\ U_n \end{Bmatrix} = \begin{Bmatrix} F_1 \\ F_2 \\ \vdots \\ CF_i \\ \vdots \\ F_n \end{Bmatrix} \tag{3.77}$$

This modification to the K and F matrices produces a method with symmetric matrices. If the boundary is moving and the normal angles change, the K and F matrix must be updated between every iteration. This can imply nonlinear behavior of K and F. The biggest problem with this method is the angle β is applied in a discrete manner instead of a continuous manner for higher order p-elements. This method works perfectly for elements with linear polynomials only, but when considering an element with a p-value of 2 or higher, the angle β will be exact at the nodes, but the edge modes cannot display a varying change in β. This implies that the option to apply a boundary integral condition to represent β is essential for higher order elements. In this case, (3.73) is used within the LSFEM functional where β can vary through the shape functions used within the problem

framework. Both methods were examined in this research and a significant increase in accuracy was observed by using the LSFEM functional to enforce angled boundary conditions.

Finding the angle β can prove to be difficult if coordinate information is supplied using higher order element coefficients. To do this the angle can be determined from the slope of the coordinates which identifies the tangent line at the edge of a curved element edge, i.e.,

$$\beta = \tan^{-1}\left(\frac{dy}{dx}\right) + \frac{\pi}{2} \tag{3.78}$$

The challenge now is to determine the slope of the coordinates using higher order element edge coordinates. The chain rule can be applied to obtain the derivatives in terms of generalized coordinates, i.e.,

$$\frac{\partial y}{\partial x} = \frac{\partial y}{\partial \xi}\frac{\partial \xi}{\partial x} \tag{3.79}$$

The η direction can be ignored for this derivative since the coordinate derivative is only tangent to the element edge. The derivative $\frac{\partial y}{\partial \xi}$ can be determined directly through a derivative of the shape functions multiplied by the y mode coefficients. The production of the $\frac{\partial \xi}{\partial x}$ derivative is not as straight forward. $\frac{\partial x}{\partial \xi}$ can be determined directly and then $\frac{\partial \xi}{\partial x}$ can be approximated by simply taking the inverse of $\frac{\partial x}{\partial \xi}$. This is similar to the approximation method used by the Jacobian, i.e.,

$$\frac{\partial y}{\partial x} = \frac{\partial y}{\partial \xi}\left(\frac{\partial x}{\partial \xi}\right)^{-1} \tag{3.80}$$

3.3 Nonlinear Solution Methods

Many nonlinear differential equations were considered in this research. Several methods exist to solve LSFEM nonlinear problems. The first method is the direct iteration method. It is the most simple and has a large radius of convergence but a slow rate of nonlinear convergence [9]. In other words, the direct iteration method

may take longer to converge, but the initial guess does not need to be near the correct nonlinear solution point. If K and F are nonlinear, the solution follows a simple iterative scheme

$$K\left(U_{r-1}\right)U_r = F\left(U_{r-1}\right) \tag{3.81}$$

where r is the current nonlinear iteration number [9, 11]. The direct iteration scheme is the primary scheme used in this research. A good amount of success was observed using this scheme for many nonlinear problems. However, there were a few instances where the problem would not quite iterate to the full termination criterion based upon a user-prescribed tolerance level

$$\left|U_r - U_{r-1}\right|_0^2 \leq TOL \tag{3.82}$$

To fix this problem for certain cases, a scheme was needed that could avoid oscillating around the iterative convergence tolerance level.

The second nonlinear method is the under-relaxation scheme. It follows the direct iteration method using the nonlinear system

$$K\left(\overline{U}\right)U_r = F\left(\overline{U}\right) \tag{3.83}$$

where $\overline{U}$ is defined by the last two nonlinear iterations, i.e.,

$$\overline{U} = \rho^r U_{r-2} + \left(1-\rho^r\right)U_{r-1} \tag{3.84}$$

Here ρ^r defines the balancing between the two time steps and must satisfy $0 \leq \rho^r \leq 1$ [11]. This scheme proved to be successful for problems that did not converge when using the direct iterative method. A ρ^r of 0.5 to 0.8 was successfully utilized for these nonlinear cases.

One mathematical issue with the nonlinear iteration schemes shown above is that the K and F matrices formed through the least-squares finite element method-

ology are linearized before the first variation of the least-squares functional is taken. This is an assumption that helps maintain the stiffness matrix's symmetric positive definiteness. In addition, the above iterative schemes have a slower convergence rates than those found with the Newton-Raphson method. The Newton-Raphson method and the Modified Newton-Raphson method have historically reduced the required number of nonlinear iterations. In addition, these schemes will not linearize the system of differential equations before the first variation of the function is complete. However, the stiffness matrix of these methods is not symmetric due to the linearization occurring after the variation is complete. This is a major downfall, but the tangential stiffness matrix, created and solved within the Newton-Raphson method, maintains its symmetry [11]. Overall, this method exhibits fast convergence and consistent variational approaches for nonlinear problems, but is more complex in its implementation than direct iteration. This method was not implemented in this research, but that does not imply that its benefits should not be used in future studies. For the problems solved here, the direct method and under-relaxation iterative methods exhibited an acceptable rate of convergence.

3.4 Transient Discretization of LSFEM

Transient LSFEM problems were considered extensively in this research. Two options were considered. The first option is the space-time coupled approach where the temporal domain is treated as just another coordinate within the finite element shape functions, i.e.,

$$\psi = \psi(\xi, \eta, \tau) \tag{3.85}$$

This method implies that the least-squares discretization and its related variational principle is applied throughout the problem consistently. However, this method will add an entire additional dimension to the problem. This will increase the problem size significantly. The temporal domain can be cut into smaller "strips" where the time domain contains only a single time step. In this case, the initial condition for

each time step "strip" is needed to calculate the time history. Each strip is solved for in succession and will reduce system memory requirements [17].

The second option is to decouple the space-time coordinates where the temporal coordinates are discretized using a finite volume scheme and the spatial coordinates are then discretized using LSFEM. The θ-method is commonly used to discretize first-order time derivatives. As an example, a system of differential equations may include equations that contain a time derivative, e.g.,

$$A_t \frac{\partial u}{\partial t} + A_1 \frac{\partial u}{\partial x} + A_2 \frac{\partial u}{\partial y} + A_0 u = A_t \frac{\partial u}{\partial t} + A_s u = f \tag{3.86}$$

and equations that do not contain a time derivative, e.g.,

$$A_1 \frac{\partial u}{\partial x} + A_2 \frac{\partial u}{\partial y} + A_0 u = A_s u = f \tag{3.87}$$

Equation (3.86) is discretized with the θ-method for those equations with a time derivative via

$$A_t \frac{u_{n+1} - u_n}{\Delta t} + \theta A_s u_{n+1} + (1 - \theta) A_s u_n = f \tag{3.88}$$

and for those equations without a time derivative via

$$\theta_c A_s u_{n+1} + (1 - \theta_c) A_s u_n = f \tag{3.89}$$

where $n + 1$ denotes the current time step. The parameter θ denotes the portion of the time discretization that uses the implicit and explicit response. The parameter θ_c relates the steady-state portion that follows the implicit and explicit scheme. The parameter θ_c is usually selected to be equal to θ. The scheme is purely implicit if $\theta = 1$ and is purely explicit if $\theta = 0$. Both methods have a discretization error on the order of Δt. There is a special case when $\theta = 0.5$ where the order of the error improves to $O\left(\Delta t\right)^2$. This special case is identified as the Crank-Nicolson method and is the preferred method due to its reduction in error. In addition,

the θ-method is considered to be stable for $\theta \geq 0.5$. Not doing so may result in extra temporal oscillations of the solution [24]. A study comparing the space-time coupled and space-time decoupled methods were analyzed in this research using a simple one-dimensional wave problem.

Multiplying (3.88) by Δt, expanding and re-arranging terms, the above temporal discretization was rewritten in the form

$$\left(A_t + \Delta t \theta A\right) u_{n+1} = \Delta t f - \left[A_t + \Delta t \left(1 - \theta\right) A\right] u_n \tag{3.90}$$

This is similar to the standard form (3.1), but now takes the form

$$A_{total} u^{n+1} = f_{total} \tag{3.91}$$

where A_{total} and f_{total} have become

$$A_{total} = A_t + \Delta t \theta A \tag{3.92}$$

$$f_{total} = \Delta t f - \left[A_t + \Delta t \left(1 - \theta\right) A\right] u_n \tag{3.93}$$

This allowed the LSFEM code to treat the time discretization as a "black box" and solve the problem in its standard format.

3.5 Residual Weighting

Changing the residual weights in a least-squares functional can help the user create an equivalent norm (such as an $H^{1/2}$ norm), can modify matrix weighting for prioritization, and can modify local error. The user may prescribe differing weights among the norms to give priority or to change the error balancing of the problem. The least-squares functional that utilizes residual weights, Equation (3.15), is essential when considering fluid-structure interaction problems, since each domain may exhibit residual errors that differ by several orders of magnitude.

In many single-domain cases, residual weighting is not always essential to reach the solution. When considering a multi-domain problem, residual weighting is absolutely essential. It has been observed here and by others [23] that when a multi-domain problem is considered, the balancing of residual weights must be performed just to attempt to approach a reasonable solution. In fact, residual weighting in an FSI problem has been observed to be the biggest challenge when considering a simultaneous solution. If the wrong residual weights are used in an simultaneous FSI problem, one domain can dominate the solution and will make the various fields completely unbalanced and the solution nonsensical.

The fluid-structure boundary interface conditions are not always governed by standard L^2 norms. Since the present LSFEM formulation is based on L^2 norms, a conversion factor is applied to modify the boundary interface norms to become commensurate to the standard L^2 norm. The stress matching condition is governed by the $H^{-1/2}$ norm and the velocity matching condition is governed by the $H^{1/2}$ norm at the interface boundary. In application, evaluating these norms become impractical. For a linear finite interpolation, the boundary norms can become approximately equivalent to the standard L^2 norm, which has a practical implementation, by simply multiplying the functionals by some heuristic relationship using mesh size (h). The no penetration boundary interface relationship, which relates the the fluid velocity vector ($\mathbf{v}^f$), the structural velocity vector ($\mathbf{v}^s$), and the normal vectors for both the fluid ($\mathbf{n}^f$) and structure ($\mathbf{n}^s$), becomes [23, 24]

$$W_i \left| \mathbf{v}^s \cdot \mathbf{n}^s + \mathbf{v}^f \cdot \mathbf{n}^f \right|^2_{1/2} \cong W_i \sqrt{h} \left| \mathbf{v}^s \cdot \mathbf{n}^s + \mathbf{v}^f \cdot \mathbf{n}^f \right|^2_0 \tag{3.94}$$

The stress boundary interface equilibrium, which relates the fluid resultant stresses ($\boldsymbol{\sigma}^f$) and the structural stresses ($\boldsymbol{\sigma}^s$), becomes [23, 24]

$$W_i \left| \boldsymbol{\sigma}^s \cdot \mathbf{n}^s + \boldsymbol{\sigma}^f \cdot \mathbf{n}^f \right|^2_{-1/2} \cong W_i \frac{1}{\sqrt{h}} \left| \boldsymbol{\sigma}^s \cdot \mathbf{n}^s + \boldsymbol{\sigma}^f \cdot \mathbf{n}^f \right|^2_0 \tag{3.95}$$

The mesh deformation coordinate relationship, which relates elasticity based deformation ($\mathbf{d}^D$) and fluid coordinates ($\mathbf{x}^f$), becomes [23, 24]

$$W_i \left|\mathbf{d}^D - \mathbf{x}^f\right|_0^2 \cong W_i \left|\mathbf{d}^D - \mathbf{x}^f\right|_0^2 \tag{3.96}$$

It is important to note that the weighting factors still apply to each boundary interface relationship even after the norms are converted to the standard L^2 norm. Balancing each boundary residual weighting is still essential to properly prioritize the entire problem.

Determining these weights for a simple steady-state FSI is not straightforward since four or more domain types are usually considered. For example, a steady-state FSI problem will consist of a fluid domain, structural domain, an elasticity-based mesh deformation domain, and a pressure sharing relationship at the fluid-structure boundary. These four domain types have their own sets of differential equations and their own meshes. This makes for a complex weighting relationship not typically observed in single-field problems. Residual weights can be applied at three levels. They could applied at the equation level, the element level, and at the domain level.

Several methods were considered here to find the proper residual weights for an FSI problem. These methods could be applied at any level (element, equation, or field). The first method was a no-weighting method. Each equation was weighted exactly the same across every domain. This method works for a single-domain case, but rarely worked for FSI problems solved using simultaneous methods.

The second method was a user-defined weighting method where the weights were arbitrarily defined by the user. This method works for problems with a known exact solution. The user can "turn the knobs" of the residual weights until an exact solution is found. The real problem comes when an FSI problem with an unknown solution is considered. The user has no idea whether the solution they are getting

with their prescribed weights is correct or wrong due to improperly applied residual weights.

The third method is a characteristic unit scaling of the equations. The units within each equation within each domain could be scaled to produce units of the same type. Since many different types of equations are considered in LSFEM (momentum conservation, energy conservation, mass conservation, variable relationships, derivative relationships, etc.) they each have their own unit types. These unit types could be modified to fit any standard unit type such as energy, force, or nondimensional radians. In this case, each equation is scaled by the units only. Just considering unit modification is easy for the user to implement and standardize, but it does not provide prioritization of each field or equation relative to the problem accuracy.

The final method discussed here was an iterative method. This method was based on iterating the residual weights, at any level, until the residual error norms are generally low in magnitude and provide a converged solution. This method is also completely hands-off, but does take more processing time to determine the weights for a simultaneous solution. This method is based on the assumption that the overall solution will improve as the residual error values are balanced.

Iterative residual weighting methods are based on the idea that if a particular error is low, its related residual weighting is also low and that if the error is high, the residual weighting should also be high. This gives a priority to the portions of the problem that have significant error and gives a low priority to the portions that have low error. In other words, if k represents the previous iteration and $k+1$ represents the next iteration, the residual weights, W_i, that are specified for each portion of the problem are represented as

$$W_i^{k+1} = R_i^k \tag{3.97}$$

where R_i are the related residual weights for each portion of the problem i. This provides an equal level of weighting between the residual error and its relative im-

portance. This relationship has been observed to produce highly oscillatory results. The residual weights were seen to go "back and forth" where particular domains can change from a high priority status to a low priority status in one iteration and then back again to a high priority status for the next iteration. It was observed that an exponential averaging of the previous iterations residual weights was required to help smooth the convergence of the residual weights, i.e.,

$$W_i^{k+1} = \left(R_i^k R_i^{k-1}\right)^{\frac{1}{2}} \tag{3.98}$$

The weights are then nondimensionalized using

$$W_i^{k+1} = \frac{W_i^{k+1}}{\sum_{i=1}^{N} W_i^{k+1}} \tag{3.99}$$

Iteratively solving for the residual weights is similar to an optimization problem. The residual weights could be considered the design variables and the residual errors are the response. An extremely simple move limit scheme could be applied to the iterative residual weighting scheme to search for the proper residual weights. In other words, the next iteration's weights are defined as

$$W_i^{k+1} = \min\left(\left|R_i^k\right|, W_{\lim}\right) \tag{3.100}$$

which will push a given residual weight in the right direction, but it will not exceed a particular user-specified move-limit $W_{\lim}$. The weights used here could also be considered a search direction.

The residual weight averaging scheme shown above can be applied for each domain (Ω) and each boundary integral (Γ). It can also be applied to each norm governing each equation and within each norm governing each element. In other words, the weights W_i can be moved within the LSFEM integral and applied to each

equation,

$$I(u) = \int_{\Omega} \left| \sum_{i=1}^{N_{\Omega_{eqns}}} W_i \left(Au^h - f\right)_i \right|_0^2 d\Omega + \int_{\Gamma} \left| \sum_{i=1}^{N_{\Gamma_{eqns}}} W_i \left(Bu^h - g\right)_i \right|_0^2 d\Gamma \qquad (3.101)$$

or can be applied to each element,

$$I(u) = \sum_{e=1}^{N_{\Omega_{elem}}} W_e \int_{\Omega_e} \left|\left(Au^h - f\right)\right|_0^2 d\Omega_e + \sum_{e=1}^{N_{\Gamma_{elem}}} W_e \int_{\Gamma_e} \left|\left(Bu^h - g\right)\right|_0^2 d\Gamma_e \qquad (3.102)$$

A combination of the above element weighting and equation weighting could be used as well, i.e.,

$$I(u) = \sum_{e=1}^{N_{\Omega_{elem}}} W_e \int_{\Omega} \left| \sum_{i=1}^{N_{\Omega_{eqns}}} W_i \left(Au^h - f\right)_i \right|_0^2 d\Omega_e + \sum_{e=1}^{N_{\Gamma_{elem}}} W_e \int_{\Gamma} \left| \sum_{i=1}^{N_{\Gamma_{eqns}}} W_i \left(Bu^h - g\right)_i \right|_0^2 d\Gamma_e \qquad (3.103)$$

IV. The Structural Domain

Several types of analysis were considered in this study for both stand alone structural problems and FSI problems. These include a one-dimensional Euler-Bernoulli beam, nonlinear Euler Bernoulli beam, and 2D in-plane elasticity using both the LSFEM and Weak Galerkin Finite Element Method for both the steady-state and transient cases.

4.1 Linear Euler Bernoulli Beam

The original Euler-Bernoulli beam equation is represented as

$$\frac{d^2}{dx^2}\left(EI\frac{d^2w^s}{dx^2}\right) = q_{bending} \tag{4.1}$$

where w^s is the vertical bending displacement, $q_{bending}$ is the applied bending load per unit length, E is the Modulus of Elasticity, and I is the second moment area of inertia [13, 58]. This is a fourth-order, steady-state differential equation. The above equation was converted into four first-order differential equations to conform to the standard operator A used in the LSFEM formulation. If θ^s represents the slope of the bending displacement, V^s represents the internal shear force, and M^s represents the internal bending moment, then the single fourth-order equation is converted into the following system of four first-order equations.

$$\frac{\partial w^s}{\partial x} - \theta^s = 0 \tag{4.2}$$

$$EI\frac{\partial \theta^s}{\partial x} - M^s = 0 \tag{4.3}$$

$$\frac{\partial M^s}{\partial x} - V^s = 0 \tag{4.4}$$

$$\frac{\partial V^s}{\partial x} = q_{bending} \tag{4.5}$$

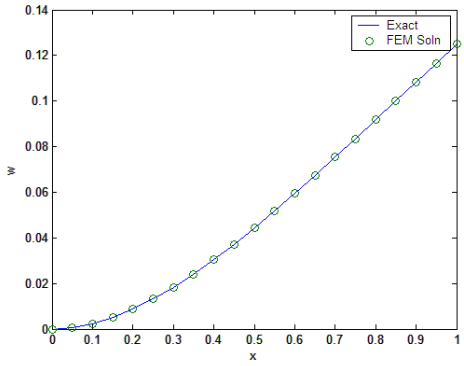

Figure 4.1 Plot of Vertical Bending Displacement for a Clamped-Free Beam Using Linear Euler-Bernoulli Analysis

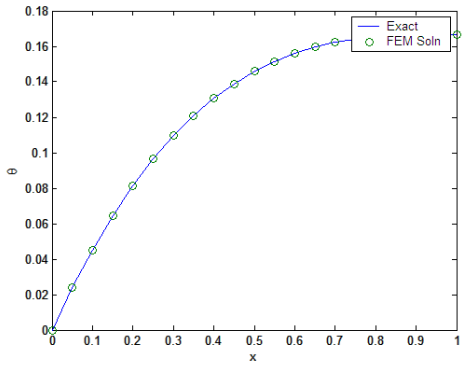

Figure 4.2 Plot of Bending Slope for a Clamped-Free Beam Using Linear Euler-Bernoulli Analysis

Next, Euler-Bernoulli beam results were compared to theory. Figure 4.1 and Figure 4.2 show the results of a clamped beam with a uniform distributed load of unit value. The results matched theory [59] and verifies the LSFEM linear beam structural equations.

4.2 Nonlinear Euler-Bernoulli Beam

The Euler-Bernoulli beam was combined with an axial deformation element to form a plane frame element for the structural dynamics. The equations generated

from force and moment static equilibrium ($\sum F_x$, $\sum F_y$, and $\sum M_z$) are

$$\rho^s A \frac{\partial^2 u^s}{\partial t^2} - \frac{dN^s}{dx} = -f_{axial} \tag{4.6}$$

$$\rho^s I_m \frac{\partial^2 w^s}{\partial t^2} - \frac{dV^s}{dx} = -q_{bending} \tag{4.7}$$

$$\frac{\partial M^s}{\partial x} - V^s + N^s \frac{\partial w}{\partial x} = 0 \tag{4.8}$$

The internal axial force is defined by N^s, the axial deformation is defined by u^s, ρ^s defines the structure's material density, I_m defines the dynamic moment of inertia for the beam, and A defines the beam's cross-sectional area. Kinematic and constitutive equations are also required to solve this system of equations [11, 60], e.g.,

$$N^s - EA \left[\frac{du^s}{dx} + \frac{1}{2} \left(\frac{\partial w^s}{\partial x} \right)^2 \right] = 0 \tag{4.9}$$

$$M^s + EI \frac{\partial \theta^s}{\partial x} = 0 \tag{4.10}$$

$$\frac{\partial w^s}{\partial x} - \theta^s = 0 \tag{4.11}$$

A clamped-clamped beam problem was considered by Reddy as a verification problem. Numerical results showing maximum beam displacement where shown in Reddy's nonlinear FEM book [11]. A maximum beam displacement of 0.7433 was observed by both Reddy and within this dissertation by using the nonlinear Euler-Bernoulli beam equations within a LSFEM scheme. This provided a quick verification and showed that the scheme was comparable to at least the $4th$ digit. Further verification was performed for a transient scenario later.

4.3 2D Elasticity

An elliptic elasticity formulation was considered. It consisted of only displacements and displacement-gradients as the unknown degrees of freedom. A total of six

types of degrees of freedom exist for this formulation. The non-elliptic formulation contained five types of degrees of freedom which were displacements and stresses. The elliptic formulation has six unknowns with eight equations. The displacement gradients are defined as

$$H_1 = \frac{\partial u_x^s}{\partial x} \tag{4.12}$$

$$H_2 = \frac{\partial u_y^s}{\partial y} \tag{4.13}$$

$$H_3 = \frac{\partial u_x^s}{\partial y} \tag{4.14}$$

$$H_4 = \frac{\partial u_y^s}{\partial x} \tag{4.15}$$

where u_x^s and u_y^s are the displacements in the x and y directions. These gradients were then applied to the equilibrium in both the x and y direction and using Hooke's Law for plane-stress, we have

$$-\rho^s \frac{\partial^2 u_x^s}{\partial t^2} + \left(\frac{E}{1-\nu^2}\right)\left(\frac{\partial H_1}{\partial x} + \nu\frac{\partial H_2}{\partial x}\right) + G\left(\frac{\partial H_3}{\partial y} + \frac{\partial H_4}{\partial y}\right) = -f_x \tag{4.16}$$

$$-\rho^s \frac{\partial^2 u_y^s}{\partial t^2} + \left(\frac{E}{1-\nu^2}\right)\left(\nu\frac{\partial H_1}{\partial y} + \frac{\partial H_2}{\partial y}\right) + G\left(\frac{\partial H_3}{\partial x} + \frac{\partial H_4}{\partial x}\right) = -f_y \tag{4.17}$$

where f_x and f_y are body forces in the x and y direction respectively, G is the Modulus of Rigidity, and ν is Poisson's ratio. The plane-strain version can also be used for the constitutive equations. Two extra constraints were applied to make the formulation elliptic. Symmetry, or rather the equality of the mixed derivative must be enforced, e.g.,

$$\frac{\partial H_2}{\partial x} = \frac{\partial H_4}{\partial y} \tag{4.18}$$

$$\frac{\partial H_3}{\partial x} = \frac{\partial H_1}{\partial y} \tag{4.19}$$

The non-elliptic formulation has five unknowns with only five equations. The stresses consist of the normal x stress (σ_x), the normal y stress (σ_y), and the shear

stress (τ_{xy}). The shear stress was assumed to be symmetric ($\tau_{xy} = \tau_{yx}$). The relationships between the displacements and the stresses are defined as (through Hooke's Law for plane-stress)

$$\sigma_x^s = \frac{E}{1-\nu^2}\left(\frac{\partial u_x^s}{\partial x} + \nu\frac{\partial u_y^s}{\partial y}\right) \tag{4.20}$$

$$\sigma_y^s = \frac{E}{1-\nu^2}\left(\nu\frac{\partial u_x^s}{\partial x} + \frac{\partial u_y^s}{\partial y}\right) \tag{4.21}$$

$$\sigma_{xy}^s = G\left(\frac{\partial u_x^s}{\partial y} + \frac{\partial u_y^s}{\partial x}\right) \tag{4.22}$$

and the equilibrium equations become

$$-\rho\frac{\partial^2 u_x^s}{\partial t^2} + \frac{\partial \sigma_x^s}{\partial x} + \frac{\partial \sigma_{xy}^s}{\partial y} = -f_x \tag{4.23}$$

$$-\rho\frac{\partial^2 u_y^s}{\partial t^2} + \frac{\partial \sigma_{xy}^s}{\partial x} + \frac{\partial \sigma_y^s}{\partial y} = -f_y \tag{4.24}$$

For the transient case, additional relationships are needed for both the displacement-displacement gradient and displacement-stress formulations. Equations that relate displacements and displacement velocities are used in the form

$$\frac{\partial u_x^s}{\partial t} = v_x^s \tag{4.25}$$

$$\frac{\partial u_y^s}{\partial t} = v_y^s \tag{4.26}$$

where v_x^s and v_y^s are the velocities in the x and y directions respectively.

The above elasticity formulations will be compared to the standard WGFEM formulation for elasticity for two problems with a known exact solution. The WGFEM formulations will now be discussed.

4.4 Weak Galerkin Finite Element Method

The Weak Galerkin approaches taken within this research use traditional finite element schemes for two-dimensional elasticity and Euler-Bernoulli beams. The traditional approaches are based on energy principles. In these cases, the Principle of Minimum Potential Energy (PMPE) is used to create useful equations for discretization. PMPE is a useful form since it is a minimization problem that exhibits clear elliptic behavior and has a unique solution [43]. In addition, if all formulated equations are of the same form, such as energy, then there are no issues with functional weighting.

4.4.1 WGFEM Two-Dimensional Elasticity. The potential energy of a linearly elastic structure can be written in the form

$$\Pi_p = U_e + \Omega_p \tag{4.27}$$

where U_e is the strain energy of the system and Ω_p is the potential of applied loads. For a system with unknown structural displacements U (discretized in the same way as in (3.17)), the strain energy is defined as

$$U_e = \frac{1}{2} U^T K U \tag{4.28}$$

and the potential of applied loads is defined through [43]

$$\Omega_p = -U^T F \tag{4.29}$$

Equilibrium is determined when the potential energy reaches a stationary state. The principle states that equilibrium is achieved when $\delta\Omega_p = 0$ for any small admissible variation of the configuration. The variation is applied to all displacement

responses in the system [43], i.e.,

$$\delta\Pi_p = \frac{\partial \Pi_p}{\partial U_1}\delta U_1 + \frac{\partial \Pi_p}{\partial U_2}\delta U_2 + \cdots + \frac{\partial \Pi_p}{\partial U_m}\delta U_m = 0 \tag{4.30}$$

The potential energy is a functional defined completely as

$$\Pi_p = \sum_{e=1}^{N_e} \int \left(\frac{1}{2} \{\varepsilon\}^T E \{\varepsilon\} - \{\varepsilon\}^T E \{\varepsilon_0\} + \{\varepsilon\}^T \{\sigma_0\} \right) dV$$

$$- \sum_{e=1}^{N_e} \int \{u\}^T \{f_b\} \, dV - \sum_{e=1}^{N_e} \int \{u\}^T \{\Phi\} \, dS \tag{4.31}$$

where

$$\{\varepsilon\} = [B] \, U \tag{4.32}$$

$[B]$ is the differential-shape operator and is specifically identified here for two-dimensional elasticity to be the strain-displacement relationships. It is identified as

$$[B] = \left[A\psi_1, A\psi_2, \ldots, A\psi_{N_n} \right] = [A\psi] \tag{4.33}$$

where

$$A\psi_i = \begin{bmatrix} \frac{\partial}{\partial x} & 0 \\ 0 & \frac{\partial}{\partial y} \\ \frac{\partial}{\partial y} & \frac{\partial}{\partial x} \end{bmatrix} \psi_i \tag{4.34}$$

$[E]$ is defined by Hooke's Law and can be defined for either plane-stress as

$$[E] = \frac{E}{1-\nu^2} \begin{bmatrix} 1 & \nu & 0 \\ \nu & 1 & 0 \\ 0 & 0 & \frac{1-\nu}{2} \end{bmatrix} \tag{4.35}$$

or for plane-strain as

$$[E] = \frac{E}{(1+\nu)(1-2\nu)} \begin{bmatrix} 1-\nu & \nu & 0 \\ \nu & 1-\nu & 0 \\ 0 & 0 & \frac{1-2\nu}{2} \end{bmatrix} \tag{4.36}$$

The body force, f_b, is a vector defined for both the x and y directions as

$$f_b = \begin{Bmatrix} f_x \\ f_y \end{Bmatrix} \tag{4.37}$$

and Φ are the surface tractions acting on the boundary

$$\Phi = \begin{Bmatrix} \phi_x \\ \phi_y \end{Bmatrix} = \begin{Bmatrix} \sigma_x^s \cos\beta + \sigma_{xy}^s \sin\beta \\ \sigma_y^s \sin\beta + \sigma_{xy}^s \cos\beta \end{Bmatrix} \tag{4.38}$$

Initial stresses $\{\sigma_0\}$ and initial strains $\{\varepsilon_0\}$ are also a part of the potential energy functional [43].

The variation of (4.31) yields the K_e and F_e matrices for in-plane elasticity. The element K_e matrix is defined as [43]

$$K_e = \int_\Omega [B]^T [E] [B] \, d\Omega \tag{4.39}$$

and the WGFEM F_e matrix is defined as

$$F_e = \int_\Omega N^T \{f_b\} \, d\Omega + \int_\Gamma N^T \{\Phi\} \, d\Gamma \tag{4.40}$$

where K_e and F_e are assembled into the global matrices K and F.

This method is a primal method where only the displacements are the unknown degrees of freedom. The stresses are recovered from each element's displacement

vector (d_e) using a post-processing method, i.e.,

$$\{\sigma_e\} = \left\{ \begin{array}{c} \sigma_x^s \\ \sigma_y^s \\ \sigma_{xy}^s \end{array} \right\} = [E]\,[B]\,\{d_e\} \tag{4.41}$$

This method will show a reduction in accuracy of the secondary variables, which are the stresses in this case, because of the differential operator being applied to the shape functions and reducing the polynomial order of the approximated stress response.

Comparing a mixed method, such as mixed LSFEM, to a primal method, such as traditional WGFEM, it is apparent that the primal methods will have fewer degrees of freedom and should have lower memory requirements and computational time, but will sacrifice accuracy of the secondary variables. In addition, primal methods cannot directly share the secondary variables with other domains without a loss in order of accuracy.

4.4.2 WGFEM Euler-Bernoulli Beam. The WGFEM K matrix is formed through the integral

$$K_e = \int_\Omega B^T EIB d\Omega \tag{4.42}$$

where EI is the flexural rigidity (modulus of elasticity E multiplied by second moment area of inertia I) and the shape-differential operator is defined as

$$B = \frac{d^2 N}{dx^2} \tag{4.43}$$

The beam formulation using WGFEM requires shape functions with a minimum p-value of 3 and C^1 continuity. The minimum p-value is needed due to the second order derivatives found in the stiffness matrix formulation. The Jacobi full-tensor product shape functions used in the first order LSFEM formulations are no

longer applicable here. The shape functions used for this analysis are prescribed by Cook as [43]

$$\psi_1 = \frac{1}{4}\left(2 - 3\xi - \xi^3\right) \tag{4.44}$$

$$\psi_2 = \frac{1}{4}\left(1 - \xi - \xi^2 + \xi^3\right) \tag{4.45}$$

$$\psi_3 = \frac{1}{4}\left(2 + 3\xi - \xi^3\right) \tag{4.46}$$

$$\psi_4 = \frac{1}{4}\left(-1 - \xi + \xi^2 + \xi^3\right) \tag{4.47}$$

These shape functions have unique properties where the evaluation of shape functions at nodes have either a value of 0 or 1 at the node locations ($\xi = [-1, 1]$). ψ_1 corresponds to the bending displacement at the left node ($\psi_1(\xi = -1) = 1$), ψ_2 corresponds to the bending slope at the left node $\left(\left(\frac{d\psi_2}{d\xi}\right)_{\xi=-1} = 1\right)$, ψ_3 corresponds to the bending displacement at the right node ($\psi_3(\xi = 1) = 1$), and ψ_4 corresponds to the bending slope at the right node $\left(\left(\frac{d\psi_4}{d\xi}\right)_{\xi=1} = 1\right)$. Each shape function is equal to zero for all other values and derivative values at the nodes.

4.4.3 Transient Discretization of WGFEM. Transient WGFEM formulations take the standard form

$$M\frac{d^2U}{dt^2} + C\frac{dU}{dt} + KU = F \tag{4.48}$$

where M is the mass matrix and C is the damping matrix. For this research, damping was ignored and the stiffness matrix was described in sections 4.4.1. The consistent mass matrix takes the form

$$M = \int_V \rho N^T N dV \tag{4.49}$$

which is a volumetric integral [43]. Traditionally, mass matrices developed using WGFEM are either lumped, consistent, or coupled. The lumped case literally

"lumps" the mass of the element at the nodes. This method is very simple to implement and is accurate for low p-values with elements with little variance in the density throughout the element. The consistent case (4.49) uses the shape functions to describe how the material is distributed throughout the element volume. The consistent method is not always the most efficient method due to poor "banding" of the mass matrix, but this method is essential for accuracy when considering higher p-values. The coupled case mixes both the lumped and consistent methods to average lower and upper bounds on frequency provided by lumped and consistent respectively, for traditional one-dimensional finite elements with low p-order.

The natural frequencies of the temporal problem are produced by assuming simple harmonic motion, thereby converting the differential equation (4.48) into an eigenvalue problem, i.e.,

$$\left[K - \omega_n^2 M\right] \overline{U} = 0 \tag{4.50}$$

The natural frequencies and their respective eigenvectors found using this method are reasonably accurate [43]. Conversely, the eigenvalue problem created by the LSFEM temporal structural case is nonlinear; hence, it is rarely used [14]. Thus, WGFEM is the preferred method for finding structural natural frequencies.

If a time history is desired, the time derivative in (4.48) can be discretized using a simple central difference method, e.g.,

$$\left(\frac{d^2U}{dt^2}\right)_n = \frac{U_{n+1} - 2U_n + U_{n-1}}{(\Delta t)^2} \tag{4.51}$$

The equation (4.48) now takes the discretized form

$$\left(\frac{1}{(\Delta t)^2} M + K\right) U_{n+1} = R_n + \frac{2}{(\Delta t)^2} M U_n - \frac{1}{(\Delta t)^2} M U_{n-1} \tag{4.52}$$

where U_n and U_{n-1} are solved or given to find the next time step's response U_{n+1} [43].

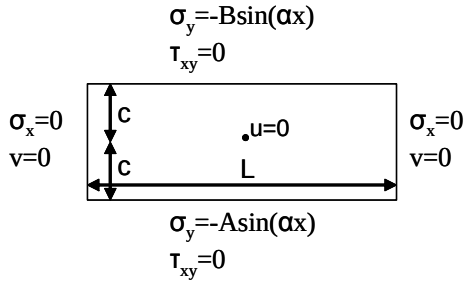

Figure 4.3 Boundary Conditions for Timoshenko and Goodier Problem Over Rectangular Domain

4.5 Example Elasticity Problems

4.5.1 Serendipity vs. Full-Tensor Product Jacobi Shape Function. An elasticity problem with a known exact solution was considered to examine the differences between the serendipity expansion and the full-tensor product Jacobi expansions. Timoshenko and Goodier provided a problem with a known stress field [61, 62]. One advantage of this problem is that the boundary conditions are relatively simple and no body forces are applied. Figure 4.3 shows the rectangular domain with given boundary conditions. For this problem, the parameters were specified using: $A = B = 0.5$, $\alpha = \pi$, $c = 0.5$, and $L = 1.0$. Figure 4.4 shows the exact solutions for this problem. The exact stress equations were provided by Fung [61] and Timoshenko and Goodier [62] and the exact displacement results were shown by Wickert and Canfield [63].

The problem was solved using both serendipity elements and full-tensor product elements. The non-elliptic elasticity formulation was applied using LSFEM. A p-refinement plot was generated comparing the LSFEM residual with respect to number of degrees of freedom. The p-refinement plot is generated by holding a mesh constant while refining the p-value (Figure 4.5). The serendipity element results were provided by Douglas Wickert [63].

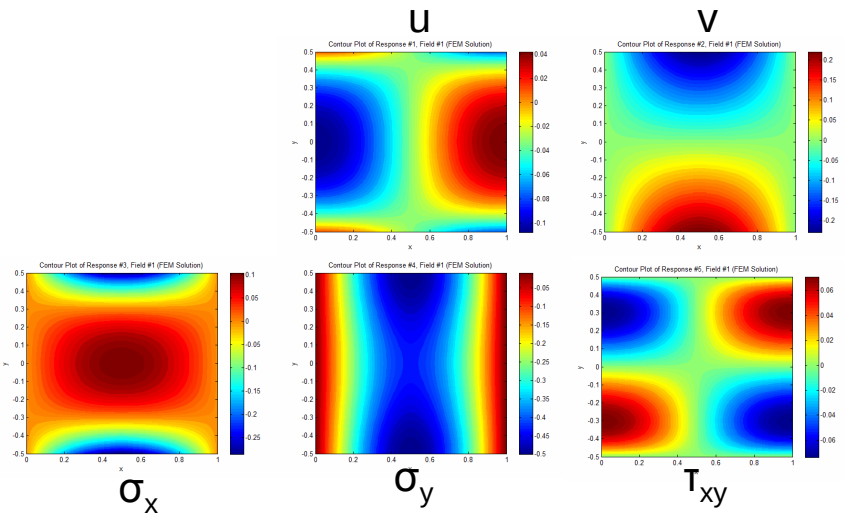

Figure 4.4 Thumbnail Plots of Exact Solution of Timoshenko and Goodier Problem

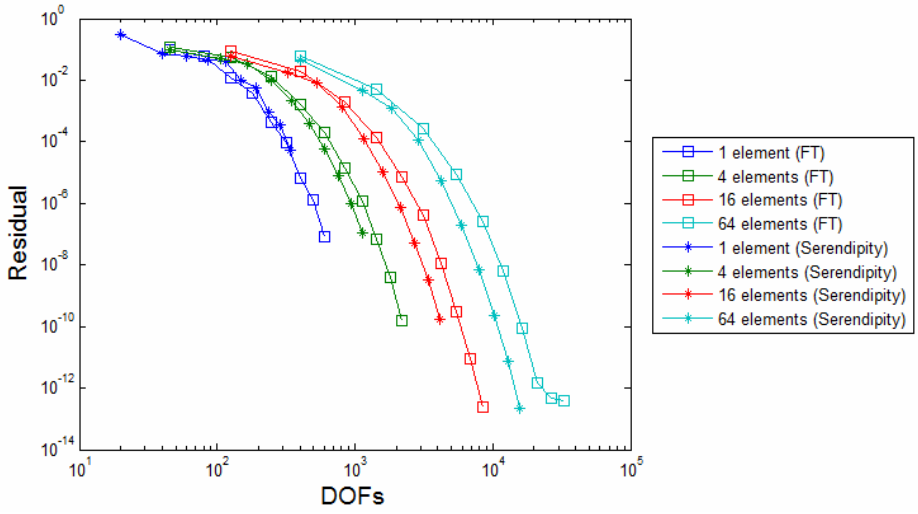

Figure 4.5 Comparison Between Serendipity Shape Functions and Full Tensor Product (FT) Shape Functions for Timoshenko and Goodier Elasticity Problem

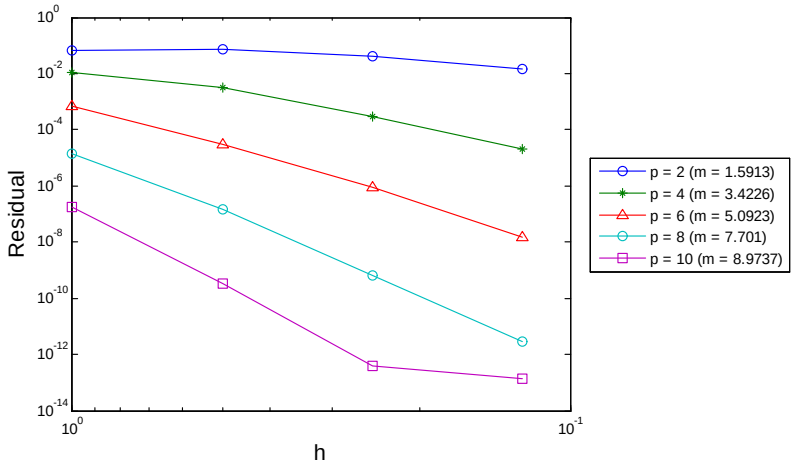

Figure 4.6 h-Convergence: 2D Elasticity Using Displacement-Displacement Gradient Formulation for Timoshenko and Goodier Elasticity Problem

The results show that the full-tensor product elements can exhibit a smaller overall residual error value for the same value of p. However, in this case, the serendipity elements may have fewer degrees of freedom. To examine efficiency, vertical slices of the graph, in Figure 4.5, show that the serendipity elements can exhibit better residual values for a given number of degrees of freedom. This is shown where the serendipity element p-refinement curves cross the full-tensor product curves.

4.5.2 Elliptic vs. Non-Elliptic Comparison.

4.5.2.1 Timoshenko & Goodier Synthetic Elasticity Problem. To examine the convergence rates between elliptic and non-elliptic formulations the same two-dimensional elasticity problem was considered [61, 62]. Using h-refinement, the results of the elliptic differential equations are shown in Figure 4.6. The slopes (m) are defined for each line of constant p-value and the error shown was generated using the least-squares residual.

Ignoring the machine error on the bottom of the graph, the results show an average convergence average slope was less than p. In fact, the average slope was

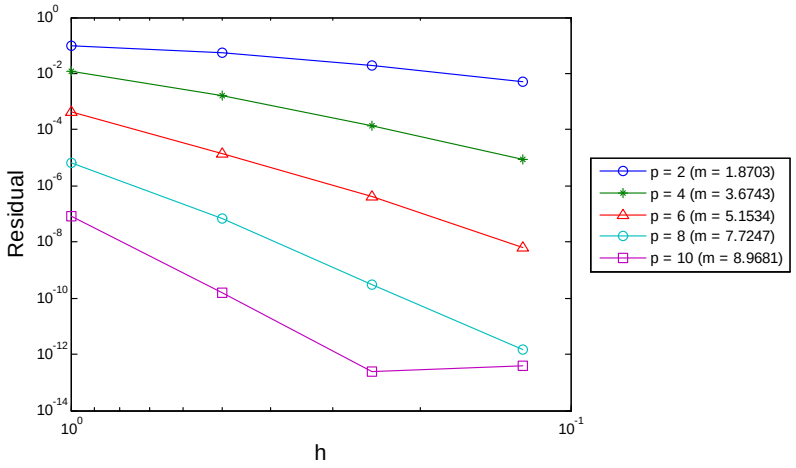

Figure 4.7 h-Convergence: 2D Elasticity Using Displacement-Stress Formulation for Timoshenko and Goodier Elasticity Problem

about $p-0.5$. The slopes shown here were less than the LSFEM residual convergence rates shown by Jiang (3.40) [9]. The second formulation consisted of the non-elliptic form of the plane stress equations. Figure 4.7 shows the relevant results.

The convergence rates for the non-elliptic formulation were very similar to the elliptic formulation $(p - 0.5)$. It appears there was little difference between the elliptic and non-elliptic residual error rates. In practical implementation, there may or may not be any real differences between a well-posed elliptic and non-elliptic formulation when using LSFEM. It has been shown here, for a simple problem, that the residual convergence rates are similar, but are slightly less than the rates guaranteed by Jiang.

4.5.2.2 Manufactured Elasticity Solution. To fully examine the differences between elliptic and non-elliptic results, response error measure must be examined instead of simply examining the least-squares residual. A response error norm

$$Error = \left| u^{exact} - u^{FEM} \right|_0 \tag{4.53}$$

was integrated over the entire domain. It explicitly takes the form

$$\left|u^{exact} - u^{FEM}\right|_0 = \left[\sum_{e=1}^{N_e}\left(\int_{\Omega}\left(u\left(\xi,\eta\right)^{exact} - u\left(\xi,\eta\right)^{FEM}\right)^2 d\Omega\right)\right]^{\frac{1}{2}} \tag{4.54}$$

This compares the finite element solution to a known exact solution that was created for each elasticity response for both the elliptic and non-elliptic forms. A new synthetic problem was created for this comparison. Manufactured problems have been commonly used to verify analysis code [64].

A fairly complex horizontal displacement field was assumed as

$$u_x^s\left(x,y\right) = \left(7x + x^7\right)\cos\left(\pi y\right) \tag{4.55}$$

A vertical displacement field was then created by solving for a $u_y^s\left(x,y\right)$ such that no horizontal body forces (f_x) exist. After that, the stresses were created using the stress-displacement relationships which only consist of derivatives of u_x^s and u_y^s. This resulted in relationships for all responses where vertical body forces ($f_y\left(x,y\right)$) are nonzero. The exact solution equations of all primary and secondary responses are shown in Appendix C.

The exact equations were applied at the edges of a square domain. All boundary conditions were based on the exact solutions evaluated at the boundary edges. Figure 4.8 shows the responses that were constrained at each wall for both the non-elliptic and elliptic formulations. Figure 4.9 shows the exact solution for this problem for displacements and stresses only.

The manufactured elasticity problem was solved using both elliptic (u-H) and non-elliptic (u-σ) formulations. Convergence rates based on slopes of h-refinement curves were generated and then compared to theory using the response L_2 error norms (3.38) and (3.39) as shown by Jiang [9]. Figures 4.10 and 4.11 show a primary response, horizontal displacement, for both the non-elliptic form and elliptic

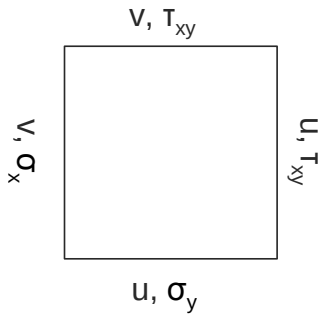

Figure 4.8 Boundary Conditions Applied to Synthetic Problem Created for LSFEM vs. WGFEM Comparisons

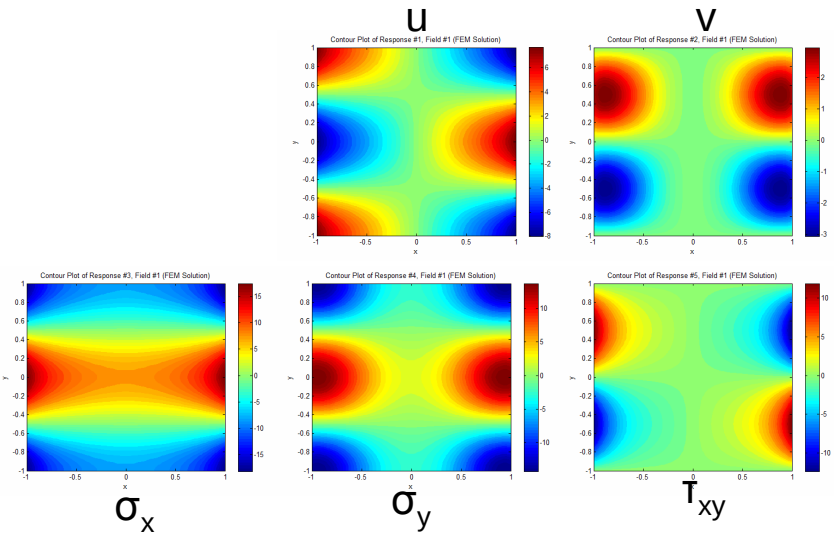

Figure 4.9 Thumbnail Plots of Exact Solution of Synthetic Problem Created for LSFEM vs. WGFEM Comparisons

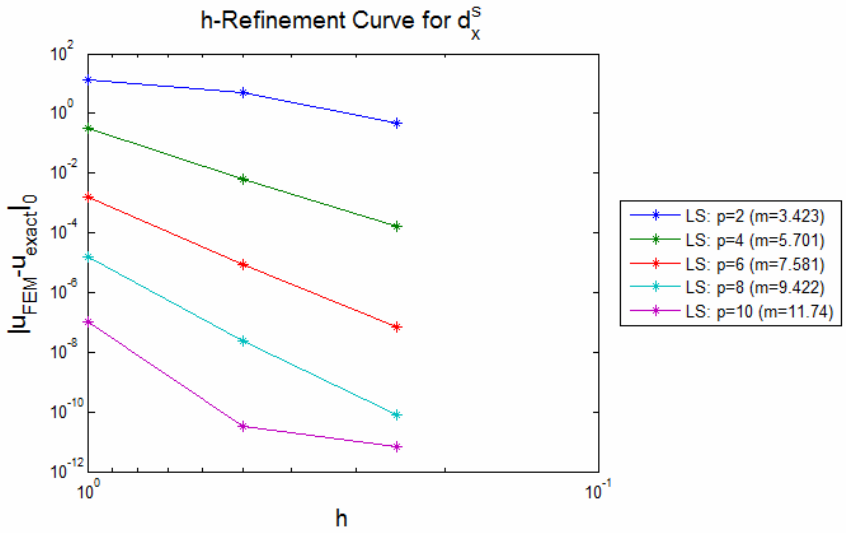

Figure 4.10 h-Refinement Plot for Primary Response for Elliptic Formulation (u-H) for Manufactured Elasticity Problem

form respectively. Figures 4.12 and 4.13 shows a secondary response for both formulations. The response H_1 was shown for the elliptic form and σ_x for the non-elliptic form.

The primary response for both the elliptic and non-elliptic formulations displayed almost identical convergence rates. In addition, the convergence rates for the displacement response for both elliptic and non-elliptic formulations were all greater than $p+1$. The rates shown here met the minimum convergence rates expected for elliptic formulations and exceeded the convergence rates guaranteed for non-elliptic formulations.

The secondary responses for both formulations also exhibited very similar convergence rates. There was very little difference observed between the elliptic and non-elliptic formulations. The average convergence rates observed for the secondary responses did not always exceed $p+1$. However, the rates shown here were very close to theoretical convergence rates for the elliptic formulation. In fact, the average convergence rate observed for the secondary responses is $p+0.8351$.

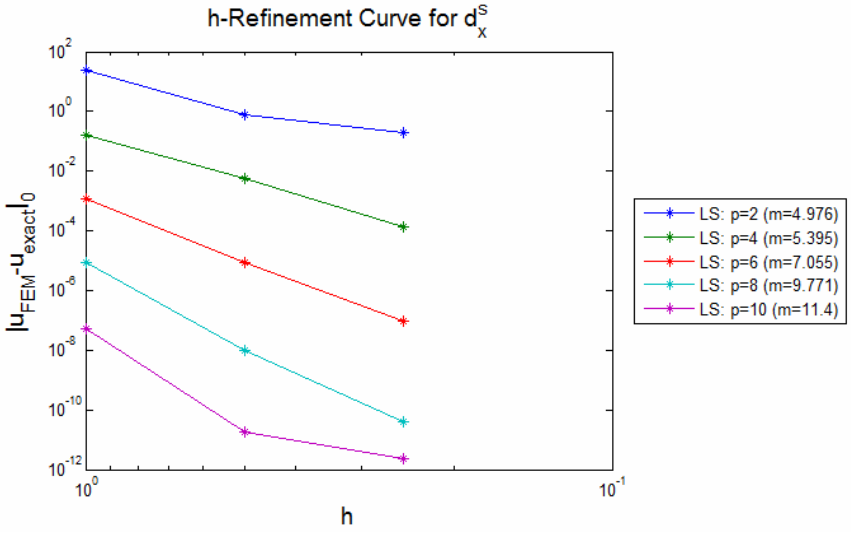

Figure 4.11 h-Refinement Plot for Primary Response for Non-Elliptic Formulation (u-σ) for Manufactured Elasticity Problem

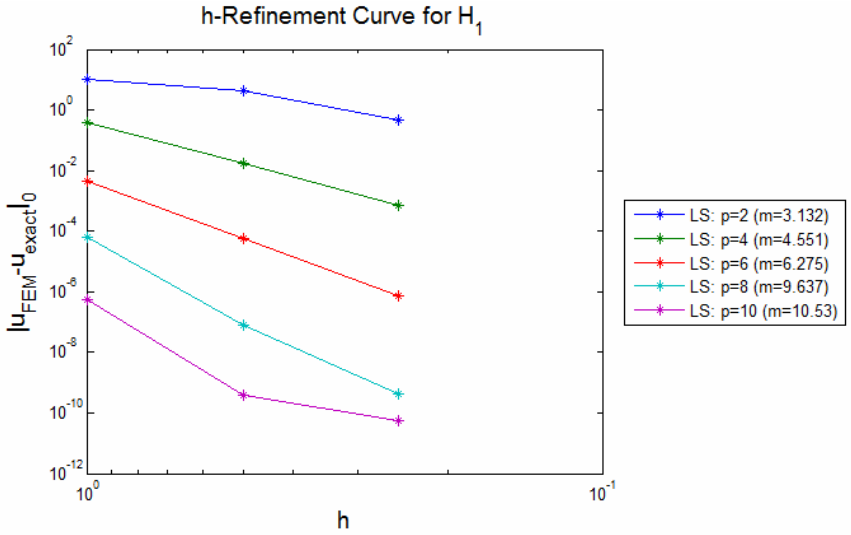

Figure 4.12 h-Refinement Plot for Secondary Response for Elliptic Formulation (u-H) for Manufactured Elasticity Problem

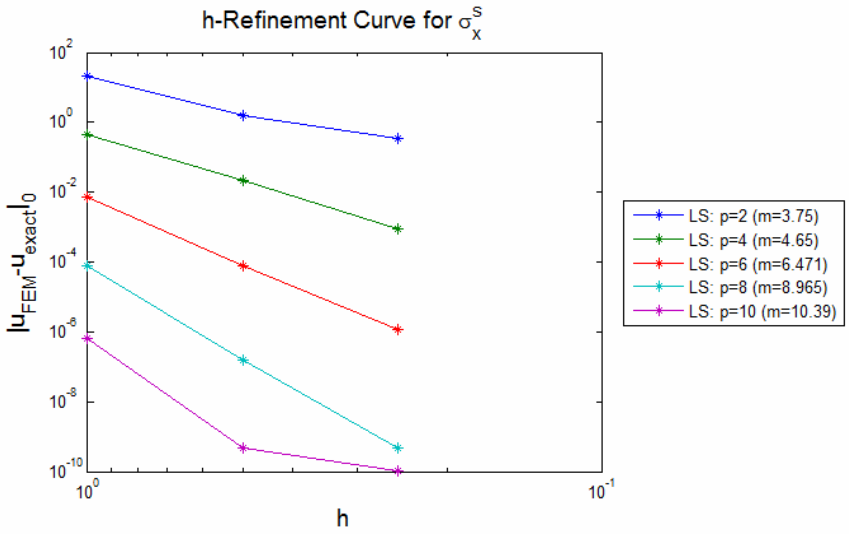

Figure 4.13 h-Refinement Plot for Secondary Response for Non-Elliptic Formulation (u-σ) for Manufactured Elasticity Problem

Most interestingly, there was no difference in accuracy between the elliptic and non-elliptic formulations. This is beneficial since the non-elliptic formulation has secondary variables, stresses, which are much easier to handle for use with boundary conditions and for FSI coupled problems. Pontaza and Reddy [18] have discussed the fact that even if no proof exists for non-elliptic formulations it does not mean that it cannot achieve equal convergence rates. It was shown that at least for this problem, there is no significant difference between the elliptic and non-elliptic formulations.

4.5.3 Mixed Least-Squares FEM vs. Primal Weak Galerkin FEM Comparison. The above synthetic problem was used to compare LSFEM and WGFEM response errors and convergence rates. The first comparison was accomplished by examining hp-refinement curves. These curves are created by increasing the p-value (increase order of polynomials) and increasing the h-value (coarsen mesh), but maintaining the number of degrees of freedom (40 modes). Figure 4.14 shows the hp-refinement results for LSFEM and WGFEM using the L_2 error norm. The non-

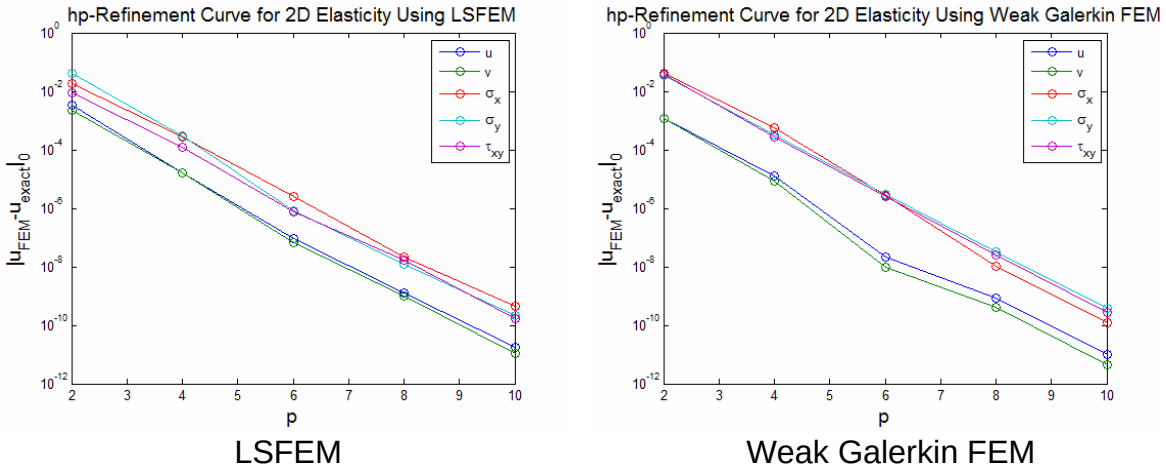

Figure 4.14 *hp*-Refinement Curves Comparing LSFEM and WGFEM Results for a Manufactured Elasticity Problem

elliptic formulation was used for the LSFEM analysis. Integrated error norms are shown for all primary and secondary response types (displacements and stresses).

As expected, the *hp*-refinement results exhibited the same slope for error of each variable. However, the LSFEM curves show a small difference between the primal variables (u_x^s, u_y^s) and the secondary variables $(\sigma_x, \sigma_y, \tau_{xy})$ whereas the WGFEM curves show a larger difference between the primal and secondary variables. This is expected since LSFEM contains the secondary variables as degrees of freedom directly where WGFEM obtains the secondary variables through a post-processing of the previously solved primal variables.

The next analysis compared the *h*-refinement curves. Figure 4.15 shows the error results for the primal variables u and Figure 4.16 shows the error results for the secondary variable τ_{xy} using the L_2 error norm. Ignoring the machine error at the bottom of the graphs, the primary variable results show WGFEM has a slightly better error value and slightly better slope. Alternatively, LSFEM shows a slightly better error value and slope for the secondary variable. The average slope for the WGFEM response was approximately $p + 1$ for the primary variable and approximately p for the secondary variable. The average slope for the LSFEM

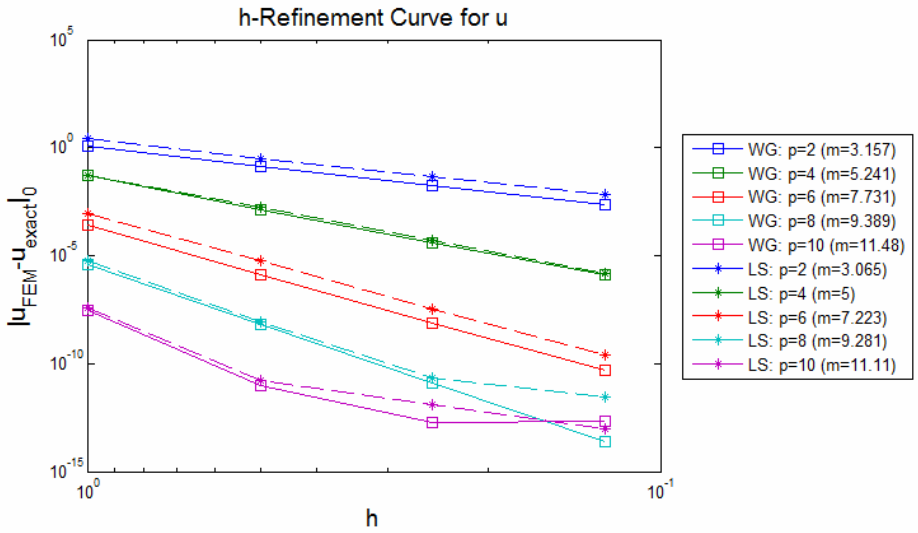

Figure 4.15 h-Refinement Curves Comparing LSFEM and WGFEM Results for Primal Variable u for a Manufactured Elasticity Problem

response was similar for both the primary variable and secondary variables. The secondary variable was very near $p + 1$, but more specifically, showed an average slope of $p + 0.8351$ across all secondary response types (includes σ_x, σ_{xy}, and τ_{xy}). LSFEM does a decent job of approximating the primary and secondary variables with similar convergence rates that are either very close to the elliptic convergence rate bound or exceed it.

The biggest advantage of WGFEM is that it only uses the displacement variables as degrees of freedom. That means LSFEM used 2.5 times as many degrees of freedom to solve the same problem. WGFEM shows an obvious increase in efficiency over LSFEM.

Primal WGFEM has been the method of choice for years and has traditionally shown success. Mixed WGFEM methods have not shown as consistent results. Selecting a mixed formulation for Weak Galerkin has been difficult and, of this date, no one has proven that any one mixed Weak Galerkin method to work as well as the traditional primal WGFEM. Conversely, LSFEM has shown great success for mixed formulations but has not shown strong success for primal formulations in two-

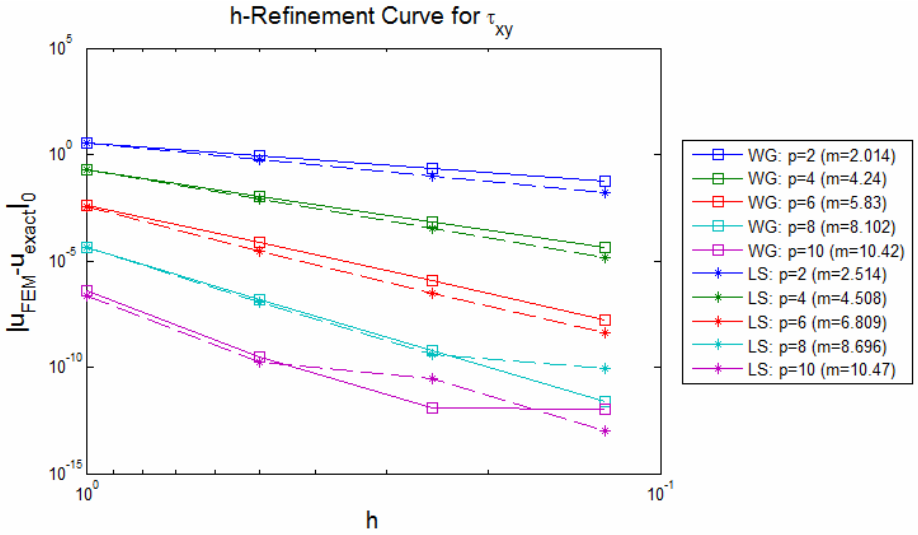

Figure 4.16 h-Refinement Curves Comparing LSFEM and WGFEM Results for Primal Variable τ_{xy} for a Manufactured Elasticity Problem

dimensional domains. C^k element continuity must be applied for primal LSFEM formulations [65].

The justification for a mixed method comes when considering FSI problems. Secondary variables, such as stress, may need to be recovered directly in order to perform a simultaneously coupled and unified formulation. LSFEM can provide the secondary variables directly and with a higher convergence rate than WGFEM. Using this type of coupling and unified formulation may provide improvement in error for FSI.

4.6 Elasticity-Based Mesh Deformation

As shown above, the primal WGFEM formulation is more efficient than the mixed LSFEM formulation due to its reduced number of degrees of freedom. When using an elasticity-based mesh deformation scheme for the fluid domain, efficiency should take precedence over accuracy. The fluid mesh deformation is arbitrary in the first place and does not need a high level of accuracy to accomplish its primary objective, which is to move a fluid domain mesh while maintaining element aspect

ratios. It would seem that WGFEM would be the optimal choice in this case due to its efficiency.

Since accuracy is not an issue, the mixed LSFEM formulation can be converted to a more efficient form. The use of condensation (3.56) and recovery (3.54) with the mixed LSFEM formulation could be used to reduce the number of LSFEM degrees of freedom. The secondary stress variables can be condensed and recovered from the primal displacement variables, because only displacement boundary conditions and no stresses are applied to the mesh deformation field. This results in a formulation just as efficient as primal WGFEM. However, this reduced LSFEM formulation is not nearly as accurate as the full mixed LSFEM formulation. Some simple example cases were examined and have shown an extreme loss in accuracy when all the secondary responses are condensed out of the problem.

4.7 Transient Formulation Study

The methods used to discretize the temporal structural problem were examined here. Several options exist for two-dimensional elasticity. The options used extensively by Kayser-Herold and Matthies [23] include a formulation that consists of only displacement velocities and stresses (v-σ) and a formulation that consists of displacement velocities and displacement gradients (v-H). Kayser-Herold showed that the v-H formulation was elliptic, but the v-σ formulation showed results with accuracy equal to or better than the v-H formulation even though it was non-elliptic. They used the v-σ formulation as their primary analysis method after the accuracies were compared between the formulations [23]. The most interesting feature of their formulations is that neither formulation used primary variables, the displacements, as a direct response. Both types of responses were of secondary type only. The displacements were recovered between each iteration for plotting or for use within a coupled problem, such as mesh deformation. They observed accurate

post-processing of primary variables, but these were not directly recoverable within the LSFEM scheme.

The v-σ formulation consisted of determining equilibrium in terms of displacement velocities and stresses, i.e.,

$$-\rho\frac{\partial v_x^s}{\partial t} + \frac{\partial \sigma_x^s}{\partial x} + \frac{\partial \sigma_{xy}^s}{\partial y} = -f_x \tag{4.56}$$

$$-\rho\frac{\partial v_y^s}{\partial t} + \frac{\partial \sigma_{xy}^s}{\partial x} + \frac{\partial \sigma_y^s}{\partial y} = -f_y \tag{4.57}$$

The stress-displacement-velocity relationships were also required. They were generated by taking the time derivative of the plane-stress stress-displacement relationships (4.20), (4.21), and (4.22):

$$\frac{\partial \sigma_x^s}{\partial t} - \frac{E}{1-\nu^2}\left(\frac{\partial v_x^s}{\partial x} + \nu\frac{\partial v_y^s}{\partial y}\right) = 0 \tag{4.58}$$

$$\frac{\partial \sigma_y^s}{\partial t} - \frac{E}{1-\nu^2}\left(\nu\frac{\partial v_x^s}{\partial x} + \frac{\partial v_y^s}{\partial y}\right) = 0 \tag{4.59}$$

$$\frac{\partial \sigma_{xy}^s}{\partial t} - G\left(\frac{\partial v_x^s}{\partial y} + \frac{\partial v_y^s}{\partial x}\right) = 0 \tag{4.60}$$

This formulation had five equations with five unknowns but required the displacements to be post-processed from the displacement velocities. The velocity boundary conditions used by Kayser-Herold and Matthies were capable of capturing the entire system's boundary conditions. Direct application of the displacement boundary conditions were not required for the problems they solved.

Another option, not examined by Kayser-Herold and Matthies, was the u-v-σ formulation. It includes the secondary variables, displacement velocities and stresses, and it includes the displacements as primary variables. This allows the primary variables to rest within the LSFEM scheme and it allows the displacements to be directly recoverable and directly shared within a coupled problem. Equations

that relate displacements and displacement velocities are

$$\frac{\partial u_x^s}{\partial t} - v_x^s = 0 \tag{4.61}$$

$$\frac{\partial u_y^s}{\partial t} - v_y^s = 0 \tag{4.62}$$

This formulation has seven equations with seven unknowns. It uses the displacement-displacement velocity relationships (4.61) and (4.62) with (4.56), (4.57), (4.20), (4.21), and (4.22). If a mixed LSFEM formulation is desired for coupled problems, its respective improvement in accuracy with respect to the secondary variables is desired, and not much concern exists for memory limits, then it should become beneficial to use the full u-v-σ formulation over the v-σ formulation.

Three questions must be answered when considering the above elasticity formulations. First, does a space-time coupled formulation increase accuracy over space-time decoupled formulations? It has been shown before that a space-time coupled approach can perform better than a space-time decoupled approach [17] and it has been noted to perform worse [9] for particular methods. Second, must an elliptic approach be used over a non-elliptic approach? Finally, if a non-elliptic approach is accurate, does it matter if the user solves the displacements with the finite element system or if the displacements are recovered between each iteration?

A simple study was performed to help answer these questions. The one-dimensional wave equation problem was considered here to help provide insight into these questions. The wave equation was used because of its simplicity and its similar characteristics to the two-dimensional transient elasticity equations. The one-dimensional wave equations can be extended to two-dimensional wave equations, which are closely related to two-dimensional elasticity [23]. The similarities that are of the most interest here are 1) the primary variables may or may not be contained within the formulation, 2) the secondary variables consist of both spatial or temporal

derivatives of the primary variables, and 3) the system can be cast in an elliptic or non-elliptic form.

The original one-dimensional wave equation takes the form

$$\frac{\partial^2 u}{\partial t^2} + c^2 \frac{\partial^2 u}{\partial x^2} = f \tag{4.63}$$

where u is the primal variable, f is the forcing function, and c is the wave speed. The second-order differential equation is reduced to its mixed first-order form before being implemented into LSFEM. The first-order form is

$$\frac{\partial v}{\partial t} - c\frac{\partial p}{\partial x} = f \tag{4.64}$$

where v and p are secondary variables which are defined as

$$v = \frac{\partial u}{\partial t} \tag{4.65}$$

$$p = c\frac{\partial u}{\partial x} \tag{4.66}$$

The symmetry constraint can be added to create an elliptic formulations, i.e.,

$$\frac{\partial p}{\partial t} - c\frac{\partial v}{\partial x} = 0 \tag{4.67}$$

The elliptic formulation combines (4.64) and (4.67). This formulation only uses secondary variables within the LSFEM scheme [23]. This means that the primal variable must be recovered between each time step using the θ-method

$$u_{n+1} = u_n + \Delta t \left[\theta v_{n+1} + (1-\theta)\, v_n\right] \tag{4.68}$$

The Crank-Nicolson method ($\theta = 0.5$) was used here for all space-time uncoupled schemes. The non-elliptic formulation combines (4.64), (4.65), and (4.66). This formulation directly recovers the primal variable and does not require (4.68) [23].

A problem with a known exact solution was considered here [66]. The problem displays a near-discontinuity in its results. This more challenging problem should help differentiate between the advantages and disadvantages of various methods. The boundary conditions applied here are $u(0,t) = u(L,t) = v(0,t) = v(L,t) = 0$. The initial conditions are $u(x,0) = 0.25x(L-x)$ and $p(x,0) = 0$. For these conditions, the solution may be expressed as a Fourier series,

$$u(x,t) = \frac{L^2}{\pi^3} \sum_{n=1}^{\infty} \left[\frac{1-(-1)^n}{n^3} \cos\left(\frac{n\pi c}{L} t\right) \sin\left(\frac{n\pi}{L} x\right) \right] \tag{4.69}$$

which uses the superposition of an infinite number of harmonic waves [12]. The time step size was determined through the Courant-Friedrich-Lewy (CFL) Condition

$$\Delta t = \frac{CFL \cdot \min(h)}{c} \tag{4.70}$$

where the maximum possible stable time step size is generated when $CFL \rightarrow 1.0$. A CFL of 0.9 was used in this study. The exact results for $0 \leq t \leq 0.12$ are shown in Figure 4.17.

Six cases of the above problem were considered. A combination of the space-time coupled formulation and uncoupled formulation were considered with the elliptic formulation and non-elliptic formulation with varying p-values. The L^2 error norms were computed for each response type.

This study showed that there was no difference in accuracy between the elliptic and non-elliptic formulations when the space-time uncoupled scheme was considered (case #1 vs. case #2). In other words, it doesn't matter which equation set is used for the uncoupled case and it doesn't matter whether the primal variables

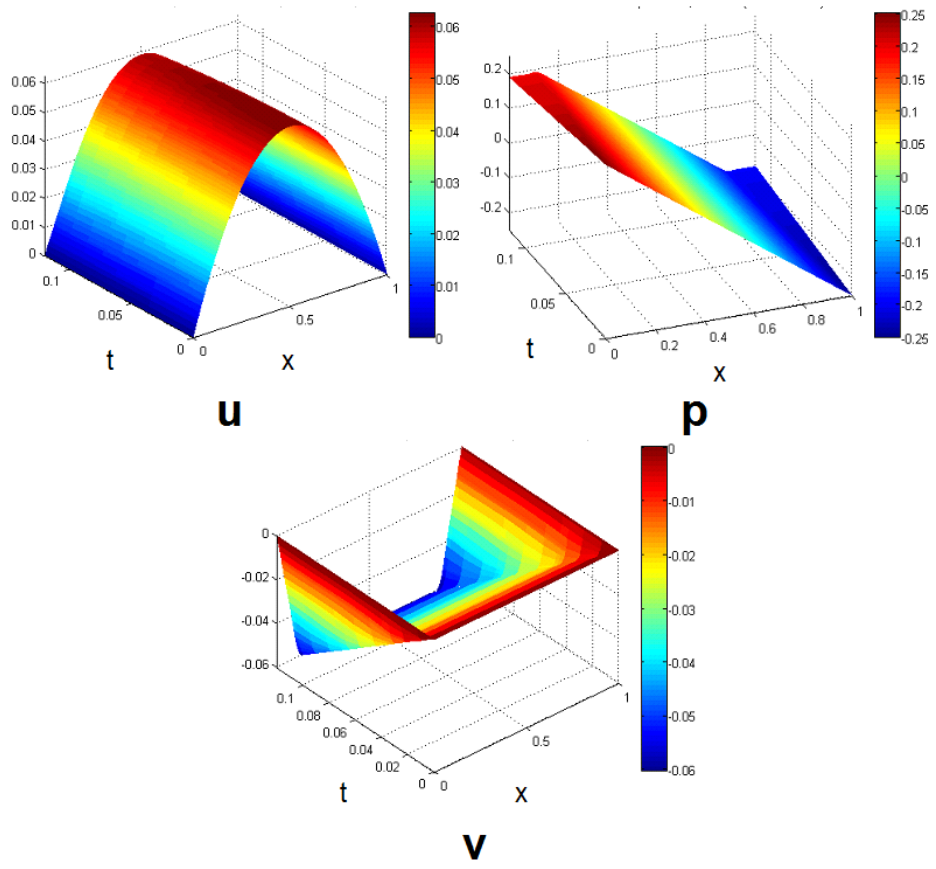

Figure 4.17 Thumbnail Plots of Exact Results for One-Dimensional Wave Equation Example Problem ($0 \leq t \leq 0.12$)

Case	x,t Coupled	Elliptic	p-value	Δt	u Error	p Error	v Error
1	No	No	5	0.04	4.177E-05	1.416E-03	1.416E-03
2	No	Yes	5	0.04	4.177E-05	1.416E-03	1.416E-03
3	Yes	No	5	0.04	5.947E-07	1.143E-04	1.150E-04
4	Yes	Yes	5	0.04	3.446E-05	1.090E-04	1.089E-04
5	Yes	No	10	0.04	3.603E-07	4.724E-05	4.500E-05
6	Yes	No	3	0.12	1.966E-05	1.372E-03	1.107E-03

Table 4.1 One-Dimensional Wave Study Case Results

are recovered during or after each iteration. This was expected since the LSFEM temporal discretization is the same as the temporal discretization used to recover the primal variables.

When the coupled case was considered (case #3 vs. case #4), the accuracy of the secondary variables was exactly the same for the elliptic and non-elliptic cases; however, the primal variable accuracy improved significantly with the non-elliptic case. This is because the primal variables were solved during each iteration of the non-elliptic case instead of being recovered between each iteration in the elliptic case. In the coupled case, the LSFEM temporal discretization is the same as the spatial discretization for secondary variables in both formulations, but not for the primary variable in the elliptic case.

Case #5 shows an improved accuracy compared to case #3 due to a large increase in p-value. This was expected and shows a higher fidelity in both the spatial and temporal derivatives.

In case #6, the time step size was increased significantly. This case was still coupled and was compared to case #1. This comparison shows that the θ-method discretized form has 3 time steps while the LSFEM discretized polynomial has an order of 3 in the temporal coordinate direction. This is not a pure "apples-to-apples" comparison, but it does show a general relationship when the same number of "time steps" were used. In this case, the LSFEM x,t-coupled discretization performed slightly better.

4.7.1 Transient Structural Problems. Kayser-Herold and Matthies experienced significant challenges when using LSFEM for a transient elasticity problem [23]. They examined a transient structural problem using several different systems of differential equations. They showed both elliptic and non-elliptic formulations. These formulations included displacement velocities with stresses (v-σ), displacement velocities with displacement gradients (v-H), and displacement velocities with a linearized

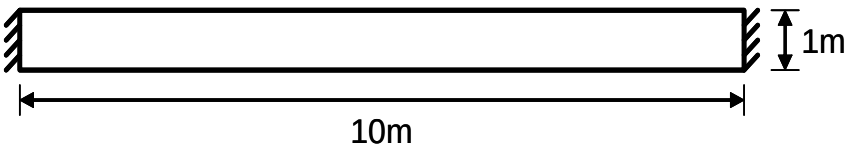

Figure 4.18 Transient Elasticity Problem Setup

stress tensor (v-m). All of these formulations were shown to be extremely sensitive to their equation residual weighting factors and all formulations were not shown to be equivalent to a WGFEM transient elasticity analysis. The best results found by Kayser-Herold and Matthies were shown by the displacement velocities with stresses formulation (v-σ), which is a non-elliptic formulation. Those results were close to WGFEM results, but they were not identical. In addition, when the LSFEM (v-σ) formulation was used in a transient FSI problem, the structural results provided additional structural damping to the system and produced incorrect results.

There were two major issues with their elasticity analysis. First, the equation residual weights that yielded a fairly accurate answer were found using a manual trial and error method. Second, the time step used for the LSFEM analysis was too large [23]. It is unknown why they did not try a smaller time step. The same transient elasticity problem solved by Kayser-Herold and Matthies was examined here but the two issues that plagued their results were avoided.

A beam which is clamped on both the left and right ends was considered here (Figure 4.18) [23]. The beam was 10 meters long and 1 meter high. Material properties were applied in a uniform manner across the entire beam. The Modulus of Elasticity was $E = 10^5$ Pa, Poisson ratio was $\nu = 0.35$, and the structural mass density was $\rho_s = 1.0\ kg/m^3$. No loads are applied to the beam at any time and damping was not considered. The beam was discretized using 10 spanwise elements. A p-value of 4 was used throughout this elasticity study.

#	ω_f (Hz)
1	3.2498
2	8.2712
3	14.8625
4	16.9930
5	22.4635
6	30.7393
7	33.8673
8	39.4714
9	48.5171
10	50.4871

Table 4.2 WGFEM Natural Frequency Results for Double Clamped Beam

Using a WGFEM analysis, the first ten natural frequencies were found (Table 4.2). These natural frequencies match results obtained by Kayser-Herold and Matthies using ANSYS 7.0.

The largest relevant frequency found by the WGFEM frequency analysis helped determine the proper time step size to use for explicit time integration. The largest frequency drove a time step size of $\Delta t = 0.0005$. This time step size was used to determine the transient response of the double clamped beam problem. It was observed here that a larger time step size, such as $\Delta t = 0.01$, will generate results which exhibit inaccurate damping. Using the proper time step size is critical in determining the transient response [43]. Since the natural frequencies found using a WGFEM analysis are more accurate than those found using a LSFEM analysis [14], it is suggested that WGFEM be used before ever using a LSFEM structural analysis so that the largest frequencies can be found to help determine the proper time step size.

A transient response was created using an initial condition of

$$v_y^s = \sin\left(\frac{\pi x}{10}\right) \tag{4.71}$$

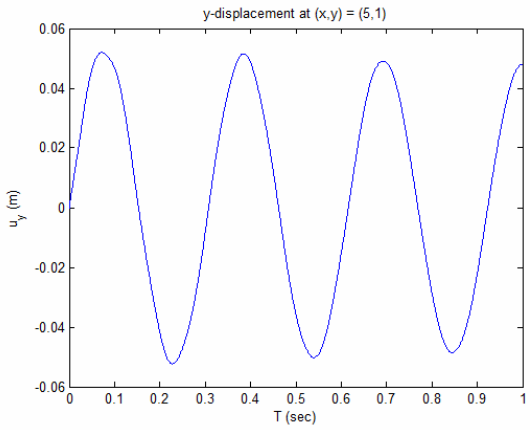

Figure 4.19 Transient Response of the Double Clamped Beam Problem Using WGFEM (Mid-Node Vertical Deformation History)

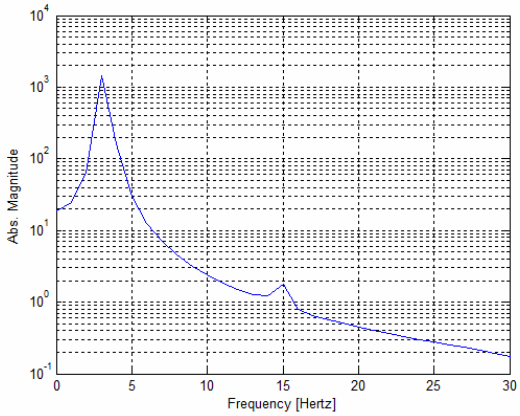

Figure 4.20 FFT of the Double Clamped Beam Transient Response Using WGFEM (Mid-Node Vertical Deformation Power Spectrum Plot)

which creates only an initial vertical velocity to generate structural motion. The transient response of the double clamped beam was found to be neutrally stable. This was expected, since there were no damping mechanisms applied to the system and no loads were applied. Figure 4.19 shows the response history of the beam and Figure 4.20 shows a Fast Fourier Transform (FFT) of the response history. The response history shows a perfectly neutrally stable response. The FFT shows that the 1^{st} and 3^{rd} natural frequencies were excited by the applied initial conditions. Different initial conditions would excite other natural frequencies.

Equation Type	Final Residual Weights (W_i)
Force Equilibrium	0.0157592
Displacement-Stress Relationship	1.1895518
Displacement-Displacement Velocity Relationship	0.0001000

Table 4.3 Equation Weightings for LSFEM 2D Elasticity

The WGFEM response produced an accurate benchmark to compare LSFEM results. The same problem was solved using a 2D in-plane elasticity LSFEM (u-v-σ) formulation. This formulation was used so all primary variables and secondary variables are directly recoverable and sharable. This is useful in a coupled scheme, such as FSI. The same time step size was used as in the WGFEM analysis. In addition, it was found that residual balancing at the equation level was essential to solve the transient elasticity LSFEM problem. The iterative residual balancing approach was used with success here (3.101). Table 4.3 shows the final equation weights generated by the iterative residual balancing approach at the equation level.

The results found using the LSFEM 2D Elasticity formulation were directly comparable to the WGFEM results (Figure 4.21 and Figure 4.22). The magnitudes and frequencies match. This shows that LSFEM can be accurate for transient elasticity analysis, as long as residual weighting at the equation level is considered and the proper time step size is used.

The above solution verifies LSFEM when using 2D in-plane elasticity. A comparable 1D solution is useful here for verification purposes. The same problem was solved using both linear and nonlinear Euler-Bernoulli beam equations. A time step size of $\Delta t = 0.01$ was used for the 1D problem. Figure 4.23 shows the temporal response and Figure 4.24 shows the frequency response for both the linear and nonlinear beam. In both cases, the results compare directly to the WGFEM and LSFEM in-plane elasticity analysis. The results were just as accurate even with a larger time step size. The problem did not exhibit nonlinear characteristics and did not require a nonlinear type of analysis, but it was useful for initial verification

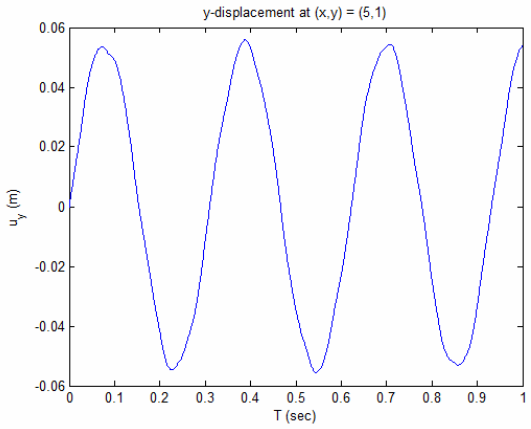

Figure 4.21 Transient Response of the Double Clamped Beam Problem Using LS-FEM 2D Elasticity (Mid-Node Vertical Deformation History)

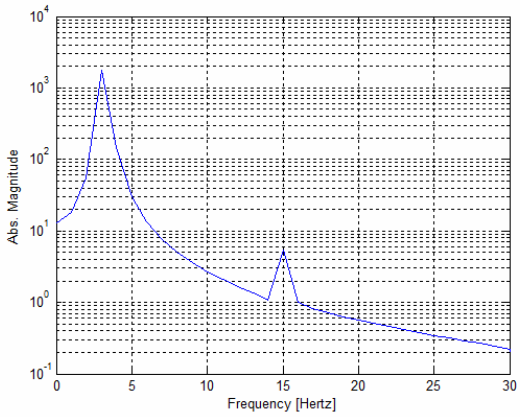

Figure 4.22 FFT of the Double Clamped Beam Transient Response Using LSFEM 2D Elasticity (Mid-Node Vertical Deformation Power Spectrum Plot)

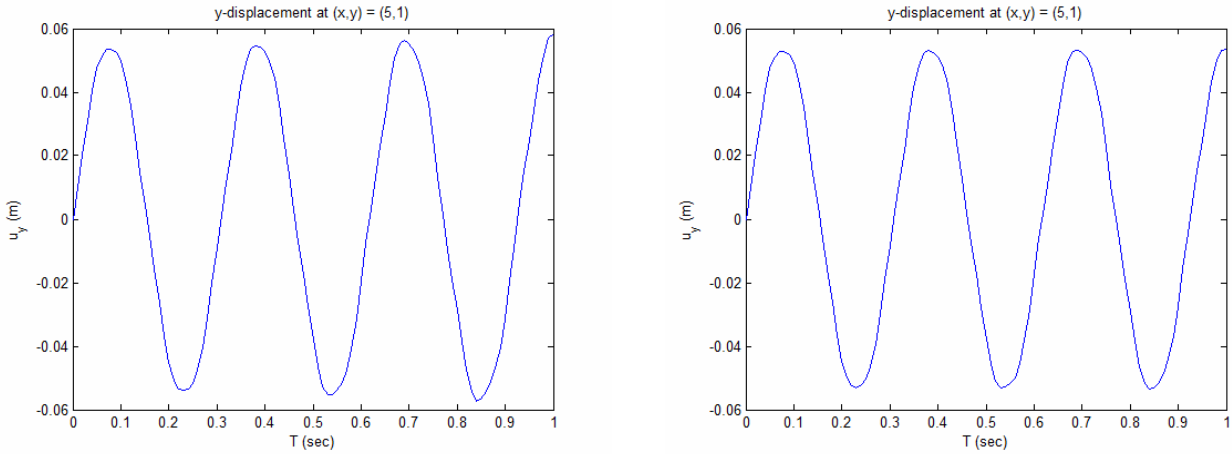

Figure 4.23 Transient Response of the Double Clamped Beam Problem Using LS-FEM with Linear (Left) and Nonlinear (Right) 1D Euler Bernoulli Beam Theory (Mid-Node Vertical Deformation History)

purposes. This implies that the beam deflections were small enough that nonlinear effects are not significant. This does not verify the influence or differences between linear and nonlinear beam analysis.

To test the nonlinear effects of the beam, the initial conditions were increased until a difference was observed between the transient responses. The first significant difference between the linear and nonlinear problems was observed when a velocity of

$$v_y^s = 7.5 \sin\left(\frac{\pi x}{10}\right) \tag{4.72}$$

was used for the problem's initial condition. As shown in Figure 4.25, only a small difference in peak magnitude (6.35%) was observed between the linear and nonlinear responses at this particular initial condition. The peak magnitude for the linear case was 0.441 and the peak magnitude for the nonlinear case was 0.413. It also appears that the nonlinear response exhibited a slightly different period than the linear response. The nonlinear effects exhibited a stiffening effect. When a higher initial condition magnitude was used, the nonlinear problem had great difficulty converging within 100 sub-iterations within each time step. This implies that more

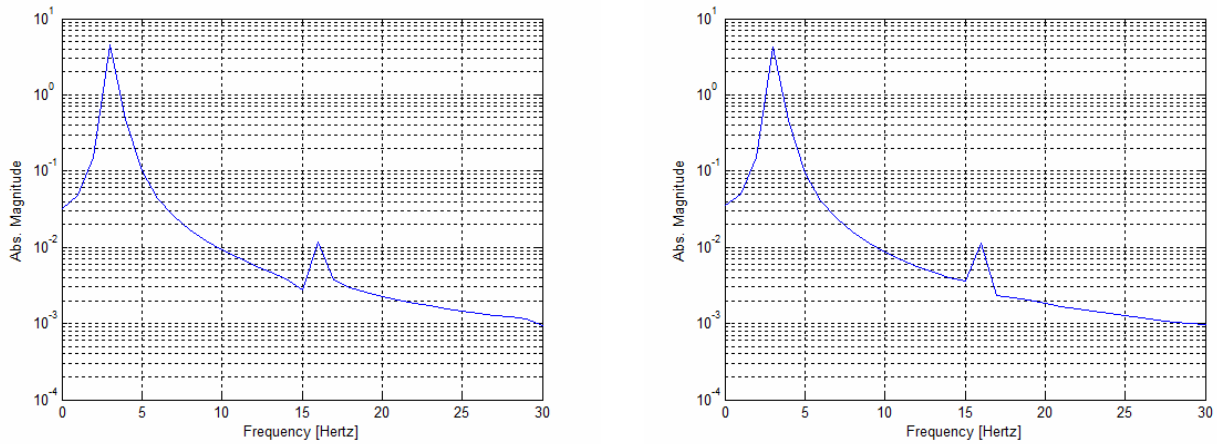

Figure 4.24 FFT of the Double Clamped Beam Transient Response Using LSFEM with Linear (Left) and Nonlinear (Right) 1D Euler Bernoulli Beam Theory (Mid-Node Vertical Deformation Power Spectrum Plot)

significant nonlinear effects are applicable for a magnitude greater than 7.5. A stronger nonlinear convergence method, such as Newton-Raphson, would help solve this problem when significant nonlinear effects are present. Unfortunately, only the direct iteration method was implemented in this research.

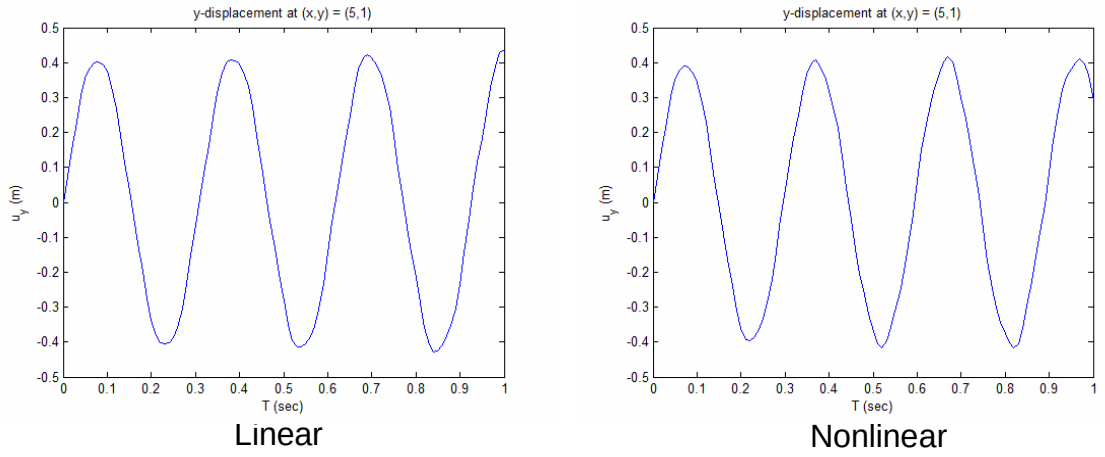

Figure 4.25 Transient Response Using a Larger Initial Velocity of the Double Clamped Beam Problem Using LSFEM with Linear (Left) and Nonlinear (Right) 1D Euler Bernoulli Beam Theory (Mid Node Vertical Deformation History)

V. The Fluid Domain

5.1 Stokes Linear Flow

The Stokes equations are a linear set of fluid equations that are good for creeping flow problems. The Stokes equations governing viscous incompressible creeping flow required minimal computational time due to their linearity. The two-dimensional and elliptic governing equations are summarized as

Mass Continuity:

$$\frac{\partial v_x^f}{\partial x} + \frac{\partial v_y^f}{\partial y} = 0 \tag{5.1}$$

Momentum Conservation (x-dir):

$$\frac{\partial p}{\partial x} + \frac{\partial \omega}{\partial y} = f_x \tag{5.2}$$

Momentum Conservation (y-dir):

$$\frac{\partial p}{\partial y} - \frac{\partial \omega}{\partial x} = f_y \tag{5.3}$$

Vorticity:

$$\frac{\partial v_y^f}{\partial x} - \frac{\partial v_x^f}{\partial y} = \omega \tag{5.4}$$

Here v_x^f and v_y^f represent horizontal and vertical velocity, p represents pressure, and ω represents vorticity [9]. This is a velocity-pressure-vorticity formulation where v_x^f, v_y^f, p, and ω are the unknown degrees of freedom of the system.

A driven cavity flow problem was solved using Stokes equations with the least-squares finite element formulation. The problem consisted of a square domain with a horizontally driven velocity on the top wall. All other walls were specified as no-slip walls. A reference pressure was provided at the bottom of the cavity. The boundary conditions are shown in Figure 5.1.

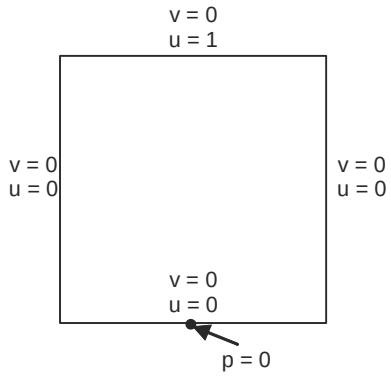

Figure 5.1 Driven Cavity Flow Boundary Conditions

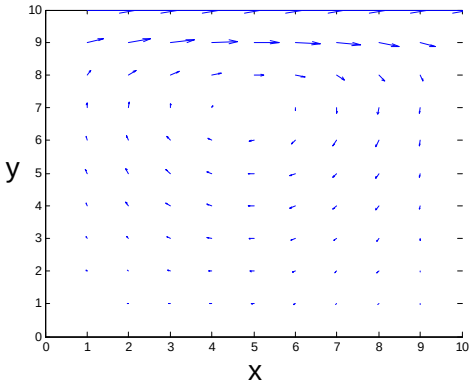

Figure 5.2 Driven Cavity Flow Results – Velocity Vector Plot

The results of the driven cavity flow problem, shown in Figure 5.2, match those published by Jiang [9]. This verifies the LSFEM implementation works well for a Stokes flow problem. This was as expected due to the smooth continuous solution which was solved using elliptic equations.

5.2 Navier-Stokes Incompressible Viscous Flow

A two-dimensional time-dependent, incompressible form of the Navier-Stokes equations using velocity (v), pressure (p), and vorticity (ω) are

$$\text{Mass Continuity: } \frac{\partial v_x^f}{\partial x} + \frac{\partial v_y^f}{\partial y} = 0 \tag{5.5}$$

Momentum Conservation (x-dir): $$\rho_f \frac{\partial v_x^f}{\partial t} + \rho_f v_x^f \frac{\partial v_x^f}{\partial x} + \rho_f v_y^f \frac{\partial v_x^f}{\partial y} + \frac{\partial p}{\partial x} + \mu \frac{\partial \omega}{\partial y} = f_x \rho_f \tag{5.6}$$

Momentum Conservation (y-dir): $$\rho_f \frac{\partial v_y^f}{\partial t} + \rho_f v_x^f \frac{\partial v_y^f}{\partial x} + \rho_f v_y^f \frac{\partial v_y^f}{\partial y} + \frac{\partial p}{\partial y} - \mu \frac{\partial \omega}{\partial x} = f_y \rho_f \tag{5.7}$$

Vorticity: $$\frac{\partial v_y^f}{\partial x} - \frac{\partial v_x^f}{\partial y} = \omega \tag{5.8}$$

where the steady-state form eliminates the time derivatives shown above [9]. Since the incompressible assumption holds, ρ_f is constant and is not a direct response. The above formulation was successfully verified using a simple Blasius plate problem with a known exact solution. The v-p-ω formulation shown above has four equations with four unknowns. Unfortunately, this formulation does not have degrees of freedom that are directly sharable with the stress equilibrium at the fluid-structure interface boundary. An alternate form of the incompressible Navier-Stokes equations uses fluid stresses (σ_x^f, σ_{xy}^f, σ_y^f) instead of vorticity, e.g.,

Mass Continuity:

$$\frac{\partial v_x^f}{\partial x} + \frac{\partial v_y^f}{\partial y} = 0 \tag{5.9}$$

Momentum Conservation (x-dir):

$$\rho_f \frac{\partial v_x^f}{\partial t} + \rho_f v_x^f \frac{\partial v_x^f}{\partial x} + \rho_f v_y^f \frac{\partial v_x^f}{\partial y} + \frac{\partial p}{\partial x} - \left(\frac{\partial \sigma_x^f}{\partial x} + \frac{\partial \sigma_{xy}^f}{\partial y} \right) = f_x \rho_f \tag{5.10}$$

Momentum Conservation (y-dir):

$$\rho_f \frac{\partial v_y^f}{\partial t} + \rho_f v_x^f \frac{\partial v_y^f}{\partial x} + \rho_f v_y^f \frac{\partial v_y^f}{\partial y} + \frac{\partial p}{\partial y} - \left(\frac{\partial \sigma_{xy}^f}{\partial x} + \frac{\partial \sigma_y^f}{\partial y} \right) = f_y \rho_f \tag{5.11}$$

Normal stress relationship (x-dir):

$$\sigma_x^f - 2\mu \frac{\partial v_x^f}{\partial x} \tag{5.12}$$

Normal stress relationship (y-dir):

$$\sigma_y^f - 2\mu \frac{\partial v_y^f}{\partial y} \tag{5.13}$$

Shear stress relationship:

$$\sigma_{xy}^f - \mu \left(\frac{\partial v_x^f}{\partial y} + \frac{\partial v_y^f}{\partial x} \right) \tag{5.14}$$

This v-p-σ formulation uses more equations and unknown degrees of freedom than the v-p-ω formulation. The additional stress degrees of freedom are desirable here since the fluid stresses are used directly when relating Cauchy solid and fluid stress tensors. Both Navier-Stokes equation sets of equations are non-elliptic.

To verify the Navier-Stokes equations, a simple Blasius Plate problem was used. This problem consists of viscous uniform flow over a plate with no-slip conditions. As Figure 5.3 shows, the left and top walls contain far field and uniform boundary conditions. These walls contain horizontal freestream and no vertical flow. The bottom wall is a no-slip wall so both vertical or horizontal velocity components are set to zero. The right wall contains exit flow conditions. The vertical velocity component is set to zero so pure horizontal flow conditions exist on this boundary. The pressure at the outlet is set to zero. No horizontal flow components were specified on the outlet since the boundary layer will generate a vertical velocity component at that location. The flow that develops over the plate shows a growing boundary layer. The boundary layer thickness at $x = 1.0$ was designed to be 0.5 inches high according to Blasius plate theory [67]. A Reynolds number of 100 and a nondimensionalized inflow velocity of 0.3 will generate the desired boundary layer thickness.

The problem was solved using 100 elements in a unitary square mesh with a p-value of 8 (Figure 5.4). Figure 5.5 shows the velocity magnitude results from a LSFEM analysis. An approximate boundary layer line was drawn on top of the velocity results. The approximate boundary layer line shows a growing thickness across the plate and it shows an approximate final layer thickness of 0.5 as expected.

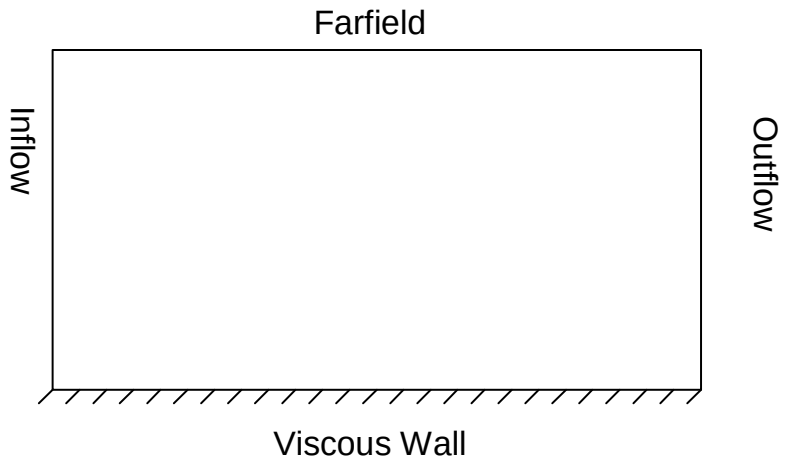

Figure 5.3 Blasius Plate Problem Boundary Conditions

The results are in agreement with the Blasius plate theory. However, the boundary layer location was identified through a peak value in the velocity instead of using the standard 99% of the inflow velocity to identify that location. This difference is stressed by analyzing the LSFEM velocity results as compared to the known exact results at the outlet ($x = 1.0$). The velocity results were plotted with respect to the vertical coordinate location (Figure 5.6). The maximum velocity shown with the LSFEM are much higher than that of the analytic results. This is a significant disparity and it does not change with respect to a finer mesh or a higher p-value.

5.3 Compressible Euler

5.3.1 Equation Development. The compressible and inviscid flow equations in conservation form without body forces are [29, 67]

$$\frac{\partial Q}{\partial t} + \frac{\partial E}{\partial x} + \frac{\partial F}{\partial y} = 0 \tag{5.15}$$

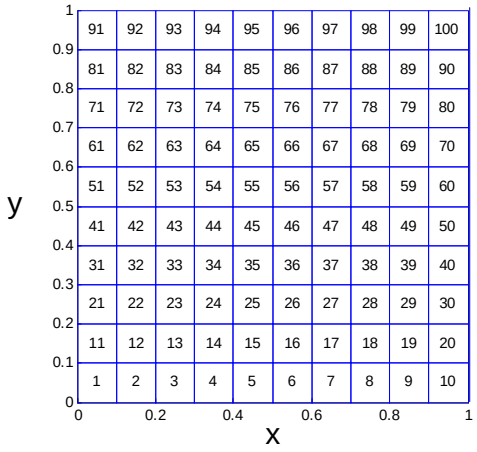

Figure 5.4 Blasius Plate Mesh

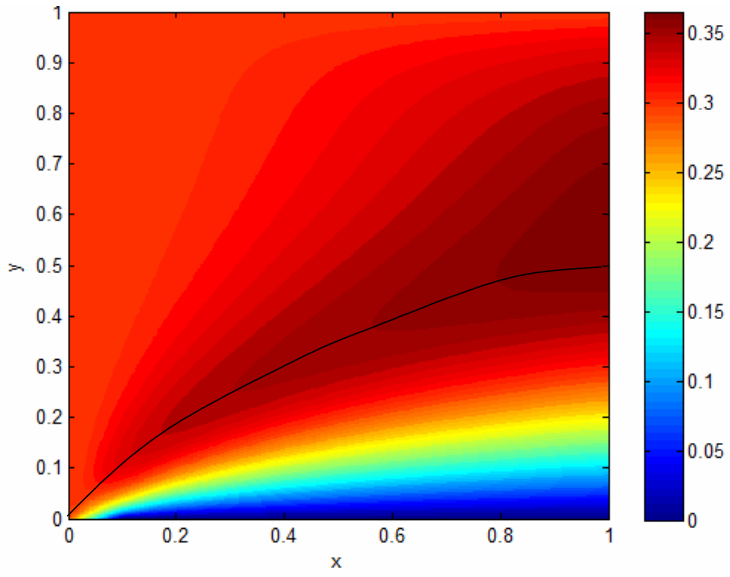

Figure 5.5 Blasius Plate Nondimensionalized Velocity Contour Results With Boundary Layer Line

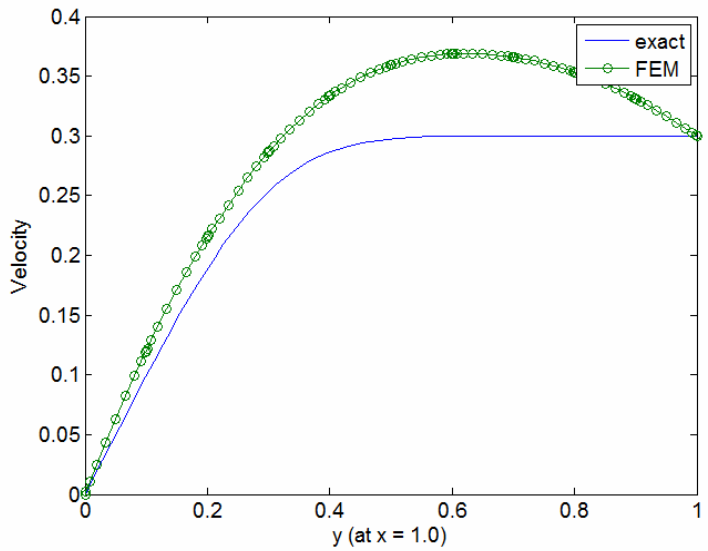

Figure 5.6 Blasius Plate Velocity Results Compared to Exact Solution at $x = 1.0$

where Q is the conservative vector is defined by specific mass (ρ_f), specific energy (E_t), and specific momentum in the x ($\rho_f v_x^f$) and y ($\rho_f v_y^f$) directions, i.e.,

$$Q = \begin{Bmatrix} \rho_f \\ \rho_f v_x^f \\ \rho_f v_y^f \\ E_t \end{Bmatrix} \tag{5.16}$$

The specific energy is defined through the internal potential energy (e) and kinetic energy

$$E_t = \rho_f \left[e + \frac{1}{2} \left| \overrightarrow{V} \right|^2 \right] = \frac{p}{\gamma - 1} + \frac{1}{2} \left(\left(v_x^f \right)^2 + \left(v_y^f \right)^2 \right) \tag{5.17}$$

E and F are the flux vectors in the x and y directions, respectively.

$$E = \begin{Bmatrix} \rho_f \widetilde{v_x^f} \\ \rho_f v_x^f \widetilde{v_x^f} + p \\ \rho_f \widetilde{v_x^f} v_y^f \\ \left(E_t + p \right) \widetilde{v_x^f} \end{Bmatrix} \tag{5.18}$$

$$F = \left\{ \begin{array}{c} \rho_f \widetilde{v_y^f} \\ \rho_f v_x^f \widetilde{v_y^f} \\ \rho_f v_y^f \widetilde{v_y^f} + p \\ (E_t + p)\, \widetilde{v_y^f} \end{array} \right\} \tag{5.19}$$

The convective velocities $\widetilde{v_x^f}$ and $\widetilde{v_y^f}$ are simply v_x^f and v_y^f, since the mesh is not moving. In this case, the flux vectors become

$$E = \left\{ \begin{array}{c} \rho_f v_x^f \\ \rho_f \left(v_x^f\right)^2 + p \\ \rho_f v_x^f v_y^f \\ (E_t + p)\, v_x^f \end{array} \right\} \tag{5.20}$$

$$F = \left\{ \begin{array}{c} \rho_f v_y^f \\ \rho_f v_x^f v_y^f \\ \rho_f \left(v_y^f\right)^2 + p \\ (E_t + p)\, v_y^f \end{array} \right\} \tag{5.21}$$

for a stationary mesh.

The conservation form is not the easiest form to use in a coupled domain analysis. The conservation variables are not always directly sharable with variables in other domains. If the user wants to directly share responses with other domains, the primitive form of the above conservation relationships is useful to develop.

The desired primitive variables are defined as

$$q = \left\{ \begin{array}{c} \rho_f \\ v_x^f \\ v_y^f \\ p \end{array} \right\} \tag{5.22}$$

and the desired form of the final conservation equations are

$$\frac{\partial q}{\partial t} + \widetilde{A_1}\frac{\partial q}{\partial x} + \widetilde{A_2}\frac{\partial q}{\partial y} = 0 \tag{5.23}$$

The matrices $\widetilde{A_1}$ and $\widetilde{A_2}$ now become the linearized portion of the differential equations that must be iterated to convergence, since the matrices are functions of the primal responses operated on by spatial derivatives. This form fits well within the LSFEM variational scheme. The matrices $\widetilde{A_1}$ and $\widetilde{A_2}$ are created by putting q in terms of Q, $(q(Q))$, Q in terms of q, $(Q(q))$, E in terms of Q, $(E(Q))$, and F in terms of Q, $(F(Q))$. Then the $\widetilde{A_1}$ and $\widetilde{A_2}$ are created [28, 29] through the relationships

$$\widetilde{A_1} = \frac{\partial q(Q)}{\partial Q}\frac{\partial E(Q)}{\partial Q}\frac{\partial Q(q)}{\partial q} \tag{5.24}$$

$$\widetilde{A_2} = \frac{\partial q(Q)}{\partial Q}\frac{\partial F(Q)}{\partial Q}\frac{\partial Q(q)}{\partial q} \tag{5.25}$$

The above process was applied to the two-dimensional conservation form and created the following primitive form of the compressible, inviscid Euler equations :Mass Continuity:

$$\frac{\partial \rho_f}{\partial t} + \rho_f\frac{\partial v_x^f}{\partial x} + v_x^f\frac{\partial \rho_f}{\partial x} + \rho_f\frac{\partial v_y^f}{\partial y} + v_y^f\frac{\partial \rho_f}{\partial y} = 0 \tag{5.26}$$

Momentum Conservation (x-dir):

$$\frac{\partial v_x^f}{\partial t} + v_x^f\frac{\partial v_x^f}{\partial x} + \frac{1}{\rho_f}\frac{\partial p}{\partial x} + v_y^f\frac{\partial v_x^f}{\partial y} = f_x \tag{5.27}$$

Momentum Conservation (y-dir):

$$\frac{\partial v_y^f}{\partial t} + v_x^f\frac{\partial v_y^f}{\partial x} + v\frac{\partial v_y^f}{\partial y} + \frac{1}{\rho_f}\frac{\partial p}{\partial y} = f_y \tag{5.28}$$

Energy Conservation:

$$\frac{\partial p}{\partial t} + p\gamma \frac{\partial v_x^f}{\partial x} + v_x^f \frac{\partial p}{\partial x} + p\gamma \frac{\partial v_y^f}{\partial y} + v_y^f \frac{\partial p}{\partial y} = 0 \tag{5.29}$$

The one-dimensional form follows similarly

Mass Continuity:

$$\frac{\partial \rho_f}{\partial t} + \rho_f \frac{\partial v_x^f}{\partial x} + v_x^f \frac{\partial \rho_f}{\partial x} = 0 \tag{5.30}$$

Momentum Conservation:

$$\frac{\partial v_x^f}{\partial t} + u \frac{\partial v_x^f}{\partial x} + \frac{1}{\rho_f} \frac{\partial p}{\partial x} = f_x \tag{5.31}$$

Energy Conservation:

$$\frac{\partial p}{\partial t} + p\gamma \frac{\partial v_x^f}{\partial x} + v_x^f \frac{\partial p}{\partial x} = 0 \tag{5.32}$$

5.3.2 One-Dimensional Verification. The 1D Euler equations were verified using a classic 1D shock tube problem [9,28]. The solution is known and is commonly used to test numerical schemes with spatial and temporal derivatives. The shock tube is assumed to have a nondimensional length of 1.0 and have different initial conditions on the left and right hand side of the tube. There exists a strong pressure and density differential which will create a shock and fluid flow as soon as the analysis begins. The following initial conditions are applied to the system:

$$\left\{ \begin{array}{c} v_x^f = 0.0 \\ p = 1.0 \\ \rho = 1.0 \end{array} \right\} \quad \text{for } x \leq 0.5 \tag{5.33}$$

$$\left\{ \begin{array}{c} v_x^f = 0.0 \\ p = 0.1 \\ \rho = 0.125 \end{array} \right\} \quad \text{for } x > 0.5 \tag{5.34}$$

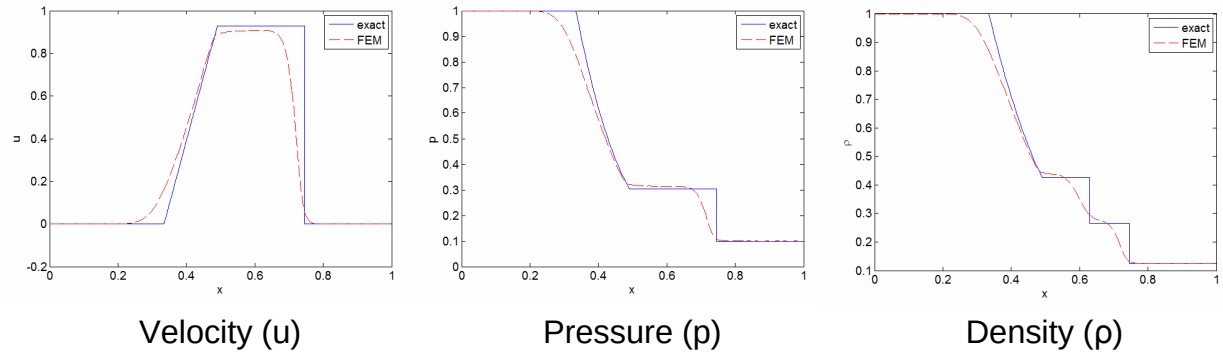

Figure 5.7 Solutions to The Shock Tube Problem ($T = 0.14$ *sec*)

The tube was discretized using 100 lengthwise elements with a p-value of 5. A time step size of 0.005 seconds was used throughout the analysis. The solution was iterated through 28 time steps ($T = 0.14$ seconds). The final solution responses are shown in Figure 5.7 and are compared to a known exact solution [28]. Figure 5.8 shows the time history from the initial conditions to the final conditions. The final results showed reasonable accuracy compared to results published by Jiang [9] and the calculated exact solution [28]. The dissipation effects are similar to a first-order accurate finite volume scheme.

5.3.3 Two-Dimensional Verification. The shock-tube problem verified the 1D Euler Compressible code. The 2D Euler code was verified using a classic airfoil problem in a uniform flow field. Not only does the airfoil test problem expand the analysis to two-dimensions, but it tests the effects of characteristic boundary conditions. The airfoil is a symmetric NACA 0012 airfoil. The advantage of this airfoil analysis is that experimental results are available for validation purposes [68]. An inflow Mach number of 0.31 was used at an angle of attack of 4.2^o. Several unique factors were considered to solve this classic airfoil problem. These unique factors include characteristic boundary conditions, balancing the residual weights for no penetration boundary conditions, and time stepping towards steady-state for hyperbolic equations.

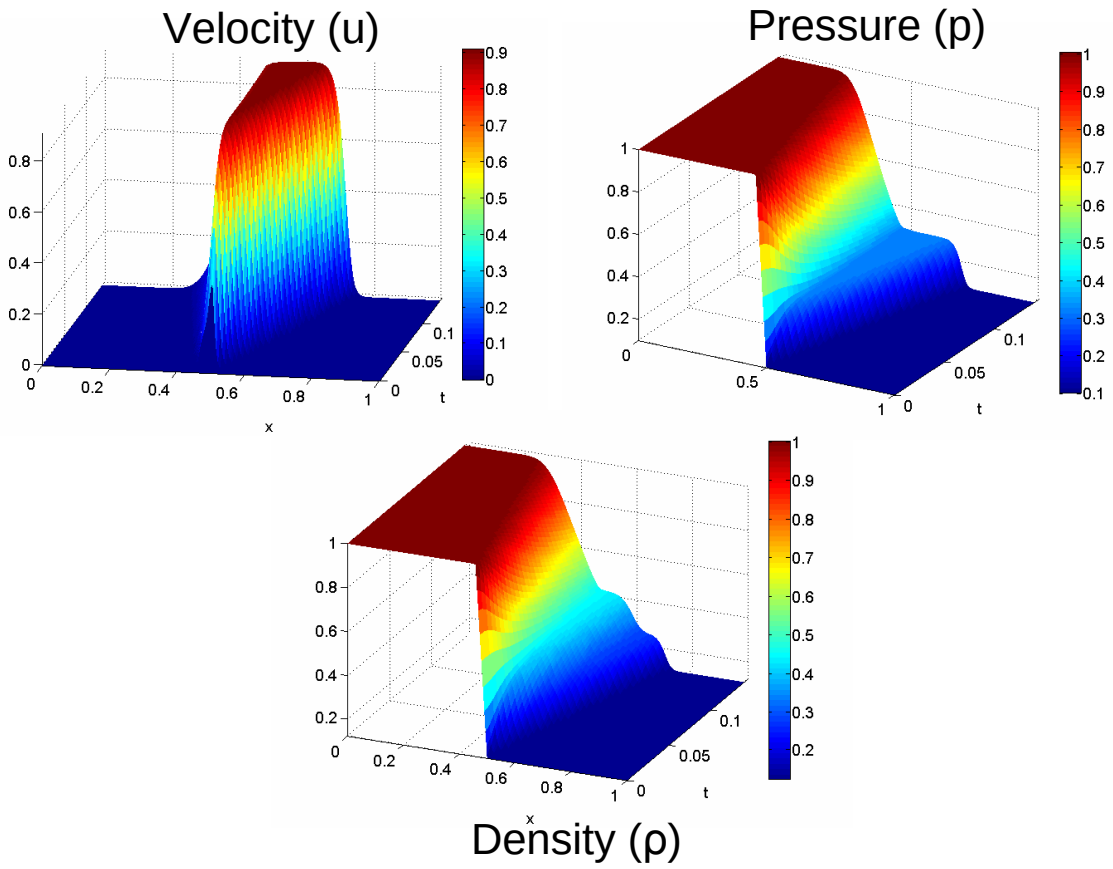

Figure 5.8 Time History of The Shock Tube Problem ($0 \leq T \leq 0.14$)

5.3.3.1 Characteristic Boundary Conditions. It is well known that characteristic boundary conditions are essential when considering a compressible and subsonic flow field [29]. The subsonic and compressible flow field will exhibit flow characteristics that are both positive and negative. This means that the characteristic directions at the walls depend on both the inner domain and outer domain. Considering this, the far field cannot simply be "clamped." This creates difficult boundary conditions for these types of problems since characteristic relationships must be used at the boundaries, because the Euler equations are considered a hyperbolic system [69–72].

Considering a compressible Euler system, there are four eigenvalues, or characteristic values of the system. The eigenvalues are defined by the normal vector ($\widehat{n}$), the convective velocity ($\widetilde{U}$), and the speed of sound (a)

$$\lambda_1 = \left|\widetilde{U}\right| \tag{5.35}$$

$$\lambda_2 = \left|\widetilde{U}\right| \tag{5.36}$$

$$\lambda_3 = \widetilde{U} + a\left|\widehat{n}\right| \tag{5.37}$$

$$\lambda_4 = \widetilde{U} - a\left|\widehat{n}\right| \tag{5.38}$$

For a subsonic system, the velocities are not greater than a, so λ_4 is negative. When considering the boundary characteristics, the inflow conditions create three upstream characteristics and one downstream characteristic and the outflow conditions also create three upstream characteristics and one downstream characteristic [71]. Figure 5.9 shows the inflow and outflow characteristic directions.

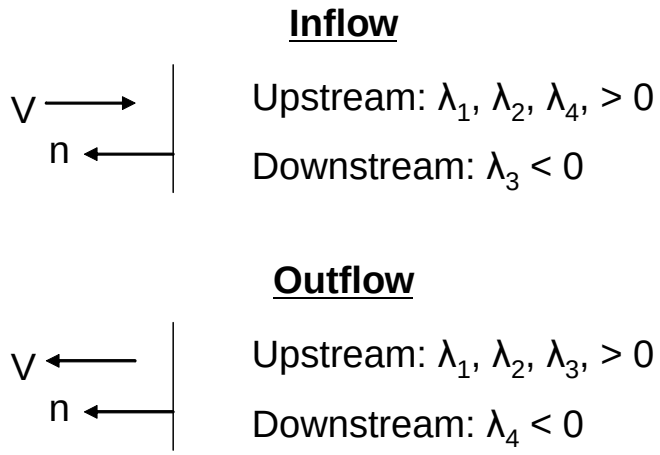

Figure 5.9 Inflow and Outflow Characteristic BC Directions

The characteristic variables are defined through [71, 72]

$$w = \left\{ \begin{array}{c} w_1 \\ w_2 \\ w_3 \\ w_4 \end{array} \right\} = L^{-1} q = \left[\begin{array}{cccc} 1 & 0 & 0 & -\frac{1}{(a_o)^2} \\ 0 & n_y & -n_x & 0 \\ 0 & n_x & n_y & \frac{1}{\rho a_o} \\ 0 & -n_x & -n_y & \frac{1}{\rho a_o} \end{array} \right] \left\{ \begin{array}{c} \rho \\ v_x^f \\ v_y^f \\ p \end{array} \right\} \tag{5.39}$$

The characteristic variables are conveniently expressed in terms of the primal variables and the system's variables. The characteristic relationship at the walls requires that the magnitude of the characteristic waves pass through the walls without returning. Enforcing this condition will help the solution converge properly. In the steady-state case, this is simply

$$\frac{dw}{dn} = 0 \tag{5.40}$$

For the transient case, it is stated as

$$\frac{dw}{dt} + \Lambda \frac{dw}{dn} = 0 \tag{5.41}$$

where Λ is a square matrix with the system eigenvalues across the diagonal.

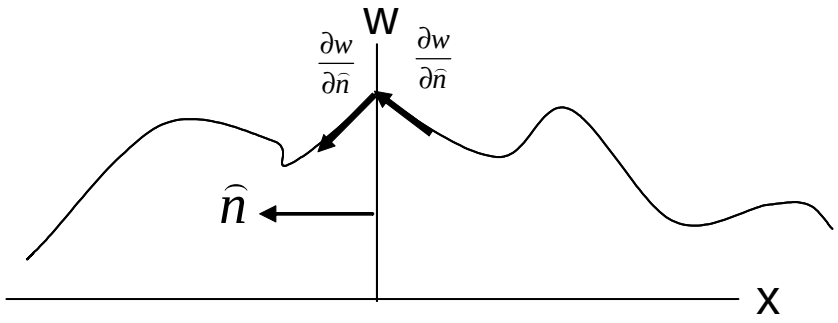

Figure 5.10 Possible Characteristic Response Through Virtual Boundary Wall

Hirsch *et al.* paid careful attention in developing boundary conditions for a finite volume scheme. They ensured that the normal derivatives taken of the characteristic variables (w) were taken outside the domain or inside the domain depending on the sign of the characteristic value at the wall [71]. For example, at an inflow wall, the 1^{st}, 2^{nd}, and 4^{th} characteristic derivatives were evaluated outside the domain whereas the 3^{rd} characteristic derivative was evaluated within the domain. The normal derivatives were based only on a first-order finite volume scheme. The external derivatives utilized the freestream conditions, whereas the internal derivatives utilized the internal domain responses. Hirsch *et al.* assumed that the slope of the characteristics were discontinuous, within the numerical scheme, at the wall boundary conditions (Figure 5.10). This is why the derivatives were evaluated either inside or outside the domain. Great success was observed by Hirsch *et al.* when using characteristic boundary conditions with a finite volume scheme [71].

A finite element scheme with these types of characteristic boundary conditions must use similar methods to determine the external derivatives. The internal derivatives are easily evaluated using the finite element shape functions within the domain that border the boundary edge. The external derivatives can be evaluated by either using a first-order finite volume scheme from the virtual boundary to the freestream conditions located at infinity or they can be evaluated by applying an

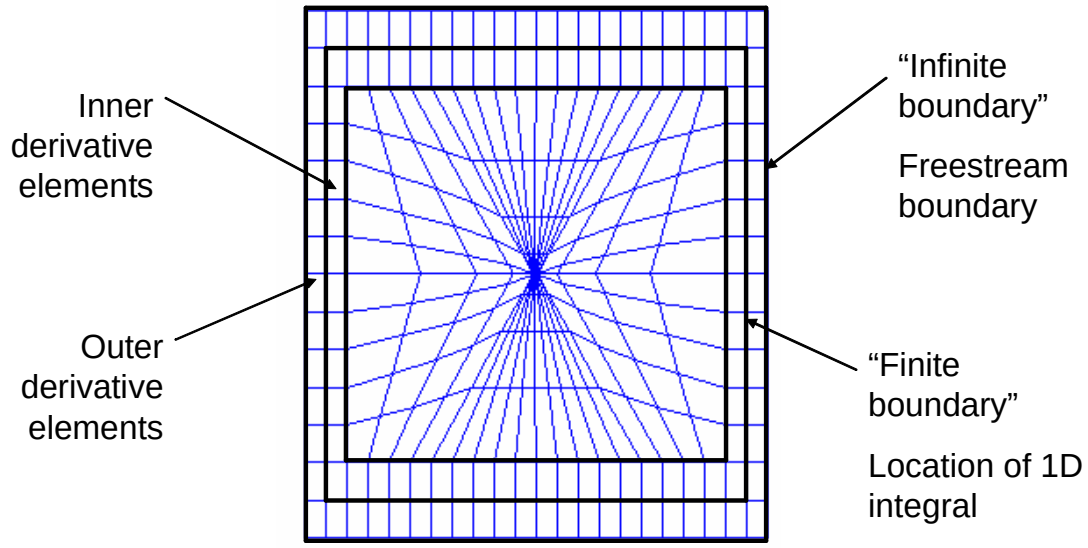

Figure 5.11 Non-Reflective Boundary Conditions Using "Infinite" Elements

extra "strip" of elements to behave as "infinite" elements [73]. This extra "strip" of elements can provide a way to determine the external derivatives using the finite element shape functions. Figure 5.11 shows an example setup of how and where the internal and external derivatives can be taken with respect to the inner and outer strips of elements.

The finite element derivatives, with respect to the virtual normal boundary, are generated using

$$\frac{\partial}{\partial n} = n_x \frac{\partial}{\partial x} + n_y \frac{\partial}{\partial y} \tag{5.42}$$

where the spatial derivatives must be expressed in terms of the element's natural coordinates,

$$\frac{\partial}{\partial n} = n_x \left(\frac{\partial \xi}{\partial x} \frac{\partial}{\partial \xi} + \frac{\partial \eta}{\partial x} \frac{\partial}{\partial \eta} \right) + n_y \left(\frac{\partial \xi}{\partial y} \frac{\partial}{\partial \xi} + \frac{\partial \eta}{\partial y} \frac{\partial}{\partial \eta} \right) \tag{5.43}$$

and the Jacobian is used to express explicitly the normal derivative operator

$$\frac{\partial}{\partial n} = n_x \left(J_{11}^{-1} \frac{\partial}{\partial \xi} + J_{12}^{-1} \frac{\partial}{\partial \eta} \right) + n_y \left(J_{21}^{-1} \frac{\partial}{\partial \xi} + J_{22}^{-1} \frac{\partial}{\partial \eta} \right) \tag{5.44}$$

Poinsot and Lele made a bold challenge to the characteristic boundary conditions implementation. They stated that the characteristic variables are smooth and continuous at the virtual boundary [72]. This is extremely useful when using finite element schemes, since the characteristic variables can be evaluated exclusively within the domain and the responses can be evaluated using finite element shape functions. There is no need to apply an extra "strip" of elements around the virtual boundary or to apply a different numerical scheme such as a finite volume scheme to evaluate the external derivatives. The freestream conditions are applied at the virtual boundary, since there is no "infinite" location to apply the freestream values. The virtual boundary values vary to allow the characteristic waves to pass through the boundary. It was suggested that the virtual boundary response values be restrained weakly using weighted boundary values instead of restraining the values strongly using clamped boundary conditions. In addition, it was suggested that the inflow conditions be restrained by the freestream velocities and density values whereas the outflow conditions be restrained by only the freestream pressure values [72].

Table 5.1 shows the various cases analyzed using various non-reflective characteristic boundary condition methods. Each case was applied to the classic 2D airfoil problem. Two methods proved to be accurate and convergent. The method that used a strip of "infinite" elements was just as accurate as the Poinsot and Lele method. It seems that either method is a reliable method to apply non-reflective boundary conditions that ensures convergence properties and still maintains problem accuracy.

5.3.4 Euler Time Stepping. Tannehill *et al.* made the critical note that if a steady-state solution is desired, it is not always accurate to only use the spatial derivatives of a hyperbolic system of equations [28]. In other words, time-stepping is typically required to accurately obtain both steady-state and transient results when using the compressible form of the Euler equations. Both methods were

Case #	Description	Convergence Properties	Accuracy Properties
1	Non-Reflective Characteristic Boundary Conditions Not Applied	Diverged	Inaccurate
2	Internal and External Derivatives with Finite Differencing	Diverged	Inaccurate
3	Internal and External Derivatives with Additional Strip of Finite Elements	Converged	Accurate
4	Internal Derivatives Only with Clamped Virtual Boundary Values	Diverged	Inaccurate
5	Internal Derivatives Only with Weighted Virtual Boundary Values	Converged	Accurate

Table 5.1 Case Study of Various Characteristic Boundary Condition Options

attempted in this research for comparison purposes. It was observed that only using the spatial derivatives generates poor results for the classic airfoil problem. Convergence was obtained quickly, but the results were smoothed across the domain and the flow field around the airfoil was completely inaccurate. When the full Euler equations were used with both temporal and spatial derivatives, the problem was solved successfully.

Transient problems utilize a uniform, or rather a global, time step size across the entire domain. If a steady-state solution is sought, a local time step could be used within each element such that the solution will march towards steady-state convergence faster. For this steady-state solution, the largest time step size was used for every element within the domain. The tailoring of the time step for each element is based on the domain's stability requirements, or rather, how fast the fluid information can pass through a particular element. This time step is based on the characteristic values within each element. The time step size for each element is similar to (4.70) and takes the form for compressible Euler flow analysis,

$$\Delta t_e = CFL \frac{A_e}{(\Lambda_c^I + \Lambda_c^J)} \tag{5.45}$$

where A_e is the area of the element and Λ_c^I and Λ_c^J are the maximum characteristic wave speeds observed for each set of element faces. The I and J directions are defined for structured mesh quadrilateral elements. The CFL constant is the same

as that used in (4.70). The characteristic speeds are determined by

$$\Lambda_c^I = \left(\left| \overrightarrow{V} \cdot \widehat{n}^I \right| + a \right) \Delta S^I \tag{5.46}$$

which is valid for the I facing edges of the element. The variable S^I is the element edge area of the I facing edges, a is the speed of sound, $\overrightarrow{V}$ is the velocity field vector, and $\widehat{n}^I$ is the normal vector facing outward from the I facing edges. The J direction is treated in a similar fashion. If a time accurate solution is desired, the minimum global time step size is determined.

$$\Delta t_G = \min \left(\Delta t_e \right) \tag{5.47}$$

5.3.5 No Penetration Boundary Conditions and Their Respective Residual Weights. The airfoil problem requires that the fluid not penetrate the airfoil surface. Since the flow is inviscid, only the normal velocity components must equal zero at the surface boundary. The tangential and normal velocity components are generated through the relationships

$$v_x^f \cdot \cos(\beta) + v_y^f \cdot \sin(\beta) - v_n^f = 0 \tag{5.48}$$

$$v_x^f \cdot \sin(\beta) - v_y^f \cdot \cos(\beta) - v_t^f = 0 \tag{5.49}$$

The normal velocity component is then set equal to zero at the airfoil surface boundary. Both the normal and tangential components are retained and post-processed to ensure accuracy of the implemented boundary conditions. The velocity component conversion relationships (5.48) and (5.49) are applied through the LSFEM boundary integral portion of the functional. For the airfoil problem, this creates a total of three systems of equations that were simultaneously solved. The first system of equations was the Euler fluid analysis, the second was the no penetration condition on the top of the airfoil, and the third was the no penetration condition

Domain Type	Final Residual Weights (W_i)
Euler Flow	10^0
Velocity Component Conversion (Top of Airfoil)	$10^{-2.25}$
Velocity Component Conversion (Bottom of Airfoil)	$10^{-2.25}$

Table 5.2 Final Residual Weights for Classic Airfoil Problem In a Uniform Flow Field

on the bottom of the airfoil. The simultaneous solution required residual weight balancing. As discussed in Section 3.2.6, applying an angled boundary condition with higher-order elements requires that the boundary condition be applied using the LSFEM boundary integral relationship. A discrete method, which would not add systems of equations to the LSFEM solution by simply replacing v_x^f and v_y^f with v_n^f and v_t^f, is inaccurate for higher-order elements.

Simultaneous solution of the three sets of equations was highly sensitive to residual weighting factors. The iterative residual weight balancing method did not work here, since each element had its own time step size where the residual calculations would be adjusted by that factor. Only a manual method of trial and error properly worked to determine the residual weights for the simultaneous domains. Those weights were finally determined once the exact solution was observed for this problem. Table 5.2 shows the final weights used. If the exact solution was not known beforehand, the correct residual weights could not have been found.

5.3.6 Airfoil Problem Results. Once convergence was achieved and the final residual weights determined, the airfoil results were compared to finite volume results and experimental results. Figure 5.12 and Figure 5.13 show the final pressure results from the classic airfoil problem. The same number of degrees of freedom were used along the airfoil surface as those used by finite volume means. A total of 80 degrees of freedom were used around the surface. For finite differencing, 80 cells were used along the surface. For LSFEM, the best solution was seen when 16 elements were used with a p-value of 5. Figure 5.12 shows the coefficient of pressure

results across the top and bottom surface of the airfoil, compared to experimental results. It was shown here that the LSFEM results did not reach the peak C_p values as those achieved through finite volume or experimental means. The finite volume results over-approximated the true peak shown by the experimental results. Other than at the leading edge of the top airfoil surface, the LSFEM results slightly underestimated both the finite volume and experimental results. The finite volume results over-approximated its pressure response throughout as compared to the experimental results. Other p-values were attempted for this problem while maintaining the same number of degrees of freedom (hp-refinement) as the finite volume and previous LSFEM airfoil problems (80 DOFs on surface of the airfoil). Surprisingly, an increase in the polynomial order or a change in the mesh size did not improve the accuracy as it compares to the finite volume or experimental solutions. The solution degenerated for a p-value less than 4. A refinement of the finite volume results was not performed here. A mesh independent solution was not shown here for the finite volume approach. A highly refined grid was used for the finite volume solution and the main goal of this analysis was to compare the methods using the same number of degrees of freedom.

It seems that both the finite volume and LSFEM schemes had difficulty matching the experimental results. The real differences between these two schemes becomes more apparent when examining memory requirements and computational time. The finite volume scheme was much faster than LSFEM and required less memory. It seems that finite volume is the method of choice, and it is for a single fluid domain problem, but the real question comes when considering a coupled problem such as FSI. A single variational scheme could provide improved accuracy overall for the coupled problem over that of a mixed approach such as a finite volume and Weak Galerkin scheme.

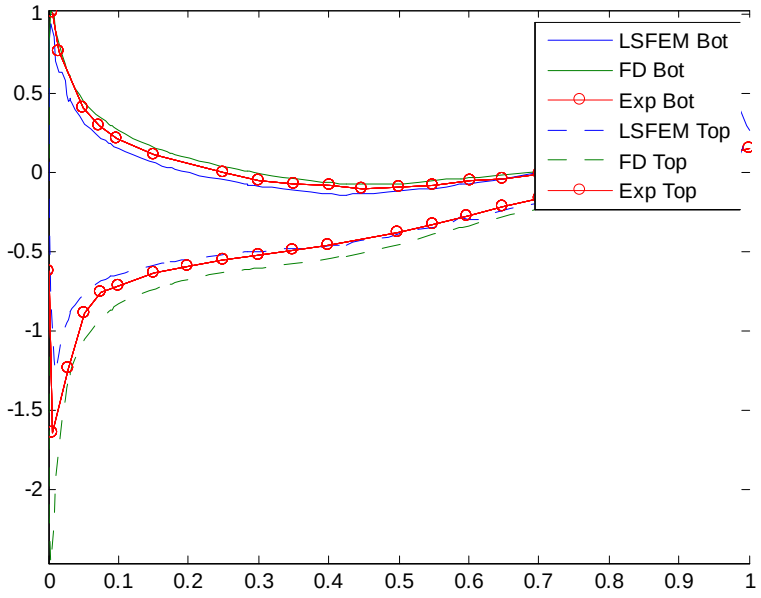

Figure 5.12 Plot of Cp on Top and Bottom of Airfoil

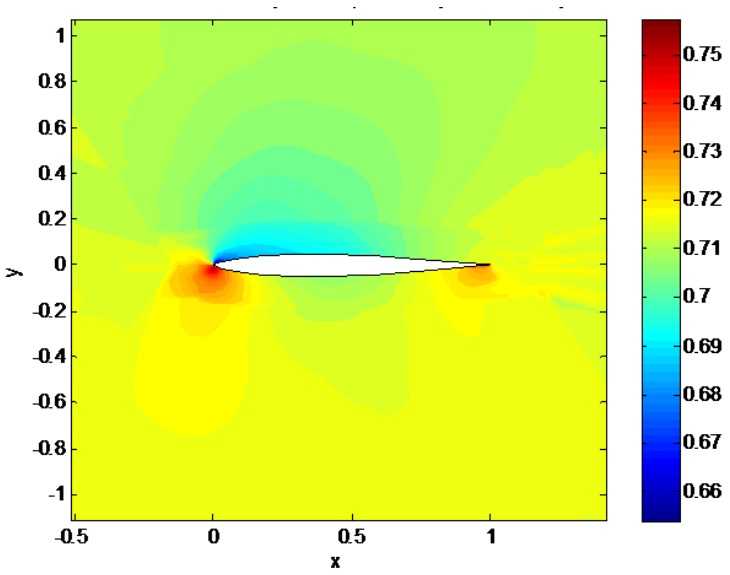

Figure 5.13 Airfoil Pressure Contour Plot

5.4 Arbitrary Lagrangian-Eulerian Formulation

5.4.1 Euler ALE. In an ALE approach, the convective velocities become relative velocities. The new convective velocities are based on both the actual velocities v_x^f and v_y^f and the grid velocities $v_{x_g}^f$ and $v_{y_g}^f$, i.e.,

$$\widetilde{v_x^f} = v_x^f - v_{x_g}^f \tag{5.50}$$

$$\widetilde{v_y^f} = v_y^f - v_{y_g}^f \tag{5.51}$$

The only other change required is to ensure that the energy associated with the pressure work done by convective velocities is negated. This is accomplished by adding $pv_{x_g}^f$ and $pv_{y_g}^f$ to the energy flux vectors [23, 24, 44–46]. The compressible Euler flux vectors become

$$E = \left\{ \begin{array}{c} \rho_f \left(v_x^f - v_{x_g}^f \right) \\ \rho_f v_x^f \left(v_x^f - v_{x_g}^f \right) + p \\ \rho_f \left(v_x^f - v_{x_g}^f \right) v_y^f \\ (E_t + p) \left(v_x^f - v_{x_g}^f \right) + p v_{x_g}^f \end{array} \right\} \tag{5.52}$$

$$F = \left\{ \begin{array}{c} \rho_f \left(v_y^f - v_{y_g}^f \right) \\ \rho_f v_x^f \left(v_y^f - v_{y_g}^f \right) \\ \rho_f v_y^f \left(v_y^f - v_{y_g}^f \right) + p \\ (E_t + p) \left(v_y^f - v_{y_g}^f \right) + p v_{y_g}^f \end{array} \right\} \tag{5.53}$$

The above conservative form was converted to the primal form using (5.24) and (5.25). In the ALE case, $v_{x_g}^f$ and $v_{y_g}^f$ become part of the differential equations. To assist with the primal Euler ALE development, it was assumed that $v_{x_g}^f$ and $v_{y_g}^f$ are not functions of q or Q, that is, they do not depend on the conservative or primal responses. In other words, the grid velocities are assumed to be completely independent of the fluid response. The final compressible and inviscid Euler ALE

form was found to be:

Mass Continuity:

$$\frac{\partial \rho_f}{\partial t} + \rho_f \frac{\partial v_x^f}{\partial x} + \left(v_x^f - v_{x_g}^f\right) \frac{\partial \rho_f}{\partial x} + \rho_f \frac{\partial v_y^f}{\partial y} + \left(v_y^f - v_{y_g}^f\right) \frac{\partial \rho_f}{\partial y} = 0 \tag{5.54}$$

Momentum Conservation (x-dir):

$$\frac{\partial v_x^f}{\partial t} + \left(v_x^f - v_{x_g}^f\right) \frac{\partial v_x^f}{\partial x} + \frac{1}{\rho_f} \frac{\partial p}{\partial x} + \left(v_y^f - v_{y_g}^f\right) \frac{\partial v_x^f}{\partial y} = f_x \tag{5.55}$$

Momentum Conservation (y-dir):

$$\frac{\partial v}{\partial t} + \left(v_x^f - v_{x_g}^f\right) \frac{\partial v_y^f}{\partial x} + \left(v_y^f - v_{y_g}^f\right) \frac{\partial v_y^f}{\partial y} + \frac{1}{\rho_f} \frac{\partial p}{\partial y} = f_y \tag{5.56}$$

Energy Conservation:

$$\frac{\partial p}{\partial t} + p\gamma \frac{\partial v_x^f}{\partial x} + \left(v_x^f - v_{x_g}^f\right) \frac{\partial p}{\partial x} + p\gamma \frac{\partial v_y^f}{\partial y} + \left(v_y^f - v_{y_g}^f\right) \frac{\partial p}{\partial y} = 0 \tag{5.57}$$

5.4.2 Navier Stokes ALE . The u-p-ω form of the Navier Stokes equations with convective velocities identified takes the form

Mass Continuity:

$$\frac{\partial v_x^f}{\partial x} + \frac{\partial v_y^f}{\partial y} = 0 \tag{5.58}$$

Momentum Conservation (x-dir):

$$\rho_f \frac{\partial v_x^f}{\partial t} + \rho_f \widetilde{v_x^f} \frac{\partial v_x^f}{\partial x} + \rho_f \widetilde{v_y^f} \frac{\partial v_x^f}{\partial y} + \frac{\partial p}{\partial x} + \mu \frac{\partial \omega}{\partial y} = f_x \rho_f \tag{5.59}$$

Momentum Conservation (y-dir):

$$\rho_f \frac{\partial v_y^f}{\partial t} + \rho_f \widetilde{v_x^f} \frac{\partial v_y^f}{\partial x} + \rho_f \widetilde{v_y^f} \frac{\partial v_y^f}{\partial y} + \frac{\partial p}{\partial y} - \mu \frac{\partial \omega}{\partial x} = f_y \rho_f \tag{5.60}$$

Vorticity:

$$\frac{\partial v_y^f}{\partial x} - \frac{\partial v_x^f}{\partial y} = \omega \tag{5.61}$$

These convective velocities are only found in the momentum conservation equations. The convective velocities are then modified to represent mesh movement. The new momentum conservation equations take the form [23, 24, 44–46]

Momentum Conservation (x-dir):

$$\rho_f \frac{\partial v_x^f}{\partial t} + \rho_f \left(v_x^f - v_{x_g}^f \right) \frac{\partial v_x^f}{\partial x} + \rho_f \left(v_y^f - v_{y_g}^f \right) \frac{\partial v_x^f}{\partial y} + \frac{\partial p}{\partial x} + \mu \frac{\partial \omega}{\partial y} = f_x \rho_f \tag{5.62}$$

Momentum Conservation (y-dir):

$$\rho_f \frac{\partial v_y^f}{\partial t} + \rho_f \left(v_x^f - v_{x_g}^f \right) \frac{\partial v_y^f}{\partial x} + \rho_f \left(v_y^f - v_{y_g}^f \right) \frac{\partial v_y^f}{\partial y} + \frac{\partial p}{\partial y} - \mu \frac{\partial \omega}{\partial x} = f_y \rho_f \tag{5.63}$$

The *u-p-σ* formulation will also result in a small difference from the original form where only the momentum conservation equations are modified, i.e.,

Momentum Conservation (x-dir):

$$\rho_f \frac{\partial v_x^f}{\partial t} + \rho_f \left(v_x^f - v_{x_g}^f \right) \frac{\partial v_x^f}{\partial x} + \rho_f \left(v_y^f - v_{y_g}^f \right) \frac{\partial v_x^f}{\partial y} + \frac{\partial p}{\partial x} - \left(\frac{\partial \sigma_x^f}{\partial x} + \frac{\partial \sigma_{xy}^f}{\partial y} \right) = f_x \rho_f \tag{5.64}$$

Momentum Conservation (y-dir):

$$\rho_f \frac{\partial v_y^f}{\partial t} + \rho_f \left(v_x^f - v_{x_g}^f \right) \frac{\partial v_y^f}{\partial x} + \rho_f \left(v_y^f - v_{y_g}^f \right) \frac{\partial v_y^f}{\partial y} + \frac{\partial p}{\partial y} - \left(\frac{\partial \sigma_{xy}^f}{\partial x} + \frac{\partial \sigma_y^f}{\partial y} \right) = f_y \rho_f$$

5.4.3 Verification of ALE. A test problem was created to verify the use of the ALE approaches developed above. The problem uses a simple uniform and square domain as an initial condition. As the solution develops, the center of the mesh deforms through a user prescribed motion. The following equation was only

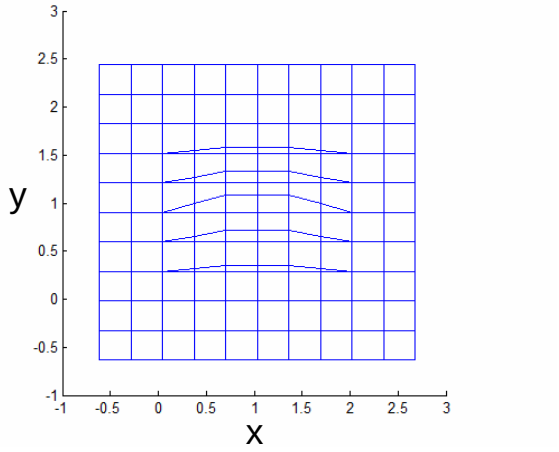

Figure 5.14 ALE Verification Problem: Mesh Deformation

applied to the two elements in the center of the mesh:

$$y\left(t\right) = 0.25\left(1 - \cos\left(\frac{2\pi t}{4}\right)\right) \tag{5.65}$$

The prescribed motion has a displacement magnitude of 0.25 and has a period of 4 seconds. The centerline nodes were moved such that the center of the mesh follows the prescribed motion and the outer two strips of elements remain stationary near the boundaries. A linear interpolation was used between the prescribed centerline motion and the stationary elements. Figure 5.14 shows a sample deformation at the maximum mesh deformation.

Uniform flow conditions were applied to the fluid ($v_x^f = 0.3100$, $v_y^f = 0.0000$, $p = 0.7143$, $\rho^f = 1.0000$, and $\omega = 0.0000$). If no mesh deformation was allowed, the solution would remain at the uniform flow conditions. The transient mesh deformation provided a mesh and problem that tested the accuracy of Navier-Stokes ALE and Euler ALE. If the conditions remain the same and do not deviate beyond the initial uniform flow conditions (excluding machine error), then the ALE approach is verified. This approach is commonly used to verify ALE approaches [23, 44–46]. If the uniform flow conditions do not change as the mesh moves, the Geometric

Conservation Law (GCL) is shown to hold properly for the given implementation. GCL states that the time rate of change of the element volume equals the grid velocity normal to the surface of each element face, i.e., [46].

$$\frac{\partial}{\partial t}\int_V dV = \int_A (\overrightarrow{v}_g \cdot \widehat{n})\, dA \tag{5.66}$$

As long as the Jacobian is updated at every time step and the time integration scheme is accurate, GCL will hold when using finite element methods [23]. This means that the grid velocities must be calculated with a high level of accuracy between each iteration.

The above problem was solved using the ALE approach for both Euler and Navier-Stokes equations. In both cases, the uniform flow conditions held through the entire temporal history using a time step size of 0.01 seconds up to a total time of 1.00 seconds. In these cases, the computed response variance was at the machine error level (10^{-14}). Figure 5.15 and Figure 5.16 show the density contour plot for the Euler ALE and Navier Stokes ALE results, respectively. The same unchanging results were observed for all response types. In other words, even though the mesh was moving with respect to time, all types of fluid responses exhibited no change. This was the desired response.

The ALE approach allows for the fluid domain to remain accurate while mesh deformation is used. This is essential for transient FSI problems since the structure will provide boundary deformation and will create a fluid mesh that is moving with respect to time. In other words, it allows the implementation of a Lagrangian system (structure) to interface with an Eulerian system (fluid) accurately.

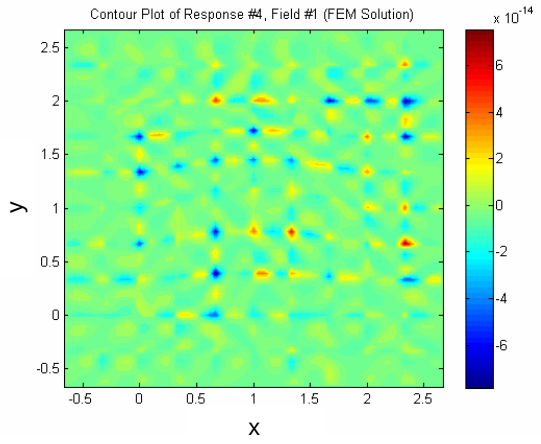

Figure 5.15 Contour Plot of Density for the Euler ALE Verification Problem

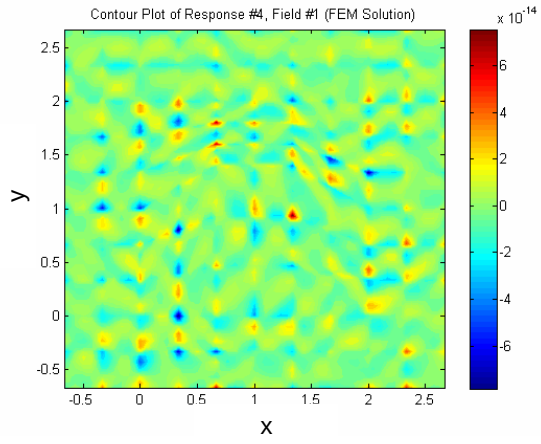

Figure 5.16 Contour Plot of Density for the Navier-Stokes ALE Verification Problem

VI. Fluid-Structure Interaction Theory and Methodology

6.1 Simultaneous Coupling of Multiple Fields

Using finite elements for both types of domains creates a set of simultaneous equations that can be solved for both fluids and structures concurrently. In the case of fluid-structure coupled problems, each domain depends on the other domain's degrees of freedom. Structural deformations change as the aerodynamic pressures change, and aerodynamic pressures change as the structure deflects and changes the boundary's shape. Not only does the boundary move, but mesh coordinates in the interior of the fluid domain will also change. In the transient scenario, the velocities at the boundary between the structural domain and the fluid domain must also match. In the inviscid case, the normal velocities must match at the boundary.

A concurrent set of equations is possible to solve the coupled problem with shared degrees of freedom, i.e.,

$$\begin{bmatrix} [K_S] & [K_{SF}] \\ [K_{SF}] & [K_F] \end{bmatrix} \begin{Bmatrix} U_S \\ U_F \end{Bmatrix} = \begin{Bmatrix} F_S \\ F_F \end{Bmatrix} \tag{6.1}$$

where subscript S represents structural components and subscript F represents fluid components of the problem. The variables U_S and U_F are defined in Appendix B for each type of fluid and structural analysis used in this dissertation. Both linear and nonlinear fluid equations were used for various fluid and structural domains. Unique benefits were observed when using the fully-coupled equation above. The most notable benefit was that the common implementation of the fluid and structural domains and their coupled components facilitated a simultaneous solution.

Another possible domain governs the mesh deformation. This domain could be characterized by an elasticity-based mesh deformation scheme where the mesh deformation has its own analysis type and will determine mesh movement. This

domain can also be implemented into a fully simultaneously coupled system

$$\begin{bmatrix} [K_S] & [K_{SF}] & [K_{SD}] \\ [K_{SF}] & [K_F] & [K_{FD}] \\ [K_{SD}] & [K_{FD}] & [K_D] \end{bmatrix} \begin{Bmatrix} U_S \\ U_F \\ U_D \end{Bmatrix} = \begin{Bmatrix} F_S \\ F_F \\ F_D \end{Bmatrix} \tag{6.2}$$

where the subscript D represents the mesh deformation domain. This domain utilized two-dimensional plane-stress equations. Least-squares finite elements were used for all three domains for consistency.

In a two-field formulation (6.1), the coupled matrices, K_{SF} and K_{FS}, contain the coupled information between the structure and fluid domain. Since LSFEM is always symmetric, the K_{SF} and K_{FS}^T matrices are always equal and the global coupled stiffness matrix will remain symmetric. These coupled matrices are built by sharing degrees of freedom between the fluid and structural domain. For the steady-state case, the only sharable degrees of freedom are the structural load and the fluid pressure. In the transient scenario, structural velocities will be shared with fluid velocities. These degrees of freedom are equated and then directly assembled together into a global coupled matrix that is then solved simultaneously instead of sequentially. Unfortunately, the coupled matrices cannot contain the displacement information from the mesh deformation domain to the fluid domain for the steady-state case. In a transient scenario, displacements of the mesh deformation domain can be converted into grid velocities for the fluid domain.

After each iteration, the matrix K_F is updated whether the fluid is linear or nonlinear due to the movement of the fluid-structure interface. The fluid boundary must move and, generally, the fluid elements change shape and their respective Jacobians require an update. The matrix K_S also requires updating for a nonlinear structural problem.

The three-field formulation adds the elasticity-based mesh movement scheme to the global coupled matrix. The global stiffness matrix is still symmetric. The

matrix K_{SF} still contains pressure information from the fluid domain to the structural domain. With the third field, the matrix K_{SD} relates the structural displacements to the mesh deformation displacements. The matrix K_{FD} contains only zeroes since mesh deformation velocities cannot transfer directly to fluid velocities. Fluid grid velocities cannot be shared degrees of freedom even when using an ALE approach, because grid velocities are not solved directly using LSFEM. Grid velocities are only solved between solution iterations. If the fluid domain uses nonlinear fluid equations, a fluid stiffness matrix update is performed anyway.

6.2 Simultaneous vs. Sequential Coupling

The two-field and three-field simultaneous methods show how the K and F matrices are formed to generate a simultaneous solution. Appendix B and (3.21) and (3.22) show how the K and F matrices are formed using the specific differential operators for each analysis type. A sequential solution can be generated using the same types of analysis for each domain and cross-domain relationships as the simultaneous solution of (6.1) and (6.2). The core difference between the schemes is how the relationships are applied and in what order. The simultaneous scheme, as shown in Figure 6.1, depicts a single dynamic system where the boundary velocities match, the boundary stress and pressure equilibrium match, and the boundary deformations match. These relationships and the fluid, structure, and elasticity-based mesh deformation domain are all solved simultaneously. After that, the fluid mesh is updated and then its mesh velocities are updated. These mesh updates are performed between each iteration instead of during the simultaneous solution. The sequential solution flows differently (Figure 6.2). The sequential solution begins by solving the fluid first. After that, the fluid stresses and pressures are transferred to the structural domain. Next, the structure equations are then solved and then the boundary displacements are transferred to the mesh deformation domain. The mesh deformation domain is solved next. After that, the fluid mesh is updated and

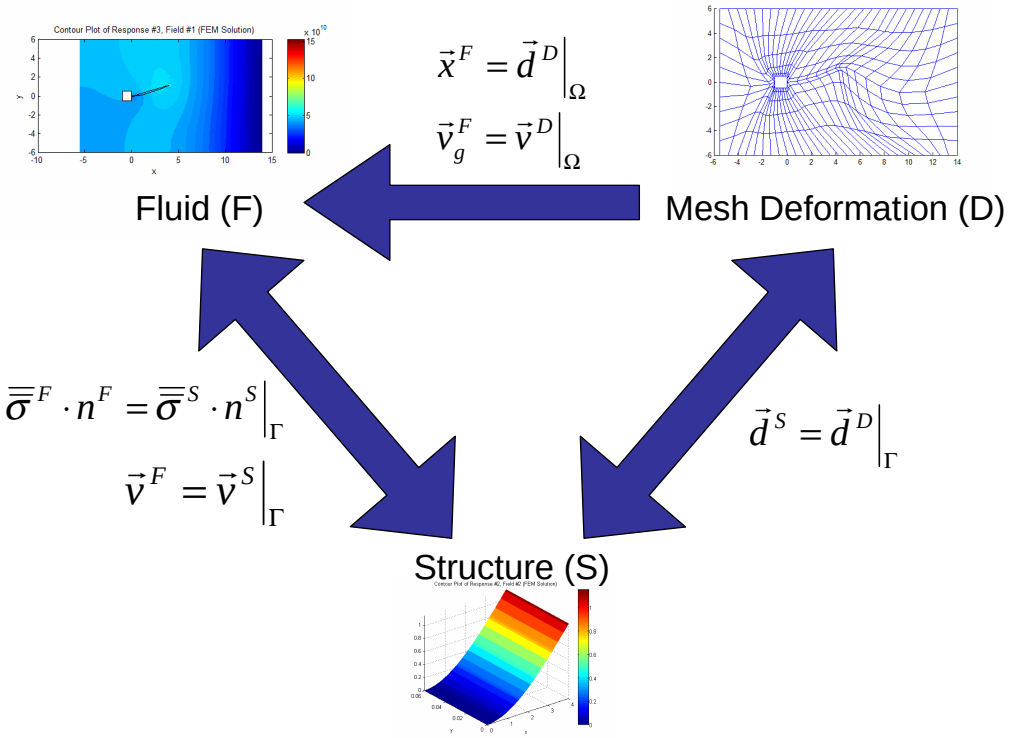

Figure 6.1 Simultaneous Fluid-Structure Interaction Process

the boundary velocities are updated and are then applied as boundary conditions to the fluid domain.

The sequential method follows the traditional scheme. The boundary relationships are transferred to the other domain by an "over-the-fence" methodology. Each domain is solved individually and is not part of a single dynamic system. Bendiksen has noted that the sequential scheme may result in poor convergence properties and may require more degrees of freedom than is necessary [19]. The simultaneous scheme is treated as a single dynamic system where the boundary relationships are directly shared without a virtual boundary. Bendiksen noted that simultaneous schemes exhibit better convergence properties and may not require as many degrees of freedom for both the fluid and structure to obtain the same level of accuracy. In addition, LSFEM fits well within the simultaneous scheme since its mixed first order

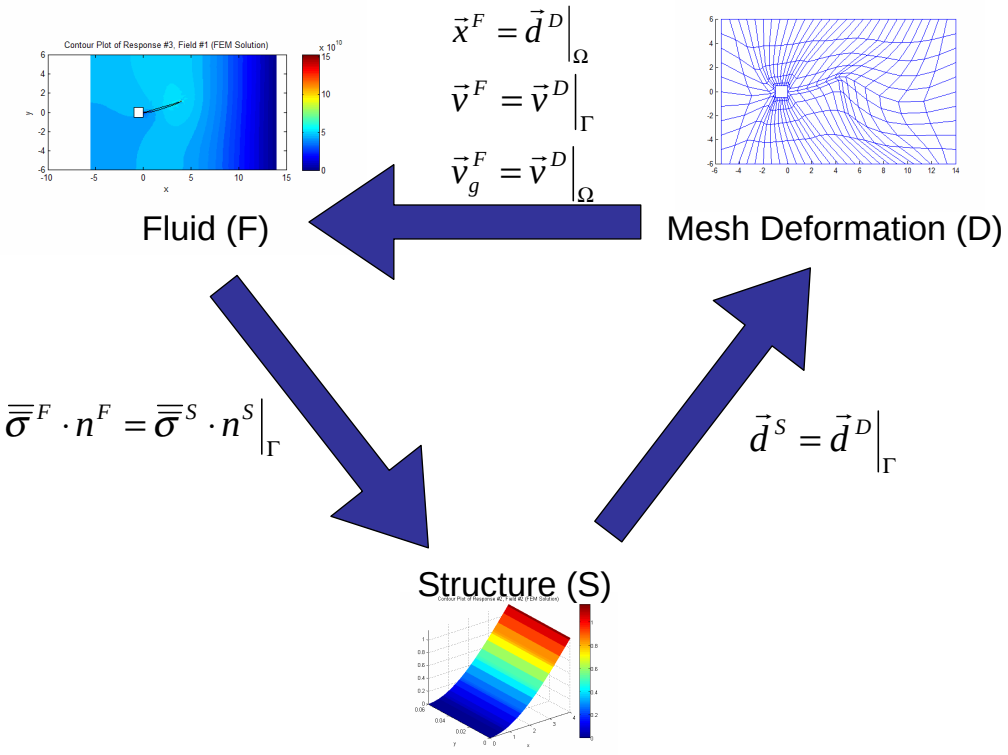

Figure 6.2 Sequential Fluid-Structure Interaction Process

form allows both primary and secondary variables to be shared directly. This allows for a single "black-box" to be used to help create a single dynamic system.

6.3 Mesh Movement Schemes

Several options exist in using mesh movement schemes used within an FSI problem. The main options examined here are user-specified mesh movement scheme and an elasticity-based mesh movement scheme. The user specified approach will usually include a simple scheme that involves vertical or horizontal scaling to move the mesh. A vertical scaling scheme was examined here for a two-field coupled FSI problem. The scheme used

$$\left\{x_i^{n+1}\right\} = \left\{x_i^n\right\} + d_i^s \left\{T_{scale}\right\} \tag{6.3}$$

where T_{scale} is a vector that represents the proportional horizontal or vertical node placement ($\{x^n\}$) of the original mesh for the i^{th} row or column of nodes respectively, d_i^s is the boundary deformation connect to the i^{th} row or column, and n represents the iteration number. A user-specified scheme allows the user to generate all mesh movement position and velocities between iterations instead of using a fully simultaneous analysis which would include a mesh deformation analysis domain. The mesh deformation domain would increase computation time and memory requirements if used. The two-field coupled approach can exhibit computational efficiency (within each iteration) as long as the user-specified mesh deformation scheme is possible.

An elasticity-based scheme uses a structural-type analysis to determine mesh movement. For a two-dimensional fluid domain used within a coupled FSI scheme, it is overlaid with a two-dimensional in-plane elasticity domain. The fluid mesh is updated through the elasticity-based scheme and completed after each iteration. This creates a three-field simultaneously coupled scheme.

The modulus of elasticity constant for the mesh deformation domain was typically picked to be 10^9 times less than any connecting structural domain. This was done such that the mesh deformation domain, even it is elasticity based, does not affect the structure's response by adding stiffness to the structure.

6.3.1 Mesh Deformation Prediction. If a FSI problem is to be solved at time step $n+1$, the Eulerian fluid mesh must have nodes whose coordinates are also defined at time step $n+1$ (noted as: $\overrightarrow{d}^{n+1}$). After the n^{th} time step is completed, the boundary deformations at the n^{th} time step generate $\overrightarrow{d}^{n}$. If the solution is desired at time step $n+1$, the $\overrightarrow{d}^{n+1}$ is unknown and can be extrapolated via

$$\overrightarrow{d}^{n+1} = 2\overrightarrow{d}^{n} - \overrightarrow{d}^{n-1} \tag{6.4}$$

so the appropriate fluid mesh is used [29]. A linear extrapolation is shown above. This extrapolation may be used as an initial guess for the $n+1$ time step. Once the initial guess is used and a full solution is completed at time step $n+1$, the new $\overrightarrow{d}^{n+1}$ should be used to determine the location of the fluid mesh for the next time step. Once the first nonlinear sub-iteration is completed for the next time step, the mesh is updated using a user-specified or an elasticity-based mesh movement scheme.

6.4 Nonconformal Mesh Interaction

6.4.1 Nonconformal Mesh Interaction Theory. An important ability of the least-squares formulation is the influence of the boundary integral portion of the least squares residual. This directly applies to the fluid-structure interface boundary. If a nonconformal mesh exists between the fluid and structure meshes, the boundary integral can specify how the shared degrees of freedom are related without forcing conformal node locations at the boundary.

Least-squares can be used similar to the mortar element scheme [40,41]. Consider a nonconformal mesh boundary where a general response $u(x)$ is desired to

be equal along x between two domains A and B (Figure 6.3). The least-squares boundary integral becomes

$$R_\Gamma = \int_\Gamma \left| u_A(x) - u_B(x) \right|_0^2 d\Gamma \tag{6.5}$$

where the residual goes towards zero as the general response u is equal along the interaction boundary.

The residual may be integrated piecewise using the smallest sections observed between the nodes on the interface between the two domains. Considering a sample scenario (Figure 6.3), the residual integral becomes

$$R_\Gamma = \int_\Gamma (\cdot)\, d\Gamma = \int_{x_1}^{x_2} (\cdot)\, d\Gamma + \int_{x_2}^{x_6} (\cdot)\, d\Gamma + \int_{x_6}^{x_3} (\cdot)\, d\Gamma + \int_{x_3}^{x_4} (\cdot)\, d\Gamma \tag{6.6}$$

The responses u_A and u_B are defined by differing shape functions and each discretization is defined differently

$$u_A(x) = N_A d_A \tag{6.7}$$

$$u_B(x) = N_B d_B \tag{6.8}$$

The residual now becomes

$$R_\Gamma = \int \left(N_A d_A - N_B d_B \right)^T \left(N_A d_A - N_B d_B \right) dx \tag{6.9}$$

as defined by the discretization in (6.7) and (6.8).

6.4.2 Examination of Nonconformal Mesh Interaction. The nonconformal mesh methodology was implemented for two problems with known analytical solutions. A Poisson equation was solved using an inner domain and boundary interfaces. The same p-value was used between the two portions of the problem, but different element sizes were used at the boundary (Figure 6.4). The p-value was

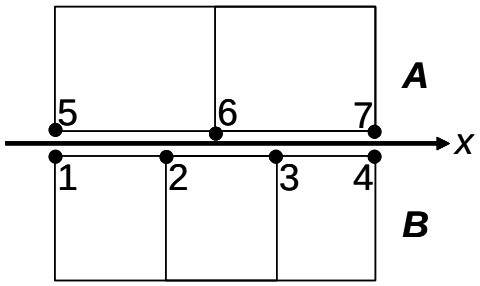

Figure 6.3 Nonconformal Mesh Example

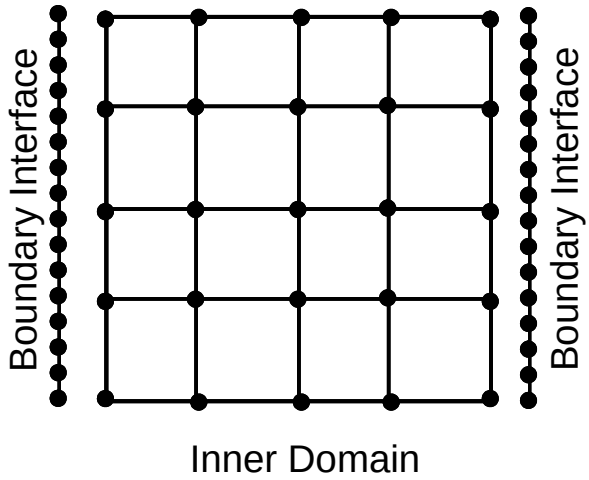

Figure 6.4 Example Nonconformal Mesh For Poisson's Inner Domain With Boundary

increased to study the *hp*-convergence of the nonconformal mesh methodology. An *hp*-convergence study includes increasing the *p*-value (increase order of polynomials), increasing *h*-value (coarsen mesh), but the number of degrees of freedom remained the same. Figure 6.5 shows that the nonconformal accuracy is better than the conformal mesh at low *p*-values and has similar convergence rates as the conformal mesh convergence rates. This indicates success of the proposed methodology.

The manufactured elasticity problem proposed in Section 4.5.2.2 (Figure 4.8 and Figure 4.9) was considered here with the nonconformal mesh interaction methodology. The standard square domain was split into two halves. Two domains were

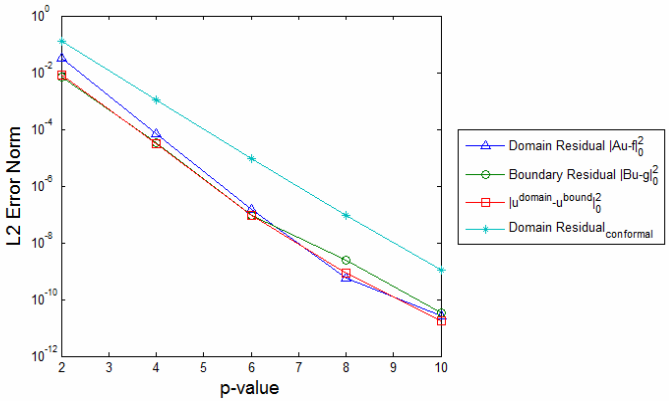

Figure 6.5 Convergence of Solution On Interface With Nonconformal Mesh Using Same p-value for Inner Domain and Boundary Integral (Case A)

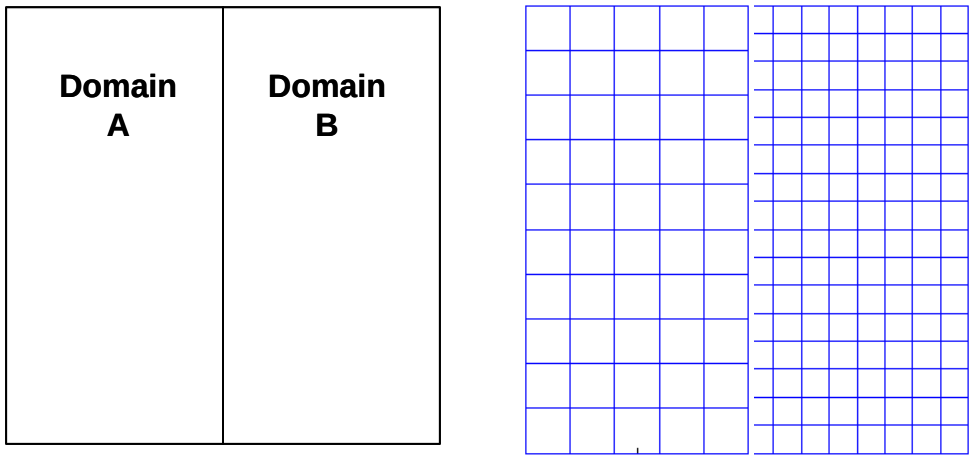

Figure 6.6 Example of Meshes Used to Split Domain in Two Pieces For Nonconformal Mesh Study

used with different mesh sizes and/or different p-values. A sample mesh configuration is shown in Figure 6.6.

The first case (Case A) used a nonconformal mesh using the same p-value between both domains but domain B contained two times as many degrees of freedom as domain A. The p-value was varied similarly for both domains ($2 \leq p \leq 10$). An hp-refinement curve was generated for this case using the L_2 response error norm (Figure 6.7). This case exhibited standard hp-refinement rates/slopes for this problem ($m = 1$). Even though different meshes are used on each side of the domain

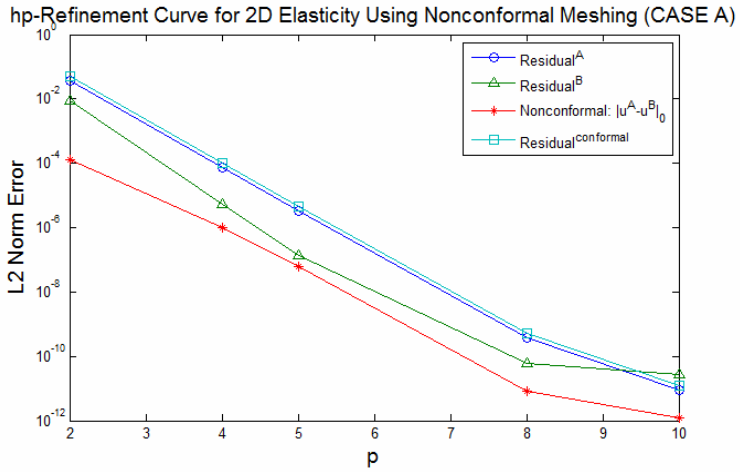

Figure 6.7 *hp*-Refinement Curve for Case A

and the centerline of the domain does not contain a conformal mesh condition, the accuracy still improves at the proper rate and achieves a consistent level of accuracy.

The second case (Case B) used a nonconformal mesh where only one domain varied its p-value and mesh size. The h and p-values varied for domain A ($2 \leq p \leq 10$) to maintain its number of degrees of freedom (and remain consistent with *hp*-refinement curve generation) while the domain B p-value was held constant ($p = 5$). The number of total domain degrees of freedom did not change as the p-value for domain A varied. This case showed that the lower-order domain will dominate the error exhibited throughout the domain. The *hp*-refinement curves maintained the proper rate of improvement with the p-value until the p-value of 5 was reached. After that point, domain B dominated the error of the problem and curves plateaued from that point on.

The problems seemed to exhibit consistent accuracy when using the proposed nonconformal mesh methodology. The lowest-order accuracy of the two domains dominates the overall solution accuracy and maintains its accuracy order. In other words, the nonconformal mesh interaction does not introduce additional error to the system.

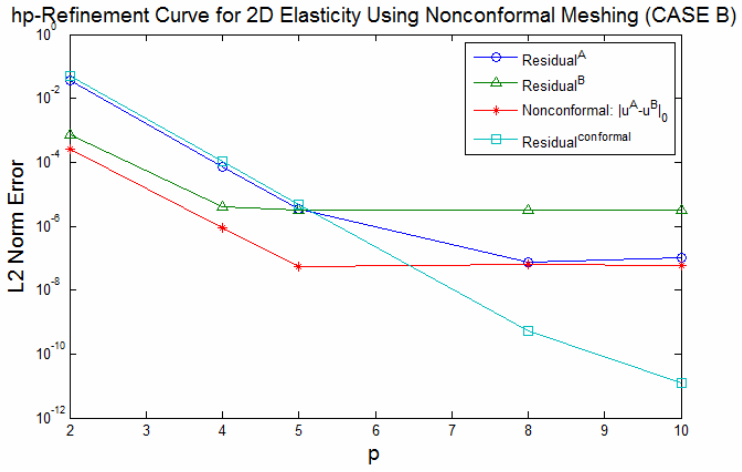

Figure 6.8 *hp*-Refinement Curve for Case B

To truly examine if the error was consistent, each domain half was solved independently with strongly applied boundary conditions at the mid-line interaction boundary. The boundary conditions were applied using the known analytic solution at the mid-line location. Solving the problem this way provides residual error values without regard to unique nonconformal methods. This analysis is independent of any special method which may or may not introduce error into the system. Figure 6.9 shows the comparison for both domains between the nonconformal residual error values and the independent residual error values for Case A. Figure 6.10 shows the same comparison for Case B. Both cases show that the nonconformal solution exhibited better accuracy throughout. This was unexpected but shows that the nonconformal methodology is just as good or better than the independent solution.

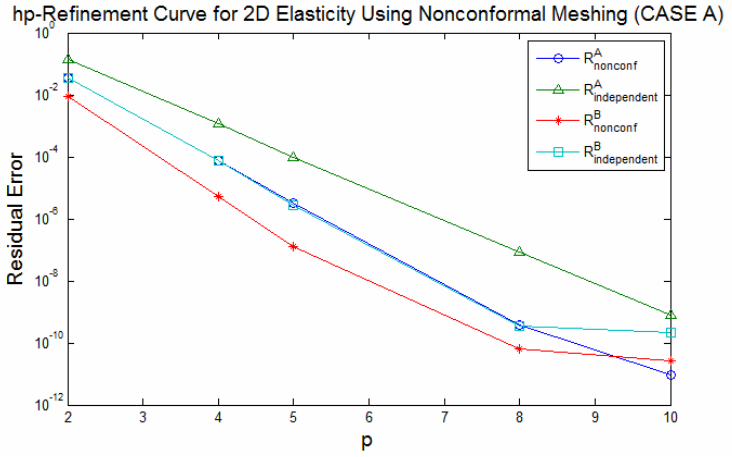

Figure 6.9 *hp*-Refinement Curve for Case A Examining Consistent Error Rates Between Nonconformal and Independent Solutions

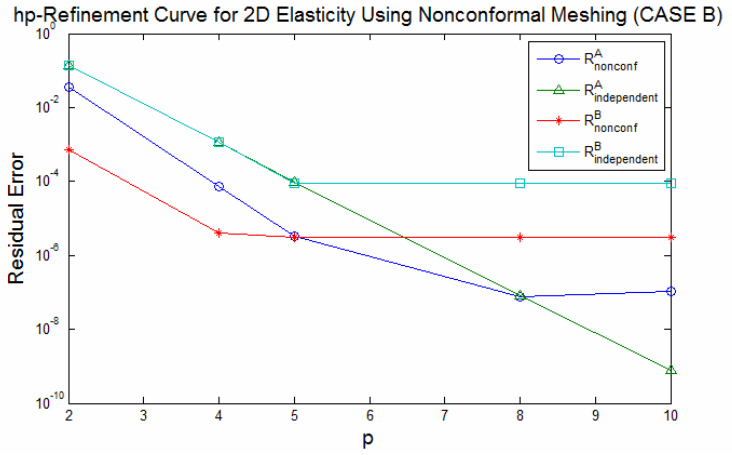

Figure 6.10 *hp*-Refinement Curve for Case B Examining Consistent Error Rates Between Nonconformal and Independent Solutions

VII. Steady-State Fluid-Structure Interaction

Several problems were considered to demonstrate and verify the simultaneous LSFEM FSI approach for steady-state problems. The first problem considered was a simple driven cavity flow problem with a flexible right wall. This problem demonstrates the implementation of the simultaneous LSFEM FSI. The problem was completed using the two-field and three-field simultaneously coupled approaches. The second problem included a Double Channel Flow Problem with a known exact solution at the interface boundary [74]. The fluid domain consisted of a simple Poiseuille driven channel fluid flow. In addition, the exact solution is only known at the boundary and not within every domain across the FSI problem. It was found that residual weighting is critical when considering multiple domain problems. The Method of Manufactured Solutions (MMS) [64] was used to create an FSI problem with a known solution everywhere within the system. This allowed the response error related to the exact solution to be generated everywhere within the FSI problem. Refinement curves and their rates were created and compared to theory.

7.1 Two-Field Simultaneously Coupled Problem – Driven Cavity Flow with Flexible Wall

The two-field coupled LSFEM FSI formulation was implemented using a driven cavity Stokes flow problem with a flexible right wall which was represented as a simple linear Euler-Bernoulli beam. The fluid pressure and beam distributed load were treated as equivalent degrees of freedom and were assembled using a conformal mesh. The problem was defined such that all cross-domain degrees of freedom were conveniently collocated. Figure 7.1 shows how the domains were connected together.

The nonlinear problem was iterated until steady-state convergence was reached. Since the two-field coupled LSFEM equations were used for this problem, simple proportional scaling (6.3) was used to move the nodes horizontally. Figures 7.2 and

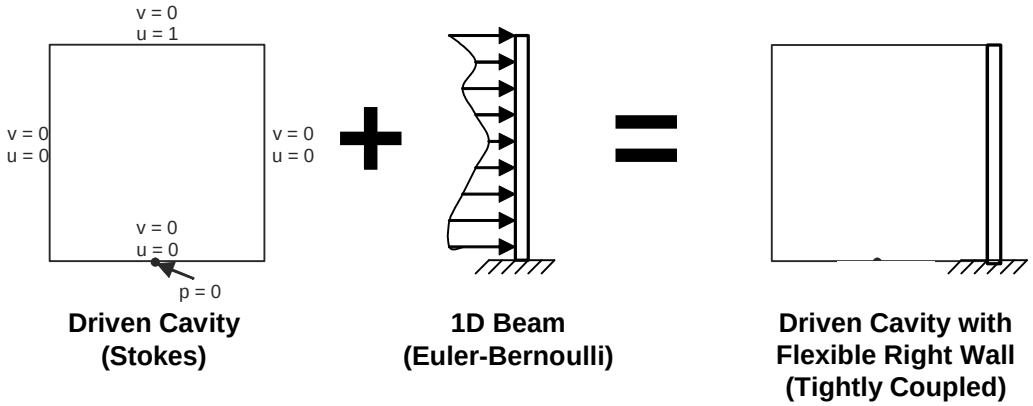

Figure 7.1 Assembly of Driven Cavity Flow with Flexible Right Wall with Two-Fields

7.3 show the pressure and velocity results, respectively. The final deformed mesh is shown over the contour results.

A side wall was selected to be flexible because of the high pressure gradient observed to exist on that wall. Figure 7.2 shows how the high pressure values were observed on the right wall, which resulted in a significant beam displacement.

7.2 Three-Field Simultaneously Coupled Problem – Driven Cavity Flow with Flexible Wall

The previous section showed successful implementation of the simultaneous LSFEM formulation. Unfortunately, the mesh deformation scheme is too simple and can only work for simple geometry. A more robust mesh deformation scheme is required for more complex shapes. An elasticity-based mesh deformation scheme was used to develop the three-field formulation. The same driven cavity flow with a flexible wall problem was used again except a mesh deformation field was incorporated using a plane-stress least-squares approximation. In addition, the bending displacements (w) were shared with the mesh deformation displacements (d_x) at the interaction wall. Figure 7.4 shows how the problem was assembled together with three domains.

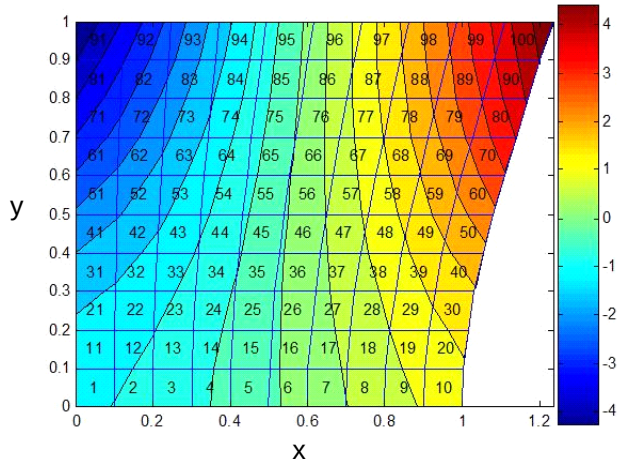

Figure 7.2 Pressure Contours Using Two-Field Scheme

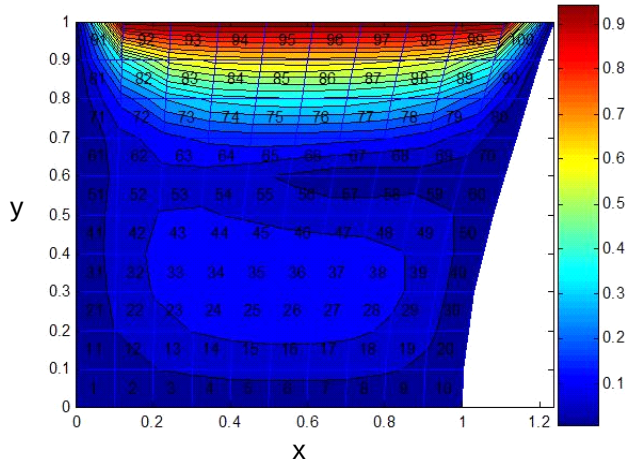

Figure 7.3 Velocity Magnitude Contours Using Two-Field Scheme

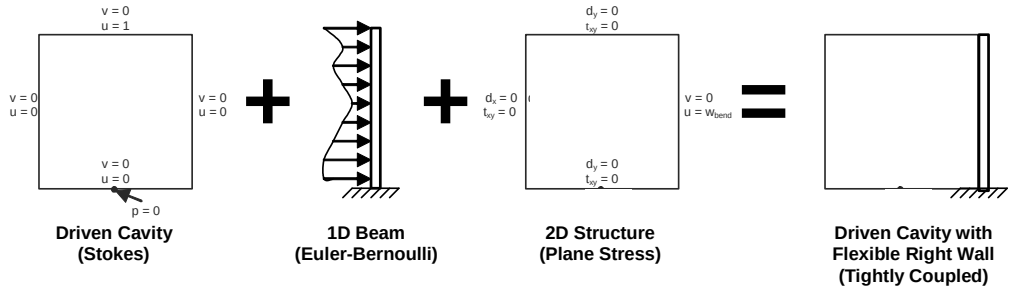

Figure 7.4 Assembly of Driven Cavity Flow with Flexible Right Wall Using Three Fields

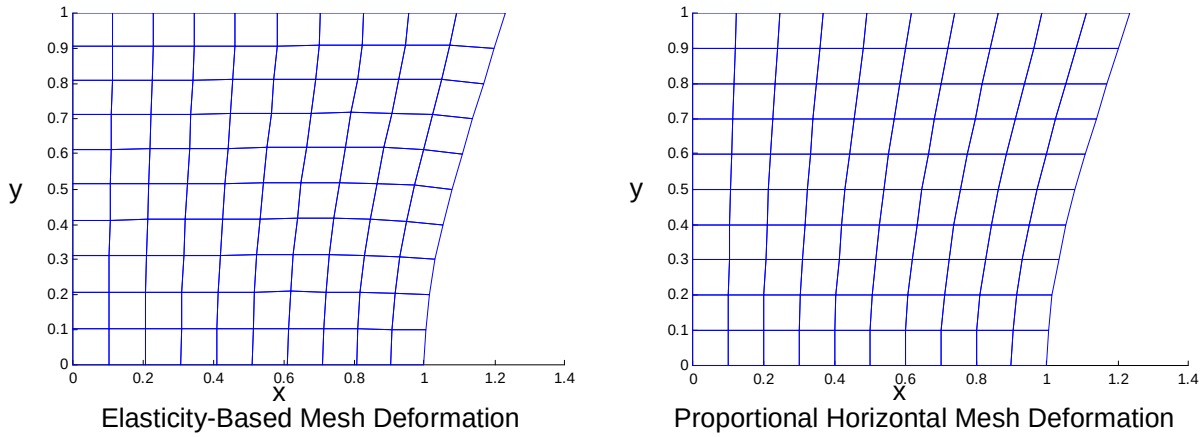

Figure 7.5 Comparison of Different Mesh Movement Schemes for Driven Cavity Flow with Flexible Right Wall Problem

Figure 7.5 shows a final mesh comparison between the elasticity based (three-field) and proportional horizontal mesh deformation (two-field) schemes. In the proportional horizontal mesh scheme, elements near the deformed boundary show higher skewing than the elements contained in the elasticity based scheme. This is because the nodes only translate horizontally while the elasticity based scheme distributes the nodes better because they can move in all directions. In addition, the elasticity-based scheme allows for a fully simultaneous three-field approach.

Figures 7.6 and 7.7 show the pressure and velocity results of the driven cavity flow with a flexible wall problem. The final results closely match the results from the two-field scheme. No observable differences were seen between the responses of the two-field and three-field schemes.

The results matched, but the processing time did not. The three-field scheme showed a 26% increase in processing time due to the addition of the mesh deformation field. However, the three-field scheme converged with 20% fewer iterations. In addition, the scheme allows the implementation of more complex geometry and boundary deformations.

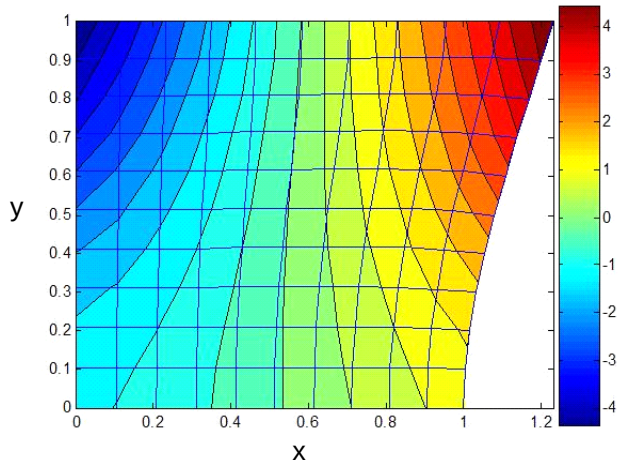

Figure 7.6 Pressure Contours for Driven Cavity Flow with Flexible Right Wall Problem Using Three-Field Scheme

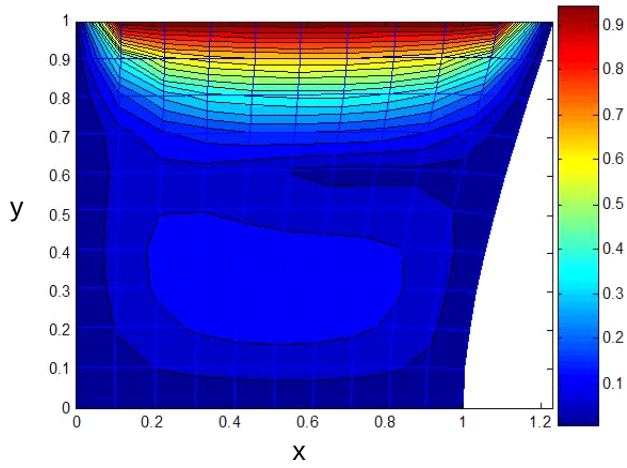

Figure 7.7 Velocity Magnitude Contours for Driven Cavity Flow with Flexible Right Wall Problem Using Three-Field Scheme

7.3 Double Channel Flow Problem with Flexible Beam

A simple problem was considered to demonstrate and verify accurate coupling of a fluid-structure interaction problem. Wang presented a double channel flow problem with a flexible beam separating the channels [74]. The problem presented by Wang has an analytical solution which provides a means to verify the proposed coupling methodology.

The problem considered for verification consisted of two channels of uniform initial height, $H_i(x)$. The top channel ($i = 1$) had an initial height of 0.02 meters and the bottom channel ($i = 2$) had an initial height of 0.04 meters. Both channel lengths were 0.75 meters. Both channels have the same maximum and average velocity profiles throughout, but since the channels have different heights, the flow rates must be different ($Q_1 = 177 \cdot 10^{-6}, Q_2 = 354 \cdot 10^{-6} \frac{m^2}{s}$). The channels were separated by a thin beam with a uniform cross-section height of δ =0.01 meters and a modulus of elasticity of $E = 200GPa$. The beam had the same length as the channel lengths. The channels were considered to converge at their right ends, so the pressure values were constrained to be equal at the right end of each fluid domain. The differing flow rates on the top and bottom channels produce a pressure difference that acts across the beam length. The beam displacement $w(x)$ generates new non-uniform heights for each channel. The new channel height relationships are defined through

$$h_i(x) = H_i(x) - w(x) \tag{7.1}$$

Similar to Wang, the channel fluid flow was analyzed using incompressible Navier-Stokes fluid equations [74]. The top and bottom of each channel were considered as no-slip walls where the velocity is zero. Each channel can be considered a Poiseuille channel flow problem. Therefore, $\frac{dp}{dy}$ is constant for a given x coordinate. [67] Considering this, the inflow and outflow profiles are known for each channel, since the mass flow rates in and out of each channel are constant.

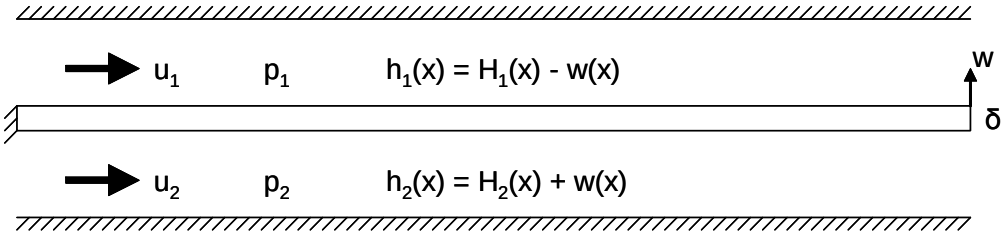

Figure 7.8 Double Channel Flow Problem

Shear stresses exist on each wall due to the no-slip wall condition. The viscosity value was assumed to be μ =0.001$\frac{kg}{m \cdot s}$ and the density was assumed to be ρ =1000$\frac{kg}{m^3}$. Since the beam has pressure loads and in-plane shear loads acting on each side, the nonlinear beam with axial and bending displacements and loads was considered. The beam boundary conditions consisted of a clamped condition on the left end and a free condition on the right end (Figure 7.8).

The analytical results provided by Wang were compared to the results obtained using the simultaneously coupled LSFEM scheme. The loads were summed and equilibrium was enforced between the upper channel pressure, the lower channel pressure, and the beam's distributed load. The distributed load acting on the beam is not directly obtainable as a degree of freedom. The load was obtained by using the steady-state form of (4.7). A boundary interaction LSFEM term was included in the simultaneous problem,

$$R_\Gamma = p_2 - p_1 - \frac{\partial V}{\partial x} \tag{7.2}$$

The bending deformation influence on the fluid domains was considered through mesh deformation. The meshes were updated through the elasticity-based scheme after each solution iteration. A mesh deformation scheme was used and resulted in a three-field, simultaneously coupled scheme.

Both fluid meshes were discretized using 25 length-wise elements and four height-wise elements. The mesh deformation meshes were discretized in the same

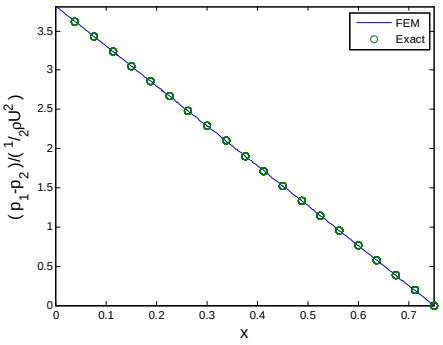

Figure 7.9 Pressure Difference, Uniform Cross-Section (Laminar) for Double Channel Flow Problem

way, since they were overlaid directly on the fluid domains. The beam and pressure relationship meshes were one-dimensional and had 25 lengthwise elements. A p-value of 4 was used throughout the problem.

The net pressure results acting on the beam are shown in Figure 7.9. Both the FEM results and the analytical results provided by Wang are shown in the figure. The bending displacement results are shown in Figure 7.10. Both plots show an excellent match to Wang's analytical solution and verify the LSFEM three-field, simultaneously coupled scheme for this simple problem. The results generated here were created using a user-defined set of residual weights for each field (Table 7.1). The user-defined set was generated through trial and error until the exact solution was observed. It was discovered that the structural domain required a low weighting to make the solution balanced. If the structural domain had a high weight or a weight equal to other field-types, then the structural domain would begin to dominate the solution at the expense of accuracy in the fluid domain. On the other hand, the fluid domain was far less sensitive to residual weights. It was observed here that proper residual weights were related to problem type. However, the same balanced weights determined here were used for a refined double channel problem with a refined mesh and higher p-value, and the same results were achieved. This implies that the balanced weights are not necessarily dependent on h- or p-values.

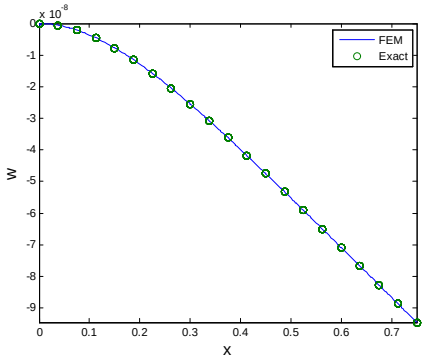

Figure 7.10 Bending Displacement, Uniform Cross-Section (Laminar) for Double Channel Flow Problem

Domain Type	Final Residual Weights (W_i)
Fluid (Γ^F)	10^5
Structure (Γ^S)	10^{-2}
Mesh Deformation (Γ^D)	10^{-7}
Stress Equilibrium (Γ^{FS})	10^0

Table 7.1 Final Weights for Wang's Double Channel Flow Problem

7.4 Residual Weighting Case Study

Wang's double channel flow problem was used to examine various residual weighting methods. It is desirable to find a "hands-off" residual weight balancing method that is applicable for problems without a known solution. Fourteen different cases were considered using various combinations of residual error balancing methods. All cases were compared to the exact solution of Wang's FSI problem. The maximum percent error was determined for the beam's maximum bending displacement and the maximum net pressure generated on the beam by the fluid domain. Table 7.2 shows the results of the case study.

The first case, the pure sequential solution, did not require any residual weights. Each fluid, structure, and mesh deformation domain has already been shown to have good residual weights at its equation level for a steady-state analysis. This was shown for individual fluid and structural problems used for original verification. The results for this double channel flow problem were very close to the exact solution

Case	Method	% Displacement Error	% Δp Error	Usable?
1	Pure Sequential Solution	0.003%	0.001%	Yes
2	No Scaling	96.773%	93.043%	No
3	Manual (User Prescribed)	0.006%	0.004%	Yes
4	Nondimensional Units	99.997%	0.002%	Half
5	Energy Units	99.971%	0.034%	Half
6	Field Averaging	0.004%	0.001%	Yes
7	Field Move Limits	99.998%	0.251%	No
8	Element/Equation Averaging	81.684%	29.899%	No
9	Equation Averaging	79.014%	29.876%	No
10	Element Averaging	27.360%	29.775%	No
11	Equation Pairing Averaging	0.005%	0.002%	Yes
12	Normalize A Using Max Norm	99.998%	91.145%	No
13	Normalize A Using Min Norm	99.998%	87.665%	No
14	Normalize A Using L2 Norm	93.225%	29.451%	No

Table 7.2 Results for Residual Weighting Case Study

for both the fluid and structure. No residual weights were considered at all since each was solved on its own and require no balancing. For the FSI problems solved here, sequential methods typically worked well for steady-state problems and simple transient FSI problems. Alternatively, Bendiksen has shown that for highly complex and nonlinear transient FSI problems, simultaneous solutions were better [19].

The second case included a simultaneous solution without any residual weighting factors. Poor results were observed for all domains and the need for residual weight balancing for multiple simultaneously solved domains was justified. The manual method, the third case, showed success (as shown above). Unfortunately, the manual method is only applicable for problems with a known solution, since the user can manually adjust the residual weights until the solution matches the known result. This is nearly impossible for a problem with an unknown solution.

Cases four and five included modifying the differential equations such that they have the same type of units. Case 4 modified the equations into nondimensional form and case 5 modified the equations such that each equation was in energy units. The equations were modified using user-specified characteristic units. Modifying the

characteristic units of the differential equations to either energy units or nondimensional units proved to only work for the fluid domain. The fluid domain is considered "easy" for this problem and the fluid equations were observed to be fairly insensitive to residual weight modification (at the equation level). The poor residual error of the structural domain was not fixed through either unit modification method.

The sixth case was the field averaging method by implementing (3.98) and (3.99). It was a strong method that was completely "hands-off" and accurate using a simultaneous solution. If residual error balancing is considered to be similar to an optimization problem, then the field averaging method would contain the fewest design variables (residual weights). The equation averaging (3.101), the element averaging (3.102), and the element/equation averaging (3.103) methods proved to have too many residual weights and the simultaneous problem becomes very challenging to balance. The residual error balancing behaved in a highly coupled and highly nonlinear fashion. Considering too many "design variables" makes this problem too difficult to properly balance the residual weights such that the correct solution is found.

The equation pairing method grouped similar types of equations together. This is similar to design variable linking in optimization problems [75]. For example, the structural domain has five equations. Two of those equations are force equilibrium and the other three are displacement-stress relationships. For case eleven, the two equilibrium equations had the same weighting and the three displacement-stress relationships had the same weighting. This showed a significant reduction in unknown residual weighting factors. The equation pairing method seemed to work since there were fewer unknown weights to balance.

Cases 12 through 14 were used to examine the effects of adjusting each row of the matrix differential operator A such that its norm would be improved and the condition number of the A matrix would improve. Three different norms were

attempted. The L2 norm

$$A_{i_{new}} = \frac{A_i}{|A_i|_0} \tag{7.3}$$

the max norm

$$A_{i_{new}} = \frac{A_i}{|A_i|_{\max}} \tag{7.4}$$

and the min norm

$$A_{i_{new}} = \frac{A_i}{|A_i|_{\min}} \tag{7.5}$$

were applied to each operator A. The right hand side was similarly modified by the respective matrix norm

$$f_{i_{new}} = \frac{f_i}{|A_i|_0} \tag{7.6}$$

This method proved to not improve the solution for any case. It showed that the matrix condition number does not improve or help balance the least-squares functional such that a reasonable solution can be achieved.

7.5 Fluid-Structure Interaction Problem Created by Method of Manufactured Solutions (MMS)

The double channel flow problem was a good test using fairly simple types of analysis. It is desirable to obtain not only a comparison to an exact solution at a boundary, but to obtain domain-wide error and to obtain error convergence rates for non-trivial problems. Tremblay *et al.* presented a method for creating benchmark problems to verify FSI code [64]. Not only can it verify the FSI code altogether, but it can verify each component of the FSI problem.

MMS involves nine generalized steps to produce a benchmark FSI problem. The first step is to consider an FSI problem with a fluid domain and structural domain with some user defined final displaced boundary $f(x)$. The problem may look like what is shown in Figure 7.11. Creating some nonzero $f(x)$ is essential to make the problem non-trivial. The next step is to find a divergence-free velocity

field consistent with $f(x)$. The rules that govern this step are detailed by Tremblay *et al.* [64]. After that, a structural displacement field is defined by the user where $d_y = f(x)$ and $d_x = 0$ at the bottom of the structural domain. Once the displacement fields are known, the stress responses can be produced using Equations (4.20), (4.21), and (4.22). After that, the μ and p fluid expressions are generated through the stress equilibrium equations. The Neumann-type equilibrium equations can be based on fluid velocities and structural stresses, which are already determined values, i.e.,

$$\left(2\mu\frac{\partial u}{\partial x} - p\right) n_x + \mu\left(\frac{\partial u}{\partial y} + \frac{\partial v}{\partial x}\right) n_y = \sigma_x^s n_x + \sigma_{xy}^s n_y \tag{7.7}$$

$$\mu\left(\frac{\partial u}{\partial y} + \frac{\partial v}{\partial x}\right) n_x + \left(2\mu\frac{\partial v}{\partial y} - p\right) n_y = \sigma_{xy}^s n_x + \sigma_y^s n_y \tag{7.8}$$

These can also be written in terms of the fluid stresses directly, e.g.,

$$-pn_x + \sigma_x^f n_x + \sigma_{xy}^f n_y - \sigma_x^s n_x - \sigma_{xy}^s n_y = 0 \tag{7.9}$$

$$-pn_y + \sigma_y^f n_y + \sigma_{xy}^f n_x - \sigma_{xy}^s n_x - \sigma_y^s n_y = 0 \tag{7.10}$$

This pair of equations will be solved simultaneously for the two unknowns $\mu(x)$ and $p(x)$. These expressions are assumed to be only functions of x throughout the fluid domain. With $\mu(x)$ known, the fluid stresses can be determined. Once all the fluid and structural responses are determined, the structural body forces and fluid body forces can be determined. This will generate complicated body forces, but it will balance the differential equations properly.

A boundary displacement field of

$$f(x) = 1 + 0.03\left(1 - \cos\left(2\pi x\right)\right) \tag{7.11}$$

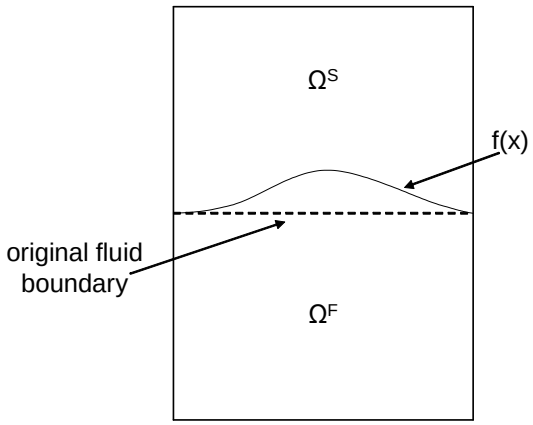

Figure 7.11 Fluid and Structure Domain with Prescribed Final Boundary Displacement

was assumed in this study. The MMS steps described above were followed using Cartesian coordinates. The exact results for the fluid responses are shown in Figure 7.12 and the structural responses are shown in Figure 7.13.

With a known exact solution for an FSI case, the errors can be determined across all domains. A total of four domains were used for this problem. Incompressible Navier-Stokes formulation with stress responses (v-p-σ) was used for the fluid domain, a non-elliptic two-dimensional elasticity formulation was used for the structural domain, an elasticity-based mesh deformation was utilized to move the mesh, and the stress vector equilibrium was applied to the boundary interface. The fluid domain consisted of no-slip walls on the top and bottom, and the velocities and pressure were defined as specified by the exact solution on the left and right walls. The structural domain consisted of the displacements as prescribed by the exact solution on the top, left, and right walls. The bottom interface wall was allowed to remain flexible. The boundary interface shares the fluid stresses and pressure with the structural stresses. The problem was solved using a simultaneously coupled LSFEM scheme with varying p and h-values to verify the FSI code and to determine convergence rates. Additionally, an iterative residual weight balancing scheme was used at the field level. The scheme proved to be successful where the optimal

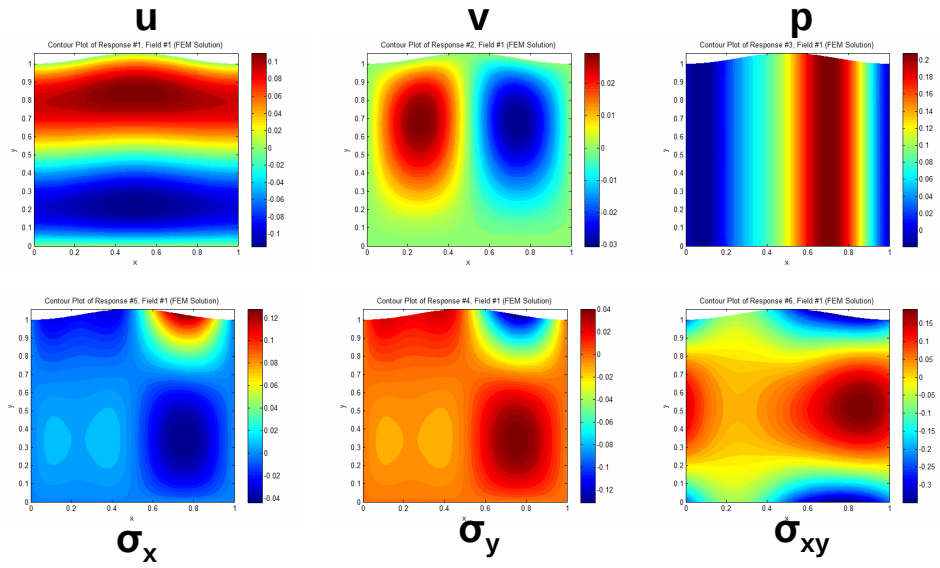

Figure 7.12 Thumbnail Plots of Exact Fluid Results for MMS Problem

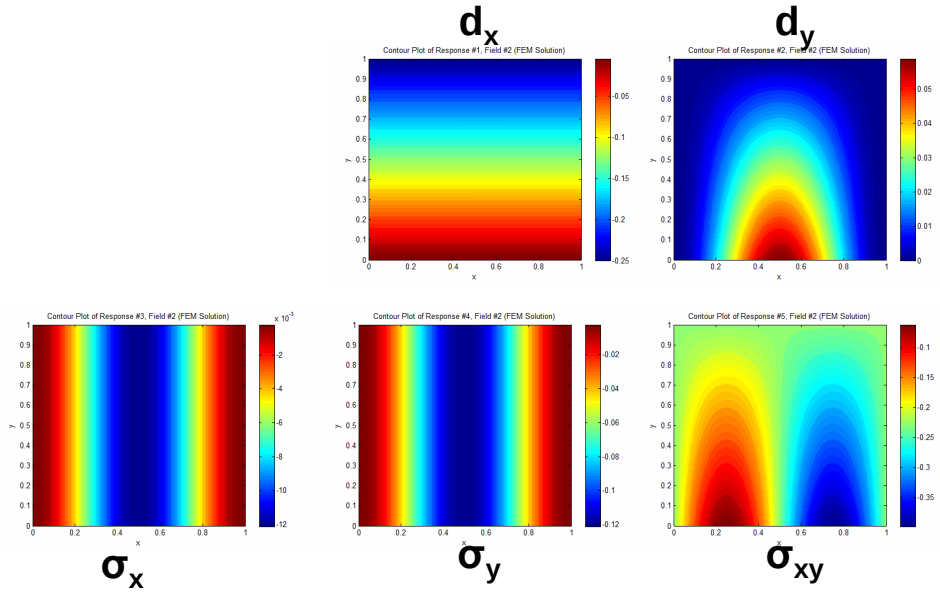

Figure 7.13 Thumbnail Plots of Exact Structural Results for MMS Problem

Domain Type	Final Residual Weights (W_i)
Fluid (Ω^F)	$4.244 \cdot 10^{-7}$
Structure (Ω^S)	0.998
Mesh Deformation (Ω^D)	$4.405 \cdot 10^{-11}$
Stress Equilibrium (Γ^{FS})	$1.621 \cdot 10^{-3}$

Table 7.3 Final Weights for MMS Problem

weights are shown in Table 7.3. The same balanced weights determined here were used for a refined double channel problem with a refined mesh and higher p-value, and the same results were achieved. This implies that the balanced weights are not necessarily dependent on h- or p-values.

It was shown with the double channel problem that the sequential solution did not require residual weight balancing. A study was performed here to examine if this holds true here for the MMS problem. The sequential solution for the MMS problem still includes a simultaneous portion. The structure must be solved with the stress boundary equilibrium relationship, because it includes only two equations for three structural unknowns. In other words, the sequential solution of the MMS problem is not a pure sequential scheme. The small simultaneous portion can have its own residual weights. Three cases were considered. The first case is the simultaneous solution, the second is the sequential with residual weight balancing used for its small simultaneous portion, and the third case is a sequential solution with no residual weight balancing. The L_2 response error norms for each response type are shown in Table 7.4 for a MMS domain with 100 elements a p-value of 4. Table 7.5 shows the same error norms but for a domain with much fewer elements and a much higher p-value (25 elements and p-value of 8). The error norms were integrated across each respective domain and compared directly to the known exact solution.

Both Table 7.4 and Table 7.5 show accurate results for all three cases for both meshes. All error norms were very similar among the three cases for a given mesh. This implies that the weights for the small simultaneous portion of the sequential

Response Type	Simultaneous	Sequential (With W_i Balancing)	Sequential (No W_i Balancing)
Fluid (Ω^F)	Ω^F Error	Ω^F Error	Ω^F Error
v_x^f	1.10163e-006	1.17288e-006	1.15902e-006
v_y^f	1.11475e-006	1.16918e-006	1.15044e-006
p	4.52583e-005	4.56235e-005	4.51687e-005
σ_x^f	3.47342e-005	3.49112e-005	3.47481e-005
σ_y^f	3.35338e-005	3.37074e-005	3.36111e-005
σ_{xy}^f	2.33850e-005	2.35318e-005	2.32276e-005
Structure (Ω^S)	Ω^S Error	Ω^S Error	Ω^S Error
u_x^s	2.03816e-007	2.11050e-007	1.79030e-007
u_y^s	1.62487e-006	1.63018e-006	1.61079e-006
σ_x^s	2.77653e-005	2.79779e-005	1.53533e-005
σ_y^s	1.37449e-004	1.38980e-004	7.96606e-005
σ_{xy}^s	2.68994e-005	2.72075e-005	1.60016e-005
Stress Equilibrium (Γ^{FS})	Γ^{FS} Error	Γ^{FS} Error	Γ^{FS} Error
p	2.06189e-004	2.08182e-004	2.05781e-004
σ_x^f	1.62437e-004	1.63301e-004	1.58109e-004
σ_y^f	1.98109e-004	1.99679e-004	1.97716e-004
σ_{xy}^f	1.36062e-004	1.36839e-004	1.30997e-004
σ_x^s	2.09876e-004	2.10487e-004	1.26573e-004
σ_y^s	3.40429e-004	3.43054e-004	3.23441e-004
σ_{xy}^s	1.30448e-004	1.31469e-004	1.04479e-004

Table 7.4 Error Comparisons for Sequential Vs. Simultaneous Solutions for MMS Problem (100 Elements with p-value of 4)

Response Type	Simultaneous	Sequential (With W_i Balancing)	Sequential (No W_i Balancing)
Fluid (Ω^F)	Ω^F Error	Ω^F Error	Ω^F Error
v_x^f	1.33852e-007	5.88315e-008	3.86703e-008
v_y^f	1.05694e-007	4.98314e-008	3.24532e-008
p	9.76650e-007	3.91216e-007	2.89434e-007
σ_x^f	3.69702e-007	3.23781e-007	2.63803e-007
σ_y^f	3.99870e-007	3.41250e-007	3.08079e-007
σ_{xy}^f	3.68122e-007	2.92652e-007	2.19656e-007
Structure (Ω^S)	Ω^S Error	Ω^S Error	Ω^S Error
u_x^s	6.75704e-009	3.61934e-009	1.48192e-009
u_y^s	8.42724e-008	1.84999e-008	1.19533e-008
σ_x^s	2.78081e-007	8.26302e-007	2.47712e-007
σ_y^s	5.20752e-007	1.74091e-006	5.95197e-007
σ_{xy}^s	3.35606e-007	5.86459e-007	1.75334e-007
Stress Equilibrium (Γ^{FS})	Γ^{FS} Error	Γ^{FS} Error	Γ^{FS} Error
p	4.20378e-006	1.83042e-006	1.27052e-006
σ_x^f	2.32566e-006	2.69655e-006	1.88110e-006
σ_y^f	2.46142e-006	2.23274e-006	1.84261e-006
σ_{xy}^f	2.47811e-006	2.51870e-006	1.78596e-006
σ_x^s	3.20806e-006	7.90030e-006	2.58359e-006
σ_y^s	2.14329e-006	2.68926e-006	2.31604e-006
σ_{xy}^s	2.14967e-006	2.77007e-006	1.78353e-006

Table 7.5 Error Comparisons for Sequential Vs. Simultaneous Solutions for MMS Problem (25 Elements with p-value of 8)

solution are adequate at their default values (1.0). Residual weight balancing was not necessary to balance the structural domain equations with the stress equilibrium relationship. For this problem it was shown that the sequential solution without residual weight balancing performed just as well as the sequential solution with balancing and the simultaneous solution. Since a sequential solution without balancing exhibits fewer total iterations (20-50% reduction) and lower processing time per iteration (2X reduction), it seems to be beneficial to utilize a sequential solution without balancing for this problem. This was shown for both the double channel flow problem and the MMS problem. This could imply that steady-state FSI problems can be sequentially solved as accurately and more efficiently than simultaneous solutions.

Curves for h-refinement were created for the fluid and structural domain as compared to the exact solution. Figures 7.14 and 7.15 show the h-refinement for a primary variable (v) and a secondary variable (p), respectively, for the fluid domain using the L_2 response error norm. Figure 7.16 shows the h-refinement for the primary structure response (d_y) and Figure 7.17 shows the secondary structure response (σ_{xy}). All response types show an average refinement rate of approximately p with a lower bound of $p-1$ and an upper bound of $p+1$. In this case, not all p-values exhibited optimal refinement rates for either elliptic or non-elliptic formulations. No theorem currently exists that bounds the error from one domain to the next. In the FSI case, if the boundary deformation is not matched perfectly, the boundary error will propagate to the fluid domain and it will affect the error throughout. This creates a condition that could amplify error for coupled problems and stray from the theoretical elliptic and non-elliptic bounded error rates. The proven and published error refinement rates are based on singular domain solutions only [9, 57]. No proof currently exists for refinement rates for multiple domain problems.

If the approximate finite element solution does not produce an accurate boundary deformation then the fluid's boundary spatial coordinates will not be accurately placed. For this case, the error on the boundary will become larger. In the case

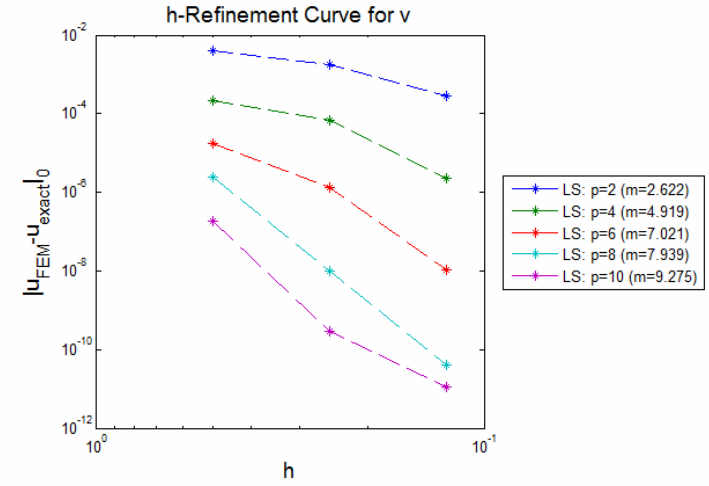

Figure 7.14 h-Refinement Curve for Fluid Primary Response (v) for MMS Problem

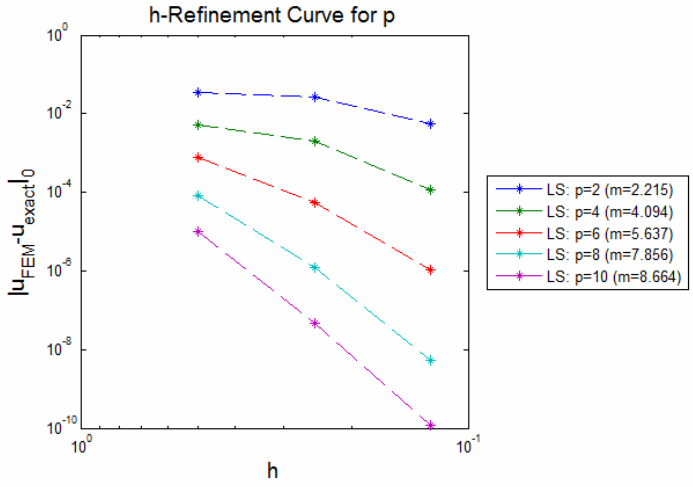

Figure 7.15 h-Refinement Curve for Fluid Secondary Response (p) for MMS Problem

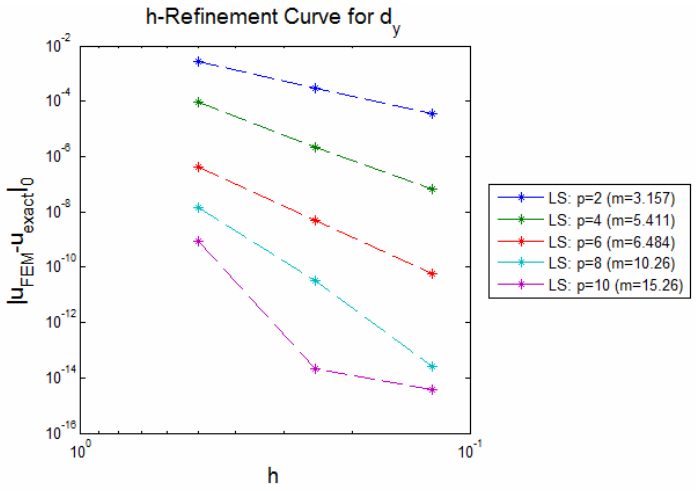

Figure 7.16 h-Refinement Curve for Structure Primary Response (d_y) for MMS Problem

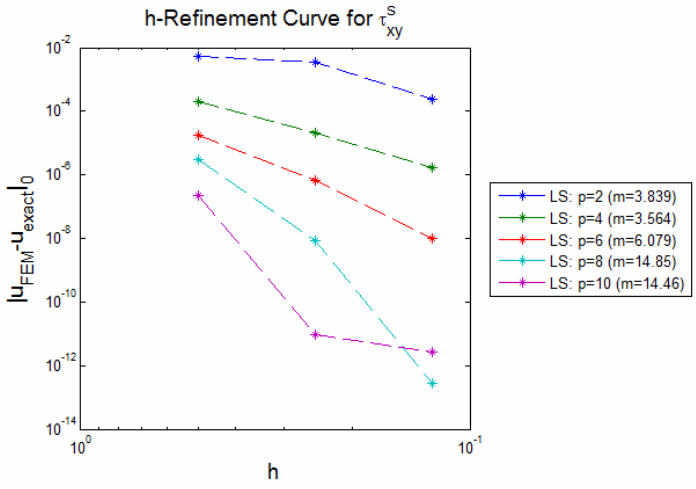

Figure 7.17 h-Refinement Curve for Structure Secondary Response (τ_{xy})

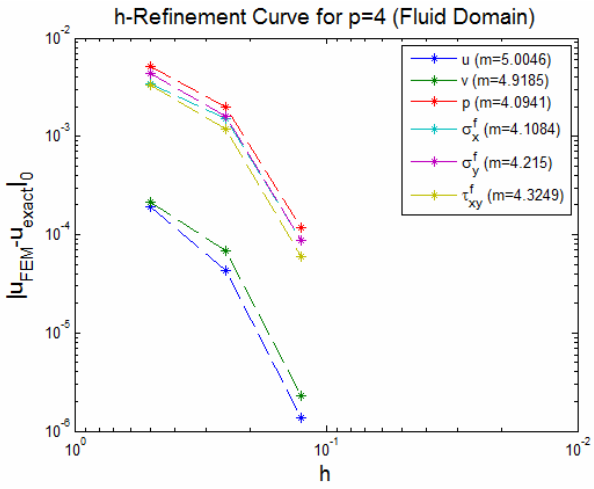

Figure 7.18 h-Refinement Curve for All Fluid Responses Using a p-value of 4 for MMS Problem

of higher-order p-elements, the element's Jacobian is isoparametric and matches the order of the finite element interpolation. The higher-order shape functions will allow the edges of each element to bend and curve to help capture curved boundaries. This allows for larger elements to be used along that boundary. However, if the p-value is low and only a few elements are used, the edge coordinates of elements that touch the boundary will be a poor approximation of the edge shape. Especially in the case where the boundary is defined by a cosine function instead of a polynomial, some small error will exist for any polynomial that attempts to capture its shape. In fact, for this problem, when mesh size decreases from 0.5 to 0.25, a sudden improvement in the refinement rate is observed for a p-value of 4 (Figure 7.18). It seems that for a coarse mesh, a p-value of 4 cannot capture the boundary shape well. Alternatively, a mesh size of 0.5 worked well for a p-value of 5 and it could capture the boundary well and maintain constant convergence rates for both coarse and fine meshes (Figure 7.19). Additionally, if the fluid response error is examined closely (Figure 7.20), it shows that the peak errors, which drive the overall error, rest on the interface boundary.

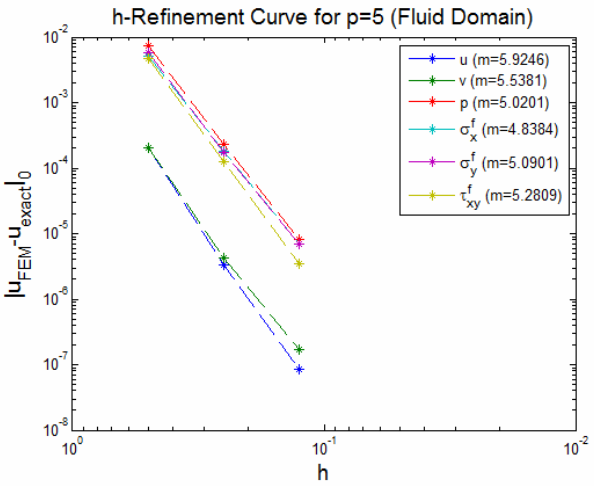

Figure 7.19 h-Refinement Curve for All Fluid Responses Using a p-value of 5 for MMS Problem

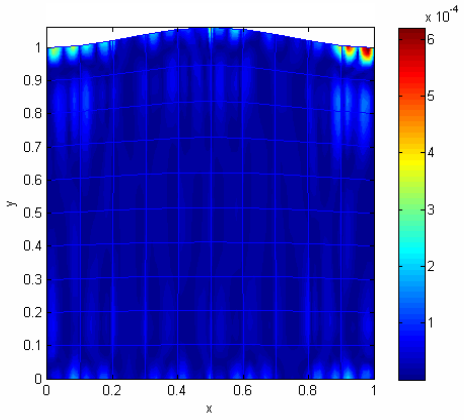

Figure 7.20 Error Contour Plot for Secondary Fluid Response p for MMS Problem

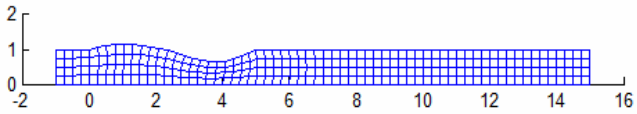

Figure 7.21 Sample Mesh Deformation from Collapsible Tube Problem (Problem Dimensions Shown)

MMS was useful for verifying the simultaneously coupled LSFEM FSI code considering the steady-state scenario. It also verified both the fluid and structure portions of the code.

7.6 Collapsible Tube Problem

A very challenging problem shown by Heil [76] consists of a tube with driven flow properties with a flexible top section that is modeled with a nonlinear structure. The sample problem solved by Heil consisted of a $16m$ long tube that is $1m$ tall. Only $5m$ of the top wall is flexible starting at 1m from the left. Figure 7.21 shows a sample deformed boundary and mesh generated for this problem. The figure also shows the problem dimensions.

This problem was selected for replication due to its challenging nature. The fluid is nonlinear and the structure is highly nonlinear allowing both horizontal and vertical deformations and a pre-stress condition. The fluid was modeled using Navier-Stokes equations. For this analysis, the v-p-σ formulation was used. The structure functional was shown by Heil

$$I = \int_0^L [F]\, dx = \int_0^L \left[h\sigma_0\gamma + \frac{h\gamma^2}{2} + \frac{h^3\kappa^2}{24} - f_{ext} \cdot R_w\Delta \right] dx \qquad (7.12)$$

where h is the tube height, γ is the geometrically nonlinear extensional strain, σ_0 is the applied pre-stress, κ is the wall curvature, f_{ext} is the wall traction vector on the structure, and R_w is the structure location vector including structure deformation.

κ is defined through

$$\kappa = \frac{\left[\frac{\partial^2 d_y}{\partial x^2}\left(1 - \frac{\partial d_x}{\partial x}\right) - \frac{\partial^2 d_x}{\partial x^2}\frac{\partial d_y}{\partial x}\right]}{\Delta} \tag{7.13}$$

where Δ is defined as

$$\Delta = \sqrt{\left(1 + \frac{\partial d_x}{\partial x}\right)^2 + \left(\frac{\partial d_y}{\partial x}\right)^2} \tag{7.14}$$

The vector R_w is defined as

$$R_w = [r_x + d_x, r_y + d_y] \tag{7.15}$$

which for this problem with the given dimensions becomes

$$R_w = [x + d_x, 1 + d_y] \tag{7.16}$$

The wall traction vector is defined through

$$f_{ext} = [f_1, f_2] \tag{7.17}$$

where f_1 and f_2 are defined as

$$f_1 = \left(Qp^f - p_{ext} - \sigma_x^f\right) n_x - \sigma_{xy}^f n_y \tag{7.18}$$

$$f_2 = -\sigma_{xy}^f n_x + \left(Qp^f - p_{ext} - \sigma_y^f\right) n_y \tag{7.19}$$

p_{ext} is a user-specified external pressure applied from outside the tube. Q is a non-dimensional parameter consisting of both structural and fluid properties.

$$Q = \frac{u_{avg}^f \mu}{E} \tag{7.20}$$

With all the variables specified for the structural functional, the next step required to implement this into a LSFEM scheme involves transforming the functional

into a system of differential equations. Cook provided equations for easy conversion from the functional to the derivative equation form. For a one-dimensional problem the transformation equations are

$$\frac{\partial F}{\partial d_x} - \frac{\partial}{\partial x}\frac{\partial F}{\partial d_{x,x}} + \frac{\partial^2}{\partial x^2}\frac{\partial F}{\partial d_{x,xx}} = 0 \tag{7.21}$$

$$\frac{\partial F}{\partial d_y} - \frac{\partial}{\partial x}\frac{\partial F}{\partial d_{y,x}} + \frac{\partial^2}{\partial x^2}\frac{\partial F}{\partial d_{y,xx}} = 0 \tag{7.22}$$

This provides the two core differential equations each of 5^{th} order. To reduce these equations down to the standard LSFEM 1^{st} order form, eight intermediate variables were introduced. They are defined as follows:

$$u_1 = \frac{\partial F}{\partial d_{x,x}} \tag{7.23}$$

$$u_2 = \frac{\partial F}{\partial d_{x,xx}} \tag{7.24}$$

$$u_3 = \frac{\partial u_2}{\partial x} \tag{7.25}$$

$$u_4 = \frac{\partial d_x}{\partial x} \tag{7.26}$$

$$v_1 = \frac{\partial F}{\partial d_{y,x}} \tag{7.27}$$

$$v_2 = \frac{\partial F}{\partial d_{y,xx}} \tag{7.28}$$

$$v_3 = \frac{\partial v_2}{\partial x} \tag{7.29}$$

$$v_4 = \frac{\partial d_y}{\partial x} \tag{7.30}$$

This produces a total of 10 differential equations with 10 responses to solve this nonlinear structure. The above formulation was modified so the tractions (f_{ext}) were also defined as unknowns or sharable degrees of freedom. This resulted in 10

differential equations and 12 unknowns but two of the unknowns were shared directly with the equilibrium condition applied at the boundary.

The above problem was solved using both simultaneous and sequential methods and using two prescribed externally applied pressures. The non-dimensional properties identified here are as follows: $Re = 500$, $Q = 10^{-2}$, $h = 10^{-2}$, and $\sigma_0 = 10^3$. The inflow velocity profile is defined as

$$u(y) = 6y(1-y) \tag{7.31}$$

which results in an average velocity of $u^f_{avg} = 1.0$. The first case external pressure was 1.524 and the second case was 3.247. These two externally applied pressures should produce a new vertical wall location at $x = 3.5$ of 1.000 and 0.5446 respectively [76]. This wall location was selected due to its peak deformation. The first case, if done properly, should produce no deformation.

A simultaneous solution generated a converged result after 63 nonlinear iterations (Figure 7.22) for the first case. The problem exhibited the expected highly nonlinear behavior. The new vertical wall location at $x = 3.5$ was 0.9839 which has 1.61% error with respect to the results shown by Heil [76]. Figure 7.23 shows the vertical deformation profile for the first case. Figure 7.24 shows the fluid pressure for this case which resulted in a nearly uniform Poisselle driven flow problem. These results were very near the results shown by Heil for both the fluid and structure [76].

The same case was solved using sequential methods. Figure 7.25 shows the nonlinear convergence history which showed great difficulty in convergence using sequential methods. It never converged through a total of 100 iterations and showed no signs of approaching convergence. Figure 7.26 shows the vertical structural deformations at 100 iterations which shows significant errors in vertical displacement. Figure 7.27 shows the fluid pressure plot and shows the extreme pressure gradients around the large displacements near the flexible portion of the tube. This problem

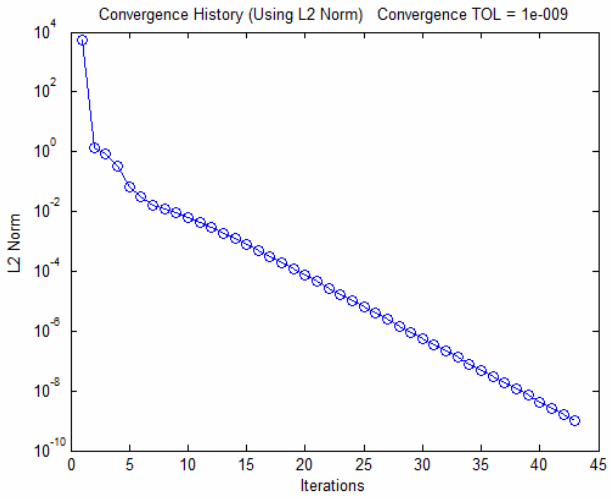

Figure 7.22 Nonlinear Convergence History for Steady-State Collapsible Tube Problem Using Simultaneous Solution Method (Case #1)

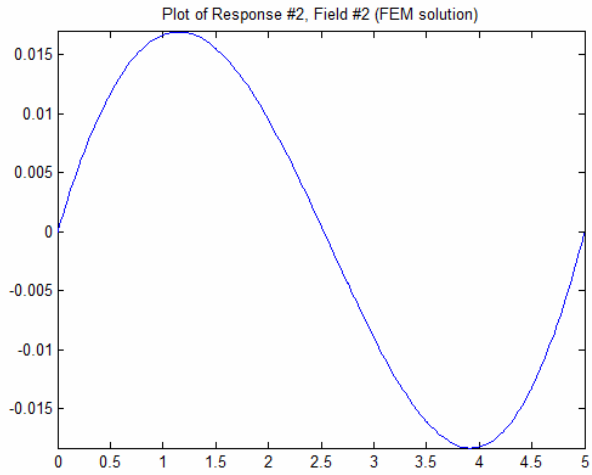

Figure 7.23 Vertical Deformations for Steady-State Collapsible Tube Problem Using Simultaneous Solution Method (Case #1)

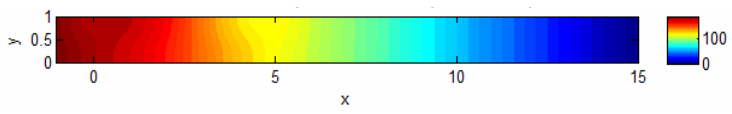

Figure 7.24 Fluid Pressure Profile for Steady-State Collapsible Tube Problem Using Simultaneous Solution Method (Case #1)

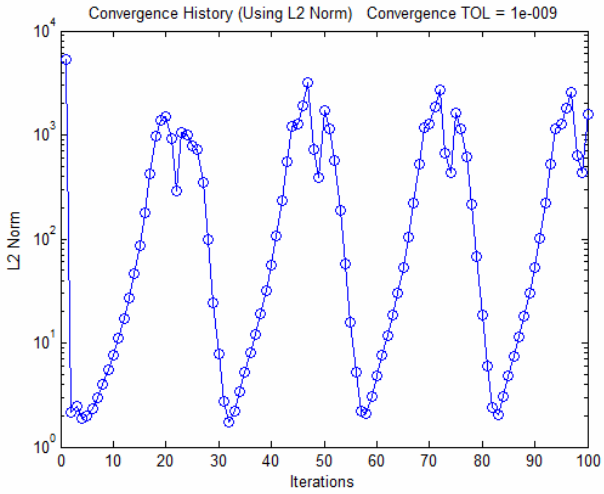

Figure 7.25 Nonlinear Convergence History for Steady-State Collapsible Tube Problem Using Sequential Solution Method (Case #1)

showed that for a highly nonlinear steady-state FSI problem, simultaneous methods can provide stronger convergence properties over sequential methods.

This first case exhibited accuracy for the simultaneous solution and verified the challenging nature of this problem. The second case exhibited the same nonlinear difficulties but showed a reduction in accuracy. The larger external pressure created larger deformations but were not as large as those reported by Heil [76]. The vertical wall location at $x = 3.5$ converged to be 0.8438 when Heil reported the correct wall location to be 0.5494 [76]. This is an error of 35.4% between the two analyses. This is a significant error which shows that there is a certain level of inaccuracy involved with the LSFEM method for this problem and its formulation. The sequential method was also used for this second case. Similar to Case #1, the sequential method exhibited great difficulty converging this problem.

7.7 Domain Weighting Sensitivity to h- and p-values

The need to provide the correct residual weights for each domain is critical for multi-domain problems when using LSFEM. The iterative residual weight balancing method provided a successful solution for the steady-state FSI problems shown in this

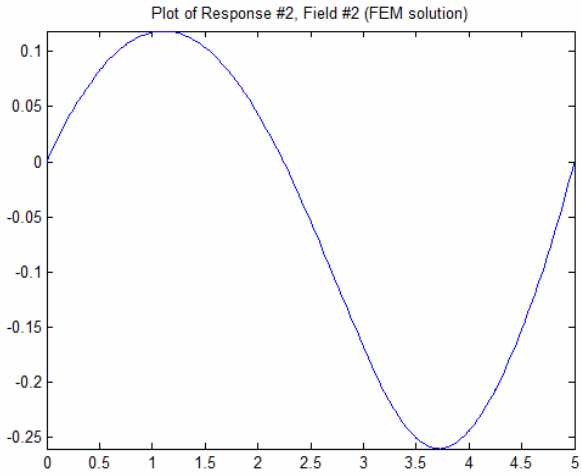

Figure 7.26 Vertical Deformations for Steady-State Collapsible Tube Problem Using Sequential Solution Method (Case #1)

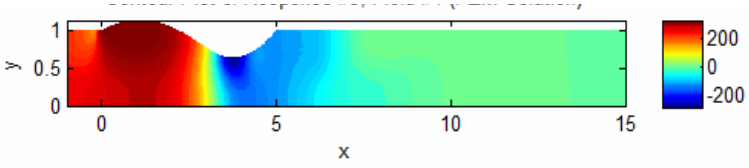

Figure 7.27 Fluid Pressure Profile for Steady-State Collapsible Tube Problem Using Sequential Solution Method (Case #1)

chapter. An examination of these final balanced weights follows. Their dependence on h- and p-values were examined to determine if there was a trend that could be used for future problems.

The first residual weight examination included hp-refinement. Figure 7.28 shows the balanced weights using hp-refinement for the MMS FSI problem. The p-values were refined, but the mesh was coarsened, in order to keep the number of degrees of freedom the same for every domain used within the coupled problem. The refinement plot shows very little sensitivity to the hp-refinement. In fact, the structure and the boundary interface weights showed absolutely no dependence on an increasing p-value without change to the number of degrees of freedom. The fluid and mesh deformation domain weights showed slight dependence on its p-value. In fact, the fluid domain showed no sensitivity for a p-value from 6 to 10. The mesh deformation domain showed the highest slope, but its weight had very little effect on the solution. Different weights, including weight values as high as those for the fluid domain, were used on the mesh deformation domain and the solution did not change at all. It was observed many times in this work that the fluid, structure, and boundary interface domains were the critical domains such that their domain residual weights had to be balanced in order to find a reasonable and/or accurate solution. It was observed that the mesh deformation domain's weight does not need to be balanced with the other domains.

The effect of h-refinement was also examined. The MMS FSI problem was solved for various element sizes and the convergence slopes were examined. Figure 7.29 shows the h-refinement curve. Similar to the hp-refinement, there was almost no sensitivity of the balanced residual weights with respect to the h-values. The residual weight slopes of the fluid and mesh deformation were the only domains that exhibited some dependence on mesh size. In fact, the dependence can be considered negligible; the slopes were less than 2 for all domains. The same h-refinement trends and the same weights were shown for other p-values (p =2, 4, 8, and 10). In

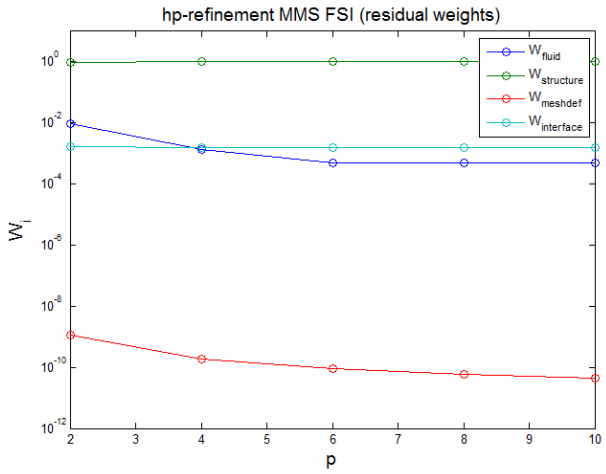

Figure 7.28 *hp*-Refinement of Balanced Residual Weights for MMS FSI Problem

other words, this study showed very little dependence on mesh size or shape function order.

This refinement study showed little to no dependence on h- and p-values. It was shown that the user could find the proper domain weights for low p-values with a coarse mesh and use those weights to determine a higher-order solution with refined h- and p-values. This means that the residual weight balancing could be used on a computationally cheap problem and then those weights could be fixed for a refined problem and still achieve highly accurate solutions.

Even though h- and p-values had very little effect on determining proper residual weights, it was observed that balanced residual weights varied with problem type. It was shown that residual weights used on one problem will not work on another. As an example case, the final balanced weights used for the double channel problem were applied to the MMS problem. These weights generated poor results. Alternatively, the final balanced weights used for the MMS problem were also unsuccessfully applied to the double channel problem. It is suggested here that future LSFEM users should not rely on one problem to define residual weights for another.

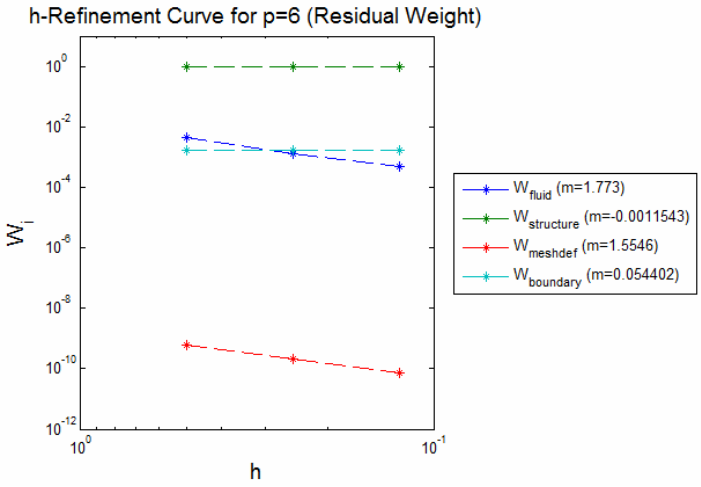

Figure 7.29 h-Refinement of Balanced Residual Weights for MMS FSI Problem (p-value = 6)

As soon as the boundary conditions change or if the domains change, the residual weights must be redetermined completely.

7.8 Domain Weighting Sensitivity to Material Properties

Since no significant dependence was shown with respect to h- or p-values, the double channel problem was solved several times while changing the Modulus of Elasticity (E). Figure 7.30 shows the change in each domain's residual weight by changing E from 10 GPa to 1000 GPa. For all E values, the solutions at the interface boundary match the known analytic solution at that location for each property value [74]. The figure shows little to no dependence on this property value. This shows that the property values might not strongly dictate what the residual weights should be for this problem.

7.9 Comparison of LSFEM-LSFEM to LSFEM-WGFEM FSI Solutions

Kayser-Herold and Matthies compared results of an FSI problem using a scheme that used LSFEM for both the fluid and structure (LSFEM-LSFEM) to a scheme that used LSFEM for the fluid and WGFEM for the structure (LSFEM-WGFEM).

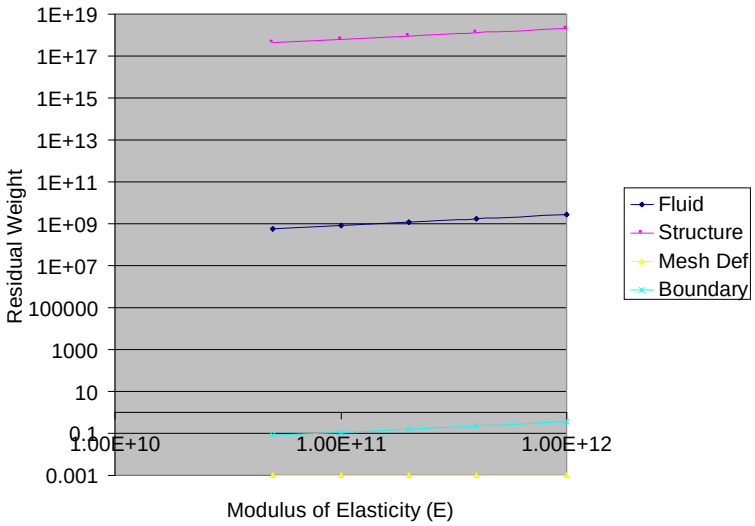

Figure 7.30 Residual Weight Dependence on Modulus of Elasticity for Double Channel Flow Problem

They showed poor results for the LSFEM-LSFEM scheme and accurate results for the LSFEM-WGFEM scheme. They mentioned that the issues with the LSFEM-LSFEM were unknown at that time [23].

The iterative residual weight balancing method has been absolutely critical here for multi-domain problems. Kayser-Herold and Matthies used manual weight balancing methods to attempt to make those LSFEM-LSFEM problems work. In fact, they used simple problems, such as single-domain problems, to define their residual weights for more complex problems, such as FSI problems [23]. This could prove to have been a critical error.

A similar comparison was performed here. The MMS FSI problem was solved using both WGFEM and LSFEM for the structural domain. LSFEM was used to solve for the fluid, boundary interface, and mesh deformation domains. Since the structural stress boundary conditions are implicit instead of direct degrees of freedom within a WGFEM scheme using (4.40) and (4.38), the coupled problem was solved sequentially for both LSFEM-LSEFM and LSFEM-WGFEM schemes. The sequential solution for the LSFEM-WGFEM scheme consisted of solving the

fluid domain first. After that, the fluid pressures and stresses were converted into resultant forces in the x and y directions. Those resultant forces were used as right hand side values (4.40) within the WGFEM scheme for the structural domain. After that, the displacements from the structural domain were used as boundary conditions for the mesh deformation domain. It was a purely sequential solution without any simultaneous portions.

A simultaneous solution for LSFEM-WGFEM was unsuccessful due to the inability to balance the multiple domains. For a pure LSFEM-LSFEM simultaneous scheme, it was possible to balance each domain, since there was an residual error indicator that was based on the same norm and functional throughout. This is not the case for the simultaneous LSFEM-WGFEM scheme. This created a situation where the WGFEM weighting factor could not be figured into the simultaneous solution successfully. This drove the pure sequential solution for the LSFEM-WGFEM case.

Table 7.6 shows the LSFEM-WGFEM vs. LSFEM-LSFEM L_2 response error comparisons. The L_2 response error values were integrated across the entire domain and were compared directly with the known exact solution. The table shows the results from the MMS FSI problem using a p-value of 4. The LSFEM-LSFEM error was consistently 10^3 times better than the LSFEM-WGFEM case. This was shown for both the structure and fluid domains. The boundary interface error was improved by a factor of 10^2 for LSFEM-LSFEM. Even though the error values were significantly different between the two schemes, the contour plots of the responses appeared very similar (Figure 7.31). It was nearly impossible to differentiate between the two schemes' responses and the exact solution with the naked eye. In other words, the LSFEM-WGFEM scheme was accurate, just not as accurate as the LSFEM-LSFEM scheme.

This comparison was completed for other p-values. The LSFEM-WGFEM solution did not converge as well as the LSFEM-LSFEM solution. The error for

the LSFEM-WGFEM scheme did not improve even with p-refinement. Table 7.7 shows the same comparison except for a p-value of 8. This shows that the LSFEM-WGFEM has reached a limit in its accuracy.

The reduction in the convergence rate for the LSFEM-WGFEM scheme could mainly come from the fact that the stresses were applied as a right hand side value within the WGFEM scheme instead of being directly sharable degrees of freedom in a LSFEM scheme. LSFEM has already been shown to hold a better convergence rate with respect to the secondary variables, but that accuracy is magnified in a coupled problem when the error can transfer to other domains. This will affect the error throughout, since the coupled problem is dependent on the stress boundary accuracy.

The main reason for the accurate LSFEM-LSFEM solution, even though Kayser-Herold and Matthies produced poor results for that scheme, was because proper residual weights were used for the multiple domain problem. Kayser-Herold and Matthies used manually adjusted weights from other simpler problems and did not rebalance the weights for their FSI problem [23]. This may create unreliable results for a steady-state or transient FSI problem.

7.10 Examination of Nonconformal Mesh in FSI Solutions

The benefits of a nonconformal mesh in a coupled FSI problem are apparent. Most FSI problems require a fluid domain with a fine mesh and/or a high polynomial order with a structure that needs fewer degrees of freedom to obtain the same level of accuracy within each domain. In fact, it was shown in Tables 7.4 and 7.5 that even though the same number of elements and polynomial order was used within the fluid and structural domain, the structure consistently exhibited a better error value (by a factor of $10^1 - 10^2$) than the fluid error. This implies that a coarser structural domain or a finer fluid domain would produce similar error values between

Response Type	LSFEM-WGFEM	Response Type	LSFEM-LSFEM
Fluid (Ω^F)	Ω^F Error	Fluid (Ω^F)	Ω^F Error
v_x^f	1.44591E-03	v_x^f	1.15892E-06
v_y^f	1.07913E-03	v_y^f	1.15088E-06
p	7.47513E-03	p	4.51499E-05
σ_x^f	3.38192E-03	σ_x^f	3.47383E-05
σ_y^f	3.14865E-03	σ_y^f	3.36043E-05
σ_{xy}^f	4.71469E-03	σ_{xy}^f	2.32214E-05
Structure (Ω^S)	Ω^S Error	Structure (Ω^S)	Ω^S Error
u_x^s	3.96261E-04	u_x^s	1.78895E-07
u_y^s	2.17139E-03	u_y^s	1.61041E-06
σ_x^s	2.96364E-03	σ_x^s	1.53404E-05
σ_y^s	1.52591E-02	σ_y^s	7.96433E-05
σ_{xy}^s	9.31650E-03	σ_{xy}^s	1.59913E-05
Stress Equilibrium (Γ^{FS})	Γ^{FS} Error	Stress Equilibrium (Γ^{FS})	Γ^{FS} Error
p	2.12825E-02	p	2.05715E-04
σ_x^f	1.66133E-02	σ_x^f	1.58065E-04
σ_y^f	1.59324E-02	σ_y^f	1.97619E-04
σ_{xy}^f	1.18321E-02	σ_{xy}^f	1.30933E-04
ϕ_x	1.05990E-02	σ_x^s	1.26473E-04
ϕ_y	8.08637E-03	σ_y^s	3.23345E-04
		σ_{xy}^s	1.04412E-04

Table 7.6 Error Comparisons for LSFEM-LSFEM vs. LSFEM-WGFEM Schemes for MMS FSI Problem (p=4)

Response Type	LSFEM-WGFEM	Response Type	LSFEM-LSFEM
Fluid (Ω^F)	Ω^F Error	Fluid (Ω^F)	Ω^F Error
v_x^f	1.43657E-03	v_x^f	3.86702E-08
v_y^f	1.08149E-03	v_y^f	3.24531E-08
p	7.97496E-03	p	2.89434E-07
σ_x^f	3.47391E-03	σ_x^f	2.63803E-07
σ_y^f	3.20336E-03	σ_y^f	3.08079E-07
σ_{xy}^f	4.79951E-03	σ_{xy}^f	2.19656E-07
Structure (Ω^S)	Ω^S Error	Structure (Ω^S)	Ω^S Error
u_x^s	3.97637E-04	u_x^s	1.48192E-09
u_y^s	2.15617E-03	u_y^s	1.19533E-08
σ_x^s	2.95813E-03	σ_x^s	2.47712E-07
σ_y^s	1.52552E-02	σ_y^s	5.95197E-07
σ_{xy}^s	9.32570E-03	σ_{xy}^s	1.75334E-07
Stress Equilibrium (Γ^{FS})	Γ^{FS} Error	Stress Equilibrium (Γ^{FS})	Γ^{FS} Error
p	2.28463E-02	p	1.27052E-06
σ_x^f	1.65237E-02	σ_x^f	1.88110E-06
σ_y^f	1.58746E-02	σ_y^f	1.84261E-06
σ_{xy}^f	1.25420E-02	σ_{xy}^f	1.78596E-06
ϕ_x	1.12330E-02	σ_x^s	2.58359E-06
ϕ_y	9.93517E-03	σ_y^s	2.31604E-06
		σ_{xy}^s	1.78353E-06

Table 7.7 Error Comparisons for LSFEM-LSFEM vs. LSFEM-WGFEM Schemes for MMS FSI Problem (p=8)

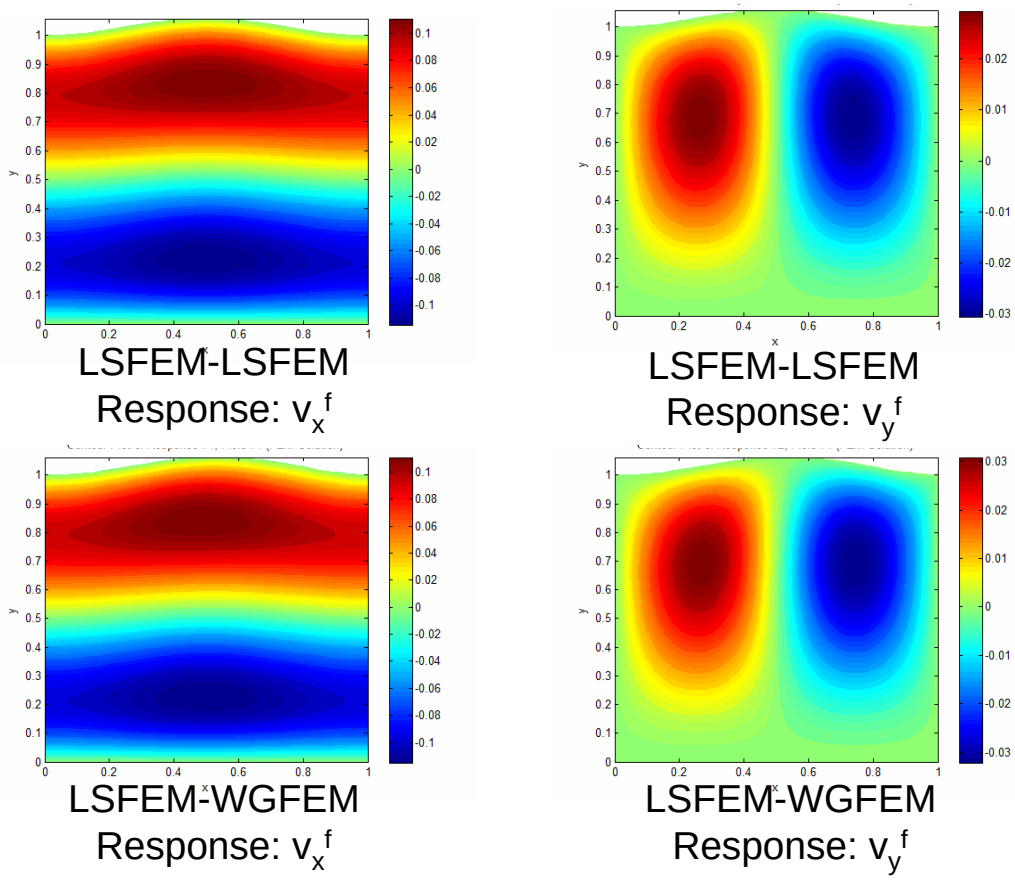

Figure 7.31 Fluid Velocity Contour Plots for LSFEM-LSFEM vs. LSFEM-WGFEM Case Study

the domains. In addition, it seems that the order of accuracy of the structural solver is stronger than that of the fluid solver.

Nonconformal meshing was examined for the MMS FSI problem. To do this, new resultant force relationships were created for each domain. This allows a single response to be equated, either weakly or strongly, at a boundary. This was done because the nonconformal LSFEM scheme that was implemented here uses a one-to-one relationship. Instead of using a boundary relationship that relates four fluid responses to three structural responses (7.9) and (7.10), resultant forces were generated for each domain so that their one-to-one relationship could be equated.

The fluid stresses and pressures are converted to resultant forces (ϕ_x^f, ϕ_y^f) on the boundary,

$$-pn_x + \sigma_x^f n_x + \sigma_{xy}^f n_y - \phi_x^f = 0 \tag{7.32}$$

$$\sigma_{xy}^f n_x - pn_y + \sigma_y^f n_y - \phi_y^f = 0 \tag{7.33}$$

the structure stresses are converted to resultant forces (ϕ_x^s, ϕ_y^s) on the boundary,

$$\sigma_x^s n_x + \sigma_{xy}^s n_y - \phi_x^s = 0 \tag{7.34}$$

$$\sigma_{xy}^s n_x + \sigma_y^s n_y - \phi_y^s = 0 \tag{7.35}$$

and then the resultant forces are equated, i.e.,

$$\phi_x^f - \phi_x^s = 0 \tag{7.36}$$

$$\phi_y^f - \phi_y^s = 0 \tag{7.37}$$

The resultant force values are directly shared for a conformal mesh case or they are weakly equated using LSFEM nonconformal mesh methods for the nonconformal case.

For this problem, another nonconformal mesh was required at the structure and mesh deformation interface boundary to match boundary displacements. The fluid domain is updated using a mesh deformation domain with the same mesh size and polynomial order. The response from the mesh deformation is used to define the fluid domain mesh. The polynomial order used for the fluid Jacobian must be the same as the mesh deformation domain's responses unless a weakly enforced relationship is desired across the entire domain. If a weak relationship is not desired across the entire domain, then the fluid and mesh deformation domains must have the same mesh size and polynomial order. Since the structure shares responses with both domains, those paired responses must be equated using nonconformal meshing. As such, the displacements at the interface boundary are weakly equated through the boundary integral

$$d_x^s - d_x^D = 0 \tag{7.38}$$

$$d_y^s - d_y^D = 0 \tag{7.39}$$

The system of equations, including (7.32-7.39), were solved simultaneously. The first case (Case A) includes varying the structural domain's p-value from 2 to 4 while keeping the fluid domain's p-value at 5. This was performed using hp-refinement where each domain had the same number of degrees of freedom at the boundary interface (41 modes on the edge). This means that for a p-value of 2 there were twenty edge elements, for a p-value of 4 there were ten edge elements, and for a p-value of 5 there were eight edge elements. Table 7.8 shows the L_2 response error norm results of Case A and Figure 7.32 shows sample meshes. Other p-values were analyzed, but they did not show an improvement beyond a p-value of 4. This was expected, since the fluid domain was held at a p-value of 5 throughout and it limited how accurately the problem could be solved since the number of degrees of freedom were constant throughout. Similar results were shown for other nonconformal mesh studies performed within this research (Section 6.4.2). All error

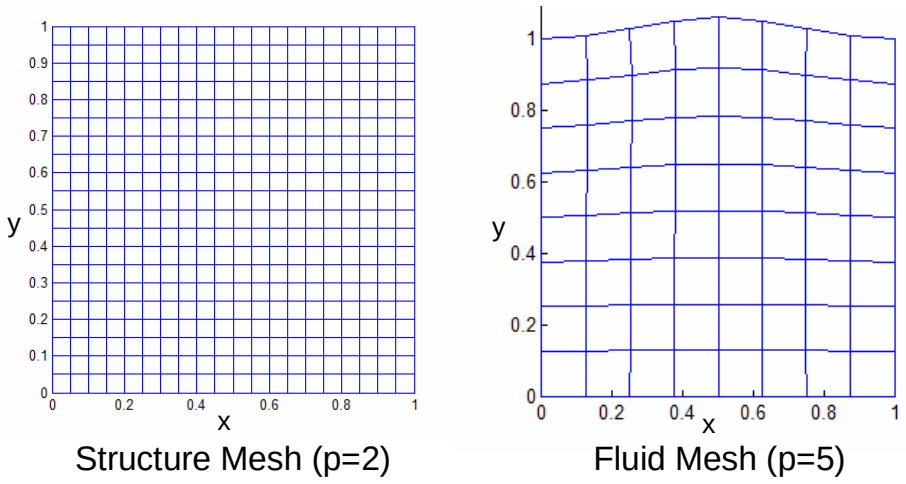

Figure 7.32 Sample Nonconformal Meshes for Case A (MMS FSI Problem)

values were comparable to the conformal cases. In fact, the error values were a little better due to the fact that the fluid domain had a higher p-value, which improved accuracy on the fluid side.

Case B included keeping the p-values the same between the fluid and structural domains but the fluid always had twice as many degrees of freedom on the boundary interface. hp-refinement was used as before. Figure 7.33 shows sample meshes for each domain for a p-value of 4. Table 7.9 shows the results from this case study. It shows that the solution was improved from a conformal mesh case. This was expected since more degrees of freedom were used for the fluid domain and should improve the problem's overall accuracy. This example demonstrates that the nonconformal mesh methodology was successful using LSFEM for FSI problems.

Response	Nonconformal ($p = 2$)	Nonconformal ($p = 4$)	Conformal ($p = 2$)	Conformal ($p = 4$)
Fluid (Ω^F)	Ω^F Error	Ω^F Error	Ω^F Error	Ω^F Error
v_x^f	8.89771E-06	1.53886E-07	2.07293E-05	1.48249E-06
v_y^f	6.43913E-06	1.36838E-07	1.94184E-05	1.19589E-06
p	1.84712E-04	7.84766E-06	5.88630E-04	3.69020E-05
σ_x^f	5.71071E-05	6.15685E-06	3.75388E-04	2.60150E-05
σ_y^f	6.17173E-05	6.49535E-06	4.27374E-04	2.43861E-05
σ_{xy}^f	4.46730E-05	2.57866E-06	3.56675E-04	1.40549E-05
Structure (Ω^S)	Ω^S Error	Ω^S Error	Ω^S Error	Ω^S Error
u_x^s	7.33010E-07	1.92023E-08	2.92216E-06	1.33135E-07
u_y^s	1.47682E-05	3.67300E-07	8.71639E-06	2.10977E-06
σ_x^s	1.31697E-05	1.05336E-06	1.62271E-04	5.62331E-06
σ_y^s	4.28406E-04	5.27928E-06	4.92029E-04	2.40900E-05
σ_{xy}^s	4.99006E-05	1.43216E-06	1.58260E-04	7.49081E-06
Stress (Γ^{FS})	Γ^{FS} Error	Γ^{FS} Error	Γ^{FS} Error	Γ^{FS} Error
p	5.33536E-04	1.54444E-05	9.71766E-04	7.49314E-05
σ_x^f	1.59049E-04	7.82698E-06	3.45449E-04	3.53263E-05
σ_y^f	2.70503E-04	8.07868E-06	4.95392E-04	3.79874E-05
σ_{xy}^f	9.66957E-05	1.00473E-05	1.11354E-03	4.77296E-05
σ_x^s	4.32653E-05	9.36793E-06	8.61834E-04	4.87450E-05
σ_y^s	8.01716E-04	1.73249E-05	9.72909E-04	8.50407E-05
σ_{xy}^s	1.05721E-04	7.10668E-06	9.43793E-04	3.06839E-05
Nonconformal d (Γ^{FS})	Γ^{FS} Diff	Γ^{FS} Diff	Γ^{FS} Diff	Γ^{FS} Diff
d_x	1.05054E-14	1.04939E-14	N/A	N/A
d_y	4.29726E-06	3.82585E-08	N/A	N/A
Nonconformal ϕ (Γ^{FS})	Γ^{FS} Diff	Γ^{FS} Diff	Γ^{FS} Diff	Γ^{FS} Diff
ϕ_x	1.82233E-05	2.25666E-06	N/A	N/A
ϕ_y	2.52517E-04	3.23227E-06	N/A	N/A

Table 7.8 Error Values for FSI Nonconformal Study (Case A)

Response	Nonconformal ($p = 2$)	Nonconformal ($p = 4$)	Conformal ($p = 2$)	Conformal ($p = 4$)
Fluid (Ω^F)	Ω^F Error	Ω^F Error	Ω^F Error	Ω^F Error
v_x^f	3.21716E-06	2.35550E-07	2.07293E-05	1.48249E-06
v_y^f	3.23851E-06	1.76984E-07	1.94184E-05	1.19589E-06
p	1.34762E-04	2.21760E-06	5.88630E-04	3.69020E-05
σ_x^f	1.10666E-04	1.72183E-06	3.75388E-04	2.60150E-05
σ_y^f	1.15139E-04	1.55132E-06	4.27374E-04	2.43861E-05
σ_{xy}^f	5.41894E-05	8.63464E-07	3.56675E-04	1.40549E-05
Structure (Ω^S)	Ω^S Error	Ω^S Error	Ω^S Error	Ω^S Error
u_x^s	4.58845E-07	8.55150E-09	2.92216E-06	1.33135E-07
u_y^s	3.01387E-06	7.29471E-08	8.71639E-06	2.10977E-06
σ_x^s	1.65145E-05	1.17190E-07	1.62271E-04	5.62331E-06
σ_y^s	3.85828E-04	3.35722E-06	4.92029E-04	2.40900E-05
σ_{xy}^s	2.48331E-05	3.17934E-07	1.58260E-04	7.49081E-06
Stress (Γ^{FS})	Γ^{FS} Error	Γ^{FS} Error	Γ^{FS} Error	Γ^{FS} Error
p	4.27273E-04	6.72181E-06	9.71766E-04	7.49314E-05
σ_x^f	3.61207E-04	2.87974E-06	3.45449E-04	3.53263E-05
σ_y^f	3.84701E-04	2.91775E-06	4.95392E-04	3.79874E-05
σ_{xy}^f	1.85681E-04	2.52983E-06	1.11354E-03	4.77296E-05
σ_x^s	8.66802E-05	7.60476E-07	8.61834E-04	4.87450E-05
σ_y^s	8.46663E-04	8.13260E-06	9.72909E-04	8.50407E-05
σ_{xy}^s	1.06530E-04	1.19966E-06	9.43793E-04	3.06839E-05
Nonconformal d (Γ^{FS})	Γ^{FS} Diff	Γ^{FS} Diff	Γ^{FS} Diff	Γ^{FS} Diff
d_x	3.23882E-14	3.17404E-14	N/A	N/A
d_y	7.54833E-14	2.58283E-14	N/A	N/A
Nonconformal ϕ (Γ^{FS})	Γ^{FS} Diff	Γ^{FS} Diff	Γ^{FS} Diff	Γ^{FS} Diff
ϕ_x	5.42403E-05	1.00164E-06	N/A	N/A
ϕ_y	1.22079E-04	6.36775E-07	N/A	N/A

Table 7.9 Error Values for FSI Nonconformal Study (Case B)

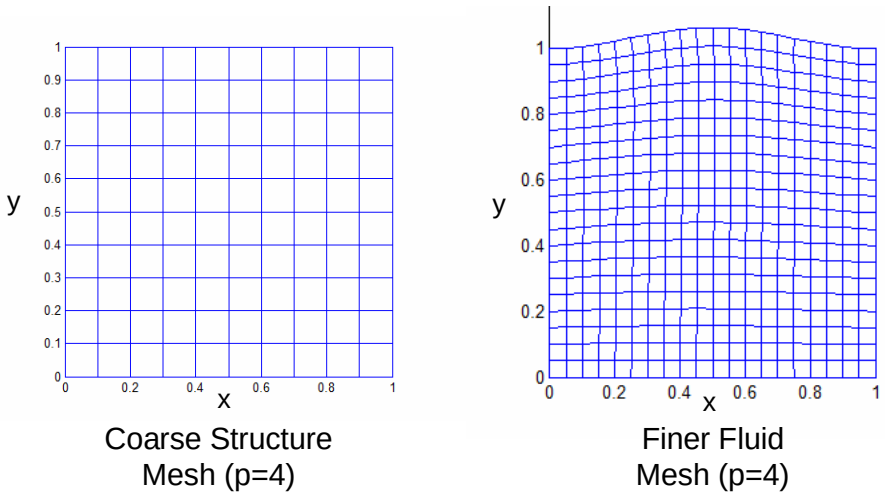

Figure 7.33 Sample Nonconformal Meshes for Case B (MMS FSI Problem)

VIII. Transient Fluid-Structure Interaction

Transient FSI problems are difficult to solve and have proven to challenge numerical schemes when sequential solution schemes are applied [19]. It was shown in previous chapters that simultaneous and sequential schemes provide very similar results for steady-state FSI problems. Since simultaneous multi-domain LSFEM schemes require residual weight balancing, the steady-state sequential solution scheme provided the same level of accuracy with significantly lower processing time. For steady-state, the sequential method was preferred. For transient problems, Bendiksen argued that simultaneous methods may show a significant improvement over sequential solution methods for complex problems. In fact, he showed that convergence and accuracy can be improved with fewer degrees of freedom in a simultaneous solution scheme.

8.1 Example Transient FSI Problem Using MMS

8.1.1 Problem Properties. A new MMS FSI problem was created for transient FSI investigation. The steady-state MMS problem described in Section 7.5 was modified slightly such that the boundary deformation has a harmonic response, e.g.,

$$d_x^s = 0 \tag{8.1}$$

$$d_y^s = 1 + h\left(1 - \cos\left(2\pi x\right)\right)\sin\left(2\pi t\right) \tag{8.2}$$

This creates a new MMS problem with new responses within the fluid, structure, and boundary interface. This new transient MMS FSI problem was complex enough to challenge Bendiksen's argument whether simultaneous solutions will provide accuracy improvement over a sequential solution. In addition, this complex problem provided a known exact solution to compare numerical results from the LSFEM analysis.

The first analysis was performed to compare simultaneous and sequential solutions using only a single time step of 0.01 seconds. This time step size was smaller than the minimum time step size dictated by the CFL condition for both the fluid and structural domains ($\min(\Delta t) = 0.36$ sec). The transient solution should be convergent using this time step. The transient form of the v-p-σ Navier Stokes formulation was used for the fluid and the transient u-v-σ structural formulation was used for the structure. Each time step included several nonlinear subiterations to reach proper nonlinear problem convergence. Each time step was converged to a relative convergence of 10^{-9} between nonlinear subiterations.

Residual balancing was performed similarly to the steady-state MMS FSI problem except the structural domain was balanced at the equation level where similar equations were paired by their equation type. This was done because it was shown in Section 4.7.1 that the transient structure requires balancing at the element level. In other words, the residual balancing was performed at the domain level for the fluid and residual balancing was performed at the equation pairing level for the structure. This means that the fluid requires only one residual weight whereas the structure requires three weights. This means that the convergence with respect to the residual weight balancing is easier for the fluid than the structure.

8.1.2 Single Time Step Results (T=0.01 sec). Table 8.1 shows the integrated L_2 response error norms from a single time step. Very little difference in error was observed between the sequential and simultaneous solutions. In addition, the error values here were higher than that observed for the steady-state MMS FSI problem. This is due to the lower-order accuracy provided by the discretization of the temporal derivative for the selected time step. The Crank-Nicolson method was used here and it provides an accuracy on the order of Δt^2. Since the time step size was 0.01 seconds, the order of the error should be somewhere near 10^{-4}. This was observed throughout the fluid and structural domains. This implies that the temporal discretization drives the accuracy of this problem.

Response Type	Simultaneous	Sequential
Fluid (Ω^F)	Ω^F Error	Ω^F Error
v_x^f	2.25968e-004	1.15305e-004
v_y^f	1.32324e-004	2.28616e-004
p	4.54705e-003	1.02859e-002
σ_x^f	1.49659e-003	1.02176e-003
σ_y^f	7.56980e-004	7.65443e-004
σ_{xy}^f	3.19149e-003	3.51992e-003
Structure (Ω^S)	Ω^S Error	Ω^S Error
u_x^s	2.30352e-007	2.30300e-007
u_y^s	1.46175e-006	1.46327e-006
σ_x^s	2.84958e-006	4.64316e-006
σ_y^s	5.20613e-006	4.56480e-005
σ_{xy}^s	1.46345e-005	1.51212e-005
v_x^s	4.60704e-005	4.60600e-005
v_y^s	2.13707e-004	2.14693e-004
Stress Equilibrium (Γ^{FS})	Γ^{FS} Error	Γ^{FS} Error
p	4.20029e-003	2.58490e-002
σ_x^f	5.74661e-003	4.01084e-003
σ_y^f	4.04916e-003	3.73267e-003
σ_{xy}^f	4.55699e-004	8.12926e-003
σ_x^s	1.06315e-006	4.53707e-005
σ_y^s	1.90939e-005	6.48516e-004
σ_{xy}^s	4.16041e-005	7.14165e-005

Table 8.1 Error Comparisons for Sequential Vs. Simultaneous Solutions for Transient MMS FSI Problem Using Only One Time Step (t=0.01 secs, 100 Elements with p-value of 4)

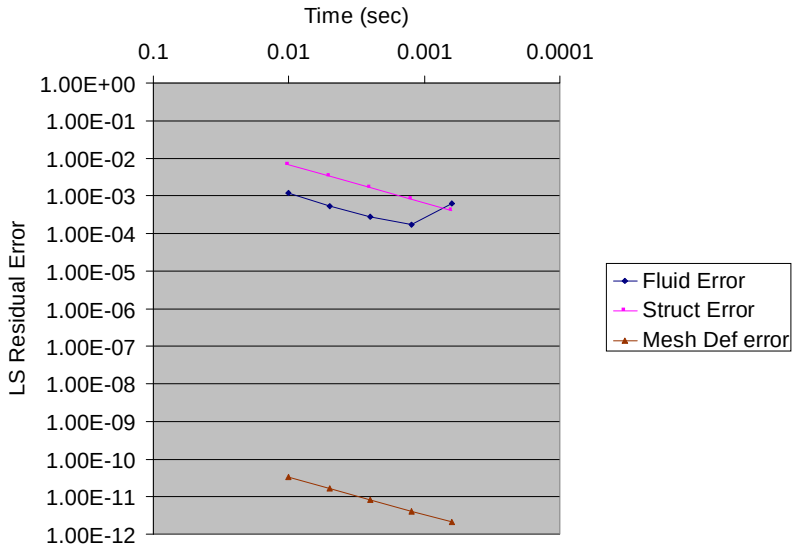

Figure 8.1 Δt-Refinement Examining the LSFEM Residual for Transient MMS FSI Problem Using Simultaneous Method ($t = 0.01$ seconds, 100 Elements with p-value of 4)

8.1.3 Dependence on Error With Respect to Time Step Size. A time step size study was performed on this problem to examine the effects of time step size and to test when the LSFEM spatial discretization overcomes the finite volume temporal discretization. The same problem was solved to a final time of 0.01 seconds but several different time step sizes were used. Time step sizes of 0.000625, 0.00125, 0.0025, 0.005, and 0.01 seconds were used. Figure 8.1 shows the LSFEM residual error for each domain using Δt-refinement. The figures show that the refinement produces a constant convergence rate with respect to Δt from 0.01-0.00125 seconds. For time steps smaller than 0.00125 seconds, the fluid convergence rate flattens out which implies that the spatial discretization error will dominate. As expected, the error is on the order of $n\Delta t^2$ for the averaged response error.

The same examination into Δt refinement was performed using a sequential method. Figure 8.2 shows similar residual values for all domains. It also shows the same time step size when the spatial discretization dominates for this problem.

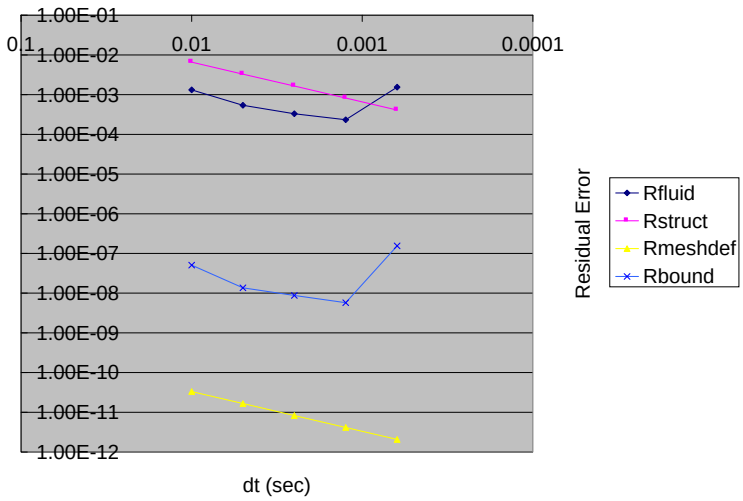

Figure 8.2 Δt-Refinement Examining the LSFEM Residual for Transient MMS FSI Problem Using Sequential Method ($t = 0.01$ seconds, 100 Elements with p-value of 4)

8.1.4 Multiple Time Step Results (T=0.25 sec). The next analysis included 25 total time steps. This creates the maximum boundary deformation and should push the accuracy of the scheme. The same time step was used as before (0.01 *sec*). Table 8.2 shows the results from this analysis. In this case, the sequential solution performed poorly. Not only were the error values from the sequential solution off by a factor of $10^1 - 10^2$ compared to the simultaneous solution, but the accuracy was visually apparent. Figure 8.3 shows the error contour plots between the simultaneous and sequential solution for horizontal fluid velocity. Not only are the error values apparent, but the boundary deformation is entirely inaccurate. Similarly, Figure 8.4 shows the error plots for the vertical structure displacement. These responses govern the boundary displacement. Large error values were observed for the sequential solution, whereas the simultaneous solution remained fairly accurate. In fact, the simultaneous solution was on the order of the temporal discretization error over 25 time steps ($2.5 \blacksquare 10^{-3}$).

Response Type	Simultaneous	Sequential
Fluid (Ω^F)	Ω^F Error	Ω^F Error
v_x^f	2.19762e-003	1.54297e-002
v_y^f	1.18154e-003	6.75323e-003
p	3.55386e-002	1.46692e-001
σ_x^f	5.84948e-003	2.73866e-002
σ_y^f	3.60075e-003	2.57544e-002
σ_{xy}^f	6.39200e-003	6.38235e-002
Structure (Ω^S)	Ω^S Error	Ω^S Error
u_x^s	7.81146e-005	3.55236e-004
u_y^s	6.15686e-004	7.47124e-003
σ_x^s	1.24302e-003	5.72693e-002
σ_y^s	9.96661e-003	5.80121e-001
σ_{xy}^s	3.10044e-003	3.70797e-002
v_x^s	7.66873e-004	2.08542e-002
v_y^s	7.09156e-003	4.08084e-001
Stress Equilibrium (Γ^{FS})	Γ^{FS} Error	Γ^{FS} Error
p	6.38655e-002	4.23169e-001
σ_x^f	9.13863e-003	1.31696e-001
σ_y^f	1.11481e-002	1.17152e-001
σ_{xy}^f	1.55688e-002	1.93881e-001
σ_x^s	5.07238e-003	3.52355e-001
σ_y^s	5.44680e-002	3.37536e+000
σ_{xy}^s	1.42448e-002	1.75113e-001

Table 8.2 Error Comparisons for Sequential Vs. Simultaneous Solutions for Transient MMS FSI Problem Using 25 Time Steps (t=0.25 secs, 100 Elements with p-value of 4)

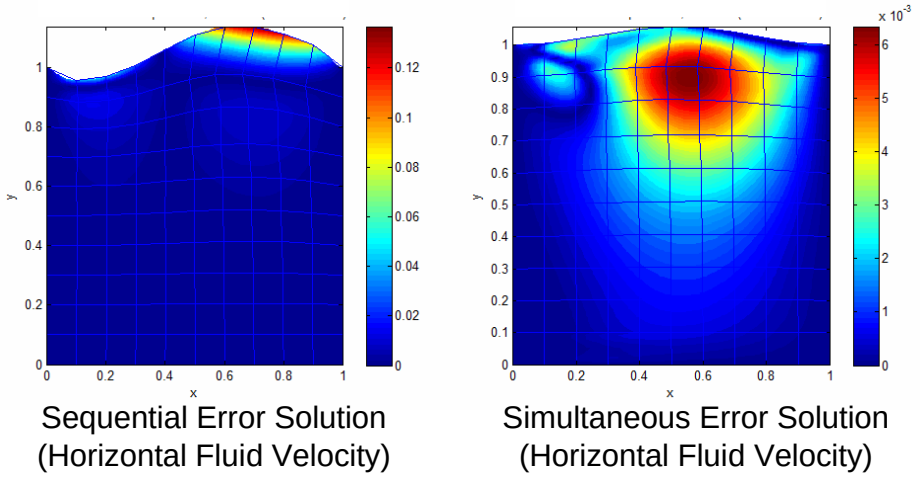

Figure 8.3 Horizontal Fluid Velocity Error Contour Plot for Sequential vs. Simultaneous Comparison for Transient MMS FSI Problem (t=0.25 *sec*)

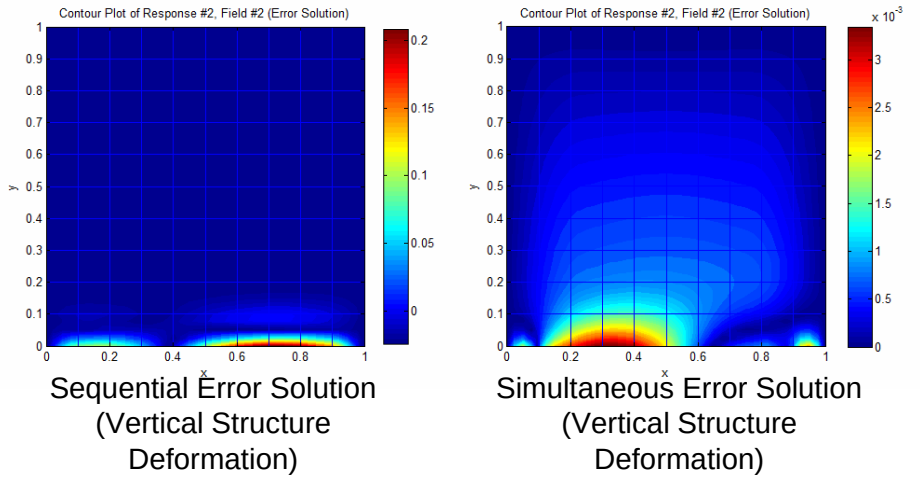

Figure 8.4 Vertical Structure Displacement Error Contour Plot for Sequential vs. Simultaneous Comparison for Transient MMS FSI Problem (t=0.25 *sec*)

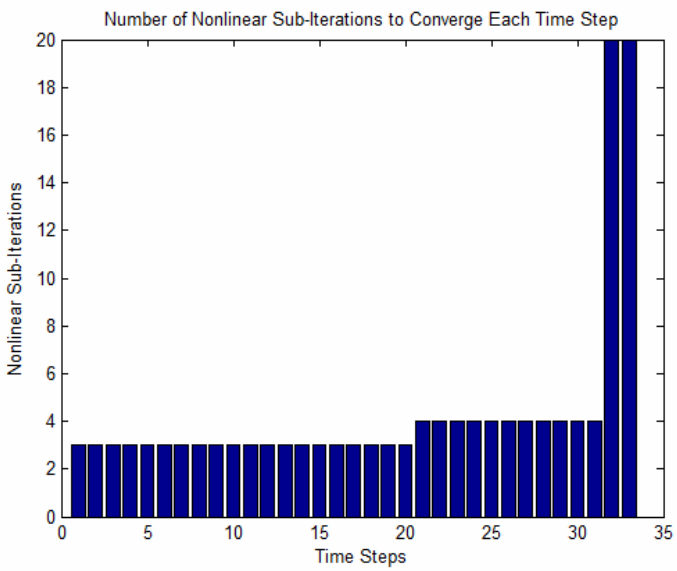

Figure 8.5 Number of Nonlinear Sub-Iterations Required to Converge Each Time Step

8.1.5 Examination of Time Step Size Refinement for Sequential Solution Accuracy. An attempt was performed to improve the sequential method's accuracy. A much smaller time step was attempted here (Δt=0.001 *sec*). The solution diverged quickly after 32 time steps. Figure 8.5 shows the number of nonlinear sub-iterations required within each time step to reach convergence. Figure 8.6 shows how the total iterative norm blows up after the total number of iterations reaches a divergent point. The sequential method showed similar poor convergence properties for other FSI problems [25, 26]. In retrospect, it is surprising that the sequential method using a time step size of 0.01 *sec* was able to converge at all. An even smaller time step size was used (Δt=0.0001 *sec*) and still showed poor convergence behavior. This confirms the fact that sequential methods in a transient FSI scheme require a unique method to converge [19, 25, 26]. A small time step size will not fix all poor convergence sequential solutions.

8.1.6 Full Period Results (T=1.00 sec). The next analysis included 100 time steps to a total time of 1.0 *sec*. The simultaneous method was able to solve

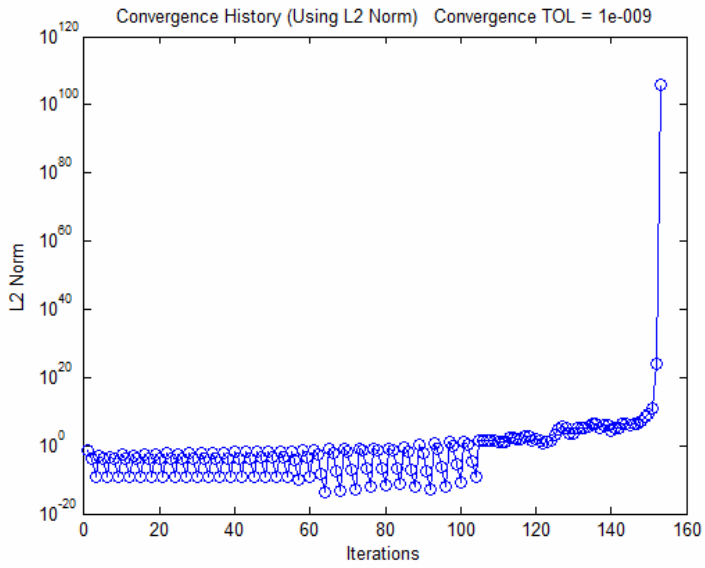

Figure 8.6 L^2 Norm History Through All Iterations (Sub-Iterations and Time Step Iterations)

the problem successfully (Table 8.3). As shown in the table, the error is consistent with $n\Delta t^2$. This created a high pressure response error norm (Figure 8.7). There were no surprises beyond that. The sequential method results were not shown here due to the sequential method's poor convergence ability. It was not possible to solve this problem using the sequential method.

This problem showed that Bendiksen's argument for simultaneous solutions for FSI problems is valid for this transient MMS problem. In addition, it verifies the transient LSFEM code for simultaneous solutions.

It is advantageous for future work to examine transient FSI using a space-time coupled approach such that the temporal discretization error would not factor into the solution. Only the LSFEM discretization would become a factor and it would be a pure examination into LSFEM FSI. Unfortunately, a space-time coupled approach here would require three-dimensional FEM where x, y and t would be the coordinates. Three-dimensional elements were not programmed into this code.

Response Type	Simultaneous
Fluid (Ω^F)	Ω^F Error
v_x^f	2.99420e-004
v_y^f	3.99616e-004
p	2.65711e-001
σ_x^f	2.41337e-003
σ_y^f	2.28175e-003
σ_{xy}^f	2.56883e-003
Structure (Ω^S)	Ω^S Error
u_x^s	2.50481e-004
u_y^s	6.73278e-004
σ_x^s	2.97778e-003
σ_y^s	5.45499e-003
σ_{xy}^s	2.02368e-003
v_x^s	1.05415e-003
v_y^s	6.03527e-003
Stress Equilibrium (Γ^{FS})	Γ^{FS} Error
p	8.00236e-001
σ_x^f	2.38161e-002
σ_y^f	2.19263e-002
σ_{xy}^f	3.33759e-002
σ_x^s	3.89135e-004
σ_y^s	3.89480e-003
σ_{xy}^s	1.77479e-003

Table 8.3 Error for Simultaneous Solutions for Transient MMS FSI Problem Using 100 Time Steps (t=1.00 secs, 100 Elements with p-value of 4)

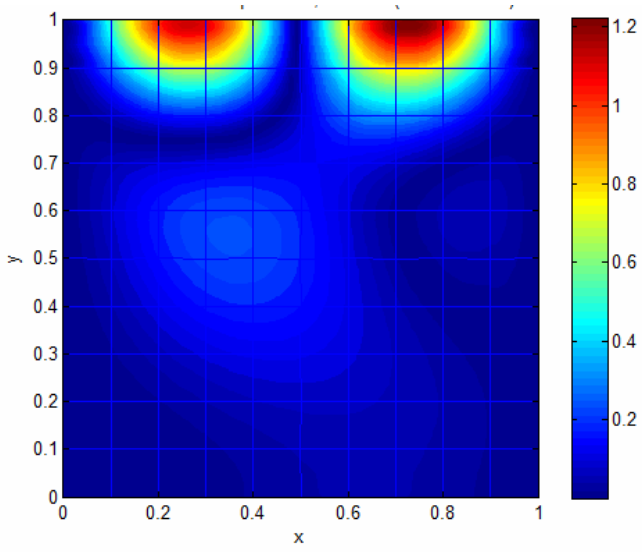

Figure 8.7 Pressure Error Plot for Transient MMS Problem (T=1.00 *sec*)

Implementing such a thing would provide benefit in future examinations of LSFEM FSI.

8.1.7 Dependence on Balanced Domain Residual Weights With Respect to Time Step Size. The next analysis examined how balanced residual weights depend on the size of Δt. Residual weight dependence on h-values, p-values, and property values such as Modulus of Elasticity have been examined. All these cases showed little to no dependence on those values. Figure 8.8 also shows that there is also no dependence on the size of the time step.

The next examination into residual weights involved how residual weights change as time progresses. Figure 8.9 shows how the residual weights change through time. This was performed on the MMS problem to 0.25 *sec*. All residual domain weights exhibited only a slight change with time. The weights change abruptly at the beginning but smooth out with only slight changes afterwards.

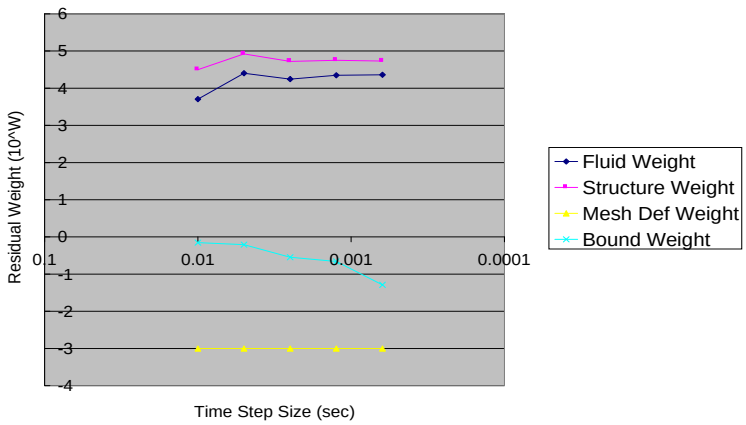

Figure 8.8 Residual Weight Dependence on Δt for Transient MMS Problem

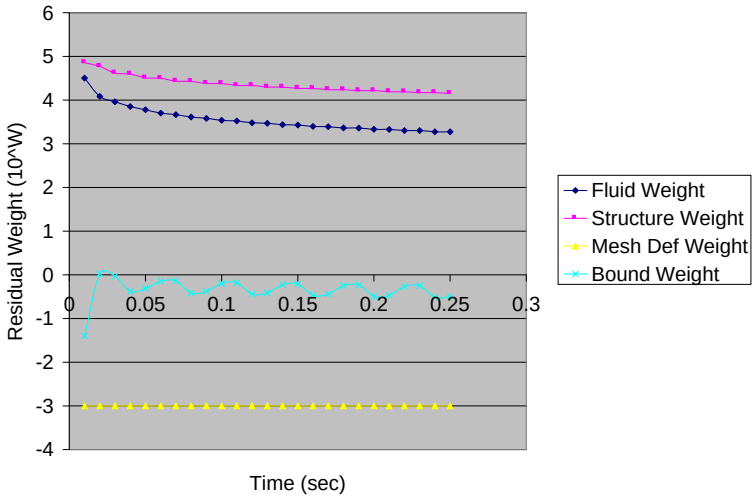

Figure 8.9 Residual Weight Evolution Through Time for Transient MMS Problem

8.2 Example Transient Collapsible Tube FSI Problem

The collapsible tube problem was attempted using transient FSI methods. The same problem conditions as those shown in Section 7.6 were used here except the external pressure was 1.667 and the velocity boundary conditions at the interface wall must match

$$\left[v_x^f, v_y^f\right] = \frac{\partial R_w}{\partial t} \tag{8.3}$$

The same transient simultaneous solution methods as those used for the above transient MMS problem were used here. Unfortunately, the problem was not able to converge for various time step sizes. The problem exhibited highly oscillatory deformations. In addition, the deformation were so large that the mesh would cross itself and create "negative space". Despite several attempts, convergence was never reached. It is unknown where the source of this error originated. It could be a result of highly nonlinear behavior, inadequate solution methods, improper problem formulation, or inadequate code.

IX. Conclusions

9.1 Research Goals

The main objective of this research was to compare the least-squares finite element method to other commonly used methods and implement the least-squares finite element formulation for simultaneously coupled FSI problems. This was achieved by first comparing the least-squares finite element method to other traditional numerical methods such as finite differencing and Weak Galerkin finite element methods and, second, by comparing the simultaneously coupled fluid structure interaction method to a sequentially coupled method. It was demonstrated that each unique capability required to accomplish a transient gust analysis for the joined-wing sensor-craft was feasible and accurate. This provided a "proof of technology" for the least-squares finite element method in the context of FSI. In addition, challenging problems were used for both steady-state and transient FSI with a known analytic solution and a LSFEM simultaneous solution was successful in solving those problems. It was shown that LSFEM is comparable to other common methods and it is an accurate method to use for FSI problems.

9.2 Research Contributions

The work completed here had new and unique aspects relevant to the aerospace research community. Contemporary research has been completed in the area of LSFEM formulations for FSI problems [23,24]. However, those researchers had limited success. Although they succeeded in examining various formulations of fluid and structural LSFEM and in examining linear steady-state LSFEM FSI, they had great difficulty solving complex and nonlinear steady-state FSI problems, transient FSI problems, and transient structural problems using LSFEM in either a simultaneous or sequential formulation. The research presented here overcame those obstacles by implementing an iterative residual balancing method. This method was a critical

aspect of successfully solving FSI via LSFEM. A unique residual weight balancing scheme was created that roughly doubled the computational expense but was capable of finding the residual weights necessary to solve transient structure problems, complex and nonlinear steady-state FSI problems, and nonlinear transient FSI problems.

Other essential ideas and comparisons were also shown through this research. LSFEM is comparable to WGFEM for structures and finite differencing for fluids. LSFEM exhibited better error values and convergence rates, relative to WGFEM, for the secondary variables. Those secondary variables are commonly used for equilibrium in FSI problems. LSFEM exhibited solid accuracy for incompressible Navier-Stokes and for linear Stokes analysis. LSFEM did not perform as well as finite differencing for a compressible Euler problem since it could not match peak values at key points within the problem but it was able to match the rest of the problem closely. In addition, LSFEM is a highly capable method for nonconformal meshing, which is a practical necessity for FSI. Nonconformal meshing works well with LSFEM due to the boundary integral that is a natural feature of the least-squares formulation. Overall, LSFEM is a flexible method capable of handling many different types of analyses using a single "black-box". It was shown that LSFEM can be used accurately for fluids, structures, boundary interface relationships, weak boundary conditions, and nonconformal meshes in either a sequential or simultaneous scheme for steady-state problems or a simultaneous scheme for transient problems.

9.3 Summary of Code Verifications Performed

A major task that was required before any comparisons or key abilities were demonstrated was to verify each portion of the code used within this research. Many problems were completed so that the code could be verified properly. If an exact solution was known throughout the analysis domain, refinement curves of response

errors relative to the analytic response were created for that problem to provide verification.

The first task performed was to verify the one-dimensional and two-dimensional basic LSFEM code. A simple one-dimensional Euler-Bernoulli beam problem and a simple two-dimensional Poisson's problem provided exact solutions for comparison. These problems were solved using LSFEM code successfully. Although extraordinarily simple, these examples laid the foundation for the code to solve other steady-state problem types. The next problem consisted of a simple one-dimensional wave problem. This problem was transient in nature and provided a way for the code to be verified using temporal derivatives. Space-time coupled and decoupled formulations were both verified for the one-dimensional wave problem.

Structural formulations were fully tested and verified here. A nonlinear Euler Bernoulli beam problem was solved successfully for a steady-state case by comparing results taken from Reddy's nonlinear FEM textbook [11]. After that, three problems using two-dimensional in-plane elasticity were analyzed. For the first problem, Timoshenko and Goodier provided an exact solution for comparison purposes [61]. The second problem was created using the method of manufactured solutions [64]. Since this problem was manufactured, the exact solution was known for comparison purposes. Refinement curves were created for these two problems where the convergence rates met or were near minimum criteria. In addition, WGFEM code was verified using the manufactured elasticity problem.

After the steady-state structural problems were verified using both WGFEM and LSFEM code, the transient realm was examined for structures. Unique residual weight balancing was required to obtain proper solutions for a simple clamped-clamped beam problem with an initial velocity applied. Once the iterative residual weight balancing scheme was applied, the proper weights were determined for this problem using four different types of analysis. A linear beam, a nonlinear beam,

in-plane elasticity using LSFEM and in-plane elasticity using WGFEM were used successfully for this transient problem.

Fluid formulations were also fully tested here. First, to continue testing the transient LSFEM code, a one-dimensional shock-tube problem was solved successfully using compressible and inviscid Euler equations. The shock tube problem also verified the coupled and decoupled space-time formulations for transient LSFEM by comparison with commonly published results [9]. After that, a classic airfoil in uniform flow with an angle of attack was considered. LSFEM results were compared to results obtained from finite volume code and to experimental data provided from other published works [68]. A linear fluid was also examined here. Stokes flow, which is good for creeping flow, was used to solve a driven cavity flow problem. This problem had published results for comparison purposes [9]. The results matched those published results. Incompressible and viscous Navier-Stokes equations were then verified. A Blasius plate problem was considered where the boundary layer thickness matched. In addition, Navier-Stokes equations were verified for a driven Poiseuille flow problem and for a manufactured problem. The next step was to verify Euler ALE and Navier-Stokes ALE approaches. A problem with a moving internal mesh was examined using uniform flow. The mesh was deformed with a prescribed transient motion. Even though the mesh deformed, the uniform flow did not change. This verified ALE for both fluid formulations.

Nonconformal meshing was also examined. Three problems were successfully solved using nonconformal meshes. The first consisted of Poisson's problem where the domain and the weak boundary conditions had different meshes. The second consisted of the manufactured structural problem with the domain split into two separate meshes that were joined in the middle through nonconformal meshing. The third problem consisted of a steady-state FSI problem that was created using MMS. All three problems showed accurate results even though a virtual interface was used to match boundary conditions or to match responses in the middle of a domain.

The next problems verified were coupled FSI problems. Three steady-state problems and one transient FSI problem were solved successfully. The first problem was a driven cavity flow problem with a flexible right wall. This problem was solved using two-field and three-field coupled methods. Both methods demonstrated the implementation, but no published results exist and no analytic solution was known for comparison. For independent verification, two more steady-state FSI problems were considered with a known exact solution. A double channel flow problem with a known solution [74] at the interface boundary was solved successfully. The fluid flow was a simple driven Poiseuille flow and the structure was a linear Euler-Bernoulli beam. Even though this was a simple problem, residual weights were critical to solve this multi-domain problem. The iterative residual weight balancing scheme was required to successfully solve this problem using a simultaneous solver. The next steady-state problem solved was a manufactured FSI solution [64]. It had non-trivial boundary conditions and responses. It also provided a way to generate refinement curves for response errors, since the solution was known throughout the entire problem. It provided a way to fully verify the LSFEM code for simultaneous and sequential steady-state solutions. MMS was also applied to a transient FSI problem. It had transient boundary input and non-trivial body forces and responses throughout the system. It challenged the code's capability and computational speed. It too had a known analytic solution for comparison purposes. The transient FSI problem was solved successfully using both LSFEM-LSFEM and LSFEM-WGFEM schemes.

Overall, many problems were solved successfully using LSFEM. It was shown that LSFEM is a capable and accurate scheme but may not always provide the most efficient method when residual weights are critical to solving a particular problem.

9.4 Summary of Comparisons Performed

The comparisons performed within this research provided insight into the behavior of LSFEM for both single domain and multi-domain problems. LSFEM was compared to other commonly used numerical methods for both structures and fluids. Nonconformal mesh methods were compared to conformal mesh results. Residual weight balancing was examined where multiple methods were compared to determine accuracy and feasibility. Different shape function expansion bases were also considered when using LSFEM. Elliptic and non-elliptic formulation results were also compared. Finally, simultaneous and sequential solution methods were compared for coupled FSI problems.

The first major comparison included comparing LSFEM to WGFEM for in-plane elasticity. It was shown that LSFEM exhibited better values and a stronger convergence rate for the secondary structural variables. The convergence rate for WGFEM secondary variables was typically p whereas the LSFEM secondary variables convergence rate averaged $p + 0.8351$ which was nearly $p + 1$, the convergence rate shown for the primary variables for both the WGFEM and LSFEM analyses. Although, LSFEM did show better accuracy with respect to the secondary variables, it came at a cost of 2.5 times as many degrees of freedom. This cost provides benefit for coupled problems, such as FSI, since those secondary variables are directly sharable within a LSFEM scheme.

Elliptic and non-elliptic formulations were also considered here. It was shown that even though the guaranteed convergence rates for elliptic formulations is $p + 1$, which is one order greater than non-elliptic formulations (p), the results for non-elliptic formulations performed just as well as the elliptic formulations. This was shown for two structural problems. No proof currently exists to show that non-elliptic formulations can perform as well as elliptic results, but it has been shown here and elsewhere [15, 16, 18] that well-posed non-elliptic formulations may be just as capable. In many cases the non-elliptic formulations are posed in terms of pri-

mary and secondary variables that are useful for most boundary conditions and for most coupled problems. Therefore, these primitive variable formulations are recommended for FSI despite being non-elliptic.

With the assistance of Wickert [63], it was shown that the shape function basis used for a FEM approximation can affect accuracy and efficiency of an FEM scheme. Serendipity shape functions were compared to full-tensor product shape functions. As expected, the serendipity expansion basis was more efficient. There are situations with the serendipity expansion basis where a higher p-value can be used with a coarse mesh and achieve the same level of accuracy. However, when the same p-value was used with the same mesh size, the full-tensor product expansion basis was more accurate.

Nonconformal mesh methods were compared to conformal meshes conditions. It was shown that the nonconformal meshing using the methods prescribed here are accurate and comparable to conformal mesh conditions. When a problem is solved using two different meshes, the mesh with the lower accuracy will dominate the entire domain's accuracy. For example, if the same p-value is used throughout, but different mesh sizes are used, the coarser mesh will drive the error and will "corrupt" the finer mesh. In addition, if different p-values are used for different meshes and the degrees of freedom are the same on each side, or if the mesh sizes are exactly the same at the boundary, the mesh with the lower p-value will drive the error of the entire solution.

LSFEM was compared to finite differencing for a classic airfoil fluid flow problem. The results showed similar accuracy with respect to the pressure profile on the surface of the airfoil. However, finite volume results were shown to reach a higher peak on the front top edge of the airfoil and matched the peak of experimental results closely. It was also shown that the LSFEM solution was very sensitive to residual weights with respect to the fluid domain and the no-penetration boundary conditions on the surface of the airfoil. Even though sufficiently accurate results

were achieved using LSFEM, they were not quite as good as finite volume results. Iterative residual weight balancing methods did not work for this fluid problem, so manual methods were used to determine proper weights. It might be a case where the proper residual weights were not found. If they were found, LSFEM might be as accurate finite volume methods. On the other hand, Navier-Stokes did produce accurate results for several individual fluid and FSI problems. Proper weights were successfully determined using iterative residual weight balancing methods. This may very well be a case where proper LSFEM residual weights are critical to accuracy. If proper weights are not determined, then the accuracy of LSFEM is questionable.

It was shown that some simultaneous LSFEM problems are capable of being solved accurately without the need to modify the residual weights. For example, it was shown that steady-state problems with simultaneously applied weak boundary conditions do not always require residual weight balancing. However, it was shown that transient cases and multi-domain cases need properly balanced residual weights or the problems will be completely inaccurate. Even if the problem uses time-marching to reach steady-state solutions, residual weight balancing is essential. Manual methods, iterative methods, unit modification methods, differential operator matrix normalization methods, no scaling, and move limit methods were examined to help find proper residual weights. It was shown that manual methods can work if the user already knows the solution beforehand. This is impractical and most problems require a "hands-off" method to determine the weights. The iterative method that uses domain averaging or equation pairing are the methods that seemed to work consistently without the need to know the exact solution beforehand. Unit modification, move limits, and matrix normalization methods did not work. In addition, weighting at the element level and at the single equation level will not always work as there are too many residual weights to balance. It was also shown that for steady-state cases, sequential solutions work without weighting. This was not necessarily the case for transient cases.

A steady-state FSI problem was solved sequentially using LSFEM for the fluid and then either LSFEM or WGFEM for the structure. The LSFEM-LSFEM case has the same level of accuracy as the simultaneous solution whereas the LSFEM-WGFEM case did not. A simultaneous solution was not considered with the LSFEM-WGFEM case, since proper residual weights could not be determined. This is because the WGFEM structural portion is governed by a different functional altogether. Relative to the L^2 error norm, it was shown that LSFEM-WGFEM is accurate but not nearly as accurate as the LSFEM-LSFEM scheme.

Per Bendiksen's proposal that simultaneous solutions are preferable to sequential solutions for FSI problems, simultaneous and sequential solutions were examined for both steady-state and transient scenarios [19]. It was shown that for steady-state cases that the simultaneous and sequential solutions are just as accurate and are just as efficient if the simultaneous weighting factors are known beforehand. This was true except for a highly nonlinear collapsible tube problem where a simultaneous solution was convergence whereas the sequential solution was not. If residual weights are not already known, the simultaneous solution requires much longer processing times in order to iteratively balance the residual weights. It was shown that the residual weights could be balanced on coarse meshes with low p-values and then those same weights could be used for more refined meshes and p-values for the same problem. It seems that avoiding residual weight balancing is beneficial for steady-state cases when sequential methods work perfectly well without the need for additional processing time. For the transient scenario, simultaneous solutions were shown to be much more accurate than sequential solutions. In fact, as time progressed, the sequential solution deteriorated where the solution was completely corrupt after only 25 time steps. The simultaneous case stayed at the accuracy of the temporal discretization through each time step and did not deteriorate beyond 25 time steps. This provided additional evidence that simultaneous coupled solutions do perform better than sequential coupled solutions, at least for transient scenarios.

9.5 Key Abilities Demonstrated That Are Traceable to Transient Gust Scenario

The joined-wing sensor-craft is considered a "grand-challenge" problem for FSI due to its nonlinear structural and aerodynamic behavior. Solving such a challenging problem requires a formulation with a number of unique capabilities:

1. Time-dependent nonlinear fluid dynamics
2. Time-dependent structures with geometric and follower force nonlinearities
3. Fully-coupled FSI
4. Complex model geometry
5. Time-accurate and complex mesh deformation
6. Accurately account for transient input
7. Arbitrary Lagrangian-Eulerian fluid schemes

Each of these capabilities were demonstrated successfully within this research and showed the feasibility of solving the transient and nonlinear gust scenario problem.

9.6 Issues With LSFEM

Simultaneous solutions of multi-domain and transient LSFEM problems were shown to be highly sensitive to residual weights. Inaccurate FSI solutions were shown when using unbalanced residual weights. This has also been the shown for other FSI problems solved by Kayser-Herold and Matthies [23]. Iterative residual error balancing methods were shown to work here, but it required a significant increase in computation time. The iterative residual balancing scheme took 4-20 times as many iterations to reach convergence when compared to a problem with preset residual weights.

Historically speaking, residual weight balancing has not been an issue for analysis based on energy principles. Traditional structural WGFEM solutions utilize the

Principle of Minimum Potential Energy. In these cases, the resulting equations are all of the same type (energy conservation only). In the LSFEM case, not all the equations are of the same type where the conservation equations could be based on mass, momentum, or energy. In addition, some equations in LSFEM could simply be a relationship between a response and its derivative. LSFEM can still utilize these equations accurately as long as matrix prioritization, that is, residual weighting is handled properly. The advantages of simultaneous solution methods are compromised unless the weighting difficulty is resolved.

LSFEM provides flexibility to the user to formulate various well-posed differential equations sets. This makes LSFEM capable for various types of physics. However, it seems that simultaneous LSFEM might not always be the best method due to the residual weight sensitivities for multi-domain problems. If no efficient "hands-off" method is available to determine balanced residual weights, then a multi-domain steady-state LSFEM problem should be solved in a sequential manner. As future work continues in the field of LSFEM, better methods may be created to balance residual weights. Until then, a sequential solution seems to be the preferred method to solve a unified LSFEM FSI problem, at least for steady problems.

Finally, dissipative results were observed for high-speed compressible fluids. This could become very problematic when considering transonic and supersonic regimes. Other work is on-going to examine methods to handle non-smooth results such as shocks. Jiang has examined utilizing LSFEM with h-adaptation around shock locations. The adaptation scheme refines mesh sizes around shock locations until the solution is refined to an acceptable level. Improved results were observed near the discontinuities [9]. Pontaza and Reddy have begun examining a discontinuous least-squares solution around predicted or known shock locations can improve responses around shocks [17].

9.7 Future Work

LSFEM is a very capable, accurate, and flexible methodology. Once it is implemented for one type of analysis, it is less difficult to add additional types. This is the ease of using a single "black-box" that is capable of performing analysis on both self-adjoint and non-self-adjoint equations and on both elliptic and non-elliptic systems of differential equations. Although Eason previously demonstrated its limitation [14], Pontaza and Reddy showed great success when they increased the p-value [18] and Jiang showed great success when reduced order integration was used [9]. Now, it seems that LSFEM is a limited scheme when transient structural problems and/or multiple domains are considered [23, 24]. An efficient solution to this problem is unknown at this time. An iterative solution method was shown to work well here, but it was computationally expensive. The benefit of LSFEM becomes questionable if a computationally expensive iterative residual weight balancing method is required for all multi-domain and transient structural problems. A reliable method to determine those weights is highly desirable and should be a focus of future LSFEM research.

Additional questions that should be answered include the theoretical mathematical nature of the balanced residual weights. What defines a correct weighting scheme? Are the balanced residual weights obtained through the iterative method the correct weights? Why does the residual weighting issue only arise for transient structural and multiple domain problems? Can weights be issues for other weighted integral methods such as Galerkin or collocation? These are questions that should be examined in future work of LSFEM.

More problems should be solved using a simultaneously coupled LSFEM approach. A few sample transient FSI problems to consider are a typical section airfoil [77] or a box with a flap problem [22]. These problems could be compared to traditional methods such as a WGFEM for the structure and a finite volume method for the fluid.

The unique approach of the least-squares approach has not been successfully applied to FSI problems before. Each unique capability required to solve the joined-wing transient gust problem was shown to be feasible here. The goal within this research was to show the feasibility of each of these capabilities and to compare their accuracy to other commonly used methods. These capabilities, proven to be feasible and accurate, lead to the detailed gust analysis of the joined-wing sensor-craft.

Appendix A. Code Structure

The code used in this research was written solely using Matlab. Matlab provided a great way of generating higher-order shape functions and it provided the toolboxes necessary to post-process almost any type of response. It also had the basic computing structure useful for scientific computing. The code consisted of 199 subroutines and functions. There were approximately 13,520 lines of code written.

Figure A.1 shows the code structure. This is a top-level basic description of the code only. There are many routines that have similar functions and are named similarly. Those functions are labeled with a "XXX" within the Figure to signify that several naming conventions exist for that particular type of a routine.

- Routine: LSFEM_master (*primary code*)
  - Task: Output Introduction (output version and notes to user)
  - Task: Specify Problem Type (*user specifies problem type which will set various parameters throughout*)
  - Task: Specify Options (*user specifies options such as max iterations, residual balancing scheme, plot type, etc.*)
  - Routine: shape_file_create (*create numerical Gauss quadrature samples for all domain's p-values*)
  - Loop: for # time steps (*continues until max time or steady-state is reached*)
    - Routine: LSFEM_master_mesh_specs (*generates meshes for each domain*)
      - Task: Specify Mesh Parameters (*user specifies various mesh parameters*)
      - Routine(s): sub_mesh_XXX (*generates mesh properties*)
    - Routine: LSFEM_master_ndf_initialize (*specifies # of response types for each analysis type*)
    - Routine: sub_develop_characteristics (*will generate characteristic unit scaling for each differential equation if user wants it*)
    - Routine: LSFEM_master_sharefields (*creates domain sharing properties*)
      - Routine(s): sub_share_spec_XXX (*generates sharing properties for particular problem type*)
    - Routine: LSFEM_master_nonlinear_initialize (*initializes DOFs for each domain*)
    - Loop: while not nonlinearly converged (*continues until max iterations or nonlinear convergence meets tolerance levels*)
      - Routine: sub_update_mesh (*updates mesh properties for deformable domains*)
      - Task: pre-allocate memory (*pre-allocates memory for K, F, and D for sparse or non-sparse matrices*)
      - Routine: gen2D_K or gen1D_K (depending on 1D or 2D domain, will generate K and F matrices and will apply BCs)
        - » Task: Pre-Allocate Memory (*pre-allocates memory for K, F, and D for sparse or non-sparse matrices*)
        - » Loop: for # elements (*completes tasks for each element*)
          - » Task: Specify Element's modes (*depending on bubble condensation options, will specify which modes and their respective DOFs to be used for that element*)
          - » Routine: gauss_quad or gauss_quad_1D (*performs gauss quadrature for that domain's number of gauss points*)
            - » Routine: Qp_ASi or Lp_ASi or Lp_BSi (*Applies differential operators for 2D, 1D, or nonconformal problems*)
          - » Task: Condense Bubble Modes (*will condense that element's bubble modes if options were specified*)
        - » Task: Assemble Global Matrices (*assembles each element matrices into domain's global matrices*)
        - » Task: Apply Boundary Conditions (*runs routines which create values for constrained degrees of freedom based on analysis type, grid format, and problem type*)
          - » Routine(s): sub_bc_XXX (*based on grid type and problem type, will apply basic rules for BCs*)
          - » Routine(s): sub_bc_assign_XXX_adv or sub_bc_assign_XXX (*applies BCs using generalized rules or hard coded rules*)
      - Task: Save K Matrices to Hard Drive (*saves large matrices to hard drive to save memory*)
      - Routine(s): sub_multiple_field_assembly or sub_single_field assembly (*assemble domain matrices simultaneously or sequentially*)
      - Routine: sub_rotate_original_dof (*directly rotates DOFs back if done earlier*)
      - Routine: sub_recover_bubble (*if condensed bubble modes, will recover them*)
      - Task: Generate Difference Between Nonlinear Iterations (*uses L2 norm to differentiate between nonlinear iterations*)
      - Routine: sub_residual_balancing (*creates new weighting rules based on iterative residual balancing methods*)
      - Task: Apply Underrelaxation (*applies nonlinear iterative underrelaxation rules if user specified*)
      - Task: Create DOFs for Next Iteration (*will generate new D matrices based on nonlinear and temporal convergence criteria*)
  - Routine(s): sub_post_generalizedwith_p or sub_post_generalized_with_p_1D (*creates plots for 2D or 1D problems*)
  - Routine(s) : gen2D_RES or gen1D_RES (*creates residual for each domain*)
  - Task: Save variables to hard drive and finish (*end program and save key variables*)

Figure A.1 Basic LSFEM Code Structure

Appendix B. LSFEM Differential Operators

B.1 Introduction

This appendix will provide the differential operators used to implement various LSFEM types of analysis. The differential operators (A) will be provided in the form

$$A_t \frac{\partial U}{\partial t} + A_1 \frac{\partial U}{\partial x} + A_2 \frac{\partial U}{\partial y} + A_0 U = f$$

where U is the vector of unknown response types and f is the vector of right hand side values. For the one-dimensional case, A_2 will not be provided since there is no y-direction. For the steady-state case, A_t will not be provided since there are no temporal derivatives. When a transient one-dimensional equation was considered, a space-time coupled approach was sometimes used. For that situation, the A_t matrix is simply converted to become the A_2 matrix and the y-coordinate will simply become a "t-coordinate". If a particular analysis type was considered using a space-time coupled scheme, it will be noted but the new matrices will not be shown.

B.2 One-Dimensional Equations

B.2.1 Boundary Condition Application. If a boundary condition was specified through a non-simple equation, it was typically applied weakly on a that boundary wall using LSFEM. In the case where some general response (u) equals some equation (g) at a given boundary, the relationship

$$u = g\left(x\right) \tag{B.1}$$

is applied using the following LSFEM operators:

$$A_1 = [0] \tag{B.2}$$

$$A_0 = [1] \tag{B.3}$$

$$f = \{g\} \tag{B.4}$$

$$U = \{u\} \tag{B.5}$$

B.2.2 Wave Equation Elliptic Form. The elliptic form of the one-dimensional wave equation uses the following LSFEM operators:

$$A_1 = \begin{bmatrix} -c & 0 \\ 0 & -c \end{bmatrix} \tag{B.6}$$

$$A_0 = \begin{bmatrix} 0 & 0 \\ 0 & 0 \end{bmatrix} \tag{B.7}$$

$$A_t = \begin{bmatrix} 0 & 1 \\ 1 & 0 \end{bmatrix} \tag{B.8}$$

$$f = \begin{Bmatrix} 0 \\ 0 \end{Bmatrix} \tag{B.9}$$

$$U = \begin{Bmatrix} p \\ v \end{Bmatrix} \tag{B.10}$$

The responses shown here are both secondary. The primary variable (u) is a direct response. The non-elliptic form provides the primary variables directly. The space-time coupled form can be considered here.

B.2.3 Wave Equation Non-Elliptic Form. The non-elliptic form of the one-dimensional wave equation uses the following LSFEM operators

$$A_1 = \begin{bmatrix} 0 & -c & 0 \\ 0 & 0 & 0 \\ c & 0 & 0 \end{bmatrix} \tag{B.11}$$

$$A_0 = \begin{bmatrix} 0 & 0 & 0 \\ 0 & 0 & -1 \\ 0 & -1 & 0 \end{bmatrix} \tag{B.12}$$

$$A_t = \begin{bmatrix} 0 & 0 & 1 \\ 1 & 0 & 0 \\ 0 & 0 & 0 \end{bmatrix} \tag{B.13}$$

$$f = \begin{Bmatrix} 0 \\ 0 \\ 0 \end{Bmatrix} \tag{B.14}$$

$$U = \begin{Bmatrix} u \\ p \\ v \end{Bmatrix} \tag{B.15}$$

The space-time coupled form can be considered here.

B.2.4 Axial Bar. A simple axial bar was considered. The LSFEM operators are

$$A_1 = \begin{bmatrix} AE & 0 \\ 0 & -1 \end{bmatrix} \tag{B.16}$$

$$A_0 = \begin{bmatrix} 0 & -1 \\ 0 & 0 \end{bmatrix} \tag{B.17}$$

$$f = \left\{ \begin{array}{c} 0 \\ f_{axial} \end{array} \right\} \tag{B.18}$$

$$U = \left\{ \begin{array}{c} u \\ p \end{array} \right\} \tag{B.19}$$

B.2.5 Linear Euler-Bernoulli Beam. The steady-state form of the Euler-Bernoulli beam equations include

$$A_1 = \left[\begin{array}{cccc} 1 & 0 & 0 & 0 \\ 0 & EI & 0 & 0 \\ 0 & 0 & 1 & 0 \\ 0 & 0 & 0 & 1 \end{array} \right] \tag{B.20}$$

$$A_0 = \left[\begin{array}{cccc} 0 & -1 & 0 & 0 \\ 0 & 0 & -1 & 0 \\ 0 & 0 & 0 & -1 \\ 0 & 0 & 0 & 0 \end{array} \right] \tag{B.21}$$

$$f = \left\{ \begin{array}{c} 0 \\ 0 \\ 0 \\ q_{bend} \end{array} \right\} \tag{B.22}$$

$$U = \left\{ \begin{array}{c} w^s \\ \theta^s \\ M^s \\ V^s \end{array} \right\} \tag{B.23}$$

The transient form can also be completed here. The LSFEM operators are

$$A_1 = \begin{bmatrix} 1 & 0 & 0 & 0 & 0 \\ 0 & EI & 0 & 0 & 0 \\ 0 & 0 & 0 & 1 & 0 \\ 0 & 0 & 1 & 0 & 0 \\ 0 & 0 & 0 & 0 & 0 \end{bmatrix} \tag{B.24}$$

$$A_0 = \begin{bmatrix} 0 & -1 & 0 & 0 & 0 \\ 0 & 0 & 1 & 0 & 0 \\ 0 & 0 & 0 & 0 & 0 \\ 0 & 0 & 0 & -1 & 0 \\ 0 & 0 & 0 & 0 & -1 \end{bmatrix} \tag{B.25}$$

$$A_t = \begin{bmatrix} 0 & 0 & 0 & 0 & 0 \\ 0 & 0 & 0 & 0 & 0 \\ 0 & 0 & 0 & 0 & -\rho_s I_{inertia} \\ 0 & 0 & 0 & 0 & 0 \\ 1 & 0 & 0 & 0 & 0 \end{bmatrix} \tag{B.26}$$

$$f = \begin{Bmatrix} 0 \\ 0 \\ q_{bend} \\ 0 \\ 0 \end{Bmatrix} \tag{B.27}$$

$$U = \left\{ \begin{array}{c} w^s \\ \theta^s \\ V^s \\ M^s \\ v^s \end{array} \right\} \tag{B.28}$$

The space-time coupled form can be considered here.

B.2.6 Nonlinear Euler-Bernoulli Beam. The nonlinear form of the Euler-Bernoulli beam allows the axial direction to deform. Additional responses and equations are required. The steady-state matrix operators takes the form

$$A_1 = \begin{bmatrix} EA & \theta\frac{EA}{2} & 0 & 0 & 0 & 0 \\ 0 & 1 & 0 & 0 & 0 & 0 \\ 0 & 0 & EI & 0 & 0 & 0 \\ 0 & 0 & 0 & 1 & 0 & 0 \\ 0 & 0 & 0 & 0 & 1 & 0 \\ 0 & N & 0 & 0 & 0 & 1 \end{bmatrix} \tag{B.29}$$

$$A_0 = \begin{bmatrix} 0 & 0 & 0 & -1 & 0 & 0 \\ 0 & 0 & -1 & 0 & 0 & 0 \\ 0 & 0 & 0 & 0 & 0 & 1 \\ 0 & 0 & 0 & 0 & 0 & 0 \\ 0 & 0 & 0 & 0 & 0 & 0 \\ 0 & 0 & 0 & 0 & -1 & 0 \end{bmatrix} \tag{B.30}$$

$$f = \left\{ \begin{array}{c} 0 \\ 0 \\ 0 \\ f_{axial} \\ q_{bend} \\ 0 \end{array} \right\} \tag{B.31}$$

$$U = \left\{ \begin{array}{c} u^s \\ w^s \\ \theta^s \\ N^s \\ V^s \\ M^s \end{array} \right\} \tag{B.32}$$

The transient form takes the form

$$A_1 = \left[\begin{array}{cccccccc} EA & \theta\frac{EA}{2} & 0 & 0 & 0 & 0 & 0 & 0 \\ 0 & 1 & 0 & 0 & 0 & 0 & 0 & 0 \\ 0 & 0 & EI & 0 & 0 & 0 & 0 & 0 \\ 0 & 0 & 0 & 1 & 0 & 0 & 0 & 0 \\ 0 & 0 & 0 & 0 & 1 & 0 & 0 & 0 \\ 0 & N & 0 & 0 & 0 & 1 & 0 & 0 \\ 0 & 0 & 0 & 0 & 0 & 0 & 0 & 0 \\ 0 & 0 & 0 & 0 & 0 & 0 & 0 & 0 \end{array} \right] \tag{B.33}$$

$$A_0 = \begin{bmatrix} 0 & 0 & 0 & -1 & 0 & 0 & 0 & 0 \\ 0 & 0 & -1 & 0 & 0 & 0 & 0 & 0 \\ 0 & 0 & 0 & 0 & 0 & 1 & 0 & 0 \\ 0 & 0 & 0 & 0 & 0 & 0 & 0 & 0 \\ 0 & 0 & 0 & 0 & 0 & 0 & 0 & 0 \\ 0 & 0 & 0 & 0 & -1 & 0 & 0 & 0 \\ 0 & 0 & 0 & 0 & 0 & 0 & -1 & 0 \\ 0 & 0 & 0 & 0 & 0 & 0 & 0 & -1 \end{bmatrix} \tag{B.34}$$

$$A_t = \begin{bmatrix} 0 & 0 & 0 & 0 & 0 & 0 & 0 & 0 \\ 0 & 0 & 0 & 0 & 0 & 0 & 0 & 0 \\ 0 & 0 & 0 & 0 & 0 & 0 & 0 & 0 \\ 0 & 0 & 0 & 0 & 0 & 0 & -\rho_s A & 0 \\ 0 & 0 & 0 & 0 & 0 & 0 & 0 & -\rho_s I_{inertia} \\ 0 & 0 & 0 & 0 & 0 & 0 & 0 & 0 \\ 1 & 0 & 0 & 0 & 0 & 0 & 0 & 0 \\ 0 & 1 & 0 & 0 & 0 & 0 & 0 & 0 \end{bmatrix} \tag{B.35}$$

$$f = \begin{Bmatrix} 0 \\ 0 \\ 0 \\ f_{axial} \\ q_{bend} \\ 0 \\ 0 \\ 0 \end{Bmatrix} \tag{B.36}$$

$$U = \left\{ \begin{array}{c} u^s \\ w^s \\ \theta^s \\ N^s \\ V^s \\ M^s \\ v_x^s \\ v_y^s \end{array} \right\} \tag{B.37}$$

The space-time coupled form can be considered here.

B.2.7 Compressible Inviscid Euler Flow. The compressible and inviscid Euler flow equations takes the form

$$A_1 = \left[\begin{array}{ccc} \rho & 0 & v_x^f \\ v_x^f & \frac{1}{\rho} & 0 \\ p\gamma & v_x^f & 0 \end{array} \right] \tag{B.38}$$

$$A_0 = \left[\begin{array}{ccc} 0 & 0 & 0 \\ 0 & 0 & 0 \\ 0 & 0 & 0 \end{array} \right] \tag{B.39}$$

$$A_t = \left[\begin{array}{ccc} 0 & 0 & 1 \\ 1 & 0 & 0 \\ 0 & 1 & 0 \end{array} \right] \tag{B.40}$$

$$f = \left\{ \begin{array}{c} 0 \\ 0 \\ 0 \end{array} \right\} \tag{B.41}$$

$$U = \left\{ \begin{array}{c} v_x^f \\ p \\ \rho \end{array} \right\} \tag{B.42}$$

The space-time coupled form can be considered here.

B.2.8 Pressure Equilibrium On a Beam With Top and Bottom Fluid Flow. For a beam with a net pressure applied on the top and bottom of the structure, the LSFEM operators are

$$A_1 = \left[\begin{array}{ccc} 0 & 0 & -1 \end{array} \right] \tag{B.43}$$

$$A_0 = \left[\begin{array}{ccc} -1 & 1 & 0 \end{array} \right] \tag{B.44}$$

$$f = \left\{ \begin{array}{c} 0 \end{array} \right\} \tag{B.45}$$

$$U = \left\{ \begin{array}{c} p_{top} \\ p_{bot} \\ V^s \end{array} \right\} \tag{B.46}$$

B.2.9 Neumann-Type Stress Equilibrium Relationships. An FSI problem will typically contain Neumann-type boundary conditions where full stress and pressure equilibrium is applied at the boundary. Fluid pressures and stresses contribute to the equilibrium at the boundary with a structure where only the structure stresses play a role. The net stress equilibrium uses the following LSFEM operators:

$$A_1 = \left[\begin{array}{ccccccc} 0 & 0 & 0 & 0 & 0 & 0 & 0 \\ 0 & 0 & 0 & 0 & 0 & 0 & 0 \end{array} \right] \tag{B.47}$$

$$A_0 = \left[\begin{array}{ccccccc} -n_x & n_x & 0 & n_y & -n_x & 0 & -n_y \\ -n_y & 0 & n_y & n_x & 0 & -n_y & -n_x \end{array} \right] \tag{B.48}$$

$$f = \left\{ \begin{array}{c} 0 \\ 0 \end{array} \right\} \tag{B.49}$$

$$U = \left\{ \begin{array}{c} p \\ \sigma_x^f \\ \sigma_y^f \\ \sigma_{xy}^f \\ \sigma_x^s \\ \sigma_y^s \\ \sigma_{xy}^s \end{array} \right\} \tag{B.50}$$

Another form can be considered where the net forces can be generated for each domain. The fluid domain contains the following operators:

$$A_1 = \left[\begin{array}{cccccc} 0 & 0 & 0 & 0 & 0 & 0 \\ 0 & 0 & 0 & 0 & 0 & 0 \end{array} \right] \tag{B.51}$$

$$A_0 = \left[\begin{array}{cccccc} -n_x & n_x & 0 & n_y & -1 & 0 \\ -n_y & 0 & n_y & n_x & 0 & -1 \end{array} \right] \tag{B.52}$$

$$f = \left\{ \begin{array}{c} 0 \\ 0 \end{array} \right\} \tag{B.53}$$

$$U = \left\{ \begin{array}{c} p \\ \sigma_x^f \\ \sigma_y^f \\ \sigma_{xy}^f \\ \phi_x^f \\ \phi_y^f \end{array} \right\} \tag{B.54}$$

The structural domain contains the following operators

$$A_1 = \begin{bmatrix} 0 & 0 & 0 & 0 & 0 \\ 0 & 0 & 0 & 0 & 0 \end{bmatrix} \tag{B.55}$$

$$A_0 = \begin{bmatrix} -n_x & 0 & -n_y & 1 & 0 \\ 0 & -n_y & -n_x & 0 & 1 \end{bmatrix} \tag{B.56}$$

$$f = \begin{Bmatrix} 0 \\ 0 \end{Bmatrix} \tag{B.57}$$

$$U = \begin{Bmatrix} \sigma_x^s \\ \sigma_y^s \\ \sigma_{xy}^s \\ \phi_x^s \\ \phi_y^s \end{Bmatrix} \tag{B.58}$$

With the net forces generated (ϕ_x^f, ϕ_y^f, ϕ_x^s, ϕ_y^s) for each domain, the net values can be equated at the boundary using directly shared degrees of freedom (conformal) or use nonconformal equality relationships.

B.2.10 Angled Velocity or Displacement Transformation. An angled wall can provide a situation where the degrees of freedom must be converted to normal and tangential components. A no-penetration boundary condition is typically applied this way. Velocities or displacements can be converted using these equations using a constant normal angle (β) or a variable angle with respect to a generalized coordinate for that element ($\beta(\xi)$).

$$A_1 = \begin{bmatrix} 0 & 0 & 0 & 0 \\ 0 & 0 & 0 & 0 \end{bmatrix} \tag{B.59}$$

$$A_0 = \begin{bmatrix} \cos(\beta) & \sin(\beta) & -1 & 0 \\ \sin(\beta) & -\cos(\beta) & 0 & -1 \end{bmatrix} \tag{B.60}$$

$$f = \left\{ \begin{array}{c} 0 \\ 0 \end{array} \right\} \tag{B.61}$$

$$U = \left\{ \begin{array}{c} v_x^f \\ v_y^f \\ v_n^f \\ v_t^f \end{array} \right\} \tag{B.62}$$

B.2.11 Angled Stress Transformation. Stress can also be transformed at an angle. The LSFEM operators are

$$A_1 = \left[\begin{array}{cccccc} 0 & 0 & 0 & 0 & 0 & 0 \\ 0 & 0 & 0 & 0 & 0 & 0 \\ 0 & 0 & 0 & 0 & 0 & 0 \end{array} \right] \tag{B.63}$$

$$A_0 = \left[\begin{array}{cccccc} (\cos(\beta))^2 & (\sin(\beta))^2 & 2\cos(\beta)\sin(\beta) & -1 & 0 & 0 \\ (\sin(\beta))^2 & (\cos(\beta))^2 & -2\cos(\beta)\sin(\beta) & 0 & -1 & 0 \\ \cos(\beta)\sin(\beta) & -\cos(\beta)\sin(\beta) & (\sin(\beta))^2 - (\cos(\beta))^2 & 0 & 0 & -1 \end{array} \right] \tag{B.64}$$

$$f = \left\{ \begin{array}{c} 0 \\ 0 \\ 0 \end{array} \right\} \tag{B.65}$$

$$U = \left\{ \begin{array}{c} \sigma_x^s \\ \sigma_y^s \\ \sigma_{xy}^s \\ \sigma_n^s \\ \sigma_t^s \\ \sigma_{nt}^s \end{array} \right\} \tag{B.66}$$

B.2.12 Stress To Displacement-Gradient Relationship. When using the elliptic in-plane elasticity equations, a relationship that transforms stress to displacement-gradients must be used. The LSFEM operators are

$$A_1 = \begin{bmatrix} 0 & 0 & 0 & 0 & 0 & 0 & 0 \\ 0 & 0 & 0 & 0 & 0 & 0 & 0 \\ 0 & 0 & 0 & 0 & 0 & 0 & 0 \end{bmatrix} \tag{B.67}$$

$$A_0 = \begin{bmatrix} \frac{E}{1-\nu^2} & \frac{E\nu}{1-\nu^2} & 0 & 0 & -1 & 0 & 0 \\ \frac{E\nu}{1-\nu^2} & \frac{E}{1-\nu^2} & 0 & 0 & 0 & -1 & 0 \\ 0 & 0 & G & G & 0 & 0 & -1 \end{bmatrix} \tag{B.68}$$

$$f = \begin{Bmatrix} 0 \\ 0 \\ 0 \end{Bmatrix} \tag{B.69}$$

$$U = \begin{Bmatrix} H_1 \\ H_2 \\ H_3 \\ H_4 \\ \sigma_x^s \\ \sigma_y^s \\ \sigma_{xy}^s \end{Bmatrix} \tag{B.70}$$

B.2.13 Nonconformal Relationships. The nonconformal relationships can have any number of degree of freedoms that are supposed to equal at a boundary interface. The code and differential operators were created such that the user can specify any number of responses to be used within the nonconformal relationships.

As an example, the LSFEM differential operators are shown here for four responses:

$$A_1 = \begin{bmatrix} 0 & 0 & 0 & 0 & 0 & 0 & 0 & 0 \\ 0 & 0 & 0 & 0 & 0 & 0 & 0 & 0 \\ 0 & 0 & 0 & 0 & 0 & 0 & 0 & 0 \\ 0 & 0 & 0 & 0 & 0 & 0 & 0 & 0 \end{bmatrix} \tag{B.71}$$

$$A_0 = \begin{bmatrix} 1 & 0 & 0 & 0 & -1 & 0 & 0 & 0 \\ 0 & 1 & 0 & 0 & 0 & -1 & 0 & 0 \\ 0 & 0 & 1 & 0 & 0 & 0 & -1 & 0 \\ 0 & 0 & 0 & 1 & 0 & 0 & 0 & -1 \end{bmatrix} \tag{B.72}$$

$$f = \begin{Bmatrix} 0 \\ 0 \\ 0 \\ 0 \end{Bmatrix} \tag{B.73}$$

$$U = \begin{Bmatrix} u_1^A \\ u_2^A \\ u_3^A \\ u_4^A \\ u_1^B \\ u_2^B \\ u_3^B \\ u_4^B \end{Bmatrix} \tag{B.74}$$

B.3 Two-Dimensional Equations

B.3.1 Poisson's Equation. The non-elliptic form of the Poisson's equation is shown here. The LSFEM operators are

$$A_1 = \begin{bmatrix} -1 & 0 & 0 \\ 0 & 0 & 0 \\ 0 & -1 & 0 \end{bmatrix} \tag{B.75}$$

$$A_2 = \begin{bmatrix} 0 & 0 & 0 \\ -1 & 0 & 0 \\ 0 & 0 & -1 \end{bmatrix} \tag{B.76}$$

$$A_0 = \begin{bmatrix} 0 & 1 & 0 \\ 0 & 0 & 1 \\ 0 & 0 & 0 \end{bmatrix} \tag{B.77}$$

$$f = \begin{Bmatrix} 0 \\ 0 \\ f_p \end{Bmatrix} \tag{B.78}$$

$$U = \begin{Bmatrix} u \\ v_1 \\ v_2 \end{Bmatrix} \tag{B.79}$$

B.3.2 In-Plane Elasticity. In-plane elasticity can have many different forms. First, there is an elliptic (u-H) and non-elliptic (u-σ) form. Second, the equations can be transient or steady-state. Third, the equations can assume either plane-stress or plane-strain. The steady-state non-elliptic form will be shown first for both plane-stress and plane-strain. After that, all formulations shown will consider plane-stress assumptions. Then, the steady-state elliptic form will be shown. Finally, the transient non-elliptic form will be shown.

The steady-state non-elliptic form (u-σ) of the in-plane elasticity equations assuming plane-stress are

$$A_1 = \begin{bmatrix} 0 & 0 & 1 & 0 & 0 \\ 0 & 0 & 0 & 0 & 1 \\ -\frac{E}{1-\nu^2} & 0 & 0 & 0 & 0 \\ -\frac{E\nu}{1-\nu^2} & 0 & 0 & 0 & 0 \\ 0 & -G & 0 & 0 & 0 \end{bmatrix} \tag{B.80}$$

$$A_2 = \begin{bmatrix} 0 & 0 & 0 & 0 & 1 \\ 0 & 0 & 0 & 1 & 0 \\ 0 & -\frac{E\nu}{1-\nu^2} & 0 & 0 & 0 \\ 0 & -\frac{E}{1-\nu^2} & 0 & 0 & 0 \\ -G & 0 & 0 & 0 & 0 \end{bmatrix} \tag{B.81}$$

$$A_0 = \begin{bmatrix} 0 & 0 & 0 & 0 & 0 \\ 0 & 0 & 0 & 0 & 0 \\ 0 & 0 & 1 & 0 & 0 \\ 0 & 0 & 0 & 1 & 0 \\ 0 & 0 & 0 & 0 & 1 \end{bmatrix} \tag{B.82}$$

$$f = \begin{Bmatrix} -f_x \\ -f_y \\ 0 \\ 0 \\ 0 \end{Bmatrix} \tag{B.83}$$

$$U = \left\{ \begin{array}{c} u_x^s \\ u_y^s \\ \sigma_x^s \\ \sigma_y^s \\ \sigma_{xy}^s \end{array} \right\} \tag{B.84}$$

The plane-strain equations are

$$A_1 = \left[\begin{array}{ccccc} 0 & 0 & 1 & 0 & 0 \\ 0 & 0 & 0 & 0 & 1 \\ -\frac{E(1-\nu)}{(1+\nu)(1-2\nu)} & 0 & 0 & 0 & 0 \\ -\frac{E\nu}{(1+\nu)(1-2\nu)} & 0 & 0 & 0 & 0 \\ 0 & -G & 0 & 0 & 0 \end{array} \right] \tag{B.85}$$

$$A_2 = \left[\begin{array}{ccccc} 0 & 0 & 0 & 0 & 1 \\ 0 & 0 & 0 & 1 & 0 \\ 0 & -\frac{E\nu}{(1+\nu)(1-2\nu)} & 0 & 0 & 0 \\ 0 & -\frac{E(1-\nu)}{(1+\nu)(1-2\nu)} & 0 & 0 & 0 \\ -G & 0 & 0 & 0 & 0 \end{array} \right] \tag{B.86}$$

$$A_0 = \left[\begin{array}{ccccc} 0 & 0 & 0 & 0 & 0 \\ 0 & 0 & 0 & 0 & 0 \\ 0 & 0 & 1 & 0 & 0 \\ 0 & 0 & 0 & 1 & 0 \\ 0 & 0 & 0 & 0 & 1 \end{array} \right] \tag{B.87}$$

$$f = \left\{ \begin{array}{c} -f_x \\ -f_y \\ 0 \\ 0 \\ 0 \end{array} \right\} \tag{B.88}$$

$$U = \left\{ \begin{array}{c} u_x^s \\ u_y^s \\ \sigma_x^s \\ \sigma_y^s \\ \sigma_{xy}^s \end{array} \right\} \tag{B.89}$$

The steady-state elliptic (u-H) formulation assuming plane-stress has the following differential operators:

$$A_1 = \left[\begin{array}{cccccc} 0 & 0 & \frac{E}{1-\nu^2} & \frac{E\nu}{1-\nu^2} & 0 & 0 \\ 0 & 0 & 0 & 0 & G & G \\ 1 & 0 & 0 & 0 & 0 & 0 \\ 0 & 0 & 0 & 0 & 0 & 0 \\ 0 & 0 & 0 & 0 & 0 & 0 \\ 0 & 1 & 0 & 0 & 0 & 0 \\ 0 & 0 & 0 & 1 & 0 & 0 \\ 0 & 0 & 0 & 0 & -1 & 0 \end{array} \right] \tag{B.90}$$

$$A_2 = \begin{bmatrix} 0 & 0 & 0 & 0 & G & G \\ 0 & 0 & \frac{E\nu}{1-\nu^2} & \frac{E}{1-\nu^2} & 0 & 0 \\ 0 & 0 & 0 & 0 & 0 & 0 \\ 0 & 1 & 0 & 0 & 0 & 0 \\ 1 & 0 & 0 & 0 & 0 & 0 \\ 0 & 0 & 0 & 0 & 0 & 0 \\ 0 & 0 & 0 & 0 & 0 & -1 \\ 0 & 0 & 1 & 0 & 0 & 0 \end{bmatrix} \tag{B.91}$$

$$A_0 = \begin{bmatrix} 0 & 0 & 0 & 0 & 0 & 0 \\ 0 & 0 & 0 & 0 & 0 & 0 \\ 0 & 0 & -1 & 0 & 0 & 0 \\ 0 & 0 & 0 & -1 & 0 & 0 \\ 0 & 0 & 0 & 0 & -1 & 0 \\ 0 & 0 & 0 & 0 & 0 & -1 \\ 0 & 0 & 0 & 0 & 0 & 0 \\ 0 & 0 & 0 & 0 & 0 & 0 \end{bmatrix} \tag{B.92}$$

$$f = \begin{Bmatrix} -f_x \\ -f_y \\ 0 \\ 0 \\ 0 \\ 0 \\ 0 \\ 0 \end{Bmatrix} \tag{B.93}$$

$$U = \left\{ \begin{array}{c} u_x^s \\ u_y^s \\ H_1 \\ H_2 \\ H_3 \\ H_4 \end{array} \right\} \tag{B.94}$$

The transient form of the u-σ formulation assuming plane-stress is

$$A_1 = \left[\begin{array}{ccccccc} 0 & 0 & 1 & 0 & 0 & 0 & 0 \\ 0 & 0 & 0 & 0 & 1 & 0 & 0 \\ 0 & 0 & 0 & 0 & 0 & -\frac{E}{1-\nu^2} & 0 \\ 0 & 0 & 0 & 0 & 0 & -\frac{E\nu}{1-\nu^2} & 0 \\ 0 & 0 & 0 & 0 & 0 & 0 & -G \\ 0 & 0 & 0 & 0 & 0 & 0 & 0 \\ 0 & 0 & 0 & 0 & 0 & 0 & 0 \end{array} \right] \tag{B.95}$$

$$A_2 = \left[\begin{array}{ccccccc} 0 & 0 & 0 & 0 & 1 & 0 & 0 \\ 0 & 0 & 0 & 1 & 0 & 0 & 0 \\ 0 & 0 & 0 & 0 & 0 & 0 & -\frac{E\nu}{1-\nu^2} \\ 0 & 0 & 0 & 0 & 0 & 0 & -\frac{E}{1-\nu^2} \\ 0 & 0 & 0 & 0 & 0 & -G & 0 \\ 0 & 0 & 0 & 0 & 0 & 0 & 0 \\ 0 & 0 & 0 & 0 & 0 & 0 & 0 \end{array} \right] \tag{B.96}$$

$$A_0 = \begin{bmatrix} 0 & 0 & 0 & 0 & 0 & 0 & 0 \\ 0 & 0 & 0 & 0 & 0 & 0 & 0 \\ 0 & 0 & 0 & 0 & 0 & 0 & 0 \\ 0 & 0 & 0 & 0 & 0 & 0 & 0 \\ 0 & 0 & 0 & 0 & 0 & 0 & 0 \\ 0 & 0 & 0 & 0 & 0 & 1 & 0 \\ 0 & 0 & 0 & 0 & 0 & 0 & 1 \end{bmatrix} \tag{B.97}$$

$$A_t = \begin{bmatrix} 0 & 0 & 0 & 0 & 0 & -\rho_s & 0 \\ 0 & 0 & 0 & 0 & 0 & 0 & -\rho_s \\ 0 & 0 & 1 & 0 & 0 & 0 & 0 \\ 0 & 0 & 0 & 1 & 0 & 0 & 0 \\ 0 & 0 & 0 & 0 & 1 & 0 & 0 \\ -1 & 0 & 0 & 0 & 0 & 0 & 0 \\ 0 & -1 & 0 & 0 & 0 & 0 & 0 \end{bmatrix} \tag{B.98}$$

$$f = \begin{Bmatrix} -f_x \\ -f_y \\ 0 \\ 0 \\ 0 \end{Bmatrix} \tag{B.99}$$

$$U = \begin{Bmatrix} u_x^s \\ u_y^s \\ \sigma_x^s \\ \sigma_y^s \\ \sigma_{xy}^s \end{Bmatrix} \tag{B.100}$$

B.3.3 Stokes Fluid Flow. Stokes fluid flow is useful for creeping flow only. It is conveniently a linear system of fluid differential equations. Only the steady-

state form of the Stokes equations were examined in this research. The LSFEM operators for the v-p-ω formulation are

$$A_1 = \begin{bmatrix} 1 & 0 & 0 & 0 \\ 0 & 0 & 1 & 0 \\ 0 & 0 & 0 & -1 \\ 0 & -1 & 0 & 0 \end{bmatrix} \tag{B.101}$$

$$A_2 = \begin{bmatrix} 0 & 1 & 0 & 0 \\ 0 & 0 & 0 & 1 \\ 0 & 0 & 1 & 0 \\ 1 & 0 & 0 & 0 \end{bmatrix} \tag{B.102}$$

$$A_0 = \begin{bmatrix} 0 & 0 & 0 & 0 \\ 0 & 0 & 0 & 0 \\ 0 & 0 & 0 & 0 \\ 0 & 0 & 0 & 1 \end{bmatrix} \tag{B.103}$$

$$f = \begin{Bmatrix} 0 \\ f_x \\ f_y \\ 0 \end{Bmatrix} \tag{B.104}$$

$$U = \begin{Bmatrix} v_x^f \\ v_y^f \\ p \\ \omega \end{Bmatrix} \tag{B.105}$$

B.3.4 Incompressible Navier-Stokes Fluid Flow. The incompressible and viscous Navier-Stokes fluid flow can take two forms. The first form is the velocity-pressure-vorticity formulation (v-p-ω) and the second form is the velocity-pressure-

stress formulation (v-p-σ). Both forms will be shown here and were used within this research. In addition, both forms can easily switch between transient and steady-state form by adding or removing the temporal differential operator (A_t). The v-p-ω formulation has the following LSFEM differential operators:

$$A_1 = \begin{bmatrix} 1 & 0 & 0 & 0 \\ v_x^f & 0 & 1 & 0 \\ 0 & v_x^f & 0 & -\mu \\ 0 & -1 & 0 & 0 \end{bmatrix} \tag{B.106}$$

$$A_2 = \begin{bmatrix} 0 & 1 & 0 & 0 \\ v_y^f & 0 & 0 & \mu \\ 0 & v_y^f & 1 & 0 \\ 1 & 0 & 0 & 0 \end{bmatrix} \tag{B.107}$$

$$A_0 = \begin{bmatrix} 0 & 0 & 0 & 0 \\ 0 & 0 & 0 & 0 \\ 0 & 0 & 0 & 0 \\ 0 & 0 & 0 & 1 \end{bmatrix} \tag{B.108}$$

$$A_t = \begin{bmatrix} 0 & 0 & 0 & 0 \\ 1 & 0 & 0 & 0 \\ 0 & 1 & 0 & 0 \\ 0 & 0 & 0 & 0 \end{bmatrix} \tag{B.109}$$

$$f = \begin{Bmatrix} 0 \\ f_x \\ f_y \\ 0 \end{Bmatrix} \tag{B.110}$$

$$U = \left\{ \begin{array}{c} v_x^f \\ v_y^f \\ p \\ \omega \end{array} \right\} \tag{B.111}$$

The v-p-σ formulation has the following LSFEM differential operators:

$$A_1 = \left[\begin{array}{cccccc} 1 & 0 & 0 & 0 & 0 & 0 \\ v_x^f & 0 & 1 & -1 & 0 & 0 \\ 0 & v_x^f & 0 & 0 & 0 & -1 \\ -2\mu & 0 & 0 & 0 & 0 & 0 \\ 0 & 0 & 0 & 0 & 0 & 0 \\ 0 & -\mu & 0 & 0 & 0 & 0 \end{array} \right] \tag{B.112}$$

$$A_2 = \left[\begin{array}{cccccc} 0 & 1 & 0 & 0 & 0 & 0 \\ v_y^f & 0 & 0 & 0 & 0 & -1 \\ 0 & v_y^f & 1 & 0 & -1 & 0 \\ 0 & 0 & 0 & 0 & 0 & 0 \\ 0 & -2\mu & 0 & 0 & 0 & 0 \\ -\mu & 0 & 0 & 0 & 0 & 0 \end{array} \right] \tag{B.113}$$

$$A_0 = \left[\begin{array}{cccccc} 0 & 0 & 0 & 0 & 0 & 0 \\ 0 & 0 & 0 & 0 & 0 & 0 \\ 0 & 0 & 0 & 0 & 0 & 0 \\ 0 & 0 & 0 & 1 & 0 & 0 \\ 0 & 0 & 0 & 0 & 1 & 0 \\ 0 & 0 & 0 & 0 & 0 & 1 \end{array} \right] \tag{B.114}$$

$$A_t = \begin{bmatrix} 0 & 0 & 0 & 0 & 0 & 0 \\ 1 & 0 & 0 & 0 & 0 & 0 \\ 0 & 1 & 0 & 0 & 0 & 0 \\ 0 & 0 & 0 & 0 & 0 & 0 \\ 0 & 0 & 0 & 0 & 0 & 0 \\ 0 & 0 & 0 & 0 & 0 & 0 \end{bmatrix} \tag{B.115}$$

$$f = \begin{Bmatrix} 0 \\ f_x \\ f_y \\ 0 \\ 0 \\ 0 \end{Bmatrix} \tag{B.116}$$

$$U = \begin{Bmatrix} v_x^f \\ v_y^f \\ p \\ \sigma_x^f \\ \sigma_y^f \\ \sigma_{xy}^f \end{Bmatrix} \tag{B.117}$$

The ALE approaches were also considered here. The differential operators changed for both types of formulations (v-p-ω and v-p-σ). The v-p-ω formulation LSFEM operators are

$$A_1 = \begin{bmatrix} 1 & 0 & 0 & 0 \\ v_x^f - v_{x_g}^f & 0 & 1 & 0 \\ 0 & v_x^f - v_{x_g}^f & 0 & -\mu \\ 0 & -1 & 0 & 0 \end{bmatrix} \tag{B.118}$$

$$A_2 = \begin{bmatrix} 0 & 1 & 0 & 0 \\ v_y^f - v_{y_g}^f & 0 & 0 & \mu \\ 0 & v_y^f - v_{y_g}^f & 1 & 0 \\ 1 & 0 & 0 & 0 \end{bmatrix} \tag{B.119}$$

$$A_0 = \begin{bmatrix} 0 & 0 & 0 & 0 \\ 0 & 0 & 0 & 0 \\ 0 & 0 & 0 & 0 \\ 0 & 0 & 0 & 1 \end{bmatrix} \tag{B.120}$$

$$A_t = \begin{bmatrix} 0 & 0 & 0 & 0 \\ 1 & 0 & 0 & 0 \\ 0 & 1 & 0 & 0 \\ 0 & 0 & 0 & 0 \end{bmatrix} \tag{B.121}$$

$$f = \begin{Bmatrix} 0 \\ f_x \\ f_y \\ 0 \end{Bmatrix} \tag{B.122}$$

$$U = \begin{Bmatrix} v_x^f \\ v_y^f \\ p \\ \omega \end{Bmatrix} \tag{B.123}$$

The v-p-σ formulation LSFEM operators are

$$A_1 = \begin{bmatrix} 1 & 0 & 0 & 0 & 0 & 0 \\ v_x^f - v_{x_g}^f & 0 & 1 & -1 & 0 & 0 \\ 0 & v_x^f - v_{x_g}^f & 0 & 0 & 0 & -1 \\ -2\mu & 0 & 0 & 0 & 0 & 0 \\ 0 & 0 & 0 & 0 & 0 & 0 \\ 0 & -\mu & 0 & 0 & 0 & 0 \end{bmatrix} \tag{B.124}$$

$$A_2 = \begin{bmatrix} 0 & 1 & 0 & 0 & 0 & 0 \\ v_y^f - v_{y_g}^f & 0 & 0 & 0 & 0 & -1 \\ 0 & v_y^f - v_{y_g}^f & 1 & 0 & -1 & 0 \\ 0 & 0 & 0 & 0 & 0 & 0 \\ 0 & -2\mu & 0 & 0 & 0 & 0 \\ -\mu & 0 & 0 & 0 & 0 & 0 \end{bmatrix} \tag{B.125}$$

$$A_0 = \begin{bmatrix} 0 & 0 & 0 & 0 & 0 & 0 \\ 0 & 0 & 0 & 0 & 0 & 0 \\ 0 & 0 & 0 & 0 & 0 & 0 \\ 0 & 0 & 0 & 1 & 0 & 0 \\ 0 & 0 & 0 & 0 & 1 & 0 \\ 0 & 0 & 0 & 0 & 0 & 1 \end{bmatrix} \tag{B.126}$$

$$A_t = \begin{bmatrix} 0 & 0 & 0 & 0 & 0 & 0 \\ 1 & 0 & 0 & 0 & 0 & 0 \\ 0 & 1 & 0 & 0 & 0 & 0 \\ 0 & 0 & 0 & 0 & 0 & 0 \\ 0 & 0 & 0 & 0 & 0 & 0 \\ 0 & 0 & 0 & 0 & 0 & 0 \end{bmatrix} \tag{B.127}$$

$$f = \left\{ \begin{array}{c} 0 \\ f_x \\ f_y \\ 0 \\ 0 \\ 0 \end{array} \right\} \tag{B.128}$$

$$U = \left\{ \begin{array}{c} v_x^f \\ v_y^f \\ p \\ \sigma_x^f \\ \sigma_y^f \\ \sigma_{xy}^f \end{array} \right\} \tag{B.129}$$

B.3.5 Compressible Inviscid Euler Fluid Flow. The compressible and inviscid Euler fluid flow equations use velocity, pressure, and density as system unknowns. Only the primal form was considered here. Similar to the incompressible form of the Navier-Stokes equations, the transient form is simply created by adding the A_t differential operator. The LSFEM operators are

$$A_1 = \left[\begin{array}{cccc} \rho & 0 & 0 & v_x^f \\ v_x^f & 0 & \frac{1}{\rho} & 0 \\ 0 & v_x^f & 0 & 0 \\ p\gamma & 0 & v_x^f & 0 \end{array} \right] \tag{B.130}$$

$$A_2 = \left[\begin{array}{cccc} 0 & \rho & 0 & v_y^f \\ v_y^f & 0 & 0 & 0 \\ 0 & v_y^f & \frac{1}{\rho} & 0 \\ 0 & p\gamma & v_y^f & 0 \end{array} \right] \tag{B.131}$$

$$A_0 = \begin{bmatrix} 0 & 0 & 0 & 0 \\ 0 & 0 & 0 & 0 \\ 0 & 0 & 0 & 0 \\ 0 & 0 & 0 & 0 \end{bmatrix} \tag{B.132}$$

$$A_t = \begin{bmatrix} 0 & 0 & 0 & 1 \\ 1 & 0 & 0 & 0 \\ 0 & 1 & 0 & 0 \\ 0 & 0 & 1 & 0 \end{bmatrix} \tag{B.133}$$

$$f = \begin{Bmatrix} 0 \\ f_x \\ f_y \\ 0 \end{Bmatrix} \tag{B.134}$$

$$U = \begin{Bmatrix} v_x^f \\ v_y^f \\ p \\ \rho \end{Bmatrix} \tag{B.135}$$

The ALE form was also considered here. The operators are

$$A_1 = \begin{bmatrix} \rho & 0 & 0 & v_x^f - v_{x_g}^f \\ v_x^f - v_{x_g}^f & 0 & \frac{1}{\rho} & 0 \\ 0 & v_x^f - v_{x_g}^f & 0 & 0 \\ p\gamma & 0 & v_x^f - v_{x_g}^f & 0 \end{bmatrix} \tag{B.136}$$

$$A_2 = \begin{bmatrix} 0 & \rho & 0 & v_y^f - v_{y_g}^f \\ v_y^f - v_{y_g}^f & 0 & 0 & 0 \\ 0 & v_y^f - v_{y_g}^f & \frac{1}{\rho} & 0 \\ 0 & p\gamma & v_y^f - v_{y_g}^f & 0 \end{bmatrix} \tag{B.137}$$

$$A_0 = \begin{bmatrix} 0 & 0 & 0 & 0 \\ 0 & 0 & 0 & 0 \\ 0 & 0 & 0 & 0 \\ 0 & 0 & 0 & 0 \end{bmatrix} \tag{B.138}$$

$$A_t = \begin{bmatrix} 0 & 0 & 0 & 1 \\ 1 & 0 & 0 & 0 \\ 0 & 1 & 0 & 0 \\ 0 & 0 & 1 & 0 \end{bmatrix} \tag{B.139}$$

$$f = \begin{Bmatrix} 0 \\ f_x \\ f_y \\ 0 \end{Bmatrix} \tag{B.140}$$

$$U = \begin{Bmatrix} v_x^f \\ v_y^f \\ p \\ \rho \end{Bmatrix} \tag{B.141}$$

Appendix C. Synthetic Elasticity Problem Exact Solution

The exact solution for the manufactured elasticity problem is shown here. A somewhat horizontal displacement field was assumed, i.e.,

$$u_x^s = (7x + x^7)cos(\pi y) \tag{C.1}$$

A vertical displacement was found such that f_x^s would equal zero by utilizing the force equilibrium equations. The vertical displacement was found to be

$$u_y^s = \frac{1}{-E\nu - G + G\nu^2}\left(\frac{\left(\frac{1}{8}(-G\pi^2 + G\pi^2\nu^2)x^8 + 7Ex^6 + \frac{1}{2}(-7G\pi^2 + 7G\pi^2\nu^2)x^2\right)}{\pi sin(\pi y)}\right) \tag{C.2}$$

The body forces are the left over right hand side values from the equilibrium equations. The horizontal body force was

$$f_x^s = 0 \tag{C.3}$$

and the vertical body force component was determined to be

$$\begin{aligned} f_y^s = \frac{E}{(1-\nu^2)}\left(\frac{1}{E\nu + G - G\nu^2}\left(\left(-1.2337G + 1.2337G\nu^2\right)x^8\right)x^2 sin(\pi y)\pi\right) \\ + \frac{E}{(1-\nu^2)}\left(7Ex^6 + \left(-34.5436G + 34.5436G\nu^2\right)\right)x^2 sin(\pi y)\pi \\ - \frac{\nu(7 + 7x^6)sin(\pi y)\pi}{E\nu + G - G\nu^2} \\ + G(-7 - 7x^6)sin(\pi y)\pi \\ - \frac{G}{E\nu + G - G\nu^2}\frac{(7(-9.8696G + 9.8696G\nu^2)x^6 + 210Ex944 - 69.0872G + 69.0872G\nu^2)}{\pi sin(\pi y)} \end{aligned} \tag{C.4}$$

The stresses were defined through the stress-displacement relationships The horizontal normal stress component was

$$\sigma_x^s = -\frac{E}{(1-\nu^2)}\left(\left(\frac{\nu}{E\nu+G-G\nu^2}\right)\left(\frac{1}{8}(-G\pi^2+G\pi^2\nu^2)x^8\right)cos(\pi y)\right)$$

$$-\frac{E}{(1-\nu^2)}\left(7Ex^6+\frac{1}{2}(-7G\pi^2+7G\pi^2\nu^2)x^2\right)cos(\pi y)$$

$$+\frac{E}{(1-\nu^2)}(7+7x^6)cos(\pi y) \tag{C.5}$$

The vertical normal stress component was

$$\sigma_y^s = \frac{E}{(1-\nu^2)}\left(-\frac{1}{E\nu+G-G\nu^2}+\nu(7+7x^6)cos(\pi y)\right)$$

$$+\frac{E}{(1-\nu^2)}\left(\frac{1}{8}(-G\pi^2+G\pi^2\nu^2)x^8+7Ex^6+\frac{1}{2}(-7G\pi^2+7G\pi^2\nu^2)x^2\right)cos(\pi y) \tag{C.6}$$

Finally, the shear stress was determined as

$$\sigma_{xy}^s = -G(7x+x^7)sin(\pi y)\pi$$

$$-\frac{G}{E\nu+G-G\nu^2}\frac{((-G\pi^2+G\pi^2\nu^2)x^7+42Ex^5+(-7G\pi^2+7G\pi^2\nu^2)x)}{\pi sin(\pi y)} \tag{C.7}$$

Appendix D. Method of Manufactured Solutions Applied to Fluid Structure Interaction Problems

The derived equations for the MMS FSI steady-state problem is shown here. The problem assumed that the final deformed boundary coordinates would be

$$1 + h\left(1 - \cos\left(2\pi x\right)\right) \tag{D.1}$$

on the top wall of the fluid domain (Figure D.1). The horizontal displacement was assumed to be

$$u_x^s = -\frac{y}{4} \tag{D.2}$$

The vertical displacement field was created such that the boundary deformation matched the bottom wall of the structural domain, i.e.,

$$u_y^s = (1 - y)\, h\left(1 - \cos\left(2\pi x\right)\right) \tag{D.3}$$

A value of $h = 0.03$ was assumed for this problem. The stresses relationships are then determined from the displacement equations:

$$\sigma_x^s = -\frac{1}{165} + \frac{1}{165}\cos(2\pi x) \tag{D.4}$$

$$\sigma_y^s = -\frac{2}{33} + \frac{2}{33}\cos(2\pi x) \tag{D.5}$$

$$\sigma_{xy}^s = -\frac{5}{22} + \frac{20}{11}(0.03 - 0.03y)\sin\left(2\pi x\right)\pi \tag{D.6}$$

A velocity field was created such that the divergence was zero across the entire fluid domain. In other words, mass continuity was forced throughout. The

horizontal velocity was determined as

$$v_x^f = (k+1)\, y^k \,(f-y) - k(y^{k-1}) * \left(\frac{f^2}{2} - \frac{y^2}{2}\right) \tag{D.7}$$

and the vertical velocity was determined to be

$$v_y^f = y^k \,(f-y)\, \frac{\partial f}{\partial x} \tag{D.8}$$

where the value k is an integer value picked by the user. A value of $k = 1$ produces a symmetric wall on the bottom of the fluid domain and a value of $k \geq 1$ produces a no-slip wall. A value of $k = 2$ was selected for this problem. The velocities were determined to be

$$v_x^f = 3y^2(1.03 - 0.03 * cos(2\pi x) - y) - 2y\left(\frac{1}{2}(1.03 - 0.03cos(2\pi x))^2 - \frac{1}{2}y^2\right) \tag{D.9}$$

$$v_y^f = 0.06y^2 * (1.03 - 0.03cos(2\pi x) - y)sin(2\pi x)\pi \tag{D.10}$$

The relationships for μ and p were created by enforcing equilibrium at the boundary:

$$\left(2\mu\frac{\partial u}{\partial x} - p\right) n_x + \mu\left(\frac{\partial u}{\partial y} + \frac{\partial v}{\partial x}\right) n_y = \sigma_x^s n_x + \sigma_{xy}^s n_y \tag{D.11}$$

$$\mu\left(\frac{\partial u}{\partial y} + \frac{\partial v}{\partial x}\right) n_x + \left(2\mu\frac{\partial v}{\partial y} - p\right) n_y = \sigma_{xy}^s n_x + \sigma_y^s n_y \tag{D.12}$$

This generates μ and p as functions of only x:

$$\mu = -2500000/11(14100sin(2\pi x)\pi + 900sin(2\pi x)\pi cos(2\pi x) - 62500 + 225\pi^2$$

$$-225\pi^2 cos(2\pi x)^2 - 54sin(2\pi x)\pi^3 + 54sin(2\pi x)\pi^3 cos(2\pi x)^2)/(66306250000$$

$$+477405000\pi^2 - 477000000\pi^2 cos(2\pi x)^2 - 3862500000cos(2\pi x) - 27810000cos(2\pi x)\pi^2$$

$$+27810000cos(2\pi x)^3\pi^2 + 56250000cos(2\pi x)^2 - 405000cos(2\pi x)^4\pi^2 + 859329\pi^4$$

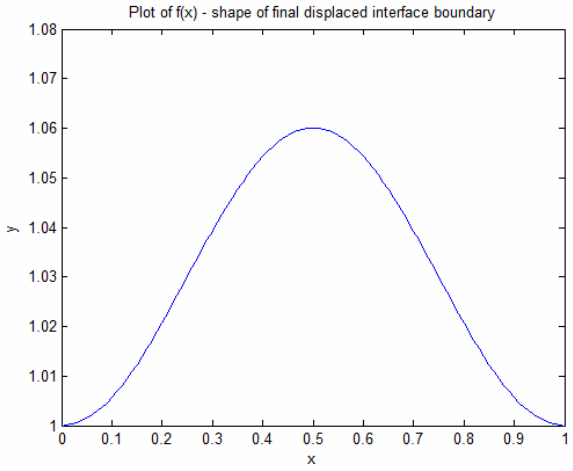

Figure D.1 Plot of Boundary Deformation

$$-1717929\pi^4 cos(2\pi x)^2 + 857871\pi^4 cos(2\pi x)^4 - 50058\pi^4 cos(2\pi x)$$

$$+100116\pi^4 cos(2\pi x)^3 - 50058\pi^4 cos(2\pi x)^5 + 729\pi^4 cos(2\pi x)^6) \quad \text{(D.13)}$$

$$p = -1/165(2709\pi^2 - 2709\pi^2 cos(2\pi x)^2 - 9cos(2\pi x)\pi^2 + 9cos(2\pi x)^3\pi^2$$

$$-11250sin(2\pi x)\pi + 25000 - 25000cos(2\pi x))/(-2500 - 9\pi^2 + 9\pi^2 cos(2\pi x)^2) \quad \text{(D.14)}$$

Figures D.2 and D.3 show the plots of μ and p, respectively.

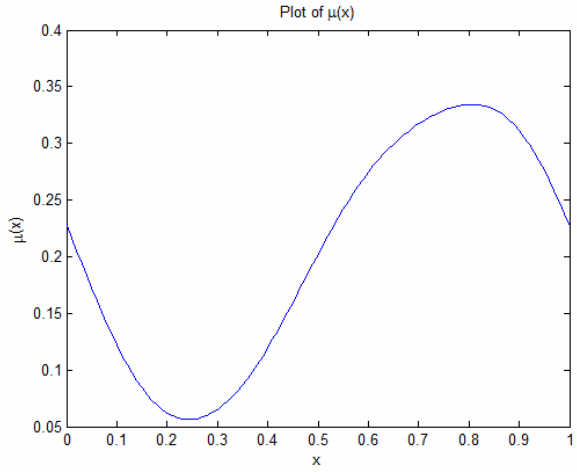

Figure D.2 Plot of Viscosity

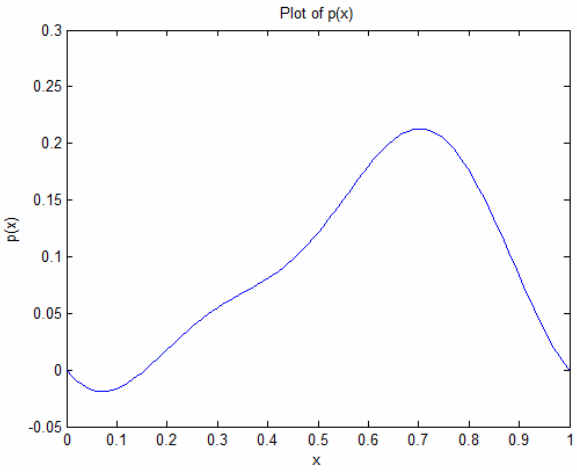

Figure D.3 Plot of Pressure

Bibliography

1. R. Roberts, R. Canfield, and M. Blair, "Joined-wing aeroelastic design with geometric nonlinearity," *Journal of Aircraft*, vol. 42, no. 4, pp. 832–848, 2005.
2. J. Wolkovich, "The joined wing: An overview," *Journal of Aircraft*, vol. 23, no. 3, pp. 161–178, 1986.
3. M. Blair and R. Canfield, "A joined-wing structural weight modeling study," No. AIAA-2002-1337, (Denver, CO), 43rd AIAA/ASME/ASCE/AHS/ASC Structures, Structural Dynamics and Materials Conference, April 2002.
4. M. Ryan, *Global Vigilance Reach and Power: America's Air Force Vision 2020*. Deptartment of the Air Force, 2001.
5. T. Lopez, "Capability assessment helps air force prepare for future." October 2005.
6. J. Jumper and J. Roche, *Air Force Handbook: 107th Congress, Second Session*. Department of the Air Force, 2002.
7. F. Johnson, "Sensorcraft-tomorrows eyes and ears of the warfighter," vol. 2, no. 1, pp. 10–11, 2001.
8. C. Rasmussen, "Joined-wing sensor-craft configuration design," Master's thesis, Graduate School of Engineering, Air Force Institute of Technology (AETC), Wright-Patterson AFB OH, March 2004. AFIT/GAE/ENY/04-M14.
9. B. Jiang, *The Least-Squares Finite Element Method*. Springer-Verlag New York, Inc., 1998.
10. S. Brenner and L. Scott, *The Mathematical Theory of Finite Element Methods*. Springer-Verlag New York, Inc., 2nd ed., 2002.
11. J. Reddy, *An Introduction to Nonlinear Finite Element Analysis*. Oxford Univeristy Press, 2004.
12. G. Smith, *Numerical Solution of Partial Differential Equations*. Oxford Univeristy Press, 3rd ed., 1985.
13. J. Reddy, *An Introduction to the Finite Element Method*. McGraw-Hill, 3rd ed., 2004.
14. E. Eason, "A review of least-squares method for solving partial differential equations," *International Journal for Numerical Methods in Engineering*, vol. 10, pp. 1021–1046, 1976.
15. J. Pontaza and J. Reddy, "Least-squares finite element formulation for shear-deformable shells," *Computational Methods of Applied Mechanical Engineering*, vol. 194, pp. 2464–2493, 2005.

16. J. Pontaza and J. Reddy, "Hierarchical least-squares shear-deformable shell elements," *International Journal for Numerical Methods in Engineering*, vol. 0, pp. 1–34, 2003.

17. J. Pontaza and J. Reddy, "Spectral/hp least-squares finite element formulation for the navier stokes equations," *Journal of Computational Physics*, vol. 190, pp. 523–549, 2003.

18. J. Pontaza and J. Reddy, "Mixed plate bending elements based on least-squares formulation," *International Journal for Numerical Methods in Engineering*, vol. 0, pp. 1–34, 2003.

19. O. Bendiksen, "Modern developments in computational aeroelasticity," *Journal of Aerospace Engineering*, vol. 218, pp. 157–177, 2004.

20. S. Weeratunga and E. Pramono, "Direct coupled aeroelastic analysis through concurrent time integration on a parallel computer," No. AIAA-1994-1550, (Hilton Head, SC), 35th AIAA/ASME/ASCE/AHS/ASC Structures, Structural Dynamics, and Materials Conference, April 1994.

21. G. Guruswamy, "A new modular approach for tightly coupled fluid/structure analysis," No. AIAA-2004-4547, (Albany, NY), 10th Multidisciplinary Analysis and Optimization Conference, August 2004.

22. B. Hubner, E. Walhorn, and D. Dinklier, "A monolithic approach to fluid-structure interaction using space-time finite elements," *Journal for Computer Methods in Applied Mechanics and Engineering*, vol. 193, pp. 2087–2104, 2004.

23. O. Kayser-Herold, "Least-squares methods for solution of fluid-structure interaction problems," Master's thesis, Institut fur Wiss. Rechnen, Technische Universitat, Braunschweig, Germany, January 2006 2006.

24. O. Kayser-Herold and H. Matthies, "A unified least-squares formulation for fluid-structure interaction problems," *Computers and Structures*, vol. 85, pp. 998–1011, 2007.

25. R. Jaiman, P. Geubelle, E. Loth, and X. Jiao, "Stable and accurate loosely-coupled scheme for unsteady fluid-structure interaction," No. AIAA-2007-334, (Reno, NV), 45th AIAA Aerospace Sciences Meeting and Exhibit, January 2007.

26. L. Crivelli and C. Farhat, "Implicit transient finite element structureal computations on mimd systems: Feti vs. direct solvers," No. AIAA-1993-1310, (La Jolla, CA), 34th AIAA/ASME/ASCE/AHS/ASC Structural Dynamics and Materials Conference, April 1993.

27. G. Karniadakis and S. Sherwin, *Spectral/hp Element Methods for Computational Fluid Dynamics*. Oxford Science Publications, 2nd ed., 2005.

28. J. Tannehill, D. Anderson, and R. Pletcher, *Computational Fluid Mechanics and Heat Transfer*. Hemisphere Publishing Corporation, 2nd ed., 1997.

29. J. Blazek, *Computational Fluid Dynamics: Principles and Applications*. Elsevier, 2nd ed., 2001.

30. J. Peraire, M. Vahdate, K. Morgan, and O. Zienkiewicz, "Adaptive remeshing for compressible flow computations," *Journal of Computational Physics*, vol. 72, pp. 449–466, 1987.

31. R. Lohner, "Adaptive remeshing for transient problems," *Computational Methods of Applied Mechanical Engineering*, vol. 75, pp. 195–214, 1989.

32. J. Baum, H. Luo, and R. Lohner, "A new ale adaptive unstructured methodology for the simulation of moving bodies," No. AIAA 1994-0414, (Reno, NV), 32nd Aerospace Sciences Meeting and Exhibit, January 1994.

33. C. Pettit and P. Beran, "Reduced order modeling for flutter prediction," No. AIAA-2000-1446, (Atlanta, GA), 41st AIAA/ASME/ASCE/AHS/ASC Structures, Structural Dynamics and Materials Conference, April 2000.

34. R. Kolonay, E. Thompson, J. Camberos, and F. Eastep, "Active control of transpiration boundary conditions for drag minimization with an euler cfd solver," No. AIAA-2007-1891, (Honolulu, HI), 48th AIAA/ASME/ASCE/AHS/ASC Structures, Structural Dynamics and Materials Conference, April 2007.

35. R. Bartels, "An elasticity-based mesh scheme applied to the computation of unsteady three-dimensional spoiler and aeroelastic problems," No. AIAA 1999-3301, (Norfolk, VA), Computational Fluid Dynamics Conference, June 1999.

36. D. Martineau and J. Georgala, "A mesh movement algorithm for high quality generalised meshes," No. AIAA 2004-614, (Reno, NV), 42nd Aerospace Sciences Meeting and Exhibit, January 2004.

37. P. Sackinger, P. Schunk, and R. Rao, "A newton-rhapson pseudo-solid domain mapping technique for free and moving boundary problems: A finite element implementation," *Journal of Computational Physics*, vol. 125, pp. 83–103, 1996.

38. S. Etienne, D. Pelletier, and A. Garon, "A monolithic formulation for unsteady fluid-structure interactions," No. AIAA-2006-0694, (Reno, NV), 44th AIAA Aerospace Sciences Meeting and Exhibit, January 2006.

39. G. Anagnostou, A. Patera, Y. Maday, and C. Mavriplis, "On the mortar element method - generalizations and implementation," (Houston, TX), 3rd Annual International Symposium on Domain Decomposition Methods for Partial Differential Equations, March 1989.

40. P. Seshaiyer and M. Suri, "Uniform hp convergence results for the mortar finite element method," *Mathematics of Computation*, vol. 69, no. 230, pp. 521–546, 1999.

41. F. Belgacem, L. Chilton, and P. Seshaiyer, "The hp-mortar finite-element method for the mixed elasticity and stokes problems," *Computers and Mathematics with Applications*, vol. 46, pp. 35–55, 2003.

42. E. Swim and P. Seshaiyer, "A nonconforming finite element method for fluid-structure interaction problems," *Computer Methods in Applied Mechanics and Engineering*, vol. 195, pp. 2088–2099, 2006.

43. R. Cook, *Concepts and Applications of Finite Element Analysis*. John Wiley and Sons, Inc., 4th ed., 2002.

44. V. Tan and T. Belytschko, "Blended mesh methods for fluid-structure interaction," *International Journal of Computational Methods*, vol. 1, no. 2, pp. 387–406, 2004.

45. C. Hirt, A. Amsden, and J. Cook, "An arbitrary lagrangian-eulerian computing method for all flow speeds," *Journal of Computational Physics*, vol. 14, pp. 227–253, 1974.

46. H. Chu, "Arbitrary lagrangian-eulerian method for transient fluid-structure interactions," *Journal of Nuclear Technology*, vol. 51, no. 3, pp. 363–377, 1980.

47. F. Brezzi and K. Bathe, "A discourse on the stability conditions for mixed finite element formulations," *Journal of Computer Methods in Applied Mechanics and Engineering*, vol. 82, pp. 27–57, 1990.

48. D. Arnold, D. Boffi, and R. Falk, "Quadrilaterial h(div) finite elements," *Journal of Numerical Analysis*, vol. 42, no. 6, pp. 2429–2451, 2005.

49. R. Snyder, J. Hur, D. Strong, and P. Beran, "Aeroelastic analysis of a high-altitude long-endurance joined-wing aircraft," No. AIAA 2005-1948, (Austin, TX), 46th AIAA Structures, Dynamics and Materials COnference, April 2005.

50. M. Patil, D. Hodges, and C. Cesnik, "Nonlinear aeroelasticity and flight dynamics of high-altitude long-endurance aircraft," *Journal of Aircraft*, vol. 38, no. 1, pp. 88–94, 2001.

51. M. Drela, "Integrated simulation model for preliminary aerodynamic, structural, and control-law design of aircraft," No. AIAA 1999-1394, (St. Louis, MO), 40th AIAA Structures, Dynamics and Materials Conference, April 1999.

52. D. Lee and C. P.C., "Nonlinear aeroelastic studies on a joined-wing with wing buckling effects," No. AIAA-2004-1944, (Palm Springs, CA), 45th AIAA/ASME/ASCE/AHS/ASC Structure, Structural Dynamics and Materials Conference, April 2004.

53. T. Strganac, P. Cizmas, C. Nichkawde, J. Gargoloff, and P. Beran, "Aeroelastic analysis for future air vehicle concepts using a fully nonlinear methodology," No. AIAA 2005-2171, (Austin, TX), 46th AIAA Structures, Dynamics and Materials COnference, April 2005.

54. D. Patil and D. Taylor, "Gust response of highly flexible aircraft," No. AIAA 2006-1638, (Honolulu, HI), 48th AIAA/ASME/ASCE/AHS/ASC Structures, Structural Dynamics, and Materials Conference, May 2006.

55. D. Patil, "Nonlinear gust response of highly flexible aircraft," No. AIAA 2007-2103, (Newport, RI), 47th AIAA/ASME/ASCE/AHS/ASC Structures, Structural Dynamics, and Materials Conference, May 2007.

56. F. Hoblit, *Gust Loads on Aircraft: Concepts and Applications*. AIAA Education Series, 1988.

57. P. Bochev and M. Gunzburger, "Finite element methods of least-squares type," *Society for Industrial and Applied Mathematics Review*, vol. 40, no. 4, pp. 789–837, 1998.

58. A. Saada, *Elasticity Theory and Applications*. Krieger Publishing Company, 2nd ed., 1991.

59. R. Hibbeler, *Mechanics of Materials*. Prentice Hall, 5th ed., 2002.

60. A. Nayfeh and P. Pai, *Linear and Nonlinear Structural Mechanics*. John Wiley and Sons, 2004.

61. Y. Fung, *Foundations of Solid Mechanics*. Prentice Hall, 1965.

62. S. Timoshenko and J. Goodier, *Theory of Elasticity*. McGraw-Hill, 3rd ed., 1969.

63. D. Wickert and R. Canfield, "Least-squares continuous sensitivity analysis of an example fluid-structure interaction problem," No. AIAA-2008-1896, (Schaumburg, IL), 49th AIAA/ASME/ASCE/AHS/ASC Structures, Structural Dynamics, and Materials Conference, April 2008.

64. D. Tremblay and D. P. S. Etienne, "Code verification and the method of manufactured solutions for fluid-structure interaction problems," No. AIAA-2006-3218, (San Francisco, CA), 36th AIAA Fluid Dynamics Conference and Exhibit, June 2006.

65. K. Surana, S. Petti, A. Ahmadi, and J. Reddy, "On p-version hierarchical interpolation functions for higher-order continuity finite element models," *International Journal of Computational Engineering Science*, vol. 2, no. 4, pp. 653–673, 2001.

66. E. Kreyszig, *Advanced Engineering Mathematics*. John Wiley and Sons, 8th ed., 1999.

67. F. White, *Viscous Fluid Flow*. McGraw-Hill, 3rd ed., 2006.

68. L. Stivers, "Effects of subsonic mach number on the forces and pressure distributions on four naca 64a-series airfoil sections at angles of attack as high as 28 degrees," *National Advisory Committee for Aeronautics*, no. 3126, pp. 1–146, 1954.

69. K. Thompson, "Time dependent boundary conditions for hyperbolic systems," *Journal of Computational Physics*, vol. 68, pp. 1–24, 1987.

70. J. Nordstrom, "The use of characteristic boundary conditions for the navier-stokes equations," *Journal of Computers and Fluids*, vol. 24, no. 5, pp. 609–623, 1995.

71. C. Hirsch, C. Lacor, and H. Deconinck, "Convection algorithms based on a diagonalization procedure for the multidimensional euler equations," No. AIAA-1987-1163, (Honolulu, HI), 8th Computational Fluid Dynamics Conference, June 1987.

72. T. Poinsot and S. Lele, "Boundary conditions for direct simulations of compressible viscous flows," *Journal of Computational Physics*, vol. 101, pp. 104–129, 1992.

73. J. Lysmer and R. Kuhlemeyer, "Finite dynamic model for infinite media," *Engineering Mechanics Division of American Society of Civil Engineers*, vol. 95, no. EM4, pp. 859–877, 1969.

74. X. Wang, "Analytical and computational approaches for some fluid-structure interaction analyses," *Journal of Computers and Structures*, vol. 72, pp. 423–433, 1999.

75. J. Arora, *Introduction to Optimum Design*. McGraw-Hill, 2001.

76. M. Heil, "An efficient solver for the fully-coupled solution of large-displacement fluid-structure interaction problems," *Computer Methods in Applied Mechanics and Engineering*, 2003.

77. D. Hodges and G. A. Pierce, *Introduction to Structural Dynamics and Aeroelasticity*. Cambridge University Press, 2002.

Vita

Major Cody C Rasmussen graduated from Cottonwood High School in Salt Lake City, Utah. He entered undergraduate studies at the United States Air Force Academy, Colorado where he graduated with a Bachelor of Science degree in Engineering Mechanics and was commissioned in the United States Air Force in June 1999.

He was stationed at Los Angeles Air Force Base immediately after being commissioned. He worked as a Systems Engineer, a program manager, and an executive officer in the Space-Based Laser Project Office under the command of the Space and Missile Systems Center. In March 2004, he earned his Masters of Science degree in Aeronautical Engineering at the Graduate School of Engineering and Management, Air Force Institute of Technology. After that, he worked as an instructor at the United States Air Force Academy in the Engineering Mechanics Department. In August, 2005 he entered the Ph.D. program at the Air Force Institute of Technology.

REPORT DOCUMENTATION PAGE

Form Approved
OMB No. 074-0188

1. REPORT DATE *(DD-MM-YYYY)*	**2. REPORT TYPE**	**3. DATES COVERED** *(From – To)*
26 Mar 09	**Doctoral Dissertation**	1 Oct 05 – 26 Mar 09

4. TITLE AND SUBTITLE

LEAST-SQUARES FINITE ELEMENT FORMULATION FOR FLUID-STRUCTURE INTERACTION

5a. CONTRACT NUMBER

5b. GRANT NUMBER

5c. PROGRAM ELEMENT NUMBER

6. AUTHOR(S)

Rasmussen, Cody C, Major, USAF

5d. PROJECT NUMBER

5e. TASK NUMBER

5f. WORK UNIT NUMBER

7. PERFORMING ORGANIZATION NAMES(S) AND ADDRESS(S)
Air Force Institute of Technology
Graduate School of Engineering and Management (AFIT/EN)
2950 Hobson Way
WPAFB OH 45433-7765

8. PERFORMING ORGANIZATION REPORT NUMBER

AFIT/DS/ENY/09-M16

9. SPONSORING/MONITORING AGENCY NAME(S) AND ADDRESS(ES)
Air Force Research Laboratory, Air Vehicles Directorate
Attn: Dr. Maxwell Blair
2210 Eighth Street, Room 220
WPAFB, OH 45433-7531 Comm : (937)255-8430

10. SPONSOR/MONITOR'S ACRONYM(S)
AFRL/RBSD

11. SPONSOR/MONITOR'S REPORT NUMBER(S)

12. DISTRIBUTION/AVAILABILITY STATEMENT
APPROVED FOR PUBLIC RELEASE; DISTRIBUTION UNLIMITED.

13. SUPPLEMENTARY NOTES

14. ABSTRACT

Fluid-structure interaction problems prove difficult due to the coupling between fluid and solid behavior. Typically, different theoretical formulations and numerical methods are used to solve fluid and structural problems separately. The least-squares finite element method is capable of accurately solving both fluid and structural problems. This capability allows for a simultaneously coupled fluid structure interaction formulation using a single variational approach to solve complex and nonlinear aeroelasticity problems. The least-squares finite element method was compared to commonly used methods for both structures and fluids individually. The fluid analysis was compared to finite differencing methods and the structural analysis type compared to traditional Weak Galerkin finite element methods. The simultaneous solution method was then applied to aeroelasticity problems with a known solution. Achieving these results required unique iterative methods to balance each domain's or differential equation's weighting factor within the simultaneous solution scheme. The scheme required more computational time but it did provide the first hands-off method capable of solving complex fluid-structure interaction problems using a simultaneous least-squares formulation. A sequential scheme was also examined for coupled problems.

15. SUBJECT TERMS
Aeroelasticity, Fluids, Structure, Fluid-Structure Interaction, Least-Squares Finite Element Method

16. SECURITY CLASSIFICATION OF:			**17. LIMITATION OF ABSTRACT**	**18. NUMBER OF PAGES**	**19a. NAME OF RESPONSIBLE PERSON**
REPORT	**ABSTRACT**	**c. THIS PAGE**			Canfield, Robert A.
U	**U**	**U**	**UU**	276	**19b. TELEPHONE NUMBER** *(Include area code)* (540) 231-5981; e-mail: bob.canfield@vt.edu